Photocatalytic Degradation of Methyl Orange Using Modified Mesoporous TiO_2 and Au_9 Clusters

By

Anahita Motamedisade

Thesis
Submitted to Flinders University
for the degree of

Doctor of Philosophy
College of Science and Engineering

04/12/2023

I dedicate this thesis, which is everything to me, to the one and only God, and to the memory of my kind and loving Dad, Mr. Mahdigholi Motamedi (1951-2018)

CONTENTS

ABSTRACT

Au nanoclusters (Au NCs) exhibit intriguing size-dependent catalytic, electronic, and optical properties. This thesis uncovers the pivotal role of Au NCs in enhancing the photocatalytic efficiency of titanium dioxide (TiO_2) through improved charge separation.

As the catalytic efficiency of these NCs is closely linked to their size, preventing Au_9 NCs' agglomeration becomes essential to enhance catalytic activity, particularly following heat treatment aimed at ligand removal. The study focuses on designing novel systems capable of adsorbing high levels of ultra-small Au_9 NCs and preventing their agglomeration during deposition and annealing processes.

The first approach to achieving this aim involves the preparation of mesoporous TiO_2 ($MTiO_2$) with a high density of surface defects, a high specific surface area, and a 3D pore network. These structures provide anchoring sites for the adsorption of Au_9 NCs, curbing their mobility and suppressing the tendency to aggregate. Another strategy involves introducing functional groups on the mesoporous TiO_2 surface through N or S functionalisation. These chemically modified $MTiO_2$ surfaces can potentially establish a more robust bond between the Au_9 NCs and the $MTiO_2$ substrate, preventing agglomeration.

Comprehensive characterisation techniques, including X-ray Diffraction (XRD), Fourier Transform Infrared Spectroscopy (FTIR), Scanning Electron Microscopy (SEM), X-ray Photoelectron Spectroscopy (XPS), Near-edge X-ray absorption fine structure (NEXAFS), Energy-Dispersive X-ray Spectroscopy (EDS), High-Resolution Transmission Electron Microscopy (HRTEM), and Scanning Transmission Electron Microscopy (STEM), provide detailed insights into the properties of the nanocomposites such as the phase type of TiO_2, surface morphology and chemistry, and elemental composition, as well as size and dispersity of the Au_9 NCs immobilised onto the substrate surface.

A comprehensive investigation into the relative impacts of surface modification and functionalisation strategies on enhancing the loading of Au_9 NCs while mitigating agglomeration is conducted using XPS. Subsequently, the most promising photocatalyst system is identified, and an in-depth analysis of its photocatalytic efficiency in the degradation of methyl orange dye is conducted. Reaction parameters are systematically examined, and their interrelationships are established by applying response surface methodology (RSM).

In this study, the deposition of Au_9 NCs onto S-functionalised mesoporous TiO_2 ($SMTiO_2$) is studied to produce efficient photocatalysts. The $SMTiO_2$ substrates prevent the agglomeration of Au_9 NCs and enhances the overall loading. Furthermore, nanocomposites of N-functionalised mesoporous TiO_2 ($NMTiO_2$) embedded with Au_9 NCs are created using a chitosan-assisted soft templating

method. The study evaluates the influence of calcination atmosphere on substrate properties and the adsorption of Au_9 NCs. The black NMTiO_2 surfaces enhance loading and prevent agglomeration of Au_9 NC even after heating, leading to improved photocatalytic effectiveness.

Transitioning to more sustainable industrial processes is crucial for addressing global challenges. This study focuses on clean drinking water scarcity, specifically addressing hazardous run-offs from chemical industries. Methyl orange (MO) dye, a common environmental pollutant, is chosen as a model compound for studying photocatalytic degradation. The study emphasizes the examination of diverse parameters affecting the degradation of MO dye and study their relationship using Response Surface Methodology (RSM).

In conclusion, the abstract encapsulates the objectives, methodologies, and key findings of the study, providing a comprehensive overview of the research conducted on Au_9 NCs and their role in enhancing the photocatalytic efficiency of TiO_2. In this comprehensive journey, our thesis elevates the art of surface modification, where science and creativity come together, opening new possibilities across various materials and systems.

DECLARATION

I certify that this thesis does not incorporate without acknowledgment any material previously submitted for a degree or diploma in any university; and that to the best of my knowledge and belief it does not contain any material previously published or written by another person except where due reference is made in the text.

Signed...Anahita Motamedisade.....
Date...04/12/2023.....

ACKNOWLEDGEMENTS

First, I would like to express my gratitude to God who is everything to me. My faith in Him gave me the motivation to keep working hard, and as a result, I was able to graduate. Life would be difficult, and I would not have achieved anything without his kindness and support. He did never forget me even when I had forgotten him sometimes during my hardships and challenges in my life. He helped me a lot anywhere and everywhere I needed and wanted. Placing some kind, knowledgeable, helpful, caring, and supportive people surrounded me had not have any reason other than his kindness, love, blessing and support.

I am constantly on the lookout for a chance to express my gratitude to my main supervisor, Professor Gunther G. Andersson. He is a devoted expert in the domains of surface and interface analysis, spectroscopy, and the physical science of materials. Professor Andersson has been an invaluable guide, helping me navigate the challenges in my research journey and enabling me to achieve a modest yet significant breakthrough in the field. His support has extended to various aspects of my academic and life pursuits. Moreover, he is a genuinely kind individual, possessing a wealth of knowledge while maintaining a humble and unassuming demeanour, which has earned him the respect of everyone he interacts with.

I would like to thank the panel of my thesis reviewer, Professors Claire Lenehan and Sarah Harmer, who were so knowledgeable, kind and patient and motivated me with their always positive attitude and helpful comments.

I would also like to really thank OGR, HDR progression team and coordinators, scholarship office and all staff working at Flinders university because of being always supportive and kind to me. I would like, from the bottom of my heart, to acknowledge Professor Colin Raston for fully supporting me in working with his facilities like VFD without any expectations. I learned a lot from his character about what the meaning of humanity is. It was a fantastic opportunity and a great experience for me to work in his unforgettable laboratory environment among his supportive, helpful, and kind students and researchers, particularly, Professor Amir Heydari, who is very expert in data analysis and always supportive, patient, and passionate during our collaboration. Indeed, I may not have graduated if his supportive presence, advice, and encouragement were not along with me. I always owe to Professor Colin Raston and his fantastic research team.

I would also like to extend my appreciation to my associate mentor, Professor David A. Lewis. He possesses a wealth of experience in the realm of organic materials, devices, and the process of bringing innovations to the market.

I would also like to thank my associate supervisor in Wine Australia- Professor Paul Smith who accepted my Winery wastewater treatment proposal as one of the Wine Australian award recipients.

He was my always humble and expert mentor and gave me this opportunity to find my industry view.

I would also like to acknowledge Professor. Martin Johnston, who was knowledgeable, kind, and helpful. Collaboration with him in one of my important projects, synthesis of Au nanoclusters, was a great experience and a fantastic chance for me knowing him to benefit his knowledge.

I would also like to thank Yanting Yin, a post-doc in our group, who was an expert and supportive person, and he kindly helped me a lot whenever and wherever I needed. Benjamin A. Chambers who was so supportive and kind in our group and gave a systemic training on the equipment and taught me how to be outstanding but such a humble. Alex Sibley helped me kindly on the measurement of Scanning Microscopy and XRD. Liam helped me on XPS measurement when I was in hurry to get a result. I would like to thank them. All group members, Abdul, Amira, Anand, Ahlam, Sunita and other colleagues, I really appreciate for your help and supports. Also, Colin's group, was really kind and supportive during working with them. you helped me a lot and I really appreciate it.

Great thanks to my Scholarships, (RTP) from Australian Government and Top-up scholarship from Wine Australia. I would also thank to Australian Nanotechnology Network, ANNF, AMMRF and Flinders Nano centre.

I owe my achievements to the unwavering support of my family, including my beautiful daughter, Aylar Farizadeh, Mother, and siblings. Their contribution is immeasurable, and my gratitude towards them knows no bounds. They showered me with unconditional love, constant encouragement, and invaluable emotional support.

I am profoundly grateful to all those who extended their love, motivation, and assistance to me. The years spent at Flinders University in Australia will forever hold a special place in my heart as unforgettable memories in my life's journey.

PUBLICATIONS AND CONFERENCES

Published and Submitted Articles from 2019-2023

1-Both Tough and Soft Double Network Hydrogel Nanocomposite based on O-carboxymethyl Chitosan / Poly (vinyl alcohol) and Graphene Oxide: A Promising Alternative for Tissue Engineering.
Ali Pourjavadi, Zahra Mazaheri Tehrani, Hamid Salimi, Farzad Seidi, **Anahita Motamedi**, Amirhossein Amanzadi, Ehsan Zayerzadeh, Meisam Shabanian
Polymer Engineering & Science published:04 April 2020.
https://doi.org/10.1002/pen.25297

2-Sensitization of TiO_2 nanoarrays by a novel Palladium decorated Naphthalene diimide functionalised graphene nanoribbons for enhanced photoelectrochemical water splitting
Hamed Esmaili, Elaheh Kowsari, Seeram Ramakrishna, **Anahita Motamedisade** and Gunther G. Andersson.
Materials Today Chemistry, Volume 24, June 2022.
https://doi.org/10.1016/j.mtchem.2022.100900

3-Calcium alginate hydrogels reinforced with cellulose nanocrystals for methylene blue adsorption: Synthesis, characterisation, and modelling.
Soraya Soleimani, Amir Heydari, Moslem Heydari, Moslem Fattahi, **Anahita Motamedisade.**
Industrial Crops and Products, Volume 192, February 2023.
https://doi.org/10.1016/j.indcrop.2022.115999

4- Au_9 Nanocluster Adsorption and Agglomeration Control through Sulfur Modification of Mesoporous TiO_2. (submitted)
Anahita Motamedisade, Martin Johnston, Amjad E.H. Alotaibi, Gunther Andersson

5- Highly Efficient Binding Au_9 Clusters to Chemically S-Modified Mesoporous TiO_2: Study of Photocatalytic Degradation of Methyl Orange Dye by Response Surface Methodology. (submitted)
Anahita Motamedisade, Amir Heydari, D. J. Osborn, Abdulrahman S. Alotabi, Gunther Andersson

6- Enhanced Photocatalytic Degradation of Methyl Orange Using Nitrogen-Functionalised Mesoporous TiO_2 Decorated with Au_9 Nanoclusters. (submitted)
Anahita Motamedisade, Martin Johnston, Amir Heydari, Yanting Yin, Abdulrahman S. Alotabi, Gunther Andersson.

Conference Oral Presentations:

1-Australian Colloids and Interface Society Conference ,2021, University of South Australia, Adelaide

2-Pacifichem 2021, International Chemical Congress of Pacific Basin Societies, USA, Hawaiian December 16 – 21, 2021.

3-33rd Australian Colloid and Surface Science Student Conference -31 January 2022

4- International Summit on Nanotechnology and Nanomaterials, ISNN 2023, 10-11 August, London, UK.

5-12th Asian Photochemistry Conference- Melbourne, 27 November-1 December 2023.

Conference Poster Presentations:

6-HDR Student Conference, 2019, Flinders University

7-Doc fest poster presentation 2020- Flinders University -Best poster award

8-AIP Publishing Horizons – Applied Physis Reviews - Energy Storage and Conversion, July 2021.

9-17th Conference of International Association of Colloid and Interface Scientists (IACIS 2022)" - 26-30 June 2022, Brisbane, Queensland

10-Nano institute poster presentation- Flinders University-2023

ABBREVIATION LIST OF CHEMICALS AND SYMBOLS

MPTMS	*3-mercaptopropyltrimethoxysilane*
$MTiO_2$	*Mesoporous TiO_2*
EISA	*Evaporation-Induced Self-Assembly method*
$SMTiO_2$	*S functionalised mesoporous TiO_2*
$NMTiO_2$	*N functionalised mesoporous TiO_2*
Au	*Gold*
N	*Nitrogen*
S	*Sulphur*
Si	*Silicon*
Pt	*Platinum*
Al	*Aluminium*
C	*Carbon*
NCs	*Nanoclusters*
NPs	*Nanoparticles*
FTO	*Fluorine-doped Tin Oxide*
P123	*Poly (ethylene glycol)-block-poly (propylene glycol)-block-poly (ethylene glycol)*
Ar	*Argon*
VFD	*Vortex Fluidic Device*
UV	*Ultraviolet*
MO	*Methyl Orange*
Hg	*Mercury*
CCD	*Central composite design*
RSM	*Response surface methodology*
TiO_2	*Titanium dioxide*
N_2	*Nitrogen gas*
O_2	*Oxygen gas*
Cat	*Catalyst*
Deg	*Degradation*
LM	*Light microscopy*
CB	*Conduction Band*
MO C.	*Methyl orange concentration*
XPS	*X-Ray photoelectron spectroscopy*
SEM	*Scanning electron microscopy*
EDS	*Energy-dispersive X-ray spectroscopy*
STEM	*Scanning transmission electron microscopy*
BJH	*Organic Light-emitting diode*
BET	*Brunauer, Emmett and Teller*
T	*Transmittance*
eV	*Electron volt*
TGA	*Thermal gravimetric analysis*
XRD	*X-ray powder diffraction*
FTIR	*Fourier transform infrared.*
NEXAFS	*Near-edge X-ray absorption fine structure*
EXAFS	*Extended X-ray absorption fine structure*
Mg	*Magnesium*
Co	*Cobalt*
Cu	*Cooper*
FWHM	*Full Width Half Maximum*
UHV	*Ultra-High Vacuum*
XP	*X-Ray photoelectron*
XAS	*X-ray absorption spectroscopy*
UHV	*Time of Flight*
XP	*Ultra-High Vacuum*
AS	*Australian Synchrotron*
DOS	*Density of states*
EBSD	*Electron backscatter diffraction*
FIB	*Focused ion beam*
FE	*Field emission*
Nm	*Nanometres*
H	*Hours*

VB	*Valence Band*
LUMO	*Lowest Unoccupied Molecular Orbit*
HOMO	*Highest Occupied Molecular Orbital*
	Conduction Band Energy
E_{VB}	*Valence Band Energy*
E_{CB}	*Conduction Band Energy*
3D	*Three-dimensional*
Ti	*Titanium*
O	*Oxygen*
TEM	*Transmission Electron Microscope*
HAADF	*High Angle Annular Dark Field*
BF	*Bright field*
ADF	*Annular dark field*
HRTEM	*High-resolution transmission electron microscope*
Mo	*Molybdenum*
ATR	*Attenuated total reflection.*
Ml	*Millilitre*
G	*Gram*
Min	*Minutes*
PPM	*Parts per million*
Mg	*Milligram*
RPM	*Revolutions per minute*
AOP	*Advanced oxidation processes*
IUPAC	*International Union of Pure and Applied Chemistry*
ANOVA	Analysis of Variance
HPLC	*Ultra-High Performance Liquid Chromatography*
ESI-TOF	*Electrospray Ionisation-Time of Flight*
MS	*Mass Spectrometry*
CO_2	*Carbon dioxide*
H_2O	*Water*

LIST OF FIGURES

LIST OF TABLES

CHAPTER 1: INTRODUCTION AND LITERATURE REVIEW

1.1. Background

1.1.1. Water pollution

The process of industrialisation up to the present day has produced many sources and classes of environmental pollution, many of which adversely affect human health. This research has focused on addressing the issue of water quality loss as one of the key factors of water risks. Chemical pollution stands as the most prevalent form of water pollution, impacting both subterranean and surface water sources. Dyes, heavy metals, and organic compounds such as polycyclic aromatic hydrocarbons, pesticides, and organochlorines are major hazardous water chemical contaminants. Dyes, often nonbiodegradable, toxic, and carcinogenic organic compounds, are released into nearby water bodies from the textile, dye manufacturing and cosmetic industries, polluting the environment and endangering human health. As shown in Figure 1.1, [1]synthetic dyes include azo, sulphur, direct, mordant, basic, acid, disperse, and reactive dyes[1] creating hazardous by-products through chemical reactions such as oxidation and hydrolysis. Watery plants also lose their photosynthetic ability because dyes impede sun rays and gas suspension, annihilating their ecosystems.[2-4]

Azo dyes represent more than 50% of the total global dye production. They are distinguished by the presence of the azo bond (–N=N–), in which R or R′ is an alkyl or aryl moiety. The important building blocks of azo dyes are aromatic amines. It has been reported that some azo compounds are stable, remain in the environment for long periods of time and cannot be detected in wastewater by simple techniques.[5,6] They are used in fabric, cosmetics, lithography, food, and medical products. Also, synthetic azo compounds are well known for their wide range of technological demands, including photonic devices, photovoltaics, laser dyes, and diabetes treatment.[1]

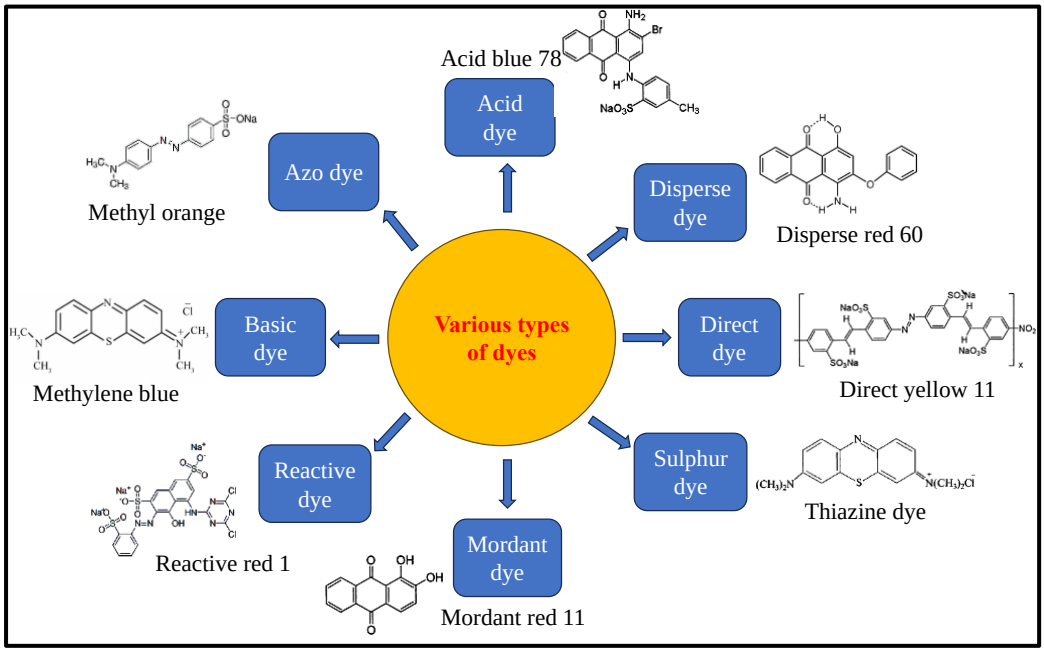

Figure 1.1.Various types of dyes[1]

1.1.1.1.Methyl orange (MO) dye

Methyl orange (MO) dye is a common Azo dye used in several industries can pose environmental risks if not handled and disposed of properly[7]. Here are some potential environmental dangers associated with MO.[8]

1) Toxicity: MO is a synthetic chemical compound, and its components can be toxic to aquatic life and other organisms if released into the environment. The dye itself may not be highly toxic, but its breakdown products or impurities could be harmful.
2) Persistence: MO can persist in the environment for a significant period, especially if it is not efficiently degraded. This persistence can lead to long-term environmental contamination.
3) Bioaccumulation: Some chemicals used in dyes, including those in MO, can be absorbed and accumulated in living organisms, potentially causing harm to the organisms and those higher up in the food chain.
4) Discharge into water bodies: Improper disposal of MO-containing wastewater into rivers, lakes, or other water bodies can lead to water pollution, disrupting aquatic ecosystems and harming aquatic organisms.
5) Affecting water quality: MO, if released in large quantities, can alter the colour of water bodies, affecting their aesthetic and potentially making it difficult for aquatic organisms to survive.

1.1.1.2.Oxidative degradation of dyes

Azo dye removal is difficult because of its solubility in water, complex structure, and synthetic nature. Therefore, it is crucial to develop efficient methods for eliminating dyes from wastewater[9-11]. Common wastewater treatments alone are not sufficient for water renewal due to the presence of such chemicals with aromatic rings resistant to chemical, photochemical, and biological degradation. Disposal of treated water results in these rings being detected everywhere.[12]

The removal of dyes in wastewater can be achieved in many ways, including chemical, physical, and biological methods, but these methods have high degradation and maintenance costs, and some of them produce secondary by-products that need further treatment, so they are not proper and economical for wastewater treatment.[13-19] Recognizing the critical importance of advancing wastewater treatment methods for long-term environmental sustainability, there has been a recent surge in interest towards heterogeneous photocatalytic systems. These systems have garnered increased attention for their capacity to effectively convert hazardous contaminants into harmless substances through complete mineralization, offering a versatile solution for diverse pollutants. Moreover, the distinct advantage of heterogeneous photocatalysis lies in its straightforward catalyst removal post-reaction, making it a superior choice for wastewater treatment when compared to homogeneous photocatalysis.[19]

In general, oxidative degradation of dyes is the most effective method for removing colour. They are referred to as advanced oxidation processes (AOPs). In an AOP method, highly reactive catalyst-like species (i.e., H_2O_2, $OH^{\cdot}$, $O_2^{\cdot -}$, O_3) are generated in situ for the mineralization of organic compounds, disinfection by-products, and water pathogens. The motivation behind this study arises from the extensive research and development efforts spanning the past three decades in the field of Advanced Oxidation Processes (AOP) and photocatalysts based on TiO_2. This chapter discusses the targeted pollutants used throughout the study. Photocatalysis and its mechanism are described in this chapter. TiO_2 nanomaterials have optical properties that underpin their suitability for many applications. For this reason, this chapter also discusses the challenges associated with TiO_2 modification and their possible solutions.[9,20-24]

1.1.2. Semiconductor photocatalyst principle

The discovery of the “Honda-Fujishima Effect” in the early 1970s led to significant interest in photocatalysis systems. Generally, a photoreaction velocity in the presence of a light-activated catalyst, can be defined as a term of ‘photocatalysis’. The overall semiconductor photoreaction process is summarised as follows:[25]

$$A + D \xrightarrow{\text{Semiconductor/ light} \geq E_{bg}} A^- + D^+$$

A semiconductor is a material that falls between a conductor and an insulator in terms of its electrical resistivity. What sets semiconductor types apart is the band gap, which represents the difference between the valence band (VB), the highest energy band occupied by electrons, and the conduction band (CB), the lowest energy band with the lowest empty band.[26] This band gap dictates the spectrum of light wavelengths that the semiconductor can absorb. When photons possess energy equal to or greater than the band gap, they can elevate electrons from the valence band (VB) to the conduction band (CB), generating pairs of electrons and holes (Figure 1.2).[27] This process is essential in photovoltaic and photocatalytic applications, as it generates charge carriers that can participate in chemical reactions, or be harvested for electrical energy.[25,28]

The position of the valence band and conduction band relative to the electrochemical energy scale, particularly in p-type and n-type semiconductors, plays a critical role in determining a semiconductor's ability to facilitate a reaction. Additionally, the band gap of the semiconductor determines the specific range of light wavelengths it can absorb. In p-type semiconductors, the valence band is closer to the electrochemical energy scale, while in n-type semiconductors, the conduction band is closer to the electrochemical energy scale. This difference in band positions influences the movement of electrons and holes (electron vacancies) within the semiconductor. When the valence band is closer to the electrochemical energy scale in p-type semiconductors, it becomes easier for holes (positive charge carriers) to move into the semiconductor from the external environment, and this can facilitate oxidation reactions (loss of electrons). Conversely, in n-type semiconductors, the conduction band being closer to the electrochemical energy scale promotes the movement of electrons into the semiconductor, which can facilitate reduction reactions (gain of electrons).[29,30]

In semiconductor particles, there are two important scenarios to consider. The first scenario involves the recombination of charge pairs, which is something we want to avoid if we aim to create an efficient photocatalyst. When charge pairs recombine, it means that the separated electrons and holes, which are crucial for driving chemical reactions in photocatalysis, come back together instead of participating in useful reactions. This recombination is a major drawback because it reduces the efficiency of the photocatalyst. The second scenario relates to the trapping of electrons and holes in the surface states of the semiconductor particles. These trapped charge carriers can react with certain substances called electron acceptors (such as H^+ or oxygen molecules) or electron donors (such as OH^- groups or organic molecules). These substances can either be adsorbed onto the surface of the particles or be in close proximity to them (Figure 1.2).[27] This trapping and subsequent chemical reactions are important for the photocatalytic process[31,32]. For a photocatalyst to be effective, it needs to strike a balance between different processes involving electrons and holes. On one hand, it must facilitate reactions that utilise these charge carriers for useful chemical transformations. On the other

hand, it should minimize processes that lead to the deactivation of the photocatalyst, such as electron-hole recombination. In essence, the photocatalyst should efficiently manage these electron-related processes to maximize its performance in driving photocatalytic reactions.

The use of semiconductors as photocatalysts is also dependent on factors such as their ease of production, their cost-effectiveness, their photostability, their non-toxicity to humans and the environment, their ability to be activated by sunlight, and their ability to catalyse reactions successfully.[27,33]

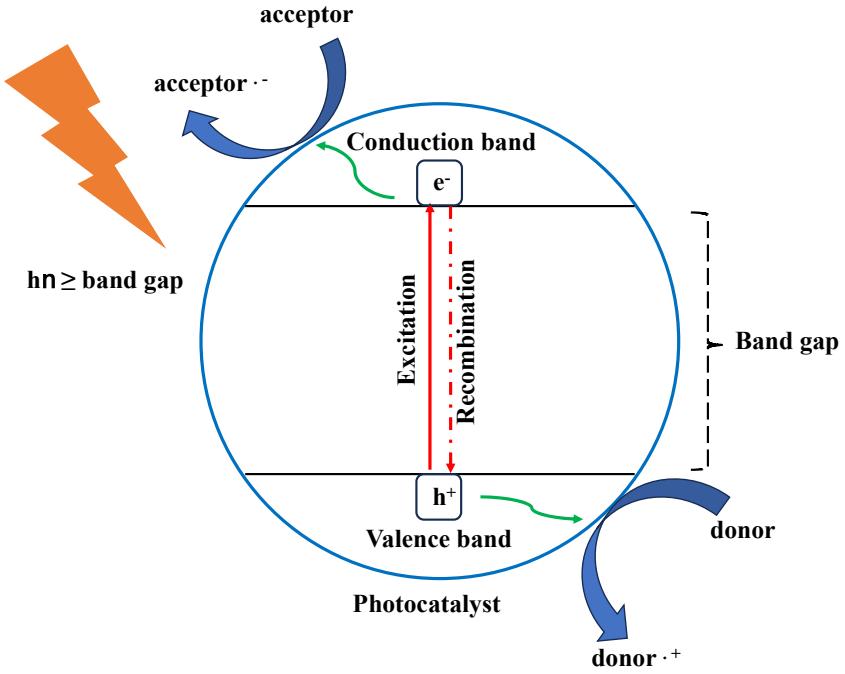

Figure 1.2. Schematic illustration of semiconductor photocatalyst activated by photogenerated electrons and holes.[27]

Different semiconductors with various band gaps, including ZrO_2, $KTaO_3$, $SrTiO_3$, ZnS, CdSe, SiC, MoS_2, WO_3, Fe_2O_3, GaP, ZnO, CdS, and TiO_2 have been utilised in photocatalysis due to desirable electronic structure composition, charge transport characteristic, light absorption features, and the excited-state lifetime[34,35]. The surface area and the quantity of active sites on the photocatalyst are pivotal factors in assessing the overall degradation rate.[18]

1.1.3. Nano porous semiconductor

The nanomaterial properties can be improved by making pores in their structure, attracting a great deal of research attention for application in catalysis, energy storage and conversion, sensing, adsorption, separation, and biotechnology.[36]

The International Union of Pure and Applied Chemistry (IUPAC) has categorised nanoporous materials into three distinct classes based on their pore sizes. These classes include microporous materials, characterised by pore sizes smaller than 2 nanometers; mesoporous materials, which have

pore sizes ranging from 2 to 50 nanometers; and macroporous materials, distinguished by pore sizes exceeding 50 nanometers.[37,38]

Today, mesoporous materials are of increasing interest to researchers. This is not only because they can act as hosts for bulky molecules but because they possess several unique structures and properties. Their tuneable large pore size, high pore volume, large surface area, and various morphologies and compositions make them suitable for a wide variety of applications, including photocatalysis, supercapacitors, medicine, electronics, biotechnology, solar cells, and lithium-ion batteries.[36]

To date, activity and synthesis of various mesoporous semiconductors, such as SiO_2, TiO_2, ZnO, Al_2O_3, Fe_2O_3, WO_3, Nb_2O_5, ZrO_2, Ta_2O_5, SnO_2, Co_3O_4, $SiTiO_4$, $ZrTiO_4$, MoS_2, $ZrW2O_8$, Ta_3N_5, and ZnS have been widely studied. However, none illustrate the enhanced properties and advantages of mesoporous TiO_2.[39-41]

1.1.4. Metal nanocluster (NCs) definition

Metal nanoclusters (NCs) are composed of a relatively small number of atoms, usually numbering in the tens or fewer. These NCs can consist of a single element or multiple elements and are typically smaller than 1.5 nm in diameter. Metal NCs have unique properties due to their small size and quantum confinement effects. Here are some key properties of metal NCs.[42-44]

1. **Size-Dependent Properties:** An important factor influencing the properties of NCs is their size. The surface area-to-volume ratio increases as the size decreases because atoms are distributed more evenly at the surface. It can result in distinctive electronic and catalytic properties.[45]
2. **Quantum Size Effects:** A discrete energy level is created by quantizing electronic energy levels at the nanoscale. A quantum confinement effect can cause colour changes in their absorption and emission spectra. These effects are especially evident in metal nanoclusters when their sizes are comparable to or smaller than electron characteristic lengths.[46]
3. **Electronic Properties:** Metal NCs are also affected by quantum confinement effects. The discrete energy levels of these materials make them suitable for electronic and catalytic applications.[47]
4. **Catalytic Activity:** The high surface area of metal NCs can provide more active chemical reaction sites, giving them unique catalytic properties. Their electronic structure and quantum size effects can also enhance catalytic activity and selectivity.[48]
5. **Surface Chemistry:** In comparison to bulk materials, nanoclusters have chemically reactive surface atoms. This makes them useful for catalysis, sensors, and other applications where surface interactions play a crucial role.[46]

6. **Stability:** The stability of nanoparticles or bulk materials may differ from that of nanoclusters. Small sizes of clusters can result in a high surface energy, increasing their aggregation and oxidation potential. Stability is often enhanced by using surface ligands or protective coatings.[49]
7. **Chemical Sensing:** They are excellent candidates for chemical and biological sensing applications due to their size-dependent properties and high surface area. They can change their optical or electrical properties upon interaction with target molecules.[50]

These properties make metal NCs promising candidates for a wide range of applications, including catalysis, electronics, photonics, sensing, medicine, and energy conversion. However, it is imperative to note that the properties of nanoclusters can be highly dependent on factors such as their composition, size, shape, and the surrounding environment.[51-53]

1.2. Titanium dioxide (TiO_2)

1.2.1. Background

TiO_2 is classified within the category of transition metal oxides and is an important candidate for several technological applications. Researchers have studied TiO_2-based nanomaterials as potential photocatalysts for environmental purification due to its low cost, photosensitivity, and low toxicity, as well as good thermal and chemical stability with the suitable band structure.[54] TiO_2 has found numerous applications to date, spanning fields such as water treatment, hydrogen production, photovoltaic cells, anti-fogging surfaces, air purification, self-cleaning coatings, enhancement of heat transfer and dissipation, photocatalytic lithography, corrosion prevention, environmentally friendly surface treatments, photochromism, and more.[55] The utilisation of solar energy as the primary radiation source to activate such photocatalysts becomes feasible when the band gap is sufficiently small. Conversely, if the band gap is high, ultraviolet radiation is required. Nevertheless, when this band gap is modified through doping, the use of TiO_2 in sunlight can lead to the degradation of contaminants in wastewater. This highlights the versatility and potential of TiO_2-based photocatalysis in addressing environmental challenges.[41,56]

1.2.2. Properties of TiO_2 semiconductor

Two factors impacting TiO_2 efficacy are its crystalline arrangement and size. Notably, TiO_2 is found in three prominent polymorphs: anatase, rutile, and brookite. Rutile, the thermodynamically stable form, prevails under various conditions.[57-60] It shapes through octahedra edge-sharing, forming extensive chains, whereas anatase results from octahedra point-sharing. Brookite, on the other hand, emerges from the interplay of edge and point sharing (See Figure.1.3[61]) When subjected to elevated temperatures during coarsening, TiO_2 brookite and anatase forms tend to transition into the rutile

configuration. In the photocatalytic systems, the rutile and anatase phases of TiO_2 have been subject to the most extensive scrutiny and research.[62-64]

In the realm of photocatalytic applications, brookite is notably limited due to the difficulty of reliable synthesis and its inherent lack of photocatalytic activity. Rutile, on the other hand, while having a smaller band gap (3.0 eV) than anatase and brookite, generally fails to perform adequately as a photocatalyst. This diminished photocatalytic efficiency associated with the rutile phase of TiO_2 is attributed to its limited light absorption, particularly within the UV range.[62,65]

Additionally, the alignment of conduction and valence band edges seen in anatase is not as pronounced in rutile. Conversely, for photocatalytic purposes, anatase is favoured among the available phases.[66,67] This preference stems from its greater electron mobility, lower dielectric constant, reduced density, diminished oxygen adsorption capacity, and elevated level of hydroxylation in comparison to rutile and brookite.[60,68]

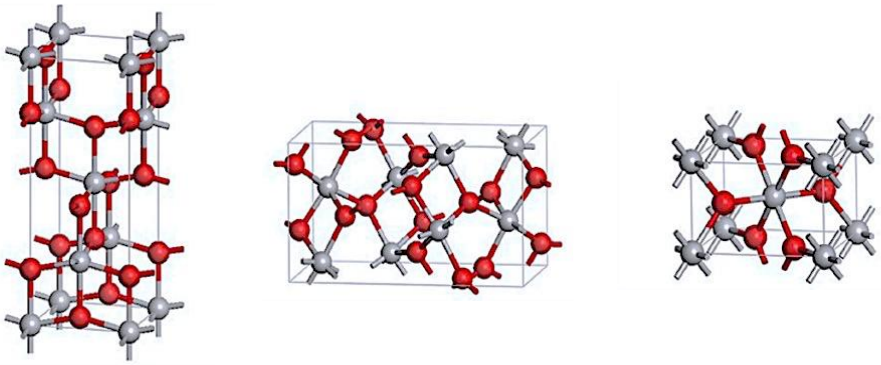

Anatase Brookite Rutile

Figure 1.3. Crystalline Tetragonal structures of rutile, anatase and brookite TiO_2 NPs (spheres: red—O_2, grey—Ti). Based on Baranowska-Wójcik et al.[61]

1.2.3. TiO_2 semiconductor in photocatalysis

TiO_2 is indeed known for its photocatalytic features, and the creation of hydroxyl radicals (OH•) plays a significant role in its ability to break down organic contaminants when exposed to UV light. This process is often referred to as photocatalysis and has a wide range of applications in environmental remediation and water purification. Here is how it works:

UV light absorption: Titanium dioxide absorbs UV light effectively.

Generation of electron-hole pairs: Under UV light exposure, TiO_2 produces pairs of electrons and holes, with electrons residing in the conduction band and holes occupying the valence band.

Reactive species formation: In photocatalytic processes, the holes generated in the valence band (VB) eventually migrate to the surface of TiO_2. They interact with water molecules or hydroxide ions (OH^-) present in a liquid environment, leading to the formation of hydroxyl radicals (OH·). Simultaneously, electrons in the conduction band (CB) are involved in reduction reactions. A variety

of radicals are produced when they react with oxygen molecules: superoxide radicals ($O2^{\cdot -}$), hydroperoxyl radicals (HOO·), hydrogen peroxide (H_2O_2), and OH· radicals. These oxygen-related species lead to organic contaminants breakdown during photocatalytic process.[69,70] The electrochemical energy scale is a fundamental concept in electrochemistry. It plays a crucial role in determining whether a chemical reaction involving electron transfer (redox reaction) is thermodynamically possible or not. The electrochemical potentials on this scale are used to assess whether electrons or holes (positive charges) can drive a given redox reaction.

Oxidation of organic contaminants: Hydroxyl radicals (OH•) are extremely reactive and can oxidize organic contaminants adsorbed on or near the TiO_2 surface. This oxidation process breaks down these contaminants into simpler and less harmful compounds.

Transformation into H_2O and CO_2: The oxidation of organic contaminants continues until they are fully mineralized into water (H_2O) and carbon dioxide (CO_2), which are non-toxic and environmentally benign (See Figure 1.4).

This photocatalytic process can be used for the degradation of a wide range of organic pollutants, including dyes, polymers, pesticides, and various other organic contaminations. It is particularly useful in water treatment and air purification systems, where TiO_2-coated surfaces or TiO_2 nanoparticles are employed to facilitate the breakdown of contaminants under UV irradiation.

However, it is important to note that the efficiency of this process depends on various factors, including the specific type of TiO_2 used, the intensity and wavelength of UV light, the concentration of contaminants, and the reaction conditions. Researchers continue to work on improving the efficiency of TiO_2 photocatalysis for practical applications.[25,60,71,72]

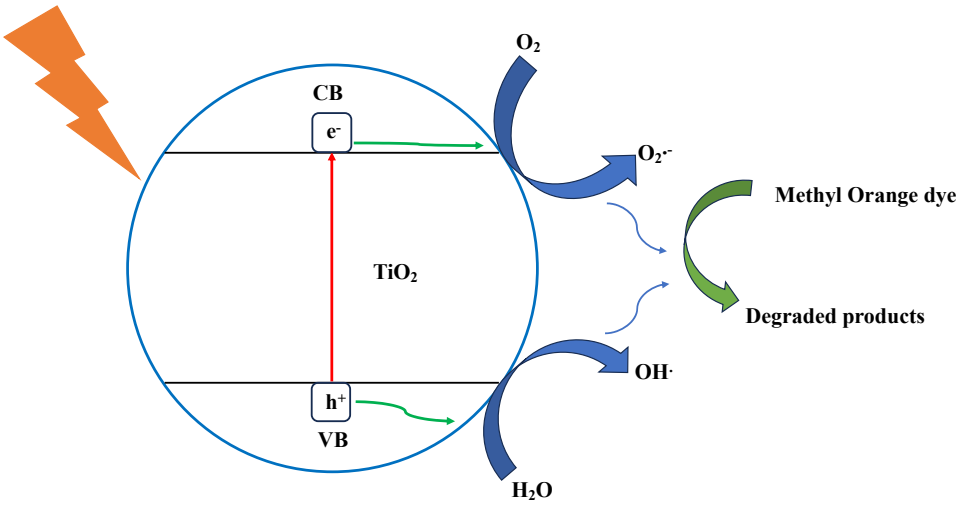

Figure 1.4. Schematic illustration of photocatalytic degradation mechanism of methyl orange using TiO_2.

1.2.4. Drawbacks of TiO_2

One of the primary disadvantages of TiO_2 is its constrained capability to absorb light within the visible spectrum. Although TiO2 demonstrates effective photocatalytic properties under UV light, its performance is limited when utilising visible light, primarily due to its wide bandgap of approximately 3.2 eV. It can only capture a small fraction (< 4%) of the solar spectrum located in the UV region. Consequently, if the band gap could be sufficiently reduced to allow absorption of visible light, it might become feasible to harness up to 40% of the solar spectrum. This limitation restricts its overall efficiency in photocatalytic reactions and solar energy conversion applications.[25,41,73,74] Secondly, photoexcitation gives rise to the formation of a positively charged region (hole) emerging from the displacement of an electron from a site. The recombination process, where the electron returns to its initial molecular orbital to fill the hole, is undesirable in photocatalysis. Both bulk and surface defect-induced charge recombination significantly curtail the photocatalytic functionality of the material.[75-77] These shortcomings collectively limit the widespread applicability of TiO_2 on a larger scale.

To address these drawbacks, significant enthusiasm has arisen in the endeavour to modify TiO_2, aiming to modify its band gap to fall within the visible light spectrum and reduce the recombination of electron-hole pairs formed during photoexcitation. These approaches aim to increase the activity of TiO_2 in photocatalytic process.[77-80] This pursuit has engendered diverse approaches, which will be expounded upon in subsequent sections of this chapter.

1.3. Surface modifications

Various approaches have been used to increase TiO_2 photocatalytic activity. To prolong the lifespan of electron-hole pairs generated through photocatalysis, various modifications can be applied, including chemical modifications such as introducing additional elements on the TiO_2 surface and/or morphological modifications that increase porosity and surface area to adsorb more co-catalysts.[41]

1.3.1. Mesoporous TiO_2 ($MTiO_2$)

Mesoporous TiO_2 ($MTiO_2$) is TiO_2 material that possesses pores with sizes ranging from 2 nm to 50 nm at the mesoscopic scale. These pores are organized in a regular pattern, allowing for the creation of a high surface area and a substantial volume of interconnected voids within the material. The porous structure of TiO_2 enhances its properties and functionalities over traditional non-porous or bulk forms and can be advantageous for several applications such as photocatalysis, sensors, energy storage devices, and drug delivery systems.[81]

Mesoporous materials like $MTiO_2$ have attracted significant interest because of their increased surface area, which facilitates higher adsorption capacity, efficient mass transport, and improved catalytic activity.[82] This advantage stems from the presence of a well-connected three-dimensional pore network, particularly notable in $MTiO_2$. In contrast, the existence of micropores can impede the diffusion of larger molecules, potentially limiting their efficacy. The controlled pore size and distribution in $MTiO_2$ can be tailored for specific purposes, enabling precise tuning of material properties and interactions with substances at the molecular level.[81,83,84] Therefore, due to their unique features, $MTiO_2$ nanoparticles known to be highly active semiconductors in several photocatalytic processes including H_2 production, water treatment, dye-sensitized solar cells, electrode production in Li-ion batteries, and biomedicine.[39,84,85]

This thesis will explore the application of functionalised $MTiO_2$ in water treatment, drawing attention to its distinctive pore structure and how it contributes to improved photocatalytic performance.

1.3.1.1.$MTiO_2$ preparation method

Numerous commercial TiO_2 products are readily accessible in the market. However, the potential for TiO_2 to acquire distinctive properties is further augmented by modifying its morphology and introducing a porous structure through diverse synthesis techniques.[81,86]

Since Antonelli and Ying discovered the first $MTiO_2$[105], a variety of shapes of them such as 2D hexagonal, hollow-sphere, 3D cubic, and lamellar have been made to improve its photocatalytic activity. These materials have thus been synthesised using diverse procedures, including evaporation-induced self-assembly (EISA), sol-gel, hydrothermal, electrodeposition, microwave, solvothermal, and sonochemical methods. [39,85,87]

Mesoporous materials (silica) were first fabricated around 1970, as a product of various procedures based primarily on the Stöber process[88]. In 1990, the creation of the surfactant-template self-assembly method for preparation of mesoporous SiO_2 has since led to its widespread adoption in mesoporous material research.[89,90]

There are ordered and disordered mesoporous structures for $MTiO_2$. Achieving ordered mesostructures necessitates the utilisation of a template or structure-directing agent, contrasting with the template-free procedures employed to attain disordered mesostructures.[39] As ordered porous structures inherently facilitate the diffusion of both products and reactants, the deployment of ordered mesoporous TiO_2 is anticipated to bolster photocatalytic efficiency. Consequently, this category of materials holds considerable promise for photocatalytic applications.[91] This aspect will be a focal point in this thesis, shedding light on the potential of ordered mesoporous TiO_2 structures to advance the field of photocatalysis.

There are two primary approaches for achieving ordered mesoporous materials, the soft templating method and the hard templating method, [86,92,93] as can be seen in Figure 1.5.[93]

Templating synthesis involves the utilisation of a specific design around which the material is synthesised. There are three steps in creating samples using this method: template preparation, target production by a sol-gel or hydrothermal method and removing the template with a physical (physical pulverization and spray method) or chemical reaction (calcination method)[83]. Several parameters can affect the final products' physicochemical features, including the Ti precursor's choice and the temperature at which it is calcinated. Calcination is necessary to eliminate the organic moieties from templates and hydrolysis of Ti alkoxides utilised as Ti precursors. This factor significantly influences the type of TiO_2 polymorph created and the size of crystalline grains, consequently directly impacting the performance of $MTiO_2$.[84]

1.3.1.1.1. Soft templating method

In the process of producing soft templates for synthesis, polymer and biopolymer molecules can very often act as templates. These polymers possess both polar and non-polar segments. Micelles are generated by their interaction with the solvent. One portion of the polymer is drawn towards the solvent, assembling outside the micelle structure. Conversely, the other segment is repelled by the solvent but attracted to other polymer segments of the same polarity. These segments come together to form the interior of the micelles. Upon reaching a critical concentration, these micelles align themselves to create liquid crystals. Adjacent to these crystals, a precursor to titania undergoes hydrolysis, resulting in the formation of a porous material. This porous structure gets filled with polymer material. Subsequently, the amorphous titanium dioxide phase crystallizes, and simultaneously, the polymer template is eliminated at elevated temperatures. The benefit of this approach lies in its simplicity and minimal synthesis stages. However, a drawback is the vulnerability of the template molecules to the high temperatures necessary for titania crystallization. This predicament always involves a trade-off between crystalline structure and specific surface area, as titania requires notably high temperatures (>400°C) to crystallize, which can lead to the degradation of most polymers.[81,94,95] Consequently, the pores collapse during the final thermal treatment, resulting in reduced specific surface area.

Block copolymers, such as pluronic P123 symmetric triblock copolymer with one hydrophilic and one hydrophobic part, are one of the common types of soft templates for making $MTiO_2$. They can be connected by polymer chains with various properties. During the production of mesoporous nanoparticles, hydrogen bonding occurs in the hydrophilic section of this polymer. This facilitates the mesoscopic phase fabrication.[96,97]

Biopolymers offer a versatile and environmentally friendly option for serving as soft templates in the production of mesoporous titanium dioxide. In this study, we used chitosan which is not only a natural and sustainable source of N and C elements but also biodegradable and biocompatible. These properties make it particularly well-suited as a template choice. Chitosan, a polycationic polysaccharide, is composed of building blocks like glucosamine and acetylglucosamine, which contain functional groups including carboxyl and amine. This unique composition obviates the need for chemical alterations when forming chelates with titanium dioxide units and fabricating the desired mesoscopic structures. After undergoing a calcination process, natural constituents of chitosan facilitate N coating without requiring further modifications.[98-102]

In another work, the Gratzel approach[120] is applied to dye-sensitized solar cells. They used mesoporous semiconductor electrodes consisting of interconnected nanocrystals such as mesoporous TiO_2 films prepared by screen printing method by using titania paste as a commercially prepared combination of Ti precursors and organic materials which can act as template during the TiO_2 synthesis process. Annealing was then applied in air at 500 °C to eliminate the organic moieties. We are inspired by this approach to make TiO_2 films suitable for use in photocatalysis systems.[103,104]

1.3.1.1.2. Hard templating method

The hard templating method is utilised for synthesizing $MTiO_2$ materials. This technique involves using a solid and porous template like silica (e.g., silica-based like SBA-15, MCM-41, MCM-48, or C-based like KIT-6, CMK-8) with a defined structure to guide the creation of mesoporous TiO_2.[105] The selected template undergoes impregnation with a precursor solution containing Ti. This precursor infiltrates the pores of the template, occupying the available spaces. Subjecting the impregnated template to elevated temperatures triggers the conversion of the titanium precursor into crystalline titanium dioxide while leaving the template unaffected. Chemical reactions during this process solidify the titanium dioxide within the pores of template. After the crystalline titanium dioxide forms, the template is removed in an extra step. Selective methods dissolve or burn the template while preserving the TiO_2 structure.[105,106]

A notable advantage of this approach is the resilience of the template at elevated temperatures, enabling Ti crystallization within the pores before template removal. However, drawbacks include the need for more synthesis steps (template synthesis and removal) which increases costs. Also, identifying templates that satisfy both high-temperature stability and well-defined pore structure requirements can be a constraint. Achieving comprehensive and uniform pore filling within the template can also pose difficulties, potentially leading to structural instability or reduced surface area.[81]

Generally, achieving stability and a high specific surface area is more straightforward with the soft template synthesis method than with hard template synthesis. This is due to the intricate impregnation step in the latter. This research, therefore, focuses on mesoporous titania synthesis using soft templates.[107,108]

However, obtaining ordered mesoporous titanium dioxide is challenging because Ti precursors tend to form particles instead of polymeric structures. Soft template synthesis leads to particle agglomerates rather than uniformly ordered porous materials. Despite this, materials with uniform pores offer benefits such as enhanced diffusion within pores and shape-selective catalysis capabilities, unlike materials with irregular pores. This is less critical for adsorption and photocatalysis research area.[83] Notably, the Ti materials produced in this study were not ordered, but this lack of order does not hinder their intended applications.

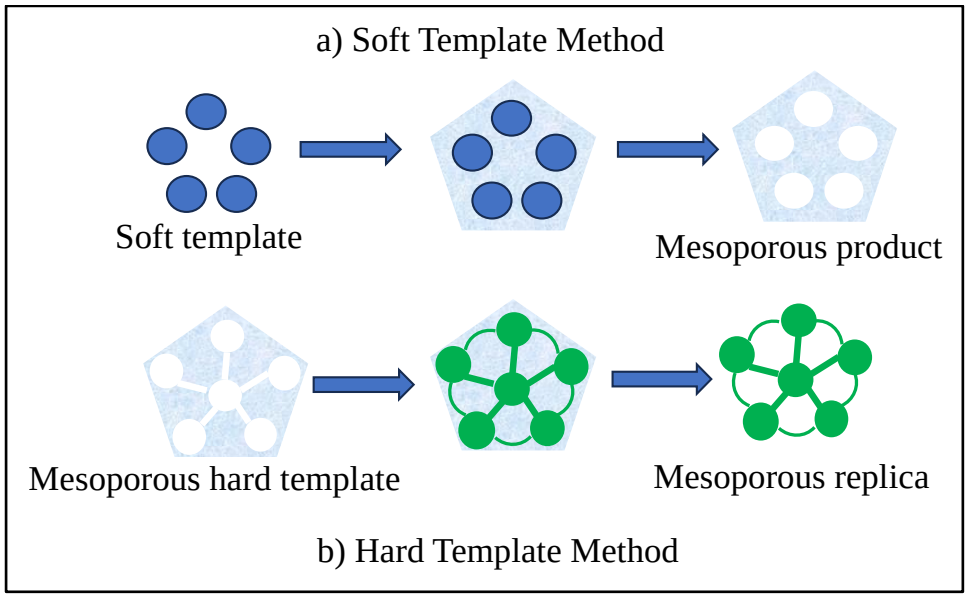

Figure 1.5. Illustration of two methods for preparation of the mesoporous structures a) Soft template method and b) Hard template method.[93]

1.3.2. Doped TiO_2

Efforts to increase the activity of TiO_2 when exposed to UV light and extend its light conversion and absorption capabilities to include the solar spectrum visible portion have predominantly revolved around augmenting it with foreign substances.[109] Incorporating foreign elements, known as doping, is a widely employed technique to decrease the energy gap and alter the electronic characteristics of TiO_2. This involves introducing additional elements into TiO_2 bulk material, thereby altering its optical behaviour. Scientific literature has documented that TiO_2 can be doped by metallic or non-metallic species. When non-metallic substances like C, N, S, P, and B as anionic species are used for doping,[110,111] they generally elevate the maximum energy level of the valence band (VB) due to their lower electronegativity compared to oxygen. Conversely, dopants containing metallic elements tend to reduce the minimum energy level of the conduction band (CB) since many of metals utilised in

doping have greater electronegativity than Ti. Noble metal dopants also possess the ability to serve as sites for capturing photoinduced charge carriers, aiding interfacial charge-transfer processes, and thereby impeding the recombination of electron-hole pairs. Therefore, in this study to improve the efficiency of the photocatalysis, doping mesoporous TiO_2 with noble metallic and non-metallic elements has been investigated.[112,113]

1.3.2.1.N doped mesoporous TiO_2

Nitrogen (N) was found as the most efficient non-metal substitution, having a similar atomic size to elemental oxygen and low ionisation energy. Therefore, many efforts have been made to increase mesoporous titania ($MTiO_2$) photocatalytic efficiency by a variety of N doping procedures. [114] For instance, N doping of mesostructured TiO_2 films with ammonia vapour treatment has been studied by Martínez-Ferrero and Kitazawa.[100,101] Improving the photocatalytic activity, maintaining the porous structure, and obtaining the optimum N substitution, of both prepared mesoporous titania films treated in an atmosphere of ammonia at 500 °C/2-4 h was approved.

$MTiO_2$ surfaces can be functionalised with the N species as either an interstitial or a substitutional N atom in the mesoporous titania matrix. Indeed, doped N may be an NO species that may exist alone or in combination with Ti-N bonds; the NO type is created by the interaction between N and O where N is close to interstitial positions; and the Ti-N bond is formed by substitution of oxygen by N atoms. The substitutional and interstitial species can make levels above the valence band, as reported for the interstitial 0.73 eV above the valence band forms. N2p levels could mix with O2p levels leading to decreasing in the titania bandgap energy, producing more electrons and holes, and increasing the photocatalytic efficiency under visible radiation. In another study, [102] it is reported that the N2p levels form a narrow band separated from the initial valence band, which can be responsible for sensitization of the surface to visible light. It also has been proved that the properties of the N doped TiO_2 are like impurity sensitization, causing the establishment of states localized in the titania band gap. As a result, N doping not only modified mesoporous TiO_2 electronic properties but also created oxygen-defective sites, hence inducing a significant effect on catalytic efficiency. Therefore, designing strategies to improve TiO_2 catalytic activity is required.[115-117] As N dopants are cost-effective and eco-friendly to modify the surface, these materials are promising for future photocatalytic applications.[99,113,118,119]

1.3.3. Mesoporous TiO_2 composites

TiO_2 is renowned for its exceptional photocatalytic capabilities, attributable to the generation of photogenerated charge carriers, including negative electrons (e^-) and positive holes (h^+). While TiO_2 boasts one of the highest photocatalytic efficiencies among semiconductors, a notable drawback

is its propensity for rapid recombination of photogenerated electron-hole pairs, which limits its overall photocatalytic performance. To address this limitation, efforts have been made to enhance TiO_2's photocatalytic prowess through the incorporation of noble metal dopants. These noble metals act as electron receptors, capturing photogenerated electrons. This mechanism is believed to suppress the recombination of electron-hole pairs and facilitate the migration of holes on the TiO_2 surface, thereby bolstering its photocatalytic activity. The deposition of noble metals onto TiO_2 has garnered significant attention, leading to numerous reviews that elucidate the roles of noble metals in photocatalysis.[120,121]

In essence, noble metals such as Pd, Au, Pt, Ir, and Ag when immobilised onto the surface of TiO_2, act as electron receptors because their Fermi levels are lower than that of TiO_2.[122] As a result, photoexcited TiO_2 acts as an electron source for these metal NCs, facilitating charge separation within the TiO_2 material. Further, due to the different Fermi levels and work functions of noble metal nanostructures (Ag, Pd, Pt, and Au) and the band-gap properties of TiO_2, direct contact between them can result in the formation of a Schottky barrier, preventing the recombination of photoinduced electron–hole pairs, and, therefore, enhancing the photocatalytic activity of the TiO_2/noble metal composite.[39] The noble metal nanoparticles can act as efficient cocatalysts, making a Schottky junction to improve visible irradiation absorption. Thus, they (I) prevent electron-hole recombination by acting as electron traps, (II) improve the surface properties of the photocatalyst, (III) increase surface electron stimulation by plasmon resonances stimulated by visible light and develop absorption of light in the visible range.[123]

Traditionally, bulk Au has been regarded as relatively unreactive, showing limited chemical and catalytic activity. Nevertheless, Haruta and his colleagues made a ground-breaking discovery that Au nanoparticles (NPs) can display remarkably high catalytic reactivity when finely distributed on specific metal oxide surfaces (in the form of Au/metal oxide nanocomposites). Au NPs with unique localized surface plasmon resonance (LSPR) based on their size and shape have been used as photo-sediments on TiO_2 surfaces to adsorb visible light. Surface plasmons of metal nanoparticles allow electron exchange through TiO_2 nanocrystals depending on lighting conditions. Additionally, when metallic islands are doped with Au, Ag, and Cu nanoparticles, they can retain approximately all the excess electrons. Hence, by altering the Fermi level of TiO_2 NPs in a cathodic manner, an equilibrium can be achieved concerning the charge saturation capacity of the nanoparticles. This has led to considerable interest in Au/metal oxide nanocomposites within the realm of catalysis, with widespread applications in critical processes like CO oxidation, selective propene oxidation, nitrogen oxide reduction, and notably in the field of photocatalytic oxidation for environmental purification purposes.[124-128]

The size of nanoparticles embedded onto the surface has a significant influence on the Ti photocatalytic properties. Decreasing the Au NP size enhances the interfacial surface between the Au NPs and the TiO_2 matrix.[129] Moreover, Kamat et al. suggest that the enhancement factor (EF) change in NPs per electron accumulated in small nanoparticles is more severe than in larger ones. Also, they found that the EF changes in NPs per electron accumulated was greater for small nanostructures compared to large ones. Thus, the enhancement of electron transfer at the electrolytic interface enhances the Fermi level shift by decreasing nanoparticle size.[130] Hence, researchers are keen on employing nanoclusters like Au NCs, which are smaller in size compared to Au NPs, to perform surface modification on TiO_2.

Tauster et al. were the first to attempt doping $MTiO_2$ with noble metals. Since then, many efforts have been made to modify $MTiO_2$ by various noble metal NPs acting separately or simultaneously according to the photoreaction conditions.[131] It has also been reported that thin films of titania decorated by metal NPs can have interesting electrical and optical characteristics. Also, an extensive range of optical applications can be obtained by controlling the size, concentration, and distribution of metal NPs. Large surface area, tuneable nanosized pores, and ordered channel structures are properties of the ordered mesoporous materials, which can be used to synthesise novel nanocomposites. Indeed, the ordered structure and the confinement effect created by the mesoporous channels in mesoporous TiO_2 thin films can effectively address the challenges associated with achieving a uniform spatial arrangement and size distribution of metal particles.[132] Therefore $MTiO_2$/Au NCs nanocomposites are promising photoelectrical materials for photocatalysis systems in several applications such as solar energy conversion for energy production and water purification.[128]

1.3.3.1. S and N modification of $MTiO_2$ surface for anchoring Au_9 NCs.

In 1986, Sato [133] was the first to report the creation of N-functionalised TiO_2 ($NTiO_2$). This breakthrough marked a significant development in the field. Subsequently, Asahi et al. [134] proposed a novel concept: the potential for narrowing the band gap by introducing N in the TiO_2 structure. This innovation was noteworthy as it involved the replacement of some crystal lattice O atoms with N atoms. It is worth noting that while numerous methods have been devised for the functionalisation of TiO_2 with N, many of these $NTiO_2$ synthesis processes present significant challenges. These challenges often involve the requirement for thermal treatment at temperatures exceeding 400°C or high-pressure conditions, typically associated with hydrothermal or solvothermal processes, and necessitate the use of N sources such as ammonium nitrate, ammonium chloride, urea, and similar compounds.[135] However, in Chapter 7, we applied a facile sol-gel method to produce N functionalised TiO_2.

Monolayers consisting of Amino or mercapto groups are interesting due to their ability to bond strongly with noble metals. For instance, (3-mercaptopropyl) trimethoxysilane (MPTMS) has been applied to form monolayers of Au colloid on silica surfaces for applications in surface-enhanced Raman scattering, biosensing, and catalysis. Because MPTMS is susceptible to moisture, the vapor deposition technique could be a suitable approach to mitigate the impact of moisture and restrict the polymerization processes. However, the surface coverage might not be comprehensive, and the time required for the reaction is typically longer compared to liquid-phase silanisation. Hsieh and colleagues were the first to document the use of aminopropylsilatrane as a bonding layer to attach AuNPs onto Si surfaces. Subsequent research has confirmed that the attachment of mercapto groups to Au, inspired by the interactions observed between Au and thiol groups in self-assembled monolayers (SAMs) on bulk Au surfaces demonstrated in the late 1980s, exhibits greater strength than that of amino groups. To illustrate, AuNPs adhering to an amino-functionalised surface can be displaced when the surface of Au NPs is more extensively modified with a SAM, which typically relies on the Au–S bond.[136,137]

Therefore S-functionalisation presents an effective method for chemically modifying surfaces to attach Au particles. The covalent linkage between Au and S yields a strong yet adjustable bond. This bonding is established through the interaction between S(sp3) hybrid orbitals and Au(6s) electrons, which indicates that S undergoes sp3-type hybridization.[138] Additionally, the involvement of Au(d) electrons significantly contributes to the Au-S bond. Many investigations employ sulfhydryl (SH) functional groups present in thiols (RSHs) to facilitate and mediate these interactions, further enhancing the connection between Au and S.[139-141]

This study focuses on designing efficient photocatalysis systems by preparing substrates to further adsorb the noble metal clusters as cocatalysts acting as photogenerated charge pair receptors to reduce their recombination. Accordingly, modification of the surface by adding functional groups with nonmetal doping is one of the effective approaches to gain this purpose. Formation of the strong binding between cocatalysts and MTiO_2 surface is a key factor in adsorbing the cocatalyst effectively and preventing their agglomeration. For this reason, using sustainable chitosan as the natural templates and N resources and MPTMS as a thiol grafting reagent is a promising approach to prepare N and S functionalised mesoporous TiO_2.

1.4. Au nanoclusters

The characteristics of metallic particles are contingent upon their size. In fact, when the size of metal particles falls below a certain threshold, their properties transition from being typically metallic to exhibiting non-metallic traits. This transition occurs at approximately a few hundred atoms, causing the energy levels to become discrete. It is important to acknowledge that this change is not abrupt but gradual. When the size of materials decreases below a specific threshold, their attributes become

sensitive to both size and shape.[142,143] These smaller metal nanoparticles, which are controlled at the atomic level, are often referred to as metal clusters. These nanoclusters exhibit unique molecular-like states, resulting in a wide range of optical, electrochemical, and other physicochemical properties. Specifically, when metal clusters are formed at extremely small sizes, typically around 1.5 nm, which is much smaller than either the de Broglie wavelength or the Fermi wavelength of conduction electrons, they display exceptional characteristics distinct from both larger nanoparticles and bulk materials. This disparity arises owing to the quantum confinement effect on the behaviour of electrons. This has sparked increasing interest in the exploration of metal NCs for photocatalytic applications, often involving the coupling of metal cluster composites with semiconductors.[144-151]

Precisely engineered Au nanoclusters (Au NCs) at the atomic level offer exceptional control for constructing nanomaterials, making them a central point of interest within the field of cluster chemistry research. Au NCs employed for surface modification exhibit smaller sizes compared to Au nanoparticles. Unlike nanoparticles, their electronic structure's dependence on size and geometric flexibility hold significant implications for altering surfaces in catalytic applications[152,153]. While Au nanoparticles usually possess a face-centred cubic (fcc) structure, the atomic arrangements of Au nanoclusters are determined by the number of constituent atoms, resulting in distinct atomic configurations[154]. Like molecules, Au NCs possess discrete electronic energy levels. In contrast, nanoparticles exhibit a continuous electronic energy band structure that resembles bulk Au.[155]

Au NCs find widespread applications in diverse fields including catalysis, biomarker development, and fluorescence detection, primarily due to their robust fluorescence stability, minimal cytotoxicity, excellent biocompatibility, and substantial Stoke shift. Recently, Au NCs have emerged as a novel co-catalyst, effectively broadening the range of light utilisation and enhancing the photo-efficiency of wide band-gap semiconductors.[156]

There are two efficient techniques for fabricating and depositing Au NCs onto surfaces. The first involves a physical method, carried out under ultra-high vacuum (UHV) conditions in a gas phase, while the second employs a chemical method, performed in a liquid phase through chemical synthesis processes. The latter method holds an advantage in terms of ease of scaling up compared to the gas-phase approach. [53,157,158]

Au NCs with a small number of metal atoms in the core, which can be combined with both inorganic and organic ligands, exhibit distinctive atom-packing arrangements, and pronounced quantization of electron energy. These characteristics encompass a considerable band gap, ultra-small cluster size, and adjustable catalytic features.[159] Furthermore, Au NCs have exhibited the capacity to enhance charge transfer processes. Their combination of catalytic and photoreactive properties renders Au NCs a superb option for multifunctional applications in photocatalysis, as they can fulfill the dual roles of catalytic centres and photosensitisers simultaneously. Notably, the photophysical

characteristics of Au NCs can be finely adjusted by modifying their size, composition, and ligand configurations.[156,159]

1.4.1. Phosphine ligated Au clusters and application in catalysis

The production of Au NCs chemically requires stabilising ligands to regulate cluster growth, prevent agglomeration through metal-metal interactions, and ensure their proper dissolution in the reaction medium. The exploration of atomically precise Au–phosphine clusters flourished between the 1970s and the mid-1990s. However, this research subsided as the focus shifted towards thiolate-protected Au clusters. The renewed enthusiasm for Au–phosphine clusters stems from the efforts of numerous researchers spanning various fields, including catalysis involving supported Au clusters, microscopic and spectroscopic characterisations, and theoretical calculations. A pivotal role in this resurgence was played by Simon et al., who not only reproduced several of these clusters but also provided comprehensive characterisations, rekindling attention to Au–phosphine clusters.[160-162]

Phosphine ligands, like triphenylphosphine (PPh_3), have attracted much interest as candidates to stabilise Au clusters due to their ability to yield ultrasmall clusters with tightly controlled size distributions. Due to their distinct steric and electronic properties, phosphine ligands also enhance cluster reactivity and electronic structure. As a result, these attributes set phosphine-ligated Au clusters apart from those protected by alkynyl or thiolate groups. The characteristics of phosphine ligands exert influence over the core size, nuclearity, geometric arrangement, flexibility, chirality, stability, reactivity, and solubility of these Au–phosphine clusters. This interplay gives rise to the diverse and intricate chemistry exhibited by Au clusters associated with phosphine ligands.[128]

The bonds established between Au and phosphine ligands are characterised by dative covalent interactions. In these interactions, the lone pair of electrons in phosphorus atoms actively participates in forming the Au–P bond. The straightforward nature of Au–P bonds stems from the fact that phosphine ligands do not exhibit terminal or bridging coordination modes. Early studies on molecular orbitals, conducted by Mingos and colleagues, revealed that phosphine ligation leads to the hybridization of Au orbitals, facilitated by the engagement of lone pair electrons. This hybridization leads to enhanced radial Au–Au bonding strength.[128]

This approach has led to the creation of Au NCs denoted as $Au_n(PPh_3)m$, such as examples like $Au_9(PPh_3)_8(NO_3)_3$ and $Au_{101}(PPh_3)_{21}Cl_5$. Following the initial synthesis and structural elucidation of $Au_{11}(PPh_3)_7(SCN)_3$ by Malatesta et al.,[163] a multitude of other Au NCs were synthesised employing both monodentate and multidentate phosphine ligands. Appealing aspects of Au–phosphine clusters are their straightforward synthesis, uncomplicated purification, and convenient crystallization process. This is in contrast to numerous Au NCs that are protected by thiolate ligands, which often necessitate intricate and costly purification methods.[164-166] In contrast, numerous Au–phosphine clusters can be purified using straightforward techniques like filtration, washing, or basic

crystallization.[167,168] The ease of crystallization offers a distinct advantage for Au–phosphine clusters, facilitating rapid advancements in their preparation process and enabling comprehensive single-crystal X-ray studies.[128]

Inherent fluxionality plays a significant role in revealing transitions between different structural configurations, offering the necessary energy to surpass transition barriers. Such structural transitions are of the utmost importance as they can influence the valence electron arrangement within clusters. Interactions with substrates and the adsorption of clusters can lead to alterations in the cluster's geometry. Consequently, evaluating the geometric arrangement of immobilised Au nanoclusters on substrates is vital to understanding their inherent structure. However, accurately characterising the exact configuration of small clusters when deposited onto solid surfaces is a major challenge, even with the currently available electron microscopy technologies.[169]

Laskin's group leveraged mass spectrometry to delve into the influence of phosphine ligands on Au clusters.[170,171] More recent advancements have been achieved by Pettibone and Hudgens, who made strides in elucidating reaction pathways and mechanisms within diphosphine-ligated Au cluster systems.[172,173] Häkkinen and co-workers have also contributed through their theoretical and computational determinations of electronic structures, doping effects, and catalytic behaviour exhibited by Au clusters.[174,175] This collective effort has breathed new life into the study of Au–phosphine clusters.

One of the most captivating and versatile clusters, namely $Au_9(PPh_3)_8(NO_3)_3$, remains a subject of in-depth investigation, even after its initial synthesis in the 1970s through the reduction of $Au(PPh_3)NO_3$ using $NaBH_4$ in EtOH.[176] Of particular significance, Simon and collaborators recently accomplished the isolation of a small subset of $Au_{14}(PPh_3)_8(NO_3)_4$ clusters. These clusters crystallized into delicate, pale-green platelets within a concentrated reaction mixture of $Au_9(PPh_3)_8(NO_3)_3$ clusters.[177] The fundamental symmetry of these clusters approximates D_{2h}, akin to that of the Au_9 cluster. Nonetheless, a notable difference arises whereas NO_3^- serves as a counter ion in the Au_9 cluster, in Au_{14}, Au (NO_3) assumes the role of a ligand. The Au–O bond, measuring 2.1 Å, plays a pivotal role in satisfying the configuration of the super atom model.

The catalytic potential of small Au particles was initially presented by Bond and colleagues in 1973 through their work on the hydrogenation and isomerization of olefins.[178] Bond and Sermon ascribed the catalytic effectiveness of Au to either surface imperfections or the small size of crystallites, with the latter being considered the more plausible explanation.[179] Despite their contributions, their findings remained overshadowed for over a decade until Haruta and his team unveiled the catalytic prowess of small Au NPs, approximately 5 nm in size, in CO oxidation in 1987.[128,180] These immobilised Au NPs exhibited superior performance compared to catalysts from the platinum group, showcasing heightened stability and activity even at low temperatures.

Concurrently, Hutchings also independently ascertained the catalytic efficiency of Au chloride in the hydrochlorination of acetylene.[181] Subsequently, a surge of studies followed, underscoring the catalytic capability of Au NPs in a diverse array of chemical processes encompassing selective hydrogenation, oxidation, cross-coupling reactions, and CO_2 conversion.[182-184]

The elevated catalytic effectiveness of Au catalysts stems from a multitude of factors: particle size, support characteristics, interactions between the support and the metal, charge exchange with the support, impurity doping, and dynamic fluxionality.[185-187] Intriguingly, the shortened Au–Au bond lengths and the quantum size phenomenon within small Au NCs also contribute to their catalytic performance (in comparison to Au NPs), furnishing them with advantageous attributes.[188,189] A benefit of employing Au NCs for heterogeneous catalysis lies in their easy deposition onto metal oxides, achieved by manipulating electrostatic interactions between ligands and supports.

Lately, there has been an increase in interest focused on photocatalytic systems, that incorporate Au clusters. This interest is driven by the dual nature of Au clusters, which can serve as both a photosensitiser with a narrow bandgap and a cocatalyst.[190,191] The existence of HOMO–LUMO gaps within Au NCs grants them resemblance to narrow bandgap semiconductors, hinting at their potential for efficient photocatalytic applications.[150] A multitude of photocatalytic processes, encompassing activities like water splitting, dye photodegradation, and the photoreduction of aromatic nitro compounds, take advantage of the distinctive attributes of Au clusters as a central component.[192-195] However, the exploration of photocatalysis involving Au clusters is still at an early phase of development.[195] Addressing fundamental inquiries surrounding the effects of ligands, charge states, electron transfer, and the nuclearity of the core size is essential to unveil the underlying mechanisms and activity driving this form of photocatalysis.

Combining Au nanoparticles with semiconductors results in the formation of hot electrons and the facilitation of charge transfer through plasmonic effects. However, the behaviour of Au clusters differs from this norm. Therefore, when integrated into semiconductor photocatalysts such as TiO_2, these Au clusters offer a range of useful features. These encompass potent absorption of visible light, proficient separation, and transfer of electron–hole pairs, and the initiation of singlet oxygen production.[156,191]

1.4.2. Methods for Au cluster deposition

Au NCs can be produced and anchored onto surfaces either through gas-phase methods under ultra-high vacuum (UHV) conditions [157] or by employing chemical synthesis process in the liquid phase. [53,158] The immobilisation of Au NCs onto a substrate, typically a metal oxide, is a fundamental requirement for a wide range of cluster-related applications, such as catalysis, photocatalysis, and

photovoltaics. Numerous techniques exist for depositing clusters onto surfaces, and some of these methods yield clusters of uniform size.[196-198]

Currently, the pulsed nozzle technique is employed for cluster deposition. Alternatively, another viable approach involves utilising the vapor pressure of clusters to coat the support surface within the controlled environment of ultra-high vacuum (UHV) conditions. For this approach to succeed, the clusters must exhibit sufficient stability to endure vaporization without undergoing decomposition. Additionally, the UHV system must be capable of maintaining a pressure level that aligns with the vapor pressure of the clusters to ensure successful deposition. This technique holds promise for precisely controlling the cluster deposition process while operating within a highly controlled UHV environment.[199] The utilisation of this method is constrained by the requirement for exceptional stability in the metal clusters. It mandates that the metal-ligand bonds be robust enough to ensure the cluster's vaporization before any disintegration of these bonds occurs. Consequently, the instances of successful applications of this technique are predominantly associated with highly stable metal clusters, often employing ligands such as metal triphenyl phosphine, carbonyl, and thiol. For example, the selection of appropriate solvents is crucial, necessitating solvents with low vapor pressures under the specific reaction conditions. The vaporization losses of these solvents can be estimated by leveraging knowledge of their vapor pressures in relation to temperature.[200-202]

An additional technique involves the electrochemical approach, which encompasses the electro-synthesis of diverse nanostructures on a solid substrate, often utilising templates like alumina. This method was initially introduced by Nielsch as a means of immobilising metals within meticulously organized alumina pores, employing a pulsed electrodeposition technique.[203]

In the context of depositing chemically synthesised metal clusters onto metal oxides, two methods have been introduced. The primary and widely employed method involves immersing the metal oxide into a solution containing the clusters. The nature of the support determines the specific form of immersion. For powder oxides, they are suspended in the solution and stirred, while wafer supports, and single crystals are dipped into the cluster solution and left to rest for a certain duration.[197,204] These methods are conducted under ambient conditions, encompassing typical room temperature and pressure. Prior to immersion, it is crucial to pre-dry the samples to eliminate any moisture that can interfere with the establishment of interactions between clusters and the support material. To prevent re-adsorption of water, the cluster itself should be handled within an inert atmosphere, often accomplished using N_2. Furthermore, the solvent employed for liquid-phase cluster deposition must maintain its monodispersity when in contact with the support. Therefore, in the liquid-phase deposition process, the choice of solvent plays a critical role. Selecting a suitable solvent can minimize the occurrence of aggregation and cluster precipitation. Solvents utilised in cluster preparation, like dichloromethane and methanol, are frequently used in this step to facilitate effective

solvent support interactions.[205] Furthermore, if titanium oxide is introduced as the support in powder form, the experimental setup undergoes modifications. In this case, it is essential for the solvent to ensure uniform dispersion of the titanium oxide, enabling all the support facets to be accessible for effective binding with the clusters. Subsequently, after the successful deposition of clusters, the solvent should be efficiently removed to avoid any undesirable impact on the clusters. Commonly employed techniques for solvent removal include methods like flowing a stream of nitrogen gas (N_2) over the sample or subjecting it to vacuum drying. These strategies are widely utilised to ensure the clusters remain intact and unaffected during the solvent removal process.[199,206]

The insights gathered by Lu and Chen emphasize a common challenge in achieving meticulous control over the cluster size of the resultant nanocomposites. The predominant approaches often occur in a solution phase, necessitating the meticulous manipulation of various experimental variables such as the chemical structure of the ligands, the ratio of metal to ligand, the type of reducing agent, the temperature of the reaction, agitation conditions, duration, and pH. These intricate adjustments aim to precisely tailor the size and properties of the synthesised and immobilised clusters.[207]

1.4.3. Detachment of triphenylphosphine ligands from Au clusters

Ligand removal is pivotal when working with chemically synthesised clusters, particularly in catalytic applications. This step is crucial in establishing active catalysts by enabling interactions between the cluster and the supporting substrate. This facilitates efficient catalytic processes for crucial reactions. This process also results in particles with exposed adsorption sites, a pivotal attribute in catalysis. Moreover, the effectiveness of metal clusters in interacting with semiconductor materials is influenced by their electronic structure. The interface between the metal cluster and the substrate, which facilitates charge transfer, holds significant importance.[208]

The removal of ligands and the enhancement of cluster core anchoring to the substrate surface are commonly achieved through oxidative processes like ozonolysis and thermal treatments like calcination under controlled atmosphere.[197] However, these methods may result in cluster aggregation due to the relatively weak interaction between Au and the metal oxide substrate. Notably, the electronic characteristics of ultra-small metal clusters strongly depend on their size. They are susceptible to changes linked to the number of atoms within the cluster's core.

In response, researchers have investigated the implementation of surface pre-treatments to mitigate Au nanocluster aggregation. For instance, Hidalgo et al. have proposed a method involving the pre-treatment of TiO_2 with sulfuric acid. This treatment results in the attachment of sulphate groups onto the particle surface, leading to a significantly stronger interaction between the support and the nanoclusters.[209]

Another study conducted by Veith et al. revealed that modifying TiO_2 through pre-treatment with both acidic and basic solutions can effectively impede the aggregation of Au nanoparticles. Specifically, they found that treating TiO_2 with H^+ ions using sulfuric acid enhances the interaction between the support and the metal clusters, thereby preventing aggregation[210]. Furthermore, separate research has indicated that enhancing the catalytic activity can be achieved through the hydroxylation of the TiO_2 surface. It is interesting to note that while this hydroxylation improved catalytic efficiency, it had no significant effect on the aggregation of Au clusters.[211]

In a recent study by Matthey et al., the focus was on investigating the nucleation of small Au clusters (<20 atoms) on various surfaces of TiO_2, including reduced, oxidized, and hydrated surfaces. The study revealed that the bond between the metal oxide and Au was strongest when an oxidized support was used. However, surfaces of TiO_2 that were hydrated exhibited a propensity for aggregation, leading to the creation of larger Au particles. Among the pre-treatment approaches examined in the study, the treatment involving H_2SO_4 emerged as the most effective in preventing cluster agglomeration during subsequent calcination. Other pre-treatment methods, such as $O_2(\Delta)$, $H_2(\Delta)$, O_3/UV, and $SnCl_2$, also exhibited promising results in retaining discrete clusters after calcination. Notably, the $H_2(\Delta)$ pre-treatment was particularly effective for its ability to discourage cluster agglomeration during ozonolysis.[197,205]

The weakened Au–P bond is also suitable as it facilitates the removal of ligands under gentle conditions. The removal of phosphine ligands plays a pivotal role in the activation of Au-based catalysts. Kilmartin et al. detailed the disengagement of phosphine ligands from the Au_6 core using an organic peroxide (TBHP) at a temperature of 95 °C.[212] Similarly, Adnan and his team noted the presence of $OPPh_3$ ligands in the catalytic reaction mixture, suggesting the elimination of PPh_3 ligands during the catalytic oxidation of benzyl alcohol at 80 °C.[213] Instances of phosphine ligands being detached from the Au core have been observed through calcination at a temperature of 200 °C[214]. For example, Anderson et al. explored the elimination of triphenylphosphines from various Au_n clusters (n = 8, 9, 11, 101) ligated with PPh_3 by subjecting them to moderate-temperature calcination (≤ 200 °C) and employing diverse conditions, including chemical etching, thereby underscoring the flexibility of the Au–P bonding in cluster manipulation and catalyst preparation.[128,215,216]

Heat treatment is often employed to remove ligands from immobilised clusters, enabling direct interaction between the substrate surfaces and nanocluster core facilitating access to surface adsorption sites.[197] Clusters attached to supports can undergo two changes when heated to approximately 200°C. Firstly, ultrasmall clusters may aggregate while still retaining their phosphine ligands, leading to the formation of larger Au particles due to their inherent mobility. Secondly, some Au clusters might form Au–O bonds, likely attributed to interactions with the oxygen present on the

TiO_2 surface. These Au–O bonds form concomitantly with the loss of phosphine ligands and increased oxidation of phosphorus atoms.[217]

Avoiding the first scenario is pivotal, as the distinctive features of nanoclusters depend on their size and consequently undergo alterations upon agglomeration. Therefore, precise control over cluster attachment to the substrate and accurate determination of cluster size are paramount for optimizing the efficiency of photocatalytic systems for oxidation and reduction reactions.[218]

This study primarily focused on devising an effective strategy to counteract the tendency of Au clusters to aggregate both during the deposition process and subsequent heat treatment.

1.5. Aim of thesis

The primary objective of this thesis is to enhance the photocatalytic activity of TiO_2 by employing two distinct surface modification strategies: morphological modification through the creation of porous structures, and chemical modification by introducing additional elements or functional groups onto the surface. This includes the integration of non-metal elements, N and S, for immobilising the Au_9 nanoclusters (NCs) as the co-catalyst.

The configuration of Au_9 NCs, determined by the number of constituent atoms, plays a pivotal role in shaping the characteristics of the modified surfaces. As the catalytic efficiency of these NCs is closely linked to their size, alterations in Au_9 NCs size led to variations in the overall effectiveness of the system. Therefore, it becomes essential to prevent Au_9 NCs agglomeration to enhance the catalytic activity, particularly following heat treatment aimed at ligand removal. Also, the enhancement of the number of active sites on the TiO_2 surface can be effective in creating an efficient photocatalytic system. Therefore, in this study, we focused on designing novel systems able to adsorb high levels of ultra-small Au_9 NCs and to prevent their agglomeration during the deposition and annealing processes.

Forming strong bonds between Au_9 NCs and the TiO_2 surface is our main purpose, as this helps increase the loading ratio and reduce the probable agglomeration of the clusters. The first approach to achieving this aim is preparation of mesoporous TiO_2 ($MTiO_2$) with high density of surface defects, high specific surface area, and 3D pore network. They can provide anchoring sites to adsorb of Au_9 NCs, curtailing their mobility and thereby suppressing the tendency to aggregate. Another strategy to counteract agglomeration involves the introduction of functional groups on the mesoporous TiO_2 surface through N or S functionalisation. These chemically modified $MTiO_2$ surfaces hold the potential to establish a more robust bond between the Au_9 NCs and the $MTiO_2$ substrate. The creation of a strong complex between the Au core and the functional groups, particularly thiol groups, lead to a more substantial and durable adsorption of clusters onto the surface.

It is necessary to undertake a comprehensive investigation into the relative impacts of surface modification and functionalisation strategies on enhancing the loading of Au_9 NCs while concurrently

mitigating agglomeration. This assessment will be conducted using XPS. Subsequently, once the most promising photocatalyst system has been identified, our objective is to conduct an in-depth analysis of its photocatalytic efficiency in the degradation of methyl orange dye. We will systematically examine the reaction parameters and establish their interrelationships through the application of response surface methodology. This analytical approach will facilitate a thorough understanding of the complex dynamics governing the photocatalytic process.

In this study, we explored the role of non-agglomerated Au_9 NCs deposited on the substrate in the photocatalytic activity for water treatment.

Therefore, the main aims of this research study can be classified as follows:

1- Synthesis of $MTiO_2$ semiconductors and Au_9 NCs as co-catalysts.
2- N and S chemically modification of the $MTiO_2$ surfaces to create stronger support-cocatalyst bindings.
3- Study of the agglomeration of the Au_9 NCs and their loading ratio by XPS after deposition and annealing processes.
4- Investigation of activity of the prepared photocatalysts in MO dye degradation and study of interaction between parameters by RSM.

1.6. References

1 Al-Tohamy, R. *et al.* A critical review on the treatment of dye-containing wastewater: Ecotoxicological and health concerns of textile dyes and possible remediation approaches for environmental safety. *Ecotoxicology and Environmental Safety* **231**, 113160 (2022).

2 Waghchaure, R. H., Adole, V. A. & Jagdale, B. S. Photocatalytic degradation of methylene blue, rhodamine B, methyl orange and Eriochrome black T dyes by modified ZnO nanocatalysts: A concise review. *Inorganic Chemistry Communications*, 109764 (2022).

3 Sriram, G. *et al.* Recent trends in the application of metal-organic frameworks (MOFs) for the removal of toxic dyes and their removal mechanism-a review. *Sustainable Materials and Technologies* **31**, e00378 (2022).

4 Hasanpour, M. & Hatami, M. Photocatalytic performance of aerogels for organic dyes removal from wastewaters: Review study. *Journal of Molecular Liquids* **309**, 113094 (2020).

5 Chung, K.-T. Azo dyes and human health: A review. *Journal of Environmental Science and Health, Part C* **34**, 233-261 (2016).

6 Hildenbrand, S., Schmahl, F., Wodarz, R., Kimmel, R. & Dartsch, P. Azo dyes and carcinogenic aromatic amines in cell cultures. *International Archives of Occupational and Environmental Health* **72**, M052-M056 (1999).

7 Wu, Y. *et al.* Superior adsorption of methyl orange by h-MoS2 microspheres: Isotherm, kinetics, and thermodynamic studies. *Dyes and Pigments* **170**, 107591 (2019).

8 Shanker, U., Rani, M. & Jassal, V. Degradation of hazardous organic dyes in water by nanomaterials. *Environmental chemistry letters* **15**, 623-642 (2017).

9 Barzinjy, A. A., Hamad, S. M., Aydın, S., Ahmed, M. H. & Hussain, F. H. Green and eco-friendly synthesis of Nickel oxide nanoparticles and its photocatalytic activity for methyl orange degradation. *Journal of Materials Science: Materials in Electronics* **31**, 11303-11316 (2020).

10 Bhankhar, A., Giri, M., Yadav, K. & Jaggi, N. Study on degradation of methyl orange-an azo dye by silver nanoparticles using UV–Visible spectroscopy. *Indian Journal of Physics* **88**, 1191-1196 (2014).

11 Selvaraj, V., Karthika, T. S., Mansiya, C. & Alagar, M. An over review on recently developed techniques, mechanisms and intermediate involved in the advanced azo dye degradation for industrial applications. *Journal of molecular structure* **1224**, 129195 (2021).

12 Molins-Delgado, D., Díaz-Cruz, M. S. & Barceló, D. Ecological risk assessment associated to the removal of endocrine-disrupting parabens and benzophenone-4 in wastewater treatment. *Journal of hazardous materials* **310**, 143-151 (2016).

13 Lee, C. S., Robinson, J. & Chong, M. F. A review on application of flocculants in wastewater treatment. *Process safety and environmental protection* **92**, 489-508 (2014).

14 Zhang, C. *et al.* Three-dimensional electrochemical process for wastewater treatment: A general review. *Chemical engineering journal* **228**, 455-467 (2013).

15 Alsheyab, M., Jiang, J.-Q. & Stanford, C. On-line production of ferrate with an electrochemical method and its potential application for wastewater treatment–A review. *Journal of Environmental Management* **90**, 1350-1356 (2009).

16 Bagal, M. V. & Gogate, P. R. Wastewater treatment using hybrid treatment schemes based on cavitation and Fenton chemistry: a review. *Ultrasonics sonochemistry* **21**, 1-14 (2014).

17 Oller, I., Malato, S. & Sánchez-Pérez, J. Combination of advanced oxidation processes and biological treatments for wastewater decontamination—a review. *Science of the total environment* **409**, 4141-4166 (2011).

18 Gogate, P. R. & Pandit, A. B. A review of imperative technologies for wastewater treatment I: oxidation technologies at ambient conditions. *Advances in environmental research* **8**, 501-551 (2004).

19 Abu Bakar, F. Towards new generation of sustainable catalysts: Study of shape and size controlled TiO2 nanoparticlesin photocatalytic degradation of industrial dye. (2014).
20 Shan, R. *et al.* Photocatalytic degradation of methyl orange by Ag/TiO2/biochar composite catalysts in aqueous solutions. *Materials Science in Semiconductor Processing* **114**, 105088 (2020).
21 Aljuaid, A. *et al.* g-C3N4 Based Photocatalyst for the Efficient Photodegradation of Toxic Methyl Orange Dye: Recent Modifications and Future Perspectives. *Molecules* **28**, 3199 (2023).
22 Kumar, R., Kumar, G. & Umar, A. Zinc oxide nanomaterials for photocatalytic degradation of methyl orange: a review. *Nanoscience and Nanotechnology letters* **6**, 631-650 (2014).
23 Saeed, M., Muneer, M., Haq, A. u. & Akram, N. Photocatalysis: An effective tool for photodegradation of dyes—A review. *Environmental Science and Pollution Research*, 1-19 (2022).
24 Rathi, B. S. & Kumar, P. S. Sustainable approach on the biodegradation of azo dyes: A short review. *Current Opinion in Green and Sustainable Chemistry* **33**, 100578 (2022).
25 Mills, A. & Le Hunte, S. An overview of semiconductor photocatalysis. *Journal of photochemistry and photobiology A: Chemistry* **108**, 1-35 (1997).
26 Teh, C. M. & Mohamed, A. R. Roles of titanium dioxide and ion-doped titanium dioxide on photocatalytic degradation of organic pollutants (phenolic compounds and dyes) in aqueous solutions: A review. *Journal of Alloys and Compounds* **509**, 1648-1660 (2011).
27 Bakar, F. B. A. *Towards New Generation of Sustainable Catalysts: Study of Shape and Size Controlled TiO2 Nanoparticles in Photocatalytic Degradation of Industrial Dye: Thesis Submitted in Partial Fulfillment of the Requirements for the Degree of Doctor of Philosophy, University of Canterbury*, University of Canterbury, (2014).
28 Khan, M. M. in *Photocatalytic Systems by Design* 1-22 (Elsevier, 2021).
29 Wisitsoraat, A., Tuantranont, A., Comini, E., Sberveglieri, G. & Wlodarski, W. Characterization of n-type and p-type semiconductor gas sensors based on NiOx doped TiO2 thin films. *Thin Solid Films* **517**, 2775-2780 (2009).
30 O'Regan, B. C. & Lenzmann, F. Charge transport and recombination in a nanoscale interpenetrating network of n-type and p-type semiconductors: Transient photocurrent and photovoltage studies of TiO2/Dye/CuSCN photovoltaic cells. *The Journal of Physical Chemistry B* **108**, 4342-4350 (2004).
31 Gupta, S. M. & Tripathi, M. An overview of commonly used semiconductor nanoparticles in photocatalysis. *High Energy Chemistry* **46**, 1-9 (2012).
32 Zhu, D. & Zhou, Q. Action and mechanism of semiconductor photocatalysis on degradation of organic pollutants in water treatment: A review. *Environmental Nanotechnology, Monitoring & Management* **12**, 100255 (2019).
33 Carp, O., Huisman, C. L. & Reller, A. Photoinduced reactivity of titanium dioxide. *Progress in solid state chemistry* **32**, 33-177 (2004).
34 Liu, B., Zhao, X., Terashima, C., Fujishima, A. & Nakata, K. Thermodynamic and kinetic analysis of heterogeneous photocatalysis for semiconductor systems. *Physical Chemistry Chemical Physics* **16**, 8751-8760 (2014).
35 Thiruvenkatachari, R., Vigneswaran, S. & Moon, I. S. A review on UV/TiO 2 photocatalytic oxidation process (Journal Review). *Korean Journal of Chemical Engineering* **25**, 64-72 (2008).
36 Li, W., Wu, Z., Wang, J., Elzatahry, A. A. & Zhao, D. A perspective on mesoporous TiO2 materials. *Chemistry of Materials* **26**, 287-298 (2013).

37 Yamauchi, Y., Suzuki, N., Radhakrishnan, L. & Wang, L. Breakthrough and future: nanoscale controls of compositions, morphologies, and mesochannel orientations toward advanced mesoporous materials. *The Chemical Record* **9**, 321-339 (2009).
38 Vivero-Escoto, J. L., Chiang, Y.-D., Wu, K. C. & Yamauchi, Y. Recent progress in mesoporous titania materials: adjusting morphology for innovative applications. *Science and technology of advanced materials* **13**, 013003 (2012).
39 Zhou, W. & Fu, H. Mesoporous TiO2: preparation, doping, and as a composite for photocatalysis. *ChemCatChem* **5**, 885-894 (2013).
40 Thahir, R., Bangngalino, H., Wahab, A. W., La Nafie, N. & Raya, I. in *IOP Conference Series: Materials Science and Engineering.* 012124 (IOP Publishing).
41 Pelaez, M. *et al.* A review on the visible light active titanium dioxide photocatalysts for environmental applications. *Applied Catalysis B: Environmental* **125**, 331-349 (2012).
42 Wilcoxon, J. & Abrams, B. Synthesis, structure and properties of metal nanoclusters. *Chemical Society Reviews* **35**, 1162-1194 (2006).
43 Aiken III, J. D. & Finke, R. G. A review of modern transition-metal nanoclusters: their synthesis, characterization, and applications in catalysis. *Journal of Molecular Catalysis A: Chemical* **145**, 1-44 (1999).
44 Jin, R. Atomically precise metal nanoclusters: stable sizes and optical properties. *Nanoscale* **7**, 1549-1565 (2015).
45 Shi, Q., Qin, Z., Sharma, S. & Li, G. Recent progress in heterogeneous catalysis by atomically and structurally precise metal nanoclusters. *The Chemical Record* **21**, 879-892 (2021).
46 Kailasa, S. K., Borse, S., Koduru, J. R. & Murthy, Z. Biomolecules as promising ligands in the synthesis of metal nanoclusters: Sensing, bioimaging and catalytic applications. *Trends in Environmental Analytical Chemistry* **32**, e00140 (2021).
47 Liu, Z. *et al.* Correlations between the fundamentals and applications of ultrasmall metal nanoclusters: Recent advances in catalysis and biomedical applications. *Nano Today* **36**, 101053 (2021).
48 Jin, R., Li, G., Sharma, S., Li, Y. & Du, X. Toward active-site tailoring in heterogeneous catalysis by atomically precise metal nanoclusters with crystallographic structures. *Chemical Reviews* **121**, 567-648 (2020).
49 Kawawaki, T. *et al.* Thiolate-protected metal nanoclusters: recent development in synthesis, understanding of reaction, and application in energy and environmental field. *Small* **17**, 2005328 (2021).
50 Qian, S. *et al.* Engineering luminescent metal nanoclusters for sensing applications. *Coordination Chemistry Reviews* **451**, 214268 (2022).
51 Moskovits, M. Metal clusters. *Annual Review of Physical Chemistry* **42**, 465-499 (1991).
52 Valden, M., Lai, X. & Goodman, D. W. Onset of catalytic activity of gold clusters on titania with the appearance of nonmetallic properties. *science* **281**, 1647-1650 (1998).
53 Turner, M. *et al.* Selective oxidation with dioxygen by gold nanoparticle catalysts derived from 55-atom clusters. *Nature* **454**, 981-983 (2008).
54 Anandan, S., Ikuma, Y. & Niwa, K. in *Solid State Phenomena.* 239-260 (Trans Tech Publ).
55 Chen, X. & Mao, S. S. Titanium dioxide nanomaterials: synthesis, properties, modifications, and applications. *Chemical reviews* **107**, 2891-2959 (2007).
56 Gaya, U. I. & Abdullah, A. H. Heterogeneous photocatalytic degradation of organic contaminants over titanium dioxide: a review of fundamentals, progress and problems. *Journal of photochemistry and photobiology C: Photochemistry reviews* **9**, 1-12 (2008).
57 Zhang, H. & Banfield, J. F. Understanding polymorphic phase transformation behavior during growth of nanocrystalline aggregates: insights from TiO2. *The Journal of Physical Chemistry B* **104**, 3481-3487 (2000).

58 Ranade, M. *et al.* Energetics of nanocrystalline TiO2. *Proceedings of the National Academy of Sciences* **99**, 6476-6481 (2002).
59 Fujishima, A., Zhang, X. & Tryk, D. A. TiO2 photocatalysis and related surface phenomena. *Surface science reports* **63**, 515-582 (2008).
60 Gupta, S. M. & Tripathi, M. A review of TiO 2 nanoparticles. *chinese science bulletin* **56**, 1639-1657 (2011).
61 Baranowska-Wójcik, E., Szwajgier, D., Oleszczuk, P. & Winiarska-Mieczan, A. Effects of titanium dioxide nanoparticles exposure on human health—a review. *Biological trace element research* **193**, 118-129 (2020).
62 Chen, X. & Selloni, A. Vol. 114 9281-9282 (ACS Publications, 2014).
63 Wold, A. Photocatalytic properties of titanium dioxide (TiO2). *Chemistry of Materials* **5**, 280-283 (1993).
64 Fujishima, A., Rao, T. N. & Tryk, D. A. Titanium dioxide photocatalysis. *Journal of photochemistry and photobiology C: Photochemistry reviews* **1**, 1-21 (2000).
65 Dharma, H. N. C. *et al.* A review of titanium dioxide (TiO2)-based photocatalyst for oilfield-produced water treatment. *Membranes* **12**, 345 (2022).
66 Sclafani, A. & Herrmann, J. Comparison of the photoelectronic and photocatalytic activities of various anatase and rutile forms of titania in pure liquid organic phases and in aqueous solutions. *The Journal of Physical Chemistry* **100**, 13655-13661 (1996).
67 Jitputti, J., Pavasupree, S., Suzuki, Y. & Yoshikawa, S. Synthesis and photocatalytic activity for water-splitting reaction of nanocrystalline mesoporous titania prepared by hydrothermal method. *Journal of Solid State Chemistry* **180**, 1743-1749 (2007).
68 Tanaka, K. Effect of crystal form of TiO_2 on the photocatalytic degradation of pollutants. *Photocatalytic purification and treatment of water and air*, 169-178 (1993).
69 Akpan, U. G. & Hameed, B. H. Parameters affecting the photocatalytic degradation of dyes using TiO2-based photocatalysts: a review. *Journal of hazardous materials* **170**, 520-529 (2009).
70 Konstantinou, I. K. & Albanis, T. A. TiO2-assisted photocatalytic degradation of azo dyes in aqueous solution: kinetic and mechanistic investigations: a review. *Applied Catalysis B: Environmental* **49**, 1-14 (2004).
71 Mills, A., Hill, C. & Robertson, P. K. Overview of the current ISO tests for photocatalytic materials. *Journal of Photochemistry and Photobiology A: Chemistry* **237**, 7-23 (2012).
72 Gupta, V. K., Jain, R., Nayak, A., Agarwal, S. & Shrivastava, M. Removal of the hazardous dye—Tartrazine by photodegradation on titanium dioxide surface. *Materials science and engineering: C* **31**, 1062-1067 (2011).
73 Serpone, N. & Emeline, A. Vol. 3 673-677 (ACS Publications, 2012).
74 Teoh, W. Y., Scott, J. A. & Amal, R. Progress in heterogeneous photocatalysis: from classical radical chemistry to engineering nanomaterials and solar reactors. *The Journal of Physical Chemistry Letters* **3**, 629-639 (2012).
75 Amano, F. *et al.* Decahedral single-crystalline particles of anatase titanium (IV) oxide with high photocatalytic activity. *Chemistry of Materials* **21**, 2601-2603 (2009).
76 Wu, Y., Liu, H., Zhang, J. & Chen, F. Enhanced photocatalytic activity of nitrogen-doped titania by deposited with gold. *The Journal of Physical Chemistry C* **113**, 14689-14695 (2009).
77 Ahmed, S., Rasul, M., Martens, W. N., Brown, R. & Hashib, M. Advances in heterogeneous photocatalytic degradation of phenols and dyes in wastewater: a review. *Water, Air, & Soil Pollution* **215**, 3-29 (2011).
78 Barkul, R., Koli, V., Shewale, V., Patil, M. & Delekar, S. Visible active nanocrystalline N-doped anatase TiO2 particles for photocatalytic mineralization studies. *Materials Chemistry and Physics* **173**, 42-51 (2016).

79 Papić, S. *et al.* Advanced oxidation processes in azo dye wastewater treatment. *Water environment research* **78**, 572-579 (2006).
80 Dozzi, M. V., Prati, L., Canton, P. & Selli, E. Effects of gold nanoparticles deposition on the photocatalytic activity of titanium dioxide under visible light. *Physical Chemistry Chemical Physics* **11**, 7171-7180 (2009).
81 Zhang, R., Elzatahry, A. A., Al-Deyab, S. S. & Zhao, D. Mesoporous titania: From synthesis to application. *Nano Today* **7**, 344-366 (2012).
82 Yang, X., Fu, H., Yu, A. & Jiang, X. Large-surface mesoporous TiO2 nanoparticles: Synthesis, growth and photocatalytic performance. *Journal of colloid and interface science* **387**, 74-83 (2012).
83 Niu, B., Wang, X., Wu, K., He, X. & Zhang, R. Mesoporous titanium dioxide: Synthesis and applications in photocatalysis, energy and biology. *Materials* **11**, 1910 (2018).
84 Bonelli, B., Esposito, S. & Freyria, F. S. Mesoporous Titania: Synthesis, properties and comparison with non-porous titania. *Titanium dioxide*, 119-141 (2017).
85 Ismail, A. A. & Bahnemann, D. W. Mesoporous titania photocatalysts: preparation, characterization and reaction mechanisms. *Journal of Materials Chemistry* **21**, 11686-11707 (2011).
86 Li, W., Wu, Z., Wang, J., Elzatahry, A. A. & Zhao, D. A perspective on mesoporous TiO2 materials. *Chemistry of Materials* **26**, 287-298 (2014).
87 Antonelli, D. M. & Ying, J. Y. Synthesis of hexagonally packed mesoporous TiO2 by a modified sol–gel method. *Angewandte Chemie International Edition in English* **34**, 2014-2017 (1995).
88 Chiola, V., Ritsko, J. E. & Vanderpool, C. D. (Google Patents, 1971).
89 Liu, J. *et al.* Preparation and characterization of highly active mesoporous TiO2 photocatalysts by hydrothermal synthesis under weak acid conditions. *Microporous and Mesoporous Materials* **124**, 197-203 (2009).
90 Nan, R. & Yi, T. Template-induced assembly of hierarchically ordered zeolite materials. *Petrochemical Technology* **34**, 405 (2005).
91 Hou, H. *et al.* Efficient photocatalytic activities of TiO 2 hollow fibers with mixed phases and mesoporous walls. *Scientific reports* **5**, 15228 (2015).
92 Xie, Y., Kocaefe, D., Chen, C. & Kocaefe, Y. Review of research on template methods in preparation of nanomaterials. *Journal of Nanomaterials* **2016** (2016).
93 Machado, A. E. *et al.* Applications of mesoporous ordered semiconductor materials—case study of TiO2. *Solar Radiation Applications*, 87-118 (2015).
94 Gajjela, S. R., Ananthanarayanan, K., Yap, C., Grätzel, M. & Balaya, P. Synthesis of mesoporous titanium dioxide by soft template based approach: characterization and application in dye-sensitized solar cells. *Energy & Environmental Science* **3**, 838-845 (2010).
95 Liu, J. *et al.* A facile soft-template synthesis of mesoporous polymeric and carbonaceous nanospheres. *Nature communications* **4**, 2798 (2013).
96 Pan, J. H., Zhao, X. & Lee, W. I. Block copolymer-templated synthesis of highly organized mesoporous TiO2-based films and their photoelectrochemical applications. *Chemical engineering journal* **170**, 363-380 (2011).
97 Wu, X., Zhang, H., Huang, K., Zeng, Y. & Zhu, Z. Rose petal and P123 dual-templated macro-mesoporous TiO2 for a hydrogen peroxide biosensor. *Bioelectrochemistry* **120**, 150-156 (2018).
98 Liu, S. *et al.* Biocompatible gradient chitosan fibers with controllable swelling and antibacterial properties. *Fibers and Polymers*, 1-9 (2022).
99 Joshi, M. M. *et al.* Visible light induced photoreduction of methyl orange by N-doped mesoporous titania. *Applied Catalysis A: General* **357**, 26-33 (2009).

100 Kitazawa, N., Sato, H. & Watanabe, Y. Effects of post-deposition chemical treatment on the formation of mesoporous titania films. *Journal of materials science* **42**, 5074-5079 (2007).
101 Martínez-Ferrero, E. *et al.* Nanostructured Titanium Oxynitride Porous Thin Films as Efficient Visible-Active Photocatalysts. *Advanced Functional Materials* **17**, 3348-3354 (2007).
102 Viswanathan, B. & Krishanmurthy, K. Nitrogen incorporation in TiO2: does it make a visible light photo-active material? *International Journal of Photoenergy* **2012** (2012).
103 Grätzel, M. Dye-sensitized solar cells. *Journal of photochemistry and photobiology C: Photochemistry Reviews* **4**, 145-153 (2003).
104 Hagfeldt, A., Boschloo, G., Sun, L., Kloo, L. & Pettersson, H. Dye-sensitized solar cells. *Chemical reviews* **110**, 6595-6663 (2010).
105 Zhang, Z., Zuo, F. & Feng, P. Hard template synthesis of crystalline mesoporous anatase TiO 2 for photocatalytic hydrogen evolution. *Journal of Materials Chemistry* **20**, 2206-2212 (2010).
106 Zhang, W. *et al.* Recent advances in the synthesis of hierarchically mesoporous TiO2 materials for energy and environmental applications. *National Science Review* **7**, 1702-1725 (2020).
107 Lu, Y. Surfactant-Templated Mesoporous Materials: From Inorganic to Hybrid to Organic. *Angewandte Chemie International Edition* **45**, 7664-7667 (2006).
108 Ru, L., Liang-Min, Y., Lan-Ni, J., Xue-Feng, Y. & Lei, D. Biomimetic synthesis of different morphology Cu2O induced by using polymer as template. *Chinese Journal of Inorganic Chemistry* **29**, 265-270 (2013).
109 Bagheri, S., Hir, Z. A. M., Yousefi, A. T. & Hamid, S. B. A. Progress on mesoporous titanium dioxide: Synthesis, modification and applications. *Microporous and Mesoporous Materials* **218**, 206-222 (2015).
110 Wang, Q. & Domen, K. Particulate photocatalysts for light-driven water splitting: mechanisms, challenges, and design strategies. *Chemical Reviews* **120**, 919-985 (2019).
111 Wang, Z., Li, C. & Domen, K. Recent developments in heterogeneous photocatalysts for solar-driven overall water splitting. *Chemical Society Reviews* **48**, 2109-2125 (2019).
112 Rosario, A. V., Christinelli, W. A., Barreto, R. N. & Pereira, E. C. Investigation of photocatalytic activity of metal-doped TiO 2 nanoparticles prepared by Pechini method. *Journal of sol-gel science and technology* **64**, 734-742 (2012).
113 Yang, Z., Qin, L., Tian, P. & Zhang, Y. Review of N and metal co-doped TiO2 for water purification under visible light irradiation. *IPCBEE* **78**, 31-40 (2014).
114 Fang, J. *et al.* Bifunctional N-doped mesoporous TiO2 photocatalysts. *The Journal of Physical Chemistry C* **112**, 18150-18156 (2008).
115 Wang, M., Zhang, X., Rao, R., Qian, N. & Ma, Y. Study on vapor-thermal synthesis and sulfur-doping of TiO2/graphene composites. *Applied Surface Science* **507**, 144856 (2020).
116 Tedja, R. *et al.* Effect of TiO 2 nanoparticle surface functionalization on protein adsorption, cellular uptake and cytotoxicity: the attachment of PEG comb polymers using catalytic chain transfer and thiol–ene chemistry. *Polymer Chemistry* **3**, 2743-2751 (2012).
117 Chen, X. *et al.* Biological renewable hemicellulose-template for synthesis of visible light responsive sulfur-doped TiO2 for photocatalytic oxidation of toxic organic and As (III) pollutants. *Applied Surface Science*, 146531 (2020).
118 Gomes, J., Lincho, J., Domingues, E., Quinta-Ferreira, R. M. & Martins, R. C. N–TiO2 photocatalysts: a review of their characteristics and capacity for emerging contaminants removal. *Water* **11**, 373 (2019).
119 Sulaiman, S. N. A., Noh, M. Z., Adnan, N. N., Bidin, N. & Ab Razak, S. N. in *Journal of Physics: Conference Series.* 012006 (IOP Publishing).

120 Sescu, A. M. *et al.* TiO2 doped with noble metals as an efficient solution for the photodegradation of hazardous organic water pollutants at ambient conditions. *Water* **13**, 19 (2021).
121 Do, H. H. *et al.* Recent progress in TiO2-based photocatalysts for hydrogen evolution reaction: A review. *Arabian Journal of Chemistry* **13**, 3653-3671 (2020).
122 Singhal, N. & Kumar, U. Noble metal modified TiO2: selective photoreduction of CO2 to hydrocarbons. *Molecular Catalysis* **439**, 91-99 (2017).
123 Kochuveedu, S. T., Jang, Y. H. & Kim, D. H. A study on the mechanism for the interaction of light with noble metal-metal oxide semiconductor nanostructures for various photophysical applications. *Chemical Society Reviews* **42**, 8467-8493 (2013).
124 Qin, Z. *et al.* Tailoring the stability, photocatalysis and photoluminescence properties of Au 11 nanoclusters via doping engineering. *Nanoscale Advances* **1**, 2529-2536 (2019).
125 De Heer, W. A. The physics of simple metal clusters: experimental aspects and simple models. *Reviews of Modern Physics* **65**, 611 (1993).
126 Fei, W. *et al.* Metal doping of Au25 (SR) 18–clusters: insights and hindsights. *Journal of the American Chemical Society* **141**, 16033-16045 (2019).
127 Muñoz-Castro, A. & Arratia-Perez, R. Spin–orbit effects on a gold-based superatom: a relativistic Jellium model. *Physical Chemistry Chemical Physics* **14**, 1408-1411 (2012).
128 Adnan, R. H., Madridejos, J. M. L., Alotabi, A. S., Metha, G. F. & Andersson, G. G. A review of state of the art in phosphine ligated gold clusters and application in catalysis. *Advanced Science* **9**, 2105692 (2022).
129 Sarina, S., Waclawik, E. R. & Zhu, H. Photocatalysis on supported gold and silver nanoparticles under ultraviolet and visible light irradiation. *Green Chemistry* **15**, 1814-1833 (2013).
130 Jakob, M., Levanon, H. & Kamat, P. V. Charge distribution between UV-irradiated TiO2 and gold nanoparticles: determination of shift in the Fermi level. *Nano letters* **3**, 353-358 (2003).
131 Bumajdad, A. & Madkour, M. Understanding the superior photocatalytic activity of noble metals modified titania under UV and visible light irradiation. *Physical Chemistry Chemical Physics* **16**, 7146-7158 (2014).
132 Cui, F. *et al.* Highly dispersed Au nanoparticles incorporated mesoporous TiO 2 thin films with ultrahigh Au content. *Journal of Materials Chemistry* **19**, 7632-7637 (2009).
133 Sato, S., Kawabata, A., Nihei, M. & Awano, Y. Chem. Phys. Lett. *Chem. Phys. Lett* **123**, 126-128 (1986).
134 Asahi, R., Morikawa, T., Ohwaki, T., Aoki, K. & Taga, Y. Visible-light photocatalysis in nitrogen-doped titanium oxides. *science* **293**, 269-271 (2001).
135 Jang, I. *et al.* Preparation of N-functionalized TiO2 particles using one-step sol–gel method and their photocatalytic activity. *Journal of Industrial and Engineering Chemistry* **37**, 380-389 (2016).
136 Marschall, R., Bannat, I., Caro, J. & Wark, M. Proton conductivity of sulfonic acid functionalised mesoporous materials. *Microporous and mesoporous materials* **99**, 190-196 (2007).
137 Chen, W.-H. *et al.* Silanization of solid surfaces via mercaptopropylsilatrane: a new approach of constructing gold colloid monolayers. *RSC Advances* **4**, 46527-46535 (2014).
138 Häkkinen, H. The gold–sulfur interface at the nanoscale. *Nature chemistry* **4**, 443-455 (2012).
139 Maksymovych, P., Voznyy, O., Dougherty, D. B., Sorescu, D. C. & Yates Jr, J. T. Gold adatom as a key structural component in self-assembled monolayers of organosulfur molecules on Au (1 1 1). *Progress in Surface Science* **85**, 206-240 (2010).
140 Daniel, M.-C. & Astruc, D. Gold nanoparticles: assembly, supramolecular chemistry, quantum-size-related properties, and applications toward biology, catalysis, and nanotechnology. *Chemical reviews* **104**, 293-346 (2004).

141 Jin, R. Quantum sized, thiolate-protected gold nanoclusters. *Nanoscale* **2**, 343-362 (2010).
142 El-Sayed, M. A. Some interesting properties of metals confined in time and nanometer space of different shapes. *Accounts of chemical research* **34**, 257-264 (2001).
143 Howard-Fabretto, L. & Andersson, G. G. Metal Clusters on Semiconductor Surfaces and Application in Catalysis with a Focus on Au and Ru. *Advanced Materials*, 1904122 (2019).
144 Joshi, K. & Krishnamurty, S. Au 26: a case of fluxionality/co-existence. *Physical Chemistry Chemical Physics* **20**, 8616-8623 (2018).
145 Chekrygina, D. *et al.* Towards the geometric structure of small supported Au 9 clusters on Si. *Scientific reports* **8**, 1-11 (2018).
146 Yang, J., Wang, D., Han, H. & Li, C. Roles of cocatalysts in photocatalysis and photoelectrocatalysis. *Accounts of chemical research* **46**, 1900-1909 (2013).
147 Zhu, M., Lanni, E., Garg, N., Bier, M. E. & Jin, R. Kinetically controlled, high-yield synthesis of Au25 clusters. *Journal of the American Chemical Society* **130**, 1138-1139 (2008).
148 Stamplecoskie, K. G., Chen, Y.-S. & Kamat, P. V. Excited-state behavior of luminescent glutathione-protected gold clusters. *The Journal of Physical Chemistry C* **118**, 1370-1376 (2014).
149 Negishi, Y. *et al.* A critical size for emergence of nonbulk electronic and geometric structures in dodecanethiolate-protected Au clusters. *Journal of the American Chemical Society* **137**, 1206-1212 (2015).
150 Stamplecoskie, K. G. & Kamat, P. V. Size-dependent excited state behavior of glutathione-capped gold clusters and their light-harvesting capacity. *Journal of the American Chemical Society* **136**, 11093-11099 (2014).
151 Jin, R. *et al.* Size focusing: a methodology for synthesizing atomically precise gold nanoclusters. *The Journal of Physical Chemistry Letters* **1**, 2903-2910 (2010).
152 Alvino, J. F. *et al.* Far-infrared absorption spectra of synthetically-prepared, ligated metal clusters with Au 6, Au 8, Au 9 and Au 6 Pd metal cores. *Rsc Advances* **3**, 22140-22149 (2013).
153 White, R., Bennett, T., Golovko, V., Andersson, G. G. & Metha, G. F. A Systematic Density Functional Theory Study of the Complete De–ligation of Ru3 (CO) 12. *ChemistrySelect* **1**, 1163-1167 (2016).
154 Qian, H., Zhu, M., Wu, Z. & Jin, R. Quantum sized gold nanoclusters with atomic precision. *Accounts of chemical research* **45**, 1470-1479 (2012).
155 Wan, X.-K., Lin, Z.-W. & Wang, Q.-M. Au20 nanocluster protected by hemilabile phosphines. *Journal of the American Chemical Society* **134**, 14750-14752 (2012).
156 Chen, Y.-S. & Kamat, P. V. Glutathione-capped gold nanoclusters as photosensitizers. Visible light-induced hydrogen generation in neutral water. *Journal of the American Chemical Society* **136**, 6075-6082 (2014).
157 Yoon, B. *et al.* Charging effects on bonding and catalyzed oxidation of CO on Au8 clusters on MgO. *Science* **307**, 403-407 (2005).
158 Chusuei, C. C. *et al.* A nanoscale model catalyst preparation: Solution deposition of phosphine-stabilized gold clusters onto a planar TiO2 (110) support. *Langmuir* **17**, 4113-4117 (2001).
159 Li, G. & Jin, R. Atomically precise gold nanoclusters as new model catalysts. *Accounts of chemical research* **46**, 1749-1758 (2013).
160 Wen, F., Englert, U., Gutrath, B. & Simon, U. (Wiley Online Library, 2008).
161 Gutrath, B. S., Englert, U., Wang, Y. & Simon, U. A Missing Link in Undecagold Cluster Chemistry: Single-Crystal X-ray Analysis of [Au11 (PPh3) 7Cl3]. *European Journal of Inorganic Chemistry* **2013**, 2002-2006 (2013).
162 Gutrath, B. S. *et al.* Molecular and Electronic Structure of the Cluster [Au8 (PPh3) 8](NO3) 2. *European Journal of Inorganic Chemistry* **2016**, 975-981 (2016).

163 McPartlin, M., Mason, R. & Malatesta, L. Novel cluster complexes of gold (0)–gold (I). *Journal of the Chemical Society D: Chemical Communications*, 334-334 (1969).
164 Negishi, Y. *et al.* Atomic-level separation of thiolate-protected metal clusters. *Nanoscale* **12**, 8017-8039 (2020).
165 Negishi, Y., Nobusada, K. & Tsukuda, T. Glutathione-protected gold clusters revisited: bridging the gap between gold (I)− thiolate complexes and thiolate-protected gold nanocrystals. *Journal of the American Chemical Society* **127**, 5261-5270 (2005).
166 Knoppe, S., Boudon, J., Dolamic, I., Dass, A. & Burgi, T. Size exclusion chromatography for semipreparative scale separation of Au38 (SR) 24 and Au40 (SR) 24 and larger clusters. *Analytical chemistry* **83**, 5056-5061 (2011).
167 McKenzie, L. C., Zaikova, T. O. & Hutchison, J. E. Structurally similar triphenylphosphine-stabilized undecagolds, Au11 (PPh3) 7Cl3 and [Au11 (PPh3) 8Cl2] Cl, exhibit distinct ligand exchange pathways with glutathione. *Journal of the American Chemical Society* **136**, 13426-13435 (2014).
168 Briant, C. E., Hall, K. P. & Mingos, D. M. P. Synthesis and structural characterisation of [Au6 (PPh3) 6]-(NO3) 2· 3CH2Cl2; an edge-shared bitetrahedral gold cluster. *Journal of organometallic chemistry* **254**, C18-C20 (1983).
169 Al Qahtani, H. S. *et al.* Atomically resolved structure of ligand-protected Au9 clusters on TiO2 nanosheets using aberration-corrected STEM. *The Journal of Chemical Physics* **144**, 114703 (2016).
170 Olivares, A., Laskin, J. & Johnson, G. E. Investigating the synthesis of ligated metal clusters in solution using a flow reactor and electrospray ionization mass spectrometry. *The Journal of Physical Chemistry A* **118**, 8464-8470 (2014).
171 Johnson, G. E., Olivares, A., Hill, D. & Laskin, J. Cationic gold clusters ligated with differently substituted phosphines: effect of substitution on ligand reactivity and binding. *Physical Chemistry Chemical Physics* **17**, 14636-14646 (2015).
172 Pettibone, J. M. & Hudgens, J. W. Synthetic approach for tunable, size-selective formation of monodisperse, diphosphine-protected gold nanoclusters. *The Journal of Physical Chemistry Letters* **1**, 2536-2540 (2010).
173 Pettibone, J. M. & Hudgens, J. W. Predictive gold Nanocluster formation controlled by metal-ligand complexes. *Small* **8**, 715-725 (2012).
174 Häkkinen, H. Atomic and electronic structure of gold clusters: understanding flakes, cages and superatoms from simple concepts. *Chemical Society Reviews* **37**, 1847-1859 (2008).
175 Johnston, R. & Wilcoxon, J. Vol. 3 (Elsevier Oxford:, 2012).
176 Van der Velden, J. *et al.* Intermediates in the formation of gold clusters. Preparation and x-ray analysis of [Au7 (PPh3) 7]+ and synthesis and characterization of [Au8 (PPh3) 6I] PF6. *Inorganic Chemistry* **23**, 146-151 (1984).
177 Gutrath, B. S. *et al.* [Au 14 (PPh 3) 8 (NO 3) 4]: An Example of a New Class of Au (NO 3)-Ligated Superatom Complexes. *Angewandte Chemie International Edition* **12**, 3529-3532 (2013).
178 Bond, G. C., Sermon, P. A., Webb, G., Buchanan, D. A. & Wells, P. B. Hydrogenation over supported gold catalysts. *Journal of the Chemical Society, Chemical Communications*, 444b-445 (1973).
179 Bond, G. & Sermon, P. Gold catalysts for olefin hydrogenation: transmutation of catalytic properties. *Gold Bulletin* **6**, 102-105 (1973).
180 Okumura, M., Fujitani, T., Huang, J. & Ishida, T. A career in catalysis: Masatake Haruta. *ACS Catalysis* **5**, 4699-4707 (2015).
181 Nkosi, B. & Adams, M. N.]. Coville, and G.]. Hutchings. *J Chern. Soc., Chern. Commun* **71** (1988).

182 Della Pina, C., Falletta, E. & Rossi, M. Update on selective oxidation using gold. *Chemical Society Reviews* **41**, 350-369 (2012).
183 Bond, G. C. Hydrogenation by gold catalysts: an unexpected discovery and a current assessment. *Gold Bulletin* **49**, 53-61 (2016).
184 Yang, D. *et al.* Controllable Conversion of CO2 on Non-Metallic Gold Clusters. *Angewandte Chemie International Edition* **59**, 1919-1924 (2020).
185 Haruta, M. Gold as a novel catalyst in the 21st century: Preparation, working mechanism and applications. *Gold bulletin* **37**, 27-36 (2004).
186 Okumura, M. & Haruta, M. Interplay of theoretical calculations and experiments for a study of catalysis by gold. *Catalysis Today* **259**, 81-86 (2016).
187 Häkkinen, H., Abbet, S., Sanchez, A., Heiz, U. & Landman, U. Structural, electronic, and impurity-doping effects in nanoscale chemistry: supported gold nanoclusters. *Angewandte Chemie International Edition* **42**, 1297-1300 (2003).
188 Lopez-Acevedo, O., Kacprzak, K. A., Akola, J. & Häkkinen, H. Quantum size effects in ambient CO oxidation catalysed by ligand-protected gold clusters. *Nature chemistry* **2**, 329-334 (2010).
189 Weiher, N. *et al.* Structure and oxidation state of gold on different supports under various CO oxidation conditions. *Journal of Catalysis* **240**, 100-107 (2006).
190 Yu, C., Li, G., Kumar, S., Kawasaki, H. & Jin, R. Stable Au25 (SR) 18/TiO2 composite nanostructure with enhanced visible light photocatalytic activity. *The Journal of Physical Chemistry Letters* **4**, 2847-2852 (2013).
191 Negishi, Y. *et al.* Controlled loading of small Au n clusters (n= 10–39) onto BaLa4Ti4O15 photocatalysts: Toward an understanding of size effect of cocatalyst on water-splitting photocatalytic activity. *The Journal of Physical Chemistry C* **119**, 11224-11232 (2015).
192 Huang, M.-H. *et al.* Self-transformation of ultra-small gold nanoclusters to gold nanocrystals toward boosted photoreduction catalysis. *Chemical Communications* **55**, 10591-10594 (2019).
193 Dai, X.-C. *et al.* Probing the advantageous photosensitization effect of metal nanoclusters over plasmonic metal nanocrystals in photoelectrochemical water splitting. *The Journal of Physical Chemistry C* **124**, 4989-4998 (2020).
194 Kurashige, W. *et al.* Au25-loaded BaLa4Ti4O15 water-splitting photocatalyst with enhanced activity and durability produced using new chromium oxide shell formation method. *The Journal of Physical Chemistry C* **122**, 13669-13681 (2018).
195 Tan, C.-L., Zhang, F., Li, Y.-H., Tang, Z.-R. & Xu, Y.-J. Au clusters-based visible light photocatalysis. *Research on Chemical Intermediates* **47**, 29-50 (2021).
196 Chen, J., Zhang, Q.-F., Bonaccorso, T. A., Williard, P. G. & Wang, L.-S. Controlling gold nanoclusters by diphospine ligands. *Journal of the American Chemical Society* **136**, 92-95 (2013).
197 Ruzicka, J.-Y. *et al.* Toward control of gold cluster aggregation on TiO2 via surface treatments. *The Journal of Physical Chemistry C* **119**, 24465-24474 (2015).
198 Andersson, G. G. *et al.* Phosphine-stabilised Au9 clusters interacting with titania and silica surfaces: The first evidence for the density of states signature of the support-immobilised cluster. *The Journal of chemical physics* **141**, 014702 (2014).
199 Abbet, S., Heiz, U., Häkkinen, H. & Landman, U. CO oxidation on a single Pd atom supported on magnesia. *Physical review letters* **86**, 5950 (2001).
200 Meier, D., Rizzi, G., Granozzi, G., Lai, X. & Goodman, D. $Ru_3(CO)_{12}$ adsorption and decomposition on TiO_2. *Langmuir* **18**, 698-705 (2002).
201 Rizzi, G. A., Magrin, A. & Granozzi, G. Substitutional $Ti_{(1-x)}Ru_xO_2$ surface alloys obtained from the decomposition of $Ru_3(CO)_{12}$ on TiO_2 (110). *Phys. Chem. Chem. Phys.* **1**, 709-711 (1999).

202 Zhao, X., Hrbek, J. & Rodriguez, J. A. The decomposition and chemistry of Ru3 (CO) 12 on TiO2 (1 1 0) studied with X-ray photoelectron spectroscopy and temperature programmed desorption. *Surface science* **575**, 115-124 (2005).
203 Nielsch, K., Müller, F., Li, A. P. & Gösele, U. Uniform nickel deposition into ordered alumina pores by pulsed electrodeposition. *Advanced Materials* **12**, 582-586 (2000).
204 Chen, J., Zhang, Q.-F., Bonaccorso, T. A., Williard, P. G. & Wang, L.-S. Controlling gold nanoclusters by diphospine ligands. *Journal of the American Chemical Society* **136**, 92-95 (2014).
205 Matthey, D. *et al.* Enhanced bonding of gold nanoparticles on oxidized TiO2 (110). *Science* **315**, 1692-1696 (2007).
206 Toyoshima, R. & Kondoh, H. In-situ observations of catalytic surface reactions with soft x-rays under working conditions. *Journal of Physics: Condensed Matter* **27**, 083003 (2015).
207 Gomes Silva, C., Juárez, R., Marino, T., Molinari, R. & García, H. Influence of excitation wavelength (UV or visible light) on the photocatalytic activity of titania containing gold nanoparticles for the generation of hydrogen or oxygen from water. *Journal of the American Chemical Society* **133**, 595-602 (2011).
208 Sudheeshkumar, V., Sulaiman, K. O. & Scott, R. W. Activation of atom-precise clusters for catalysis. *Nanoscale Advances* (2020).
209 Hidalgo, M., Maicu, M., Navío, J. A. & Colón, G. Effect of sulfate pretreatment on gold-modified TiO2 for photocatalytic applications. *The Journal of Physical Chemistry C* **113**, 12840-12847 (2009).
210 Veith, G. M., Lupini, A. R. & Dudney, N. J. Role of pH in the formation of structurally stable and catalytically active TiO2-supported gold catalysts. *The Journal of Physical Chemistry C* **113**, 269-280 (2009).
211 Veith, G. M., Lupini, A. R., Pennycook, S. J. & Dudney, N. J. Influence of support hydroxides on the catalytic activity of oxidized gold clusters. *ChemCatChem* **2**, 281-286 (2010).
212 Kilmartin, J. *et al.* Following the creation of active gold nanocatalysts from phosphine-stabilized molecular clusters. *Acs Catalysis* **2**, 957-963 (2012).
213 Adnan, R. H., Andersson, G. G., Polson, M. I., Metha, G. F. & Golovko, V. B. Factors influencing the catalytic oxidation of benzyl alcohol using supported phosphine-capped gold nanoparticles. *Catalysis Science & Technology* **5**, 1323-1333 (2015).
214 Anderson, D. P. *et al.* Chemically-synthesised, atomically-precise gold clusters deposited and activated on titania. *Physical chemistry chemical physics* **15**, 3917-3929 (2013).
215 Li, Q., Yang, S., Chai, J., Zhang, H. & Zhu, M. Insights into mechanisms of diphosphine-mediated controlled surface construction on Au nanoclusters. *Nanoscale* **14**, 15804-15811 (2022).
216 Kang, X. & Zhu, M. Transformation of atomically precise nanoclusters by ligand-exchange. *Chemistry of Materials* **31**, 9939-9969 (2019).
217 Anderson, D. P. *et al.* Chemically synthesised atomically precise gold clusters deposited and activated on titania. Part II. *Physical chemistry chemical physics* **15**, 14806-14813 (2013).
218 Mousavi, H. *et al.* Au 101–rGO nanocomposite: Immobilization of phosphine-protected gold nanoclusters on reduced graphene oxide without aggregation. *Nanoscale Advances* **3**, 1422-1430 (2021).

CHAPTER 2: EXPERIMENTAL

2.1. Materials and sample preparations

In this study, mesoporous TiO_2 ($MTiO_2$) substrates were prepared using several methods such as screen-printing method in Chapter 5, sol-gel combined with evaporation-induced self-assembly (EISA) method in Chapter 6, and sol-gel combined with homogeneous precipitation method in Chapter 7.

In the second step, $MTiO_2$ substrates were functionalised with thiol functional groups ($SMTiO_2$) and amino groups ($NMTiO_2$) using 3-mercaptopropyltrimethoxysilane (MPTMS) and chitosan polysaccharides, respectively, to obtain surfaces with improved adhesion to Au_9 nanoclusters (NCs) (Figure 2.1).

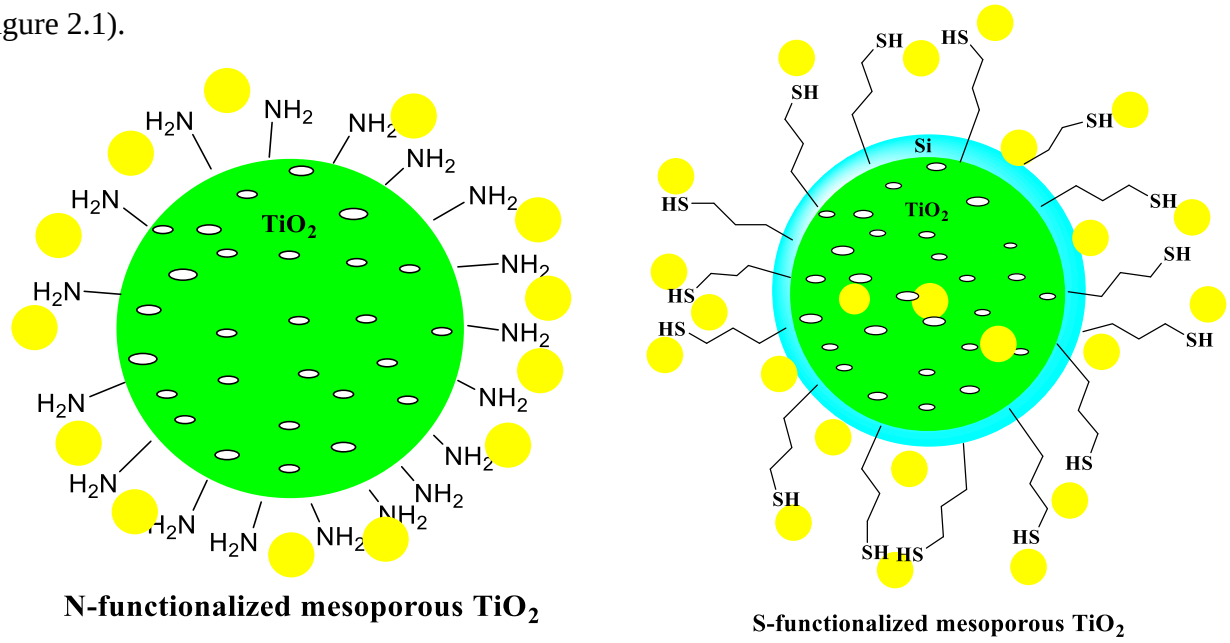

Figure 2.1. Representative examples of S-functionalised and N-functionalised mesoporous TiO_2.

2.1.1. Preparation of $SMTiO_2$ films decorated by Au_9 nanoclusters (NCs)

The Fluorine-doped Tin Oxide (FTO) substrate (TEC 15) underwent a thorough cleaning process involving ultrasonication with both deionized water and detergent, followed by a subsequent ultrasonication step with ethanol. Next, the fabrication of TiO_2 films was conducted by applying TiO_2 paste onto the FTO substrate using the screen-printing method, followed by a brief drying period at a temperature of 120°C for 5 minutes. The FTO substrate coated with the deposited titania was subsequently subjected to a controlled heating procedure within a covered petri dish, carried out in a furnace. This heating process encompassed the following temperature steps: 120°C for 5 minutes, 325°C for 10 minutes, 375°C for 10 minutes, and finally, 500°C for 30 minutes.

To prepare $SMTiO_2$ films, the $MTiO_2$ films underwent a modification involving immersion in 5 ml of toluene, followed by the addition of 0.5 ml of MPTMS as can be seen in Figure 2.2. This mixture was then subjected to reflux at 110°C for a duration of eight hours, resulting in the creation of $SMTiO_2$ film. Subsequently, the prepared functionalised film underwent a washing step using ethanol and was dried at room temperature overnight.

To create the Au_9 NCs/(S)$MTiO_2$ nanocomposites, 1 mg of Au_9 NCs crystals was dissolved in 2 ml of methanol. Afterwards, the Au_9 cluster solution was added to the completely dried $SMTiO_2$ films. The films were immersed in this solution for 1 hour, causing the film's colour to shift from white to a yellowish tone. The prepared samples underwent 5 hours of vacuum treatment at room temperature to remove any residual methanol. To avert potential aggregation or degradation, the samples were delicately placed in the sealed vials and stored in a dark environment at 4°C.

2.1.2. Preparation of $SMTiO_2$ nanoparticles (NPs)

2 g of the triblock copolymer surfactant P123 is dissolved in 12 g of absolute ethanol through 30 minutes of stirring. A solution containing 9.84 g (0.035 mol) of titanium tetraisopropoxide in 1.44 ml (0.046 mol) of HCl is then introduced to the previous solution while vigorously stirring for 10 minutes. Subsequently, the resulting Sol is poured into a Petri dish and allowed to Gel at 40 °C in an open environment for 30 minutes. Afterwards, it is left to dry under ambient conditions for 24 hours, encouraging the crosslinking and oligomerization of the TiO_2 within the sol/gel precursor. To complete the process, the prepared samples are calcined at 400 °C for 4 hours in an air environment. This step serves to eliminate the polymeric surfactant, facilitate the crystallization of TiO_2 into the anatase phase, and generate interparticle mesopores.

To prepare $SMTiO_2$ NPs, 0.1 grams of $MTiO_2$ NPs were homogeneously dispersed in 5 ml of toluene, which had previously been deoxygenated through a 15-minute N_2 purging. To this mixture, 0.5 ml of MPTMS was introduced. The combined solution was subjected to reflux at 110 °C for 8 hours, with a continuous flow of N_2 gas throughout the reaction (Figure 2.2). After the reaction was complete, the resulting products were centrifuged and washed twice in ethanol. They were then allowed to air dry overnight at room temperature.

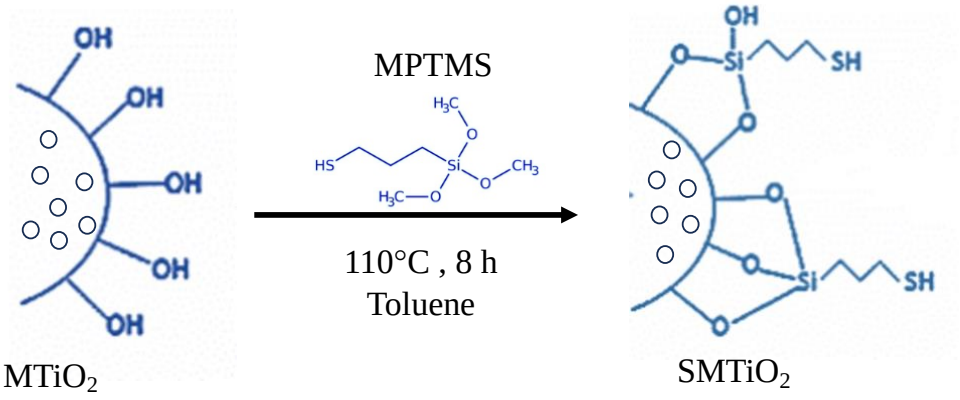

Figure 2.2. An illustration of a method for making S-functionalised mesoporous TiO_2 using 3-mercaptopropyltrimethoxysilane (MPTMS).

2.1.3. Preparation of $NMTiO_2$ NPs using chitosan as the template.

A mixture of 3 grams of chitosan powder and 100 ml of 5% v/v aqueous acetic acid was stirred for an hour to create a solution with a concentration of 3% w/w. A titanium chloride solution was prepared by combining 1.5 grams (0.0053 mol) of titanium (IV) isopropoxide with 10 ml of 37% HCl and 50 ml of deionized water. This solution was then added to the chitosan solution in a 1:1 w/w ratio of Ti precursor to chitosan solution. The resulting mixture was agitated at room temperature for a duration of two hours. Afterward, the solution was gradually dripped into 50% aqueous ammonia under continuous stirring, leading to gel formation after an hour of stabilisation in the ammonia solution. The gel that was formed underwent centrifugation, followed by two cycles of washing with deionized water and three rounds of washing with methanol. Subsequently, the particles were dried at 40 °C and subjected to calcination at temperatures of 400 °C, 500 °C, and 600 °C in the presence of air to eliminate the chitosan. This resulting photocatalyst was termed $NMTiO_2$ (1:1).

The template was eliminated from the sample during the calcination process, which induced a crystallization in the material. Notably, when the atmosphere was switched from air to Ar, a distinctive change in colouration was observed, resulting in the material taking on a black appearance.

2.1.4. Deposition of Au_9 NCs onto (S)$MTiO_2$ and $NMTiO_2$ NPs.

For the deposition of Au_9 NCs onto the surfaces of $MTiO_2$, the initial step involved preparing an Au_9 NC solution. This was accomplished by dissolving 1 mg (4.63×10^{-6} mol) of dark green Au_9 NC crystals in 2 ml of methanol. Subsequently, 10 mg of $MTiO_2$ samples were added to the prepared Au_9 NC solution. The mixture was stirred for a duration of 1 hour at room temperature. For instance, as illustrated in Figure 2.3, there is a noticeable transformation in the colour of the Au_9 NC solution, shifting from an orangish tone to a pale yellow. This colour change serves as a clear indicator of the adsorption of Au_9 NCs onto the surfaces of the prepared substrates. Notably, the degree of colour

change in the final Au_9 solution directly correlates with the extent of adsorption onto the substrate surface. In other words, the more pronounced the shift in colour towards a paler yellow, the greater the adsorption onto the substrate surface. The suspension underwent centrifugation, and the resulting sample was subjected to vacuum conditions at room temperature for approximately 5 hours to remove any remaining methanol residue. The treated sample was then securely stored in a vial with a cap, in a dark environment at approximately 4 °C, aiming to minimize the potential for aggregation or degradation of the material.

Figure 2.3. (a) Au_9 initial solution in methanol (b) white and (c) black $NMTiO_2$ suspension in Au_9 solution before deposition; Au_9 solution after deposition process for (d) white $NMTiO_2$ (e) black $NMTiO_2$ substrates

2.1.5. Ligand removal process

To remove the phosphine ligands through thermal treatment, functionalised and unfunctionalised $MTiO_2$ substrates decorated with the phosphine ligated Au_9 NCs were drop-casted onto Si wafers. Afterwards, the composite samples were subjected to annealing at a temperature of 200 °C under a vacuum environment for 10 minutes. Subsequently, the samples were permitted to gradually reach room temperature while being subjected to reduced pressure. The resulting materials were then stored in a refrigerator at 4 °C.

2.1.6. Triphenylphosphine ligand stabilised Au_9 NCs

Detailed information related to the preparation, purification, and characterisation of the triphenylphosphine ligated Au_9 NCs has been reported in Chapter 4.

2.1.7. Dye degradation photocatalytic test

To investigate the photodegradation of methyl orange (MO) dye, the $MTiO_2/Au_9$ NCs nanocomposites along with their corresponding substrates were suspended in 3 ml of MO dye solution. This experimental setup aimed to assess the degradation capability of the nanocomposites under UV light exposure. To facilitate mixing, a Vortex Fluidic Device (VFD)[1-3] equipped with two 10 W Hg lamps emitting UV light at 254 nm was employed. The experiment was designed to evaluate the photoactivity of the prepared nanocomposites using kinetic analysis, by plotting the natural

logarithm of the ratio of initial concentration to current concentration (-ln C/C_0) over time. After identifying the most effective photocatalyst based on reaction constants obtained from these kinetic plots, the degradation efficiency of this selected photocatalyst was further studied. A selected quantity of the best photocatalysts was dispersed within a 3 ml solution of the MO dye and subjected to UV light exposure for the designated duration. The experiments were conducted under consistent conditions, including a rotation speed of 900 rpm and a constant UV light intensity. Upon completion of the reaction, the catalyst particles suspended within the solution underwent centrifugation at a speed of 12,000 rpm for 10 minutes. A spectrophotometer (UV-Visible device manufactured by PerkinElmer) was employed to quantify MO concentration, with measurements taken at the peak wavelength of 466 nm.

The degradation percentage was determined using the formula provided as Equation 2.1, where the variables C_0 and C_t represent the initial concentration of MO and the concentration at the time of measurement (in ppm), respectively.

$$D(\%) = \frac{(C_0 - C_t)}{C_0} \times 100 \qquad \textit{Equation 2.1}$$

Detailed information regarding the selection of independent factors, central composite design, response surface methodology and curve fitting using python has been reported in Chapter 3.

2.2. Characterisation methods

The structures of these compositions are characterised by X-Ray photoelectron spectroscopy (XPS), near-edge X-ray absorption fine structure (NEXAFS), scanning electron microscopy (SEM), energy-dispersive X-ray spectroscopy (EDS), Scanning transmission electron microscopy (STEM), X-ray powder diffraction (XRD), Fourier transform infrared spectroscopy (FTIR), and thermal gravimetric analysis (TGA), as well as Brunauer-Emmett-Teller and Barrett-Joyner-Halenda (BET and BJH) measurement. In Chapters 6 and 7, ion beam sputtering was employed to remove a few layers from the surface to study the substrate surfaces. By applying a DC voltage ranging from 0.5 to 5 kV, Ar atoms were ionized, generating a plasma composed of ionized gas. 3 keV Ar^+ ions under a pressure of 10^{-8} mbar were utilised.

2.2.1 X-ray photoelectron spectroscopy (XPS)

XPS is a powerful surface-sensitive characterisation method utilised to investigate the elemental composition and chemical state of materials. In XPS, a sample is exposed to X-rays, which cause photoelectrons to be emitted from its surface. These photoelectrons carry information about the energy levels of the electrons within the sample's atoms, including their binding energies.[221]

By measuring the kinetic energies of the emitted photoelectrons, XPS provides insights into the elemental composition of the sample's surface. The binding energies of the photoelectrons can be correlated with specific elements, enabling the identification of the elements present and their chemical environments. This allows researchers to determine not only which elements are present but also their oxidation states and bonding configurations.[5]

XPS is particularly useful for studying surfaces and thin films, making it applicable in several research fields including materials science, catalysis, nanotechnology, and surface chemistry. It can provide information about the purity of materials, the presence of contaminants, and changes in chemical composition due to surface reactions or treatments. XPS is also quantitative, allowing for study of the atomic concentration of elements present in the top few nanometres of a material.[4,5]

Overall, XPS is a non-destructive and versatile characterisation method that offers valuable insights into the surface properties of materials, making it a valuable tool for researchers studying the characteristics and behaviour of a broad range of compounds and interfaces.[6]

In response to electromagnetic radiation, materials emit electrons because of the photoelectric effect. When the energy carried by photons exceeds the binding energy of electrons within a molecule, those electrons are ionized. The disparity between the energy of the photon and the binding energy of the electron yields the kinetic energy of the emitted electron, which is quantified using a hemispherical analyser (HSA). This relationship is described by Einstein's photoelectric equation as shown in Equation 2.2, illustrates this relationship:[7]

$$E_{kin}=E_{photon}-\Phi_{spec}-E_{bin} \qquad \text{(Equation 2.2)}$$

In this equation, E_{kin} represents the kinetic energy of the electrons, E_{photon} is the energy of the incident photon, Φ_{spec} is the work function of the spectrometer (a constant), and E_{bin} is the binding energy of the electrons. The work function of the spectrometer remains unchanged, as it is consistent for all measurements.

The energy of the incident photon dictates whether electrons from the surface atoms' valence or core levels are detected. Figure 2.4[8] depicts the essential components of an X-ray Photoelectron Spectroscopy which are an electron detector and an X-ray source, a hemispherical electron energy analyser. When exposed to light from the X-ray source at a specific angle, the sample's surface emits electrons. The quantity of emitted photoelectrons and their kinetic energies are quantified during this process.

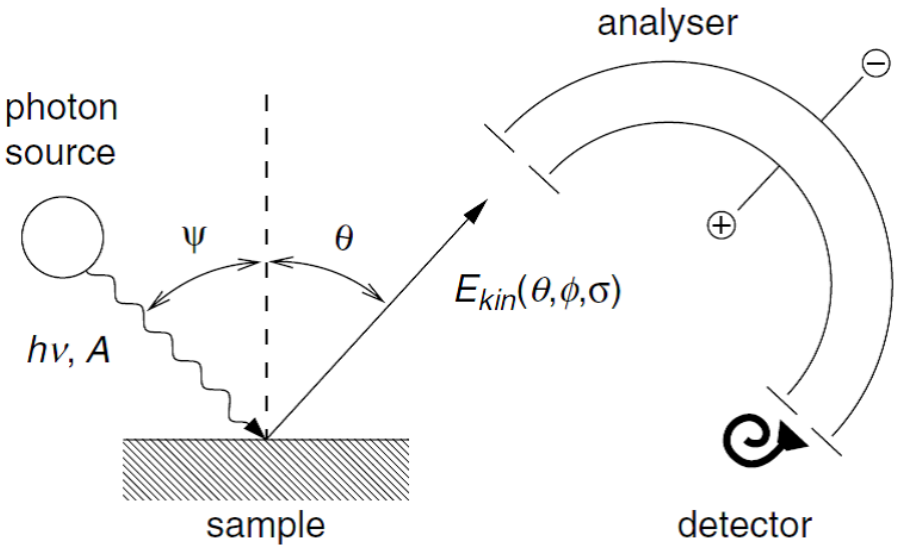

Figure 2.4. The operational concept of a photoemission spectrometer involves generating monochromatic photons with energy hν by illuminating the sample surface at a specific angle ψ using a light source.[8]

Photoelectron spectroscopy is renowned for being a surface-sensitive analytical technique owing to the limited distance electrons can travel within a material before interacting with neighbouring atoms or electrons. This distance is referred to as the "mean free path." Figure 2.5[8,9] illustrates the mean free path of electrons within monolayers for various electron energies. The diminishment of electron intensity is elucidated by the Equation 2.3.[9]

$$I(d,E,\alpha)=I_0 \exp\left(-d/\cos(\alpha)\cdot\lambda(E)\right) \qquad \text{(Equation 2.3)}$$

In this equation, I signifies the measured intensity, I_0 is the initial intensity, d represents the depth from which electrons are emitted, α is the angle between the detector and the surface normal, and $\lambda(E)$ corresponds to the electron mean free path.

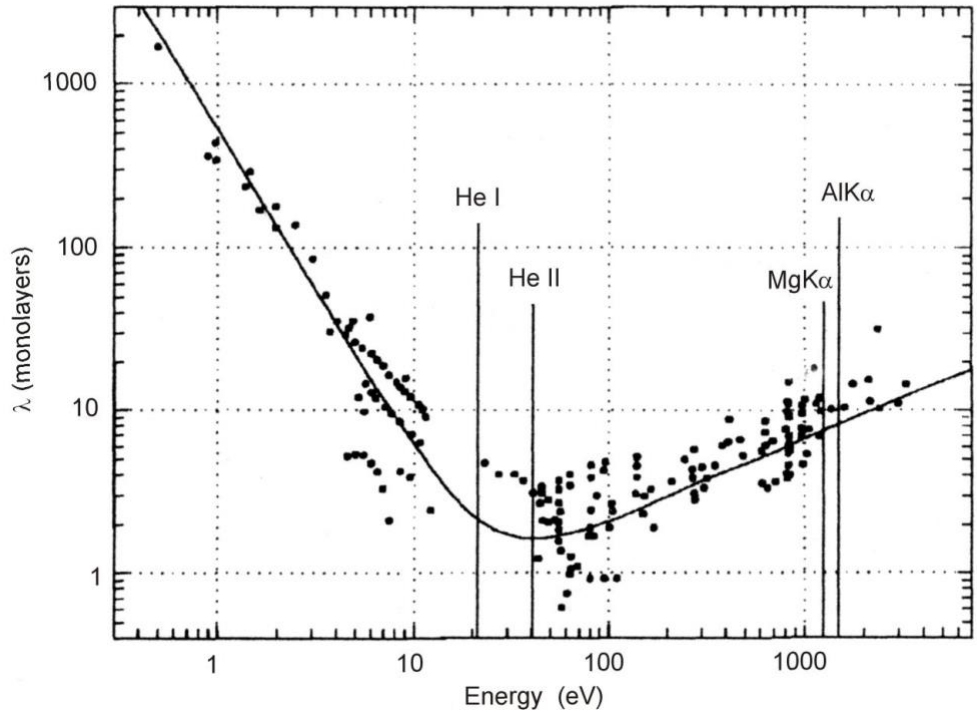

Figure 2.5. Electron mean free path[8,9].

XPS provides depth information to a depth of approximately 3-5 nm.[10] One of the primary capabilities of XPS is its ability to discern the chemical composition of elements within a sample. This technique is based on two distinct processes that result in the electron emission from the sample. The first process, known as photoexcitation, involves the transfer of the entire energy of an X-ray photon to an electron. Energy transfer leads to the release of an electron from the sample in the first process. The second process is Auger excitation, where an electron transitions from a lower binding energy level to a higher binding energy orbital (core electron) within the target atom. This transition fills the gap created by the emission of the photoelectron. The excess energy, which is the difference between the lower and higher binding energies, is emitted as either a photon or transferred to another electron, subsequently causing its ejection. The electron that is ejected secondarily is referred to as an Auger electron. It is noteworthy that photoelectron peaks in XPS spectra tend to be sharper due to their fixed binding energies, in contrast to Auger electron peaks which show broader features.[10]

In an XPS spectrum, the primary information extracted includes the peak position of elements, the full width at half maximum (FWHM) of the peaks, and the intensity of each peak[11]. The peak position uniquely identifies each element, acting as a characteristic fingerprint. The overall measurement uncertainty is influenced by the peak position, full width at half maximum (FWHM), intensity, and background collectively.

The FWHM of peaks in an XPS spectrum is directly related to the measurement's resolution. A narrower FWHM signifies higher resolution, allowing for finer discrimination between closely

spaced peaks. On the other hand, a broader FWHM can lead to reduced peak separation and potentially hinder precise identification of distinct elements.[12]

The intensity of peaks is closely tied to the concentration of the corresponding element within the sample. Peaks with higher intensities generally indicate a larger concentration of the corresponding element at the surface being analysed. This aspect is particularly useful for quantitative analysis, allowing estimation of the relative proportions of different elements present in a sample. Therefore, an XPS spectrum provides information about peak positions, FWHM, and intensities of peaks, enabling the identification of elements and quantitative assessment of their concentrations within a sample's surface layer.

The binding energy of emitted electrons, as assessed through XPS, plays a vital role in indicating the size and chemical state of deposited clusters, primarily influenced by electronic effects. This concept carries substantial significance in the interpretation of XPS spectra, offering valuable insights into the properties of the analysed materials. It is worth noting that the 4f 7/2 orbital of Au has often been chosen in numerous studies due to its effectiveness in revealing the electronic state of Au.[13]

In the following sections, we will explore in greater detail the mechanism by which binding energy, obtained from XPS measurements, provides insights into the size and chemical state of deposited clusters. The binding energy of electrons is intrinsically connected to the electronic configuration of atoms within a substance. In the context of deposited clusters, variations in size and chemical environment lead to changes in the binding energy of electrons associated with specific atomic orbitals. These shifts are a consequence of the altered electron interactions as cluster size and chemical composition change.[14]

For instance, smaller clusters exhibit distinctive quantum confinement effects due to their reduced size, leading to quantised energy levels for electrons. Consequently, the binding energy of electrons in smaller clusters deviates from that in bulk materials. Similarly, changes in the chemical state of the clusters, such as oxidation or alloying, result in shifts in the binding energy due to modifications in the electronic environment around the atoms.

By carefully analysing the binding energy values obtained from XPS spectra, researchers can deduce the electronic interactions and structural characteristics of the deposited clusters. These shifts and variations in binding energy provide insights into the surface chemistry, electronic properties, and even the interactions between the substrate and the clusters. Overall, the binding energy information acquired through XPS measurements serves as a tool for assessing the size and chemical state of deposited clusters. The shifts in binding energy reflect changes in electronic interactions, and yield information about the nature and properties of the analysed materials.[15]

The interpretation of XPS peak positions is influenced by several factors. Firstly, the oxidation state of an element significantly affects peak positions. For instance, the binding energy of Au peaks shifts from its standard bulk value of 84 eV to a higher value, typically ranging from 85.8 to 86.2 eV, depending on interactions with substrates. This shift is indicative of the oxidation state and the nature of interactions taking place, and it serves as a key indicator of chemical bonding configurations.[13] Secondly, peak positions and full width at half maximum (FWHM) in XPS spectra are influenced by both initial and final state effects. These effects depend on the elements comprising the clusters, the cluster size, and its interaction with the substrate. Initial state effects are linked to changes in electronic states due to factors such as cluster size and their interaction with the surface of the substrates. On the other hand, the final state effect relates to the de-excitation process of an atom after absorbing an X-ray photon. In the context of metal nanoclusters (NCs), the excited state can endure for a longer period compared to the corresponding bulk materials. The shift in peak positions linked to these effects frequently relies on the cluster's size and the nature of the substrate.[15] However, interpreting the shifts in peak positions for Au can be challenging. This is due to the relatively weak Auger lines, which are an indicator of the initial and final state effects. The complex interplay of these effects, combined with the weak Auger lines for Au, makes it difficult to solely rely on experimental data to differentiate between initial and final state effects in peak position shifts.[15,16]

In summary, the interpretation of XPS peak positions involves considering the oxidation state, initial and final state effects, and their interplay with the cluster size and substrate interactions. While these factors provide insights into the electronic and chemical properties of clusters, the intricacies of peak position shifts for Au often require careful analysis and consideration of multiple factors.

In Chapters 5, 6, and 7, we conducted spectroscopic measurements using an Ultra-High Vacuum (UHV) instrument at an extremely low base pressure of a few 10^{-10} mbar, as detailed in reference.[234] The primary UHV instrument built by SPECS (Berlin, Germany) has attached instrumentation for XPS, IPES, MIES/UPS and FTIR (see Figure 2.4). We utilised non-monochromatic Mg Kα radiation (energy: 1253.6 eV) by operating the X-ray source at 200 W and 12 kV. The measurement protocol involved recording survey scans at an energy step of 40 eV. Subsequently, high-resolution scans were carried out at a pass energy of 10 eV, employing a smaller step size of 0.1 eV. During the analysis, we employed the Shirley background correction method. For the high-resolution XPS, we used a fitting approach that combined Lorentzian and Gaussian peaks. To standardize the binding energy measurements, we normalized the binding energy values of the XP spectra to 285 eV. This normalization was applied to the main C 1s peak, which represents sp3 hybridized C[235]. This procedure was implemented to correct for any charging effects that might be present in the spectra. This experimental setup and analytical strategy allowed us to acquire reliable

XPS data, contributing to a comprehensive understanding of the materials under investigation. The X-ray photoelectron spectroscopy (XPS) peak fitting process yielded an error bar of around ± 0.2 eV.

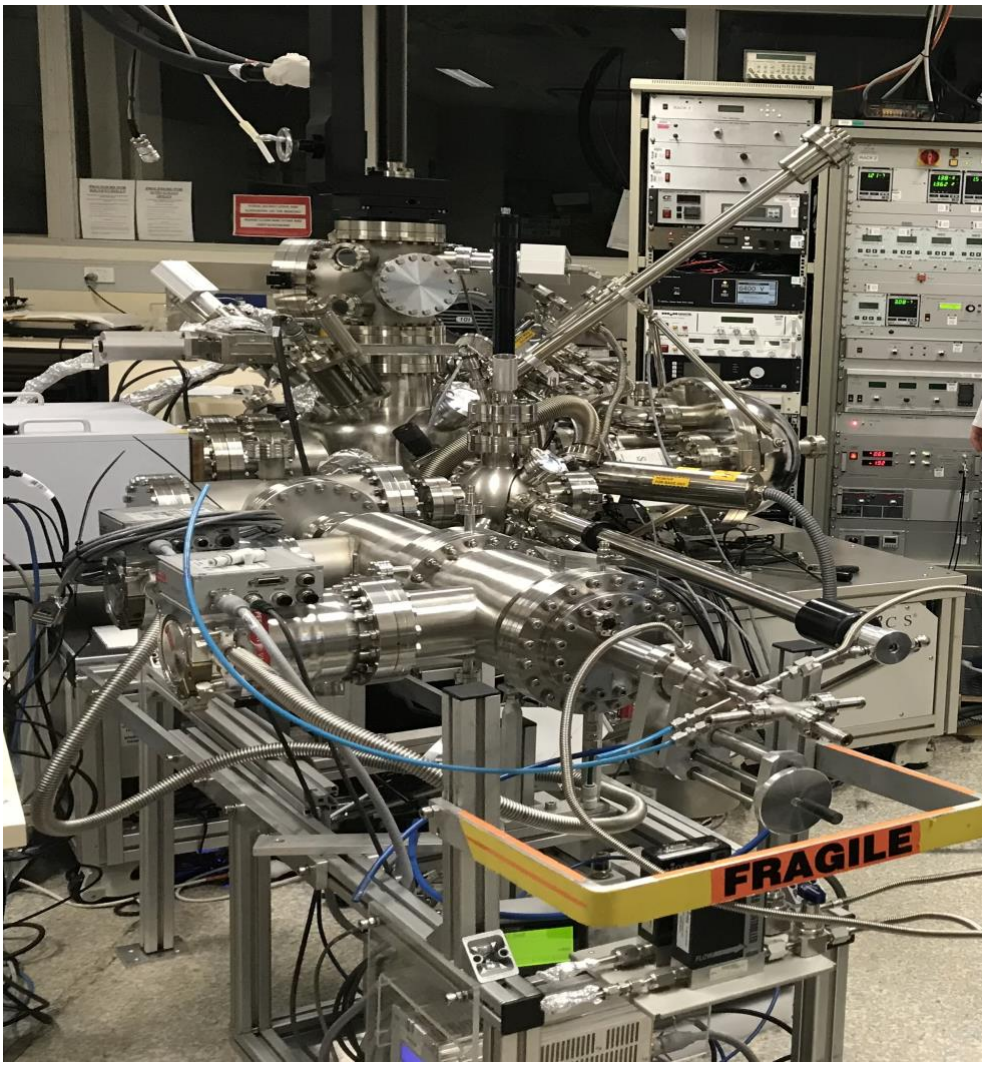

Figure 2.6. Image depicting the ultra-high vacuum (UHV) apparatus at Flinders University, equipped for X-ray Photoelectron Spectroscopy (XPS), Mass Spectrometry of Ions from Excited Surfaces (MIES), Ultraviolet Photoelectron Spectroscopy (UPS), Inverse Photoelectron Spectroscopy (IPES), and Fourier-Transform Infrared Spectroscopy (FTIR) experiments.

The primary chamber has been also equipped with an ion source (SPECS Lab PU-IQE 12/38), which played a crucial role in sputter cleaning the samples discussed in Chapters 6 and 7. To achieve this, the ion source operated at an accelerating voltage of 3kV, generating an ion current of approximately 250nA. This configuration resulted in a total ion dose of around $2x10^{15}$ ions per square centimetre. Ar^+ ions were utilised, and the settings were adjusted to ensure that the ion beam covered the entire sample by rastering across it.[19]

2.2.2 X-ray Absorption Spectroscopy (XAS)

X-ray absorption spectroscopy is utilised to deduce properties such as interatomic distances, metal-ligand bond lengths, and average coordination numbers in non-crystalline compounds, which are otherwise challenging to ascertain. This method involves measuring absorption spectra by exciting a core electron of an atom to an unoccupied orbital through X-ray excitation. X-ray absorption spectra typically exhibit a pronounced and abrupt rise in absorption intensity known as an "edge." This peak at the absorption edge corresponds to the shift between the core level and the vacant valence states of an atom. This transition is highly responsive to the immediate surroundings of the atom being studied.[20]

X-ray absorption spectroscopy (XAS) can be categorised into two primary regions: the lower-energy portion known as X-ray absorption near-edge structure (XANES), and the higher-energy segment referred to as extended X-ray absorption fine structure (EXAFS). Within XANES, there are two specific edges: the rising edge (high-energy edge) and the pre-edge (low-energy edge). The results obtained from the low-energy edges are commonly termed near-edge X-ray absorption fine structure (NEXAFS).[21,22]

XANES is commonly applied to explore attributes such as oxidation states, coordination surroundings, symmetry, and the density of states (DOS). Conversely, EXAFS is utilised to gather details about the immediate atomic arrangement, covering aspects like bond length, the identity of ligands and the coordination number. What makes XAS highly versatile is its capacity to integrate seamlessly with other techniques like UV-visible and infrared spectroscopy, as well as small-angle X-ray scattering, allowing for concurrent measurements that yield more comprehensive insights. When recording both EXAFS and XANES spectra within the energy range of 11,880 to 12,000 eV, researchers typically make use of the Au L3-edge as a reference point.[23]

Chapters 6 and 7 of the thesis showcase the photoelectron spectra obtained from Ti, S and N elements. The acquisition of these spectra took place at the Soft X-ray Beamline facility located within the Australian Synchrotron (AS). The adoption of X-ray techniques reliant on synchrotron radiation marks a substantial progression in recent times, primarily attributable to two pivotal factors.[24]

Firstly, this approach has spurred the progress of X-ray optics, enabling more precise manipulation and control of X-ray beams. This has profound implications for the characterisation of materials, especially within the realm of nanotechnology. The evolving field of nanotechnology, often referred to as the 'nanoworld,' is rapidly advancing, and the incorporation of synchrotron radiation techniques offers a fresh avenue for characterising nanostructures.

Moreover, synchrotron-based measurements benefit from notably high brightness levels and narrow energy resolutions. These features enhance the quality of data acquisition, laying the foundation for more accurate data analysis. The high brightness ensures a substantial intensity of the

X-ray beam, thereby facilitating the detection and characterisation of even minute details within the samples. The narrow energy resolution, on the other hand, allows for precise differentiation and identification of energy levels, contributing to the accuracy of the gathered data.[25]

In summary, the utilisation of the Soft X-ray Beamline at the Australian Synchrotron for photoelectron spectroscopy represents a significant advancement in characterisation techniques. This development is attributed to the synergy between synchrotron radiation, the rapid progress in nanotechnology, and the benefits of high brightness and narrow energy resolution, which collectively enhance the quality and depth of data analysis.

Indeed, NEXAFS, which stands for Near Edge X-ray Absorption Fine Structure, serves as a valuable tool for characterising materials' chemical states. This technique is particularly sensitive to the bonding environment surrounding the absorbing atom, making it akin to a fingerprint that provides insights into the chemical state of specific elements.[26]

In the context of the Chapter 6, the Ti L-edge and S k and L-edge were employed to delve into the precise structure and chemical state of Ti and S groups present on the prepared substrates. In Chapter 7, Ti L-edge and N K edge was used to investigate the exact structure and the chemical state of Ti and N groups on our prepared substrates. The experimental data were collected at the soft X-ray spectroscopy beamline located at the Australian Synchrotron. NEXAFS, in conjunction with advanced tools like the Quick AS NEXAFS Tool,[26,27] offers a precise and powerful approach to deciphering the chemical nature of materials. This methodology is especially important for understanding the properties and behaviour of substances in various applications, contributing to advancements in materials science and related fields.

2.2.3 Electronic microscopy techniques

An electron microscope is a powerful scientific instrument that uses a beam of electrons instead of visible light to magnify and visualize incredibly small objects and structures at the nanoscale. Here is a brief section describing how an electron microscope works:

1) Electron emission: The process begins with an electron source, typically a heated filament or a field emission gun. In the case of a transmission electron microscope (TEM), a sharp metal tip emits electrons when heated. For scanning electron microscopes (SEM), a heated filament emits a stream of electrons.

2) Electron lenses: After electron emission, the electron beam passes through a series of electromagnetic lenses. These lenses are responsible for focusing and shaping the beam. In a TEM, there are usually two sets of lenses: condenser lenses that converge the beam onto the specimen, and objective lenses that further focus the beam and form the final image. In an SEM, the lenses serve to focus and scan the electron beam across the specimen's surface.

3) Specimen interaction: As the focused electron beam interacts with the specimen, several processes occur. In TEM, electrons may be transmitted through the specimen, scattered, or absorbed, depending on the specimen's composition and thickness. In SEM, the electron beam scans across the specimen's surface, and various interactions like secondary electron emission, backscattered electron emission, and characteristic X-ray emission occur.
4) Image formation: In a TEM, the transmitted electrons pass through the specimen and are captured on a fluorescent screen or a digital detector to create an image. This image is a high-resolution, two-dimensional projection of the specimen's internal structure. In an SEM, signals resulting from interactions with the specimen are detected and used to create a three-dimensional surface image.
5) Rastering (SEM): In SEM, the electron beam scans the specimen's surface in a raster pattern, like how a CRT television or computer monitor displays images. This scanning motion allows for the creation of detailed and finely resolved surface images.
6) Imaging lenses (TEM): In TEM, after the electron beam passes through the specimen and forms an initial image, additional lenses are used to magnify and focus the image onto a viewing screen or a digital sensor. These imaging lenses are crucial for achieving high-resolution images in TEM.

In summary, electron microscopes work by emitting a focused beam of electrons from an electron source, using electromagnetic lenses to focus and shape the beam, interacting with the specimen to create signals, and ultimately forming images either by transmitting electrons (TEM) or by scanning and detecting various signals (SEM). These microscopes are essential tools for researchers in various fields, enabling them to study nanoscale structures and materials.[28-32]

2.2.3.1.Scanning Electron Microscope / Energy dispersive X-ray spectroscopy

Scanning Electron Microscopy (SEM) belongs to the category of electron microscopes that produce images of a sample's surface by scanning it with a focused electron beam. As these electrons engage with the atoms within the sample, diverse signals are generated, offering valuable insights into both the composition and the surface features of the specimen. To construct an image, the position of the electron beam as it scans is integrated with the intensity of the detected signals. In the most common SEM mode, atoms within the sample are excited by the electron beam, causing them to emit secondary electrons. These emitted secondary electrons are then captured and detected using a device called an Everhart-Thornley detector, which is specifically designed for detecting secondary electrons. The quantity of secondary electrons emitted, and consequently the intensity of the signal produced, is contingent upon the topography of the specimen's surface.[33]

SEM is employed to visualize objects and details within the microscale and nanoscale ranges. It is crucial to highlight the significance of preparing SEM samples appropriately to obtain high-quality images devoid of any undesirable electrical charges. For instance, even though a TiO_2 film is

intrinsically conductive and does not typically require coating with materials like Au or Pt, in some cases, a charging issue might arise. To mitigate this issue and ensure high-resolution imaging, strategies like attaching the FTO support to the sample holder using double-sided C tape were employed. This practice helps eliminate unwanted charges and enables the SEM to capture more accurate images.[31]

SEM empowers users through several methods. Here are three primary methods by which SEM empowers skilled users:[28,31,34]

1) High-magnification imaging: SEM allows users to observe samples at extremely high magnifications, typically ranging from 10x to over 100,000x. This level of magnification enables the visualization of structures and features at the nanoscale, providing valuable insights into the sample's morphology and surface topography.
2) High-resolution imaging: SEM provides exceptional resolution, which is the ability to distinguish between closely spaced objects or fine details in a sample. This high-resolution imaging is achieved by focusing a beam of electrons onto the sample's surface, allowing users to obtain detailed information about the sample's surface characteristics.
3) Elemental analysis: SEM can be equipped with EDS detectors. This feature enables skilled users to perform elemental analysis of the sample. By analysing the characteristic X-rays emitted when the electron beam interacts with the sample's atoms, users can determine the elemental composition of different regions within the sample. This is crucial for materials characterisation and identifying the presence of specific elements in a sample.[35]

In addition to these primary methods, SEM offers other capabilities such as electron backscatter diffraction (EBSD)[36] for crystallography, cathodoluminescence (CL)[37] imaging for studying luminescent properties, and more. Skilled users can leverage these techniques to gain a comprehensive understanding of the sample's microstructure, composition, and properties, making SEM a versatile tool in scientific research and materials analysis.

In the high-resolution imaging, the resolution describes the smallest measurable distance between two closely positioned points viewed head-on, effectively delineating them as separate entities. Traditional light microscopy (LM) offers a maximum resolution of approximately 200 nm. However, certain specialized SEM variants, such as Field Emission SEM (FESEM) and Focused Ion Beam SEM (FIB SEM), are equipped with resolutions surpassing 10 nm, often reaching as low as 5 nm. In our specific case, the requirement for high-resolution FESEM was driven by the necessity to accurately determine the sizes of porosities within the prepared TiO_2 film. This entailed employing a working distance of 4 millimetres alongside a spot size of 2.00, ensuring optimal conditions for capturing high-resolution images. This strategic approach effectively facilitated the attainment of the desired high-detail imaging.[38]

Depth of field is a crucial characteristic that enables the capture of intricate topographical details. The three-dimensional (3D) representation of specimen images holds paramount importance in SEM analysis.[39] Remarkably, substantial data and insights about a specimen can be gleaned even at low magnification levels. Through the utilisation of "stereo pair" SEM images, the SEM facilitates the provision of even more significant material-related information.[40]

Microanalysis is another pivotal capability, encompassing the analysis of sample composition. This involves discerning details about the material's chemical composition, its electrical characteristics, and its crystallographic attributes. The proficiency of SEM in microanalysis enables a comprehensive understanding of the specimen's makeup and characteristics.[41,42]

Morphological analysis of samples prepared in Chapters 5, 6, and 7 was conducted through SEM at Flinders Microscopy and Microanalysis which is an FEI Inspect F50 SEM equipped with an EDT secondary electron detector, concentric backscatter electron detector and Ametek EDAX EDS detector. The instrument was applied at a voltage of 10.0 KV with a spot size of 2.0. The samples, prepared after processing, were drop-casted onto Si wafers and subsequently coated with a thin layer of Pt via sputter coating, achieving a thickness of approximately 2 nm. The sample material is exposed to electron irradiation, leading to the emission of characteristic X-rays corresponding to the elements within. The emitted energy manifests as peaks in varying intensity on a spectrum profile. This profile serves to identify the specific inorganic elements contained within the sample, such as N, C, O, Au, Si, S, and Ti. [43,44]

However, the analysis is not inherently quantitative. The size of the spectrum peaks, denoting X-ray intensity, increases in direct correlation with the concentration of elements found in the sample. This technique excels at characterising discrete paint layers or individual particles within a sample, rendering the analysis highly targeted and tailored to distinct points of interest. This capability is especially valuable for examining specific areas, such as individual layers in a cross-section.

2.2.3.2. Scanning transmission electron microscopy (STEM)

Starting in the 1930s, the methods of Transmission Electron Microscope (TEM) and Scanning Transmission Electron Microscope (STEM) have been utilised to investigate the atomic-scale details of materials. In the case of TEM, it operates in a manner akin to an optical microscope. Electrons that traverse a specimen are subsequently directed onto a viewing screen or camera following their interaction with the sample, allowing for imaging at the atomic level.[45,46] To achieve optimal performance in TEM, it is crucial for the sample to have a thickness of approximately 100 nm, and the electron beam must possess substantial energy. The quality of the resulting image is determined by how electrons behave, whether they pass through the sample without scattering or get reflected

due to interactions with the sample. The presence of a lower lens beneath the sample causes electrons with varying energies to converge at distinct focal points, which can result in image blurring.

In contrast, STEM integrates principles from both TEM and SEM. In a STEM, the electron beam is tightly focused onto a small spot on the specimen, and the resolution of the microscope primarily depends on the ability to focus the beam to a fine point. This focused beam scans across the specimen in a raster pattern, and as it interacts with the specimen, various signals are collected to form an image. These signals, including transmitted electrons, backscattered electrons, and various spectroscopic signals, contribute to the final image. However, it is the precise focusing of the electron beam that enables high-resolution imaging in a STEM. By employing an exceptionally narrow electron beam with a diameter as tiny as 0.1 nm,[23] Scanning Transmission Electron Microscopy (STEM) achieves spatial resolution comparable to the distances between atoms. This focused beam is moved across a thin sample, gathering a variety of scattering data corresponding to its spatial location. An objective aperture limits the maximum angle of illumination, which encompasses the angle at which the probing electron beam interacts with the sample as it traverses through the scan coils. An array of output detectors is employed to generate diverse types of images. [47]

STEM encompasses two prominent detection modes: the Bright Field (BF) mode and the Annular Dark Field (ADF) mode. In the BF mode, on-axis transmitted electrons are captured, resembling the process in TEM, and this mode imparts crystallographic information. Importantly, this mode can accommodate thicker samples in comparison to conventional TEM. Conversely, the ADF mode in STEM introduces an innovative imaging technique termed High Angle Annular Dark Field (HAADF) imaging. HAADF imaging relies on the detection of scattered electrons that pass near atomic nuclei within the sample. This methodology yields high-resolution images endowed with chemical sensitivity and atomic number (Z-) contrast. Notably, it excels in highlighting atoms with higher Z-numbers, like Au, owing to the substantial electron scattering they exhibit. Like TEM, the process in STEM also gives rise to backscattered electrons and x-rays.[23,47]

Chapter 6 delves into the practical application of the HAADF-STEM mode in the visualization of deposited Au clusters on mesoporous titania NPs, offering an in-depth exploration of the HAADF mode. In Chapter 6, an examination of the structure and size distribution of the Au Nanoclusters (Au NCs) was conducted. This analysis utilised a High-Resolution Transmission Electron Microscope (HRTEM). Additionally, High-Angle Annular Dark-Field Scanning Transmission Electron Microscopy (HAADF-STEM) and STEM-EDS elemental maps were generated using a FEI Titan Themis STEM operating at 200 keV. To optimize data quality, the instrument was equipped with a Super-X EDS detector and a specialized low-background sample holder, which reduced unwanted background signals and improved the efficiency of X-ray signal collection. The collected data were then processed and analysed using Velox™ software developed by Thermo Fisher Scientific.

For sample preparation, dispersions of the as-prepared material were dropped onto a 300-mesh copper grid with a lacey C support film. The dispersions were prepared by sonicating the material in Milli-Q water until it was uniformly dispersed. The water was then allowed to evaporate, and the sample was placed into the sample holder. It is important to note that achieving atomic-scale resolution was challenging due to the presence of entrained ligands in the samples.

2.2.4. Brunauer, Emmett and Teller and Barrett-Joyner-Halenda (BET and BJH)

In Chapters 6 and 7 of this study, N_2 adsorption and desorption isotherms were conducted at a temperature of 77 K using a Tristar II 3020 instrument based on the BET principle. BET is utilised to measure the specific surface area of a sample. In addition, in this study, the BJH analysis technique was applied to assess pore size and volume through adsorption and desorption methods. This approach allows for an isolated examination of pore size distribution, regardless of the sample's external surface area due to particle size considerations. Measurement of the pore size can be useful for achieving knowledge about the properties of porous materials such as mesoporous TiO_2 semiconductors. Furthermore, it is useful in manufacturing consistency and evaluating product performance.[48] But how does BET Work?

In BET analysis, N_2 gas is frequently chosen for its strong affinity with most solid materials and its ready availability in high purity. Because the interaction between solid surfaces and gas molecules is often weak, the surface is cooled using liquid nitrogen (liquid N_2) to enable the detection of adsorption in meaningful quantities. Subsequently, precise volumes of N_2 gas are incrementally introduced into the sample chamber. By creating a partial vacuum, pressures lower than atmospheric pressure are achieved. It is crucial to understand that once the pressure reaches saturation, further increases in pressure do not result in additional adsorption. Highly precise pressure transducers monitor pressure changes throughout the adsorption process. Following the establishment of adsorption layers, the samples are removed from the nitrogen atmosphere and heated to release the adsorbed N_2 from the material, which is then quantified. The data collected is typically presented in the form of a BET isotherm, which plots the amount of adsorbed N_2 gas as a function of relative pressure. It is worth noting that there are six possible types of adsorption isotherms, each indicating different adsorption behaviours and surface characteristics.[49,50]

2.2.5. Attenuated total reflection Fourier-transform infrared (ATR-FTIR)

IR spectroscopy is the oldest and most widely used method not only for characterising both inorganic and organic chemicals, but also for obtaining information on chemical bonding, molecular environment, and molecular structure. The ability to study liquids, solids and gaseous samples make it a powerful tool for quantitative and qualitative studies. ATR-FTIR, or internal reflection methods,

allow in situ investigations of surface reactions on immersed solids. The ability to investigate solid particles of metal oxide in suspensions or as thin films deposited on ATR crystals has led to in situ ATR-FTIR studies of chemical reactions and adsorption on a variety of solid-gas and/or solid-liquid interfaces in a photocatalysis background. The ATR-FTIR technique is a powerful tool both for probing binding mechanisms and for characterising organic molecules adsorption onto surfaces of metal oxides in liquid media.[51,52]

The infrared spectrum ranges from 13000 cm^{-1} to 0 cm^{-1} and is categorised into three parts:

1- (From 13000 cm^{-1} to 4000 cm^{-1}), Near-Infrared region, in which the vibrational overtones of most chemical bonds are found. Data from this region is mainly used in process control or chemical industries.

2- (From 4000 cm^{-1} to 400 cm^{-1}), Mid- Infrared region is the most extensively studied region in infrared spectroscopy, primarily because it is in this range that rotational and vibrational shifts provide the most precise and informative data.

3- (From 400 cm^{-1} to 0 cm^{-1}), Far- Infrared region, is the region for which the first FTIR spectrometer was developed owing to optical resolution, excellent mechanical tolerance, and smaller wavelength source requirement. FIR is appropriate for characterising most of the metallic elementals.[53,54]

The FTIR instrument was utilised to characterise the compounds prepared in Chapters 5, 6, and 7 which was provided from Bruker optics Inc, Vertex model 80v with an external adapter for running UHV-FTIR measurements. It should be noted that an XPS instrument has been attached to this instrument and can be employed simultaneously. Michelson interferogram, sources, mirrors, beam splitters, laser, and detectors are components present in FTIR.

2.2.6. X-Ray Diffraction Analysis (XRD)

X-ray Diffraction (XRD) is an analytical technique used to investigate the crystalline structure of materials. This method involves directing a beam of X-rays onto a sample, and it detects the scattering of these X-rays as they interact with the atoms within the crystal lattice of the material. Subsequently, the diffraction pattern generated is analysed to determine the precise arrangement of atoms within the material.[55]

In XRD, the X-ray wavelength is indeed crucial and must be compatible with the interatomic spacing (also known as d-spacing) in the crystal lattice of the material being analysed. This relationship is described by Bragg's Law[56,57], which is fundamental to X-ray crystallography.

Bragg's Law states: $n\lambda = 2d \sin(\theta)$

Where:

n is an integer (the order of diffraction)

λ is the wavelength of the X-rays

d is the interplanar spacing (the distance between atomic planes in the crystal lattice)

θ is the angle of incidence or diffraction

This equation explains how X-rays interact with a crystal lattice. When the X-ray wavelength (λ) matches the interatomic spacing (d) and the angle (θ) is appropriate, the X-rays will undergo constructive interference, resulting in a strong diffraction pattern. In other words, the X-rays will scatter in a way that allows them to reinforce each other, leading to bright diffraction spots on the detector. By measuring the angles and intensities of these diffraction spots, scientists can deduce the crystal structure of the material, including information about the arrangement of atoms within the crystal lattice. Therefore, choosing the correct X-ray wavelength for XRD analysis is crucial because it determines the ability to observe diffraction patterns that provide valuable structural information about the material under investigation. Different elements and crystal structures require X-rays with specific wavelengths to produce informative diffraction patterns.[57-59]

Key information obtained from XRD includes the lattice parameters, crystal symmetry, crystal plane orientation, and interatomic distances within the crystal lattice. This technique provides insights into the material's structural properties which are crucial for understanding its physical and chemical behaviour.[60]

XRD plays a vital role in various fields, including materials science, chemistry, geology, and solid-state physics. It aids scientists in characterising materials, optimizing manufacturing processes, and advancing our understanding of the atomic arrangements that material properties.[55]

XRD involves several steps to analyse the crystallographic structure of a material. Here is a general guide on how to run XRD.[61,62]

-Sample Preparation: Powders, thin films, or single crystals are common sample types. The samples should be finely ground and uniform to ensure accurate results.

-Instrument Setup: The XRD instrument is properly calibrated and set up. This includes aligning the X-ray source, detector, and sample stage.

-Sample Loading: The sample should be positioned securely to ensure consistent results. Some instruments might require sample holders or special attachments.

-Select Measurement Parameters: The measurement parameters such as the X-ray source (Cu Kα, Mo Kα, etc.), scan range (2θ angles), and scanning speed were selected. The selection of parameters relies on the characteristics of our sample and the specific information we are aiming to obtain.

-Data Collection: The instrument will rotate the sample holder while the X-ray source emits X-rays. As the X-rays interact with the crystal lattice of the sample, they are diffracted at specific angles according to the lattice arrangement.[61,63]

In Chapters 5, 6, and 7, the analysis of the crystallographic phases of TiO2 was conducted using X-ray Diffraction (XRD). This analysis was performed using a Bruker D8 Advance Eco diffractometer equipped with a Co-Kα X-ray source (wavelength λ=1.7902 Å). To eliminate the presence of Kβ radiation, an Fe filter was applied. The X-ray source operated at a voltage of 38kV and a current of 25mA during the experiments.

2.2.7. Thermogravimetric analysis (TGA)

TGA is considered as a potent analytical method employed to examine how materials respond to heat. It tracks alterations in a sample's mass as temperature (or time) changes, all while the sample undergoes controlled heating in either an inert or reactive environment. TGA finds broad application across diverse fields like chemistry, materials science, and quality control. Below, we delve into TGA's operational principles and its notable characteristics:

- ✓ **Principal of TGA**

The principle behind TGA is relatively simple. A small sample of the material under investigation is placed in a crucible and heated at a constant rate or under a specific temperature program. As the temperature increases, the material undergoes physical and chemical changes, such as decomposition, phase transitions, or oxidation. These changes often result in the release of volatile components or the formation of new compounds.[64-67]

- ✓ **Key Features of TGA**

1) Sample preparation: TGA typically requires a small amount of sample, usually a few milligrams to a few tens of milligrams. The sample should be homogeneous, and representative of the material being studied.

2) Temperature control: TGA instruments have precise temperature control capabilities. The temperature can be increased at a constant rate (heating ramp) or maintained at specific temperature steps (isothermal). This allows for a detailed examination of the material's behaviour as a function of temperature.

3) Atmosphere control: TGA can be performed in different gas environments, including inert gases (e.g., N_2 or Ar) or reactive gases (e.g., O_2). The choice of atmosphere depends on the specific research objectives and the material being analysed.

4) Mass measurement: TGA instruments are equipped with highly sensitive balances capable of measuring minute changes in mass. As the sample undergoes thermal changes, the balance records the mass loss or gain, which is plotted as a function of temperature or time.

5) Data Analysis: TGA data is analysed to extract valuable information about the material's properties. Common analyses include determining decomposition temperatures, identifying phases or components, quantifying the amount of volatile matter, and assessing thermal stability.[66,68]

- ✓ **Application of TGA**

1) Material characterisation: TGA is used to investigate the composition, purity, and thermal stability of materials, such as polymers, pharmaceuticals, and ceramics.

2) Quality control: It is employed in quality control processes to ensure the consistency and quality of products.

3) Kinetic analysis: TGA data can be used to determine reaction kinetics and activation energy for chemical processes.

4) Environmental studies: TGA can assess the thermal behaviour of materials in various environmental conditions, including oxidative and corrosive atmospheres.

In summary, Thermogravimetric Analysis (TGA) is a versatile technique that provides insights into the thermal behaviour of materials. By monitoring changes in mass as a function of temperature or time, TGA helps researchers and analysts understand the decomposition, stability, and composition of substances, making it a valuable tool in both research and industry.[64,69]

In Chapters 5 and 7, TGA, carried out using a Perkin Elmer 8000 instrument, was employed to quantify the weight reduction of the samples over temperature. The samples underwent annealing, starting from room temperature and progressing up to 900 °C. The annealing process was carried out at a heating rate of 10°C per minute in a N_2 environment. This analysis yields insights into various physical processes, such as absorption, phase transitions, desorption, and adsorption. In addition, it provides insight into chemical processes such as chemisorption, and thermal decomposition and solid-gas reactions.

2.3. Reference

1 Yasmin, L., Chen, X., Stubbs, K. A. & Raston, C. L. Optimising a vortex fluidic device for controlling chemical reactivity and selectivity. *Scientific reports* **3**, 2282 (2013).

2 Alharbi, T. M., Li, Q. & Raston, C. L. Thin film mechano-energy induced slicing of carbon nanotubes under flow. *ACS Sustainable Chemistry & Engineering* **9**, 16044-16051 (2021).

3 Alharbi, T. M., Alotaibi, A. E. & Raston, C. L. Architected C70/Graphene Oxide Composites Prepared under Continuous Flow in a Vortex Fluidic Device: Implications for Supercapacitors. *ACS Applied Nano Materials* (2023).

4 Mahoney, J., Monroe, C., Swartley, A. M., Ucak-Astarlioglu, M. G. & Zoto, C. A. Surface analysis using X-ray photoelectron spectroscopy. *Spectroscopy Letters* **53**, 726-736 (2020).

5 Krishna, D. N. G. & Philip, J. Review on surface-characterization applications of X-ray photoelectron spectroscopy (XPS): Recent developments and challenges. *Applied Surface Science Advances* **12**, 100332 (2022).

6 Greczynski, G. & Hultman, L. X-ray photoelectron spectroscopy: towards reliable binding energy referencing. *Progress in Materials Science* **107**, 100591 (2020).

7 Arons, A. B. & Peppard, M. Einstein's Proposal of the Photon Concept—a Translation of the Annalen der Physik Paper of 1905. *American Journal of Physics* **33**, 367-374 (1965).

8 Reinert, F. & Hüfner, S. Photoemission spectroscopy—from early days to recent applications. *New Journal of Physics* **7**, 97 (2005).

9 Rangel-Mendez, J. & Streat, M. Adsorption of cadmium by activated carbon cloth: influence of surface oxidation and solution pH. *Water Research* **36**, 1244-1252 (2002).

10 Park, E. D. & Lee, J. S. Effects of pretreatment conditions on CO oxidation over supported Au catalysts. *Journal of Catalysis* **186**, 1-11 (1999).

11 Chastain, J. & King Jr, R. C. Handbook of X-ray photoelectron spectroscopy. *Perkin-Elmer Corporation* **40**, 221 (1992).

12 Porsgaard, S. *et al.* Charge state of gold nanoparticles supported on titania under oxygen pressure. *Angewandte Chemie International Edition* **50**, 2266-2269 (2011).

13 Juodkazis, K., Juodkazyt, J., Jasulaitien, V., Lukinskas, A. & Šebeka, B. XPS studies on the gold oxide surface layer formation. *Electrochemistry Communications* **2**, 503-507 (2000).

14 Koslowski, B. *et al.* Oxidation of preferentially (1 1 1)-oriented Au films in an oxygen plasma investigated by scanning tunneling microscopy and photoelectron spectroscopy. *Surface science* **475**, 1-10 (2001).

15 Borman, V., Pushkin, M., Tronin, V. & Troyan, V. Evolution of the electronic properties of transition metal nanoclusters on graphite surface. *Journal of Experimental and Theoretical Physics* **110**, 1005-1025 (2010).

16 Zafeiratos, S. & Kennou, S. A study of gold ultrathin film growth on yttria-stabilized ZrO2 (100). *Surface science* **443**, 238-244 (1999).

17 Acres, R. G. *et al.* Molecular structure of 3-aminopropyltriethoxysilane layers formed on silanol-terminated silicon surfaces. *The Journal of Physical Chemistry C* **116**, 6289-6297 (2012).

18 Briggs, D. Practical surface analysis. *Auger and X-Ray Photoelecton Spectroscory* **1**, 151-152 (1990).

19 Schmerl, N. *An Electron and Ion Scattering Spectroscopic Study of Interfaces for Organic Photovoltaic Applications*, Flinders University, College of Science and Engineering., (2018).

20 Yano, J. & Yachandra, V. K. X-ray absorption spectroscopy. *Photosynthesis research* **102**, 241-254 (2009).

21 De Groot, F. High-resolution X-ray emission and X-ray absorption spectroscopy. *Chemical Reviews* **101**, 1779-1808 (2001).

22 Wende, H. Recent advances in x-ray absorption spectroscopy. *Reports on progress in physics* **67**, 2105 (2004).
23 Al Qahtani, H. *Characterisation of Au9–Nanoclusters Deposited on Titania Surfaces Using Spectroscopic and Microscopic Techniques*, Flinders University, School of Chemical and Physical Sciences., (2016).
24 Lagomarsino, S. & Cedola, A. X-ray microscopy and nanodiffraction. *Encyclopedia of nanoscience and nanotechnology* **10**, 681-710 (2004).
25 Fong, Y.-Y. *et al.* Photoreduction kinetics of sodium tetrachloroaurate under synchrotron soft X-ray exposure. *Langmuir* **27**, 8099-8104 (2011).
26 Cowie, B., Tadich, A. & Thomsen, L. in *AIP Conference Proceedings.* 307-310 (American Institute of Physics).
27 Alotabi, A. S., Gibson, C. T., Metha, G. F. & Andersson, G. G. Investigation of the Diffusion of Cr2O3 into different phases of TiO2 upon Annealing. *ACS Applied Energy Materials* **4**, 322-330 (2021).
28 Inkson, B. J. in *Materials characterization using nondestructive evaluation (NDE) methods* 17-43 (Elsevier, 2016).
29 Zaefferer, S. A critical review of orientation microscopy in SEM and TEM. *Crystal Research and Technology* **46**, 607-628 (2011).
30 Zuo, J. M. & Spence, J. C. *Advanced transmission electron microscopy*. (Springer, 2017).
31 Mohammed, A. & Abdullah, A. in *Proceedings of the 2018 International Conference on Hydraulics and Pneumatics—HERVEX, Băile Govora, Romania.* 7-9.
32 Watt, I. M. *The principles and practice of electron microscopy*. (Cambridge University Press, 1997).
33 Zhao, J. & Liu, X. Electron microscopic methods (TEM, SEM and energy dispersal spectroscopy). (2022).
34 Goldstein, J. *Practical scanning electron microscopy: electron and ion microprobe analysis*. (Springer Science & Business Media, 2012).
35 Newbury, D. E. & Ritchie, N. W. Performing elemental microanalysis with high accuracy and high precision by scanning electron microscopy/silicon drift detector energy-dispersive X-ray spectrometry (SEM/SDD-EDS). *Journal of materials science* **50**, 493-518 (2015).
36 Wille, G., Lerouge, C. & Schmidt, U. A multimodal microcharacterisation of trace-element zonation and crystallographic orientation in natural cassiterite by combining cathodoluminescence, EBSD, EPMA and contribution of confocal Raman-in-SEM imaging. *Journal of Microscopy* **270**, 309-317 (2018).
37 Götze, J. Potential of cathodoluminescence (CL) microscopy and spectroscopy for the analysis of minerals and materials. *Analytical and bioanalytical chemistry* **374**, 703-708 (2002).
38 Zhou, W., Apkarian, R., Wang, Z. L. & Joy, D. Fundamentals of scanning electron microscopy (SEM). *Scanning Microscopy for Nanotechnology: Techniques and Applications*, 1-40 (2007).
39 Ersoy, O., Aydar, E., Gourgaud, A. & Bayhan, H. Quantitative analysis on volcanic ash surfaces: application of extended depth-of-field (focus) algorithm for light and scanning electron microscopy and 3D reconstruction. *Micron* **39**, 128-136 (2008).
40 Sato, M., Todokoro, H. & Nakagawa, M. An evaluation for the depth of field in SEM image depending on accelerating voltage. *Microscopy* **43**, 141-145 (1994).
41 Goldstein, J. I. *et al. Scanning electron microscopy and X-ray microanalysis*. (springer, 2017).
42 Reimer, L. Scanning electron microscopy: physics of image formation and microanalysis. *Measurement Science and Technology* **11**, 1826-1826 (2000).
43 Newbury*, D. E. & Ritchie, N. W. Is scanning electron microscopy/energy dispersive X-ray spectrometry (SEM/EDS) quantitative? *Scanning* **35**, 141-168 (2013).

44 Newbury, D. E. & Ritchie, N. W. Elemental mapping of microstructures by scanning electron microscopy-energy dispersive X-ray spectrometry (SEM-EDS): extraordinary advances with the silicon drift detector (SDD). *Journal of Analytical Atomic Spectrometry* **28**, 973-988 (2013).
45 Crewe, A., Wall, J. & Welter, L. A high-resolution scanning transmission electron microscope. *Journal of Applied Physics* **39**, 5861-5868 (1968).
46 Pennycook, S. *et al.* Scanning transmission electron microscopy for nanostructure characterization. *Scanning microscopy for nanotechnology: techniques and applications*, 152-191 (2007).
47 Varela, M. *et al.* Materials characterization in the aberration-corrected scanning transmission electron microscope. *Annu. Rev. Mater. Res.* **35**, 539-569 (2005).
48 Hayati-Ashtiani, M. Characterization of nano-porous bentonite (montmorillonite) particles using FTIR and BET-BJH analyses. *Particle & Particle Systems Characterization* **28**, 71-76 (2011).
49 Allanas, E., Rahman, A., Arlin, E. & Prasetyanto, E. in *Journal of Physics: Conference Series.* 012094 (IOP Publishing).
50 Hwang, N. & Barron, A. R. BET surface area analysis of nanoparticles. *The connexions project*, 1-11 (2011).
51 Dutta, A. Fourier transform infrared spectroscopy. *Spectroscopic methods for nanomaterials characterization*, 73-93 (2017).
52 Smith, B. C. *Fundamentals of Fourier transform infrared spectroscopy*. (CRC press, 2011).
53 Jaggi, N. & Vij, D. in *Handbook of Applied Solid State Spectroscopy* 411-450 (Springer, 2006).
54 Petit, S. Fourier transform infrared spectroscopy. *Developments in Clay Science* **1**, 909-918 (2006).
55 Ali, A., Chiang, Y. W. & Santos, R. M. X-ray diffraction techniques for mineral characterization: A review for engineers of the fundamentals, applications, and research directions. *Minerals* **12**, 205 (2022).
56 Speakman, S. Basics of X-ray Diffraction. *Massachusetts Institute of Technology* (2016).
57 Elton, L. & Jackson, D. F. X-ray diffraction and the Bragg law. *American Journal of Physics* **34**, 1036-1038 (1966).
58 Pope, C. G. X-ray diffraction and the Bragg equation. *Journal of chemical education* **74**, 129 (1997).
59 Warren, B. X-ray diffraction methods. *Journal of applied physics* **12**, 375-384 (1941).
60 Chauhan, A. & Chauhan, P. Powder XRD technique and its applications in science and technology. *J Anal Bioanal Tech* **5**, 1-5 (2014).
61 Dorset, D. X-ray diffraction: a practical approach. *Microscopy and microanalysis* **4**, 513-515 (1998).
62 Holder, C. F. & Schaak, R. E. Vol. 13 7359-7365 (ACS Publications, 2019).
63 Unruh, D. K. & Forbes, T. Z. X-ray diffraction techniques. *Analytical geomicrobiology: a handbook of instrumental techniques*, 215-237 (2019).
64 Bottom, R. Thermogravimetric analysis. *Principles and applications of thermal analysis*, 87-118 (2008).
65 Prime, R. B., Bair, H. E., Vyazovkin, S., Gallagher, P. K. & Riga, A. Thermogravimetric analysis (TGA). *Thermal analysis of polymers: Fundamentals and applications*, 241-317 (2009).
66 Bevis, J. *et al. Principles and applications of thermal analysis*. (Wiley Online Library, 2008).
67 Xu, W., Li, S., Whitely, N. & Pan, W.-P. Fundamentals of TGA and SDT. (2005).
68 Mukasyan, A. S. in *Concise Encyclopedia of Self-Propagating High-Temperature Synthesis* 93-95 (Elsevier, 2017).

69 Kim, Y.-B. & Song, S.-J. Principles and application of thermal analysis: DSC, DTA, TGA, TMA. *Polymer science and technology* **4**, 387-397 (1993).

CHAPTER 3: EXPERIMENTAL DESIGN AND STATISTICAL ANALYSIS

3.1. Background

Experimental design plays a pivotal role across various fields of science and industry. It involves the deliberate application of treatments to experimental units, forming a crucial part of the scientific method centred around measuring one or more responses. Effective experimentation necessitates a thorough understanding of the process and system operations. To achieve conclusive outcomes, an experimenter must plan and design experiments, followed by a comprehensive analysis of the results. Among the methodologies frequently employed for optimisation, response surface methodology (RSM) holds a prominent position. This approach is particularly advantageous as it enables the assessment of the effects of multiple factors and their interplay on one or more response variables. As such, it serves as a valuable tool in research and problem-solving.[1]To achieve this, RSM is employed in conjunction with central composite designs (CCD) to assess different phenomena comprehensively. RSM and CCD techniques have gained extensive application in diverse engineering domains, including water treatment processes, due to their ability to streamline experimental efforts. This strategy reduces the need for a large number of experiments, resulting in notable reductions in costs and time associated with the study and analysis of process conditions and the interactions between the selected parameters.[2]

When undertaking research using the RSM and employing statistical software and programming language like Design Expert, MINITAB, SPSS, or Python, the process generally involves four key steps:[3]

1. **Designing experiments:** The initial step is to plan and design a series of experiments that vary the input variables or factors within a defined range. These experiments should cover a broad enough spectrum to capture the response surface and the relationships between variables.

2. **Statistical analysis and model development:** After conducting the experiments and collecting the corresponding data, a statistical analysis is performed. This involves fitting mathematical models to the data that describe how the response variable(s) change as a function of the input variables. The aim is to create a predictive model that accurately captures the system's behaviour.

3. **Model optimisation and validation:** With the mathematical model in place, optimisation techniques are employed to find the optimal conditions for the desired response(s). These

optimal conditions can be identified through mathematical calculations or graphical representations of the response surface. Once these optimal conditions are determined, they should be validated through additional experiments or simulations.

4. **Finding the optimal point:** The goal of RSM is to identify the optimal combination of input variables that lead to the desired response(s). This involves refining the conditions to maximize or minimize the response, based on the established mathematical model. The optimal point signifies the best set of input variables for achieving the desired outcome.

The utilisation of the RSM in recent photocatalysis [4-7]studies has garnered significant attention among researchers.[8-11] The systematic procedure that should be adhered to when employing this method accurately is outlined in Figure 3.1.[3] This comprehensive approach enables researchers to navigate through the intricacies of optimizing extraction processes effectively.[3]

3.2. Design of Experiment (DOE)

DOE, which stands for Design of Experiments, is a systematic approach used in research and industrial works to optimize processes, improve product quality, and make informed decisions based on experimental data. DOE plays a vital role in various fields, including engineering, manufacturing, chemistry, biology, and social sciences. DOE helps to maximize the use of available resources, by systematically planning and conducting experiments. It allows researchers to obtain insights using a minimal number of experiments, saving time, and reducing costs. Also, DOE enables researchers to identify the most influential factors affecting a process or products. By systematically varying and controlling these factors, researchers can determine which ones have a significant impact and prioritize their efforts for optimisation or improvement.[12-15]

DOE helps to identify the optimal settings or conditions for process variables or product parameters that lead to the desired performance or quality. By systematically varying the factors and analysing the results, researchers can pinpoint the settings that result in the best outcomes, allowing for process optimisation and improved product quality. Finally, DOE allows for the study of interactions between independent factors or variables. It helps researchers understand how different factors interact with each other and whether their combined effects are additive, synergistic, or antagonistic. This knowledge is critical for understanding complex systems and developing effective strategies for improvement.[16,17]

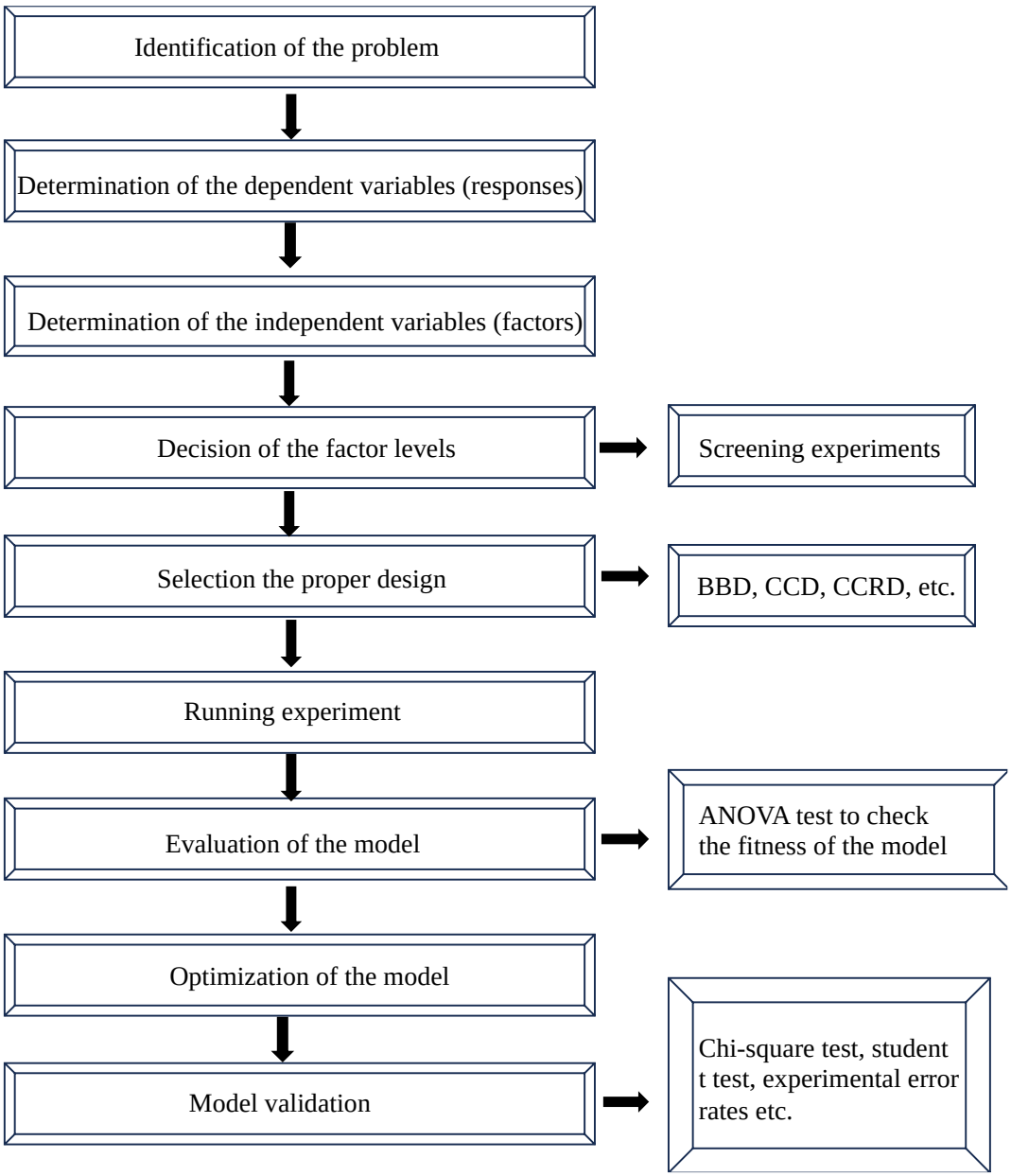

Figure 3.1. Steps for response surface methodology[3]

Overall, DOE is important because it offers a systematic and efficient approach to experimentation, enabling researchers to gain valuable insights, optimize processes, improve product quality, and make data-driven decisions. It helps organizations save resources, enhance performance, and drive innovation in various fields.[17-19]

Within the framework of RSM, two principal experimental designs are widely utilised: Box-Behnken designs (BBD) and Central Composite Design (CCD).[1] Recent improvements in optimisation studies have included the integration of alternative designs like the Central Composite Rotatable Design (CCRD) and Face Central Composite Design (FCCD)[1] to further expand the investigation of optimal conditions.[20-22]

3.3. Response Surface Methodology (RSM)

Response Surface Methodology (RSM) is a statistical technique employed to model and optimize the intricate systems. It is particularly useful when the relationship between several input variables and an output response is nonlinear. RSM involves designing a series of experiments to explore the response of a system under different combinations of input variables. By analysing the data obtained from these experiments, mathematical models are developed to describe the relationship between the input variables and the response. The primary objective of RSM is to determine the best possible values for the input variables that yield the desired response. Typically, this is accomplished by employing statistical methods like regression analysis to fit the data to a mathematical model. This model can subsequently forecast the response for various input variable combinations, enabling the identification of settings that maximize the desired outcome. RSM is widely used in various fields, including engineering, manufacturing, chemistry, and pharmaceuticals, to optimize processes, improve product quality, and reduce costs. It allows for efficient exploration of the parameter space and provides insights into the interactions between variables, enabling informed decision-making and process improvement. Overall, RSM provides a systematic approach to understand and optimize complex systems by using statistical models and experimental design principles.[23,24]

RSM was introduced in 1991 by George E. P. Box and K. B. Wilson.[25] This approach is a mathematical and statistical tool employed to model and analyse processes where the outcome of interest depends on several variables.[26,27] Its primary goal is to optimize this outcome efficiently. RSM can attain optimal conditions cost-effectively, eliminating the need for extensive experiments. Additionally, it can readily identify variable relationships by visualizing responses under various scenarios. In this context, the parameters responsible for influencing the process are referred to as independent variables, while the outcomes are termed dependent variables.[1]

RSM is employed to establish a proper approximated relationship between output and input variables. Its aim is to precisely identify the best operational conditions for the system under investigation or to determine a region within the parameter space that meets the operational requirements.[28,29]

The gathered experimental data are subjected to rigorous evaluation, aiming to fit a suitable statistical model. This model can assume various forms such as Quadratic, Linear, Cubic, or 2FI (two-factor interaction). The coefficients of this model encompass the constant term, A, B, and C, representing linear coefficients for independent variables, followed by AB, AC, and BC, symbolizing interactive term coefficients. Furthermore, A^2, B^2, and C^2 denote the quadratic term coefficients. After accurately fitting a quadratic model, the coefficients obtained are used to assess the effect of each parameter on the studied response. To discuss the linear or quadratic effect and to check the

interaction between certain parameters, the derivative of the mathematical model obtained according to the studied parameters will be used. To assess the adequacy of the model, several metrics are employed. These include the correlation coefficient (R^2), the adjusted determination coefficient (Adj-R^2), and the measure of adequate precision. The model is deemed adequate under specific conditions: its P-value is less than 0.05, the P-value for lack of fit is greater than 0.05, and R^2 exceeds 0.95. Statistical significance regarding differences between means is evaluated through the application of analysis of variance (ANOVA).[30] This robust analytical approach ensures a comprehensive scrutiny of the model's suitability and the significance of identified effects.

In summary, conducting research using RSM with statistical software involves these steps: designing experiments, developing, and validating a mathematical model, optimizing conditions, and identifying the optimal point for achieving the desired response(s). This approach allows researchers to efficiently explore and optimize complex processes by analysing the interactions between multiple variables and their impact on the response.

Coding is done according to Equation (3.1)[31].

$x_i = X_i - X_{cp}/\Delta X_i$ i= 1, 2, 3, …, k

Where x_i is the dimensionless value of the independent variable, X_i is the actual value of the independent variable, X_{cp} is the actual value of the independent variable at the centre point, and ΔX_i is the step length.

In RSM, the relationship between the independent variables (input factors) and the response variable (Y) is expressed through a functional process. This relationship is based on the dimensionless values of the independent variables, denoted as x_i, and their corresponding real values, denoted as X_i. The real value of the independent variable at the centre point is represented as X^c_p, and ΔX_i signifies the step length for each independent variable.

The functional process that analyses the responses (Y) is contingent on the input factors x_1, x_2, ..., x_k. The relationship between the response variable and the input process parameters is expressed in the following Equation (3.2)[32]:

$Y = f(x_1, x_2, ..., x_k) + e$

In this equation:

- Y represents the response variable of interest.
- $f(x_1, x_2, ..., x_k)$ is the true response function, which describes the systematic relationship between the input factors and the response variable.
- e stands for the error value, which accounts for random variations and discrepancies between the true response function and the actual observed response.

In the context of RSM, the aim is to develop a mathematical model (often represented by a polynomial equation) that captures the underlying relationship between the input factors and the response variable. This model can then be used for optimisation and prediction purposes, enabling researchers to identify optimal conditions for achieving desired responses based on the input variables.

The standard model employed in the response surface methodology can be expressed using the following Equation (3.3):[2,24]

$$Y = \beta_0 + \beta_1 x_1 + \beta_2 x_2 + .. + \beta_k x_k + \beta_{11} x_1^2 + \beta_{22} x_2^2 + ... + \beta_{kk} x_k^2 + \beta_{12} x_1 x_2 + \beta_{13} x_1 x_3 + .. + \beta_{ij} x_i x_j + e$$

In this equation:

- Y represents the response variable being studied.
- x_1, x_2, ..., x_k denote the independent variables (input factors) under investigation.
- β_0 is the intercept term, which accounts for the baseline value of the response when all independent variables are at their reference levels.
- β_i represents the linear coefficients that indicate the impact of each individual independent variable on the response.
- β_{ij} symbolizes the coefficients associated with interaction terms, reflecting how the joint effect of two independent variables influences the response.
- β_{jj} signifies the quadratic coefficients, which represent the effect of squared values of independent variables on the response.
- k denotes the number of independent parameters being considered.
- e represents the error term, encompassing random variability and unaccounted influences on the response.

This equation enables the creation of a mathematical model that encapsulates the connection between the independent variables and the response variable. This model can subsequently be employed for prediction, optimisation, and gaining insights into how various factors affect the response.

3.4. Analysis of Variance (ANOVA)

ANOVA is based on the concept of variance, which measures the variability within each treatment group and the variability between treatment groups. The main idea is to assess whether the differences between group means are greater than what would be expected due to random chance. ANOVA produces an F-statistic and associated p-value that indicate whether the observed differences

between group means are statistically significant. A p-value less than a predetermined significance threshold (often 0.05) suggests significant differences among groups. ANOVA is widely used in various fields, including social sciences, biological sciences, psychology, and business, to analyse and compare group means and investigate the effects of different factors on a response variable. It is an important tool for hypothesis testing and drawing conclusions from data with multiple groups or treatments.[24,33]

3.4.1. p-value

The p-value, also known as the probability value, is a statistical tool used to gauge the degree of evidence against a null hypothesis. It quantifies the probability of observing the provided data or results that are even more extreme, assuming the null hypothesis to be valid. In hypothesis testing, the null hypothesis (H0) represents the default or no-effect scenario, while the alternative hypothesis (H1) represents the desired or alternative outcome. The p-value serves as a tool to evaluate how probable it is to obtain the observed data assuming the null hypothesis is true. When the p-value is small (below a predetermined significance threshold, often 0.05 or 0.01), it indicates robust evidence against the null hypothesis. In such instances, the observed data are deemed statistically significant, and typically, the null hypothesis is discarded in favour of the alternative hypothesis. Conversely, when the p-value is large (above the significance threshold), it suggests that the observed data are likely to occur if the null hypothesis is accurate. In this scenario, there is insufficient evidence to reject the null hypothesis, and it is not considered statistically significant.[34]

It is vital to understand that the p-value doesn't convey details about the magnitude or practical significance of the observed effect. Its sole purpose is to gauge how strongly the evidence contradicts the null hypothesis, relying on the available data. Furthermore, it is essential to interpret the p-value while considering factors like the study's design, sample size, and the hypotheses under examination. It is always recommended to consider the p-value in conjunction with other relevant statistical measures and to interpret the results cautiously, taking into account the limitations and assumptions of the statistical analysis.[18,35]

3.4.2. 3D plots

In RSM, 3D plots are often used to visualize the relationships between multiple input variables and the response variable. These plots provide a graphical representation of the response surface, showing how the response changes as the input variables vary. 3D plots may vary depending on the experimental data and applied RSM model. They offer several important benefits and contribute to the understanding and analysis of the relationship between multiple independent variables and the response variable. 3D plots allow for a comprehensive visualisation of the response surface, which

represents how the response variable changes as the independent variables vary. They provide a clear and intuitive representation of the complex relationship between the variables, allowing researchers to identify patterns, trends, and regions of interest. Also, by examining the 3D plot, researchers can identify the combinations of independent variables that optimise the response variable. Peaks or valleys in the response surface indicate regions of maximum or minimum response, respectively, helping researchers determine the optimal settings for the variables to achieve the desired outcome.[36] 3D plots enable the detection of interactions and curvature between the independent variables. Interactions take place when the impact of one variable on the response is influenced by the level of another variable. Curvature indicates nonlinear relationships. By visualising the response surface in 3D, researchers can identify the presence of these interactions and curvature, which may have implications for process optimisation and understanding the underlying system behaviour.[2]

In summary, 3D plots in RSM provide a visual representation of the response surface, enabling researchers to understand complex relationships, identify optimal conditions, assess interactions and curvature, and effectively communicate findings. They serve as valuable tools for data exploration, analysis, and decision-making in the context of experimental design, optimisation, and modelling.

3.4.3. Perturbation

Perturbation, or perturbation analysis, is an important technique used in RSM. It involves intentionally varying the levels of independent variables around their optimal values to understand the sensitivity and robustness of the response surface. Perturbation analysis provides valuable insights into the behaviour of the system and helps researchers make informed decisions. Perturbation analysis allows researchers to assess the sensitivity of the response surface to changes in independent variables. By systematically perturbing the variables around their optimal values, researchers can observe how variations in the inputs affect the response. This information helps identify which variables have the most significant impact on the response and which are less influential. Perturbation analysis is crucial for validating the mathematical models developed in RSM. By comparing the predicted responses from the models with the actual responses obtained by perturbing the variables, researchers can assess the accuracy and reliability of the models. If the predicted and observed responses match closely, it provides confidence in the model's ability to represent the real system.[37]

Perturbation analysis provides insights into the trade-offs and decision-making process in RSM. By analysing the response surface under perturbed conditions, researchers can identify potential risks and constraints associated with the optimisation process. Perturbation analysis helps determine the regions of the response surface that are more sensitive to changes, and guides decision-making regarding the acceptable range of input variables for achieving the desired response.[38]

In summary, perturbation analysis plays a crucial role in RSM by providing insights into sensitivity, model validation, robustness assessment, decision-making, and process improvement. It helps researchers understand the behaviour of the system, validate models, make informed decisions, and optimize processes effectively.

3.4.4. What is python?

Python, a high-level, versatile programming language, was created by Guido van Rossum in 1991. It is renowned for its simplicity and readability, making it a preferred choice among programmers, both novices and experts. Python boasts a thriving and engaged community that actively contributes to its extensive standard library, which encompasses a wide array of modules and packages for diverse applications like web development, data analysis, machine learning, and more. Furthermore, this community maintains a vast ecosystem of third-party libraries, rendering Python a versatile and potent tool across various domains. Python's syntax is intentionally designed to be straightforward and easy to read, ensuring accessibility for beginners. Also, Python comes with a comprehensive standard library that provides ready-to-use modules for many common tasks. Python packages are collections of modules, functions, classes, and resources that are organized together to provide specific functionality or solve problems. Packages in Python help in structuring and organizing code, making it easier to manage and reuse.

Python provides several powerful libraries and packages for statistical analysis, making it a popular choice for data scientists, statisticians, and researchers. Here are some ways Python can be used for statistics: 1. NumPy: NumPy is an essential package for scientific computing in Python. It provides efficient numerical operations and multidimensional array objects, which are the building blocks for many statistical computations. NumPy offers functions for statistical calculations, such as mean, median, variance, standard deviation, and correlation. 2. pandas: pandas are a versatile library for data manipulation and analysis. It introduces two key data structures, Series (1D) and Data Frame (2D), which are highly useful for working with structured data. pandas provide a wide range of statistical functions and methods for descriptive statistics, data aggregation, grouping, sampling, and more. It also supports time series analysis. 3. SciPy: SciPy is a comprehensive library for scientific computing that includes several sub-packages relevant to statistics. It provides functions for probability distributions, hypothesis testing, statistical modelling, regression analysis, and optimisation. The sub-package SciPy. Stats offers a wide range of statistical distributions and statistical tests. 4. Stats Models: StatsModels is a Python library specifically focused on statistical modelling and testing. It provides a user-friendly API for performing various statistical analyses, including linear regression, generalized linear models, time series analysis, ANOVA, and more. Stats Models also offers functionality for statistical inference, hypothesis testing, and model diagnostics.[2,39]

In summary, Python is an immensely important programming language that has gained tremendous popularity and widespread adoption across various fields. Python's importance lies in its ability to empower developers, researchers, and businesses with the tools they need to solve complex problems efficiently and effectively. Its wide-ranging applications, supportive community, and simplicity have made it a cornerstone of modern software development.[2,39]

3.5. Data Analysis for photocatalytic dye degradation using RSM

According to the above-mentioned benefits of data analysis, the photodegradation results of most effective photocatalysts in methyl orange (MO) dye were analysed using RSM. This investigation involved varying three independent factors: A) denoting the concentration of MO dye (in ppm), B) representing the amount of catalyst (in mg), and C) indicating the reaction time (in minutes). These variables and their respective levels are detailed in Table 3.1.

Table 3-1.Experimental and coded levels of the selected factors.

Factor	**Unit**	**Code for each factor**	**Levels**			
			Coded levels	-1	0	+1
MO concentration	ppm	A	**Actual levels**	Min	Mid	Max
Catalyst amount	mg	B		Min	Mid	Max
Time	min	C		Min	Mid	Max

Table 3.1 delineates the presence of three distinct coded levels and corresponding actual levels for each parameter. This coding strategy spans from -1 (representing the minimum value) to +1 (indicating the maximum value) and serves the purpose of rendering all parameters dimensionless, thus facilitating a comprehensive observation of their interrelationships. Table 3.1 shows that minimum and maximum values were selected separately for each catalyst based on preliminary tests.

To accomplish this, the central composite design (CCD) methodology was harnessed, employing custom Python codes written using version 3.10.7, along with various libraries, including NumPy, Pandas, and more. The overarching objective was to strategically formulate a minimal set of experiments that would focus on the most photoactive nanocomposite, the $SMTiO_2/Au_9$ NCs in Chapter 6 and the black $NMTiO_2/Au_9$ NCs in Chapter 7. As detailed in Table 3.2, the culmination of these efforts resulted in a total of fifteen essential experiments. Table 3.2 presents the experimental conditions and degradation details for each catalysis, along with the predicted values for MO degradation to assess RSM prediction quality.

Table 3-2. Centre composite design with experimental and predicted responses

Factor 1	**Factor 2**	**Factor 3**	**Response**	**RSM**
A:MO C.	B:Cat.	C:Time	Deg.	Deg
ppm	mg	Min	%	%
Min	Min	Min	-	-
Max	Min	Min	-	-
Mid	Mid	Min	-	-
Min	Max	Min	-	-
Max	Max	Min	-	-
Mid	Min	Mid	-	-
Min	Mid	Mid	-	-
Mid	Mid	Mid	-	-
Max	Mid	Mid	-	-
Mid	Max	Mid	-	-
Min	Min	Max	-	-
Max	Min	Max	-	-
Mid	Mid	Max	-	-
Min	Max	Max	-	-
Max	Max	Max	-	-

The degradation percentage was determined using the formula provided as Equation 3.4, where the variables C_0 and C_t represent the initial concentration of MO and the concentration at the time of measurement (in ppm), respectively.

$$D(\%) = \frac{(C_0 - C_t)}{C_0} \times 100$$

After gathering experimental data, a mathematical relationship between various parameters and the degradation of MO dye was established. The quality of the curve fitting was assessed using statistical measures such as P-values and R-squared (R^2) values. Subsequently, perturbation and three-dimensional (3D) plots were generated. Through a detailed analysis of these curves, the impact of the examined parameters on the degradation of MO dye was investigated. Furthermore, the interaction between these parameters was explored by examining the three-dimensional curves and conducting an analysis of variance (ANOVA). This comprehensive approach allowed for a deeper understanding of how different factors influence the degradation process and how they may interact with each other.

3.6. Reference

1 Koç, B. & Kaymak-Ertekin, F. Response surface methodology and food processing applications. *GIDA-Journal of Food* **35**, 63-70 (2010).

2 Soleimani, S., Heydari, A., Fattahi, M. & Motamedisade, A. Calcium alginate hydrogels reinforced with cellulose nanocrystals for methylene blue adsorption: Synthesis, characterization, and modelling. *Industrial Crops and Products* **192**, 115999 (2023).

3 Aydar, A. Y. Utilization of response surface methodology in optimization of extraction of plant materials. *Statistical approaches with emphasis on design of experiments applied to chemical processes*, 157-169 (2018).

4 Singh, A. K., Giannakoudakis, D. A., Arkas, M., Triantafyllidis, K. S. & Nair, V. Composites of lignin-based biochar with BiOCl for photocatalytic water treatment: RSM studies for process optimization. *Nanomaterials* **13**, 735 (2023).

5 Galedari, M., Ghazi, M. M. & Mirmasoomi, S. R. Photocatalytic process for the tetracycline removal under visible light: Presenting a degradation model and optimization using response surface methodology (RSM). *Chemical Engineering Research and Design* **145**, 323-333 (2019).

6 Aditya, M. *et al.* Biosynthesis of rod shaped Gd2O3 on g-C3N4 as nanocomposite for visible light mediated photocatalytic degradation of pollutants and RSM optimization. *Diamond and Related Materials* **121**, 108790 (2022).

7 Le, A. T., Tan, Z.-H., Sivakumar, R. & Pung, S.-Y. Predicting the photocatalytic performance of metal/metal oxide coupled TiO2 particles using Response Surface Methodology (RSM). *Materials Chemistry and Physics* **269**, 124739 (2021).

8 Pereira, L. M. S., Milan, T. M. & Tapia-Blácido, D. R. Using Response Surface Methodology (RSM) to optimize 2G bioethanol production: A review. *Biomass and Bioenergy* **151**, 106166 (2021).

9 Mousavi, M., Soleimani, M., Hamzehloo, M., Badiei, A. & Ghasemi, J. B. Photocatalytic degradation of different pollutants by the novel gCN-NS/Black-TiO2 heterojunction photocatalyst under visible light: Introducing a photodegradation model and optimization by response surface methodology (RSM). *Materials Chemistry and Physics* **258**, 123912 (2021).

10 Malika, M. & Sonawane, S. S. The sono-photocatalytic performance of a Fe2O3 coated TiO2 based hybrid nanofluid under visible light via RSM. *Colloids and Surfaces A: Physicochemical and Engineering Aspects* **641**, 128545 (2022).

11 Hosseini, O., Zare-Shahabadi, V., Ghaedi, M. & Azqhandi, M. A. Experimental design, RSM and ANN modeling of tetracycline photocatalytic degradation using LDH@ CN. *Journal of Environmental Chemical Engineering* **10**, 108345 (2022).

12 Fisher, R. A. Design of experiments. *British Medical Journal* **1**, 554 (1936).

13 Pukelsheim, F. *Optimal design of experiments*. (SIAM, 2006).

14 Eriksson, L., Johansson, E., Kettaneh-Wold, N., Wikström, C. & Wold, S. Design of experiments. *Principles and Applications, Learn ways AB, Stockholm* (2000).

15 Hicks, C. R. Fundamental concepts in the design of experiments. (1964).

16 Elfghi, F. A hybrid statistical approach for modeling and optimization of RON: A comparative study and combined application of response surface methodology (RSM) and artificial neural network (ANN) based on design of experiment (DOE). *Chemical Engineering Research and Design* **113**, 264-272 (2016).

17 Durakovic, B. Design of experiments application, concepts, examples: State of the art. *Periodicals of Engineering and Natural Sciences* **5** (2017).

18 Mason, R. L., Gunst, R. F. & Hess, J. L. *Statistical design and analysis of experiments: with applications to engineering and science*. (John Wiley & Sons, 2003).

19 Calfee, R. & Piontkowski, D. Design and analysis of experiments. *Handbook of reading research*, 63-90 (1984).

20 Wang, J., Sun, B., Cao, Y., Tian, Y. & Li, X. Optimisation of ultrasound-assisted extraction of phenolic compounds from wheat bran. *Food chemistry* **106**, 804-810 (2008).

21 Maran, J. P., Mekala, V. & Manikandan, S. Modeling and optimization of ultrasound-assisted extraction of polysaccharide from Cucurbita moschata. *Carbohydrate polymers* **92**, 2018-2026 (2013).

22 Şahin, S. *et al.* Solvent-free microwave-assisted extraction of polyphenols from olive tree leaves: Antioxidant and antimicrobial properties. *Molecules* **22**, 1056 (2017).

23 Veza, I., Spraggon, M., Fattah, I. R. & Idris, M. Response surface methodology (RSM) for optimizing engine performance and emissions fueled with biofuel: Review of RSM for sustainability energy transition. *Results in Engineering*, 101213 (2023).

24 Salehnezhad, L., Heydari, A. & Fattahi, M. Experimental investigation and rheological behaviors of water-based drilling mud contained starch-ZnO nanofluids through response surface methodology. *Journal of Molecular Liquids* **276**, 417-430 (2019).

25 Box, G. E. & Wilson, K. B. in *Breakthroughs in statistics: methodology and distribution* 270-310 (Springer, 1992).

26 Braima, N., Maryam, A. N. A. & Odejobi, O. J. (Nigeria, 2016).

27 Adams, B. M. Design and analysis of experiments. *Journal of Quality Technology* **37**, 175 (2005).

28 Farooq, Z., REHMAN, S. U. & Abid, M. Application of response surface methodology to optimize composite flour for the production and enhanced storability of leavened flat bread (Naan). *Journal of food processing and preservation* **37**, 939-945 (2013).

29 H Pishgar-Komleh, S., Keyhani, A., Mostofi-Sarkari, M. & Jafari, A. Application of response surface methodology for optimization of picker-husker harvesting losses in corn seed. *Iranian (Iranica) Journal of Energy & Environment* **3** (2012).

30 Aydar, A., Bağdatlıoğlu, N. & Köseoğlu, O. Effect of ultrasound on olive oil extraction and optimization of ultrasound-assisted extraction of extra virgin olive oil by response surface methodology (RSM). *Grasas y Aceites* **68**, e189-e189 (2017).

31 Anderson, M. J. & Whitcomb, P. J. *RSM simplified: optimizing processes using response surface methods for design of experiments*. (Productivity press, 2016).

32 Reji, M. & Kumar, R. Response surface methodology (RSM): An overview to analyze multivariate data. *Indian J. Microbiol. Res* **9**, 241-248 (2022).

33 ALLEN, P. *DESIGN OF EXPERIMENTS FOR 21ST CENTURY ENGINEERS*. (LULU COM, 2020).

34 Kreetachat, T. *et al.* Dataset on the optimization by response surface methodology for dried banana products using greenhouse solar drying in Thailand. *Data in Brief*, 109370 (2023).

35 Lalanne, C. (Citeseer. http://citeseerx. ist. psu. edu/viewdoc/download, 2006).

36 Oketola, A. *et al.* Process Parametric optimization of spark plasma sintered Ni-Cr-ZrO2 composites using response surface methodology (RSM). *International Journal of Lightweight Materials and Manufacture* (2023).

37 Soleimani, S., Heydari, A. & Fattahi, M. Swelling prediction of calcium alginate/cellulose nanocrystal hydrogels using response surface methodology and artificial neural network. *Industrial Crops and Products* **192**, 116094 (2023).

38 Mahmoodi-Babolan, N., Heydari, A. & Nematollahzadeh, A. Removal of methylene blue via bioinspired catecholamine/starch superadsorbent and the efficiency prediction by response surface methodology and artificial neural network-particle swarm optimization. *Bioresource technology* **294**, 122084 (2019).

39 Polasky, A. D., Evans, J. L. & Fuentes, J. D. CCdownscaling: A Python package for multivariable statistical climate model downscaling. *Environmental Modelling & Software* **165**, 105712 (2023).

CHAPTER 4: PREPARATION OF PHOSPHINE-STABILISED Au_9 NANOCLUSTERS AND THEIR CHARACTERISATION BY MASS SPECTROMETRY, ^{31}PNMR, AND UV-VIS

4.1. Abstract

This research focuses on the preparation and characterisation of atomically precise Au_9 nanoclusters (Au_9 NCs) protected by triphenyl phosphine ligands. The Au_9 NCs were chemically prepared and subjected to a comprehensive analysis utilising UV-Vis spectroscopy, ^{31}P NMR, and mass spectrometry to accurately determine their structural characteristics. Notably, it was observed that a change in solvent from methanol to chloroform or other chlorine-containing solvents led to the agglomeration of the Au_9 NCs. Consequently, methanol was chosen as the primary solvent for all subsequent analyses. The UV-Vis analysis revealed spectral characteristics which are consistent with those previously reported for Au_9 NCs. Mass spectrometry patterns indicated the presence of fractions stemming from the same Au_9 NC structure. Furthermore, ^{31}P NMR spectroscopy provided crucial chemical shift data associated with the Au_9 NCs. The results presented herein unequivocally demonstrate the successful synthesis of Au_9 NCs, laying the foundation for further investigations into their distinct characteristics and possible applications.

4.2. Introduction

Au nanoclusters (Au NCs) have garnered significant interest in the field of nanotechnology owing to their distinctive size-dependent physical and chemical features. There are discrete, quantised conduction and valence bands in such small particles due to spatially confined charge carriers. As a result of the evolution of Au nanoclusters (Au NCs) from bulk state to discrete molecular orbital levels, they can be used for nano- and molecular devices.[1-5]

Au NCs are divided into naked clusters and ligand-stabilised clusters. Under vacuum conditions, naked clusters are often generated and studied as they have no ligand stabilisation. In contrast, ligand-stabilised Au NCs are typically synthesised by wet chemistry. Organic ligands surround the metal core, stabilising the cluster both sterically and electronically. There are several ligands commonly used in Au clusters, including isocyanides, carbon monoxide, halides, phosphine, thiol, and hydrides[6].

Phosphine ligand-stabilised Au NCs, which have incredible physical properties, rely heavily on the protecting phosphine ligands and the size of the Au cores.[7-10] In the same way as ligands can control cluster sizes, Au clusters can change their geometries by interacting with ligand molecules, possibly because of charge transfers caused by ligand-Au interactions that weaken Au−Au bonds. By removing the ligand from metal clusters through techniques such as reactions with peroxides,

calcination in a controlled atmosphere, and heating under vacuum, naked-metal clusters with enhanced catalytic activity can be generated.[11-13]

In addition to cluster size, geometry, and electronic structure, ligand concentration and configuration also affect nanostructure catalytic activity. The electronic structure of ligand-protected AuX (X < 10) clusters immobilised onto surfaces can be difficult to characterise experimentally; however, there is still a limited amount of information available.[14,15]

A mass spectrometer (MS) can determine the formula of a molecule by measuring the size of its core, identifying its protective ligand, and determining the structure of its ligands simultaneously.[7,16] As a technique, mass spectrometry has been challenged by the unique characteristics of ligand protected Au NCs. As challenges are overcome, mass spectrometry has become increasingly used in the analysis of small Au NCs.[17,18]

For this study, the focus was on the triphenyl phosphine stabilised Au_9 NCs, $Au_9(PPh_3)_8(NO_3)_3$, which was chemically prepared with relatively high yields, and several techniques were used to determine their structures precisely. This study described the mass spectrometer (MS) technique alongside other techniques like UV-Vis and ^{31}P NMR to characterise the triphenyl phosphine stabilised Au_9 NCs. The effect of using various solvents on the size of Au_9 NCs and ^{31}P NMR chemical shifts was also investigated.

4.3. Preparation of phosphine ligand stabilised Au_9 nanocluster (NCs)

All basic laboratory chemicals (solvents, AgCl, Tetrachloroauric acid, Triphenylphosphine, and $AgNO_3$ AR grade) have been purchased from Sigma-Aldrich and used without further purification. A freezer without light was used to store all prepared products.

4.3.1. Preparation of $Au(PPh_3)Cl$:

The protocol used in this study was adapted from Malatesta et al.[19] A solution of tetrachloroauric acid (2.010 g, 5.102 mmol) in 10 ml of absolute ethanol was added rapidly to triphenylphosphine (2.65 g, 10.10 mmol) dissolved in 75 ml of absolute ethanol, stirring at 500 rpm. This addition led to the disappearance of the yellow colour of the solution and the formation of a white precipitate. The resulting mixture was vigorously stirred at 1000 rpm for 15 minutes to ensure complete reaction. Afterward, the reaction mixture underwent centrifugation (5 minutes, 5000 rpm) to collect the white product. This solid product was then subjected to three washes with 20 ml portions of hot ethanol, using a sintered glass funnel filter with a porosity rating of 3. Following the dissolution of the solid product in 30 ml of chloroform, the solution was filtered, and the solvent was subsequently evaporated under reduced pressure. The obtained product was dried using a vacuum desiccator. For

further purification, the desired products were recrystallised from a combination of dichloromethane and methanol applying vapor diffusion, leading to the formation of needle-like white crystals.[7,20] Yield: 3.11 g, 92 %. ^{31}P NMR ($CDCL_3$, 25 °C); δ 33.16 ppm referenced to H_3PO_4.

4.3.2. Preparation of $AuPPh_3(NO_3)$:

The preparation of the powder $AuPPh_3(NO_3)$ sample followed the synthesis procedure reported by Mueting et al.[21] An $Au(PPh_3)Cl$ (3.973 g, 8.042 mmol) solution in chloroform (50 ml) was rapidly mixed with an $AgNO_3$ (3.430 g, 20.191 mmol) solution in 130 ml of ethanol and stirred for one hour in a covered reaction vessel by Al foil. To remove the AgCl by-product, a sintered glass funnel filter was used (porosity 3), and the solvent of filtrate was slowly evaporated at room temperature in a rotary evaporator. 50 ml of ethanol was used three times to wash the crude product. The obtained clusters were dissolved in 50 ml of dichloromethane, followed by 150 ml of ethanol. The dichloromethane fraction was then removed by bubbling the solution for a few hours with nitrogen flow. Filtered white crystals were rinsed by cold ethanol (3 x 5 ml) and cold diethyl ether (3 x 5 ml).[7,20]

Yield: 3.75 g, 88 %. ^{31}P NMR ($CDCL_3$, 25 °C); δ 25.2 ppm referenced to H_3PO_4.

4.3.3. Preparation of $Au_9(PPh_3)_8(NO_3)_3$:

Triphenyl phosphine-stabilised Au_9 NCs, denoted as $Au_9(PPh_3)_8(NO_3)_3$, were prepared following the procedure outlined by Wen et al.[12] Initially, a solution of 0.072 g $NaBH_4$ (1.92 mmol) in 92 ml of ethanol was combined with a solution of $Au(PPh_3)NO_3$ (4.0 g, 7.6 mmol) in 160 ml of ethanol. After filtration to remove insoluble impurities, the solvent was separated from the solution using a rotary evaporator. Remarkably, within a span of 2 hours, the solution acquired a deep red colour. The resulting solids were dissolved in 20 ml of CH_2Cl_2 and subsequently filtered through a sintered glass filter funnel with a porosity rating of 3. The solvent was removed using a rotary evaporator, yielding a black precipitate that underwent washing with 50 ml of THF. Following this rinsing step, a dark green solid remained, which was further subjected to washing with THF (3 × 50 ml) and hexanes (3 × 50 ml). To obtain the final product, the precipitate was crystallised by gradually diffusing diethyl ether into methanol at 4 °C within a five-day period, resulting in the formation of dark green crystals.[7,20]

Yield 1.32 g, 37 %. 31P NMR (CD_3OD, 25 °C); δ 57.77 ppm referenced to H_3PO_4.

4.4. Result and discussion

4.4.1. Characterisation methods:

The identity of the clusters was confirmed by the characterisation methods ^{31}P NMR, UV-Vis, and Positive ESI-TOF mass spectrometry. Recrystallisation of the clusters was carried out twice to achieve a higher purity before characterisation. However, when characterising Au_9 NCs, there were two important problems: 1- finding a suitable solvent for ^{31}PNMR and 2- finding good conditions for mass spectrometry.

Information on the structure of the prepared triphenyl phosphine stabilised Au NCs can be obtained by ^{31}P NMR which was recorded using a Varian INOVA spectrometer and deuterated solvents were purchased from Cambridge Isotopes. To characterise Au NCs and NPs using NMR spectroscopy, the ligand shell and the core nature must be taken into consideration. Due to the widening of the phosphorous peak, ^{31}P NMR will not be applicable to larger Au NPs and will not show any phosphorus in the baseline. On the other hand, for atomically precise Au NCs rather than larger NPs, ^{31}P NMR provides more valuable information on the structure because the associated chemical shift of phosphorus from the ligand allows us to distinguish between the specific cluster species present in solution. Although ^{31}P NMR is a crucial tool used in this study to characterise the various Au phosphine clusters, the challenging part of this analysis was selecting the solvent type.[10,22] Figure 4.1 shows that when $CDCl_3$ was used as a solvent, one doublet with chemical shifts of 56.56 ppm and 66.90 ppm were formed while by changing the solvent to CD_3OD, a single peak with chemical shift of 57.77 ppm was observed. To further investigate, a mixture of $CDCl_3$ and CD_3OD was also employed in characterising the Au_9 NCs. This resulted in a single peak appearing at a distinct chemical shift of 45.78 ppm, which differed notably from the initial peak observed in methanol at 57.77 ppm. This disparity may stem from the possibility of either partial or complete agglomeration of the Au_9 NCs due to their exposure to this solvent blend. This phenomenon could potentially lead to a loss of the purity of the product. However, it is worth noting that the NMR data for the ^{31}P ion, obtained in pure deuterated methanol, exhibited a singular peak that can be attributed to phosphorus binding to the Au_9 NCs. This finding aligns with previously reported result[7,20] (See Figure 4.1).

Specific cluster species in solution can be identified using the chemical shifts of the phosphorous peak associated with the ligands. ^{31}P NMR chemical shifts of the different types of Au NCs synthesised in this work with different sizes and counter ions were summarised in Table 4.1 (Figure 4.2). They are consistent with the references listed in the same Table 4.1.

Table 4-1. Experimental ^{31}P NMR isotropic chemical shifts and solvents

Clusters	Solvent	Chemical shift (^{31}P), ppm	Reference
$AuPPh_3(Cl)$	$CDCL_3$	33.16	[19]
$AuPPh_3(NO_3)$	$CDCL_3$	27.33	[21]
$Au_9(PPh_3)_8(NO_3)_3$	CD_3OD	57.77	[12]

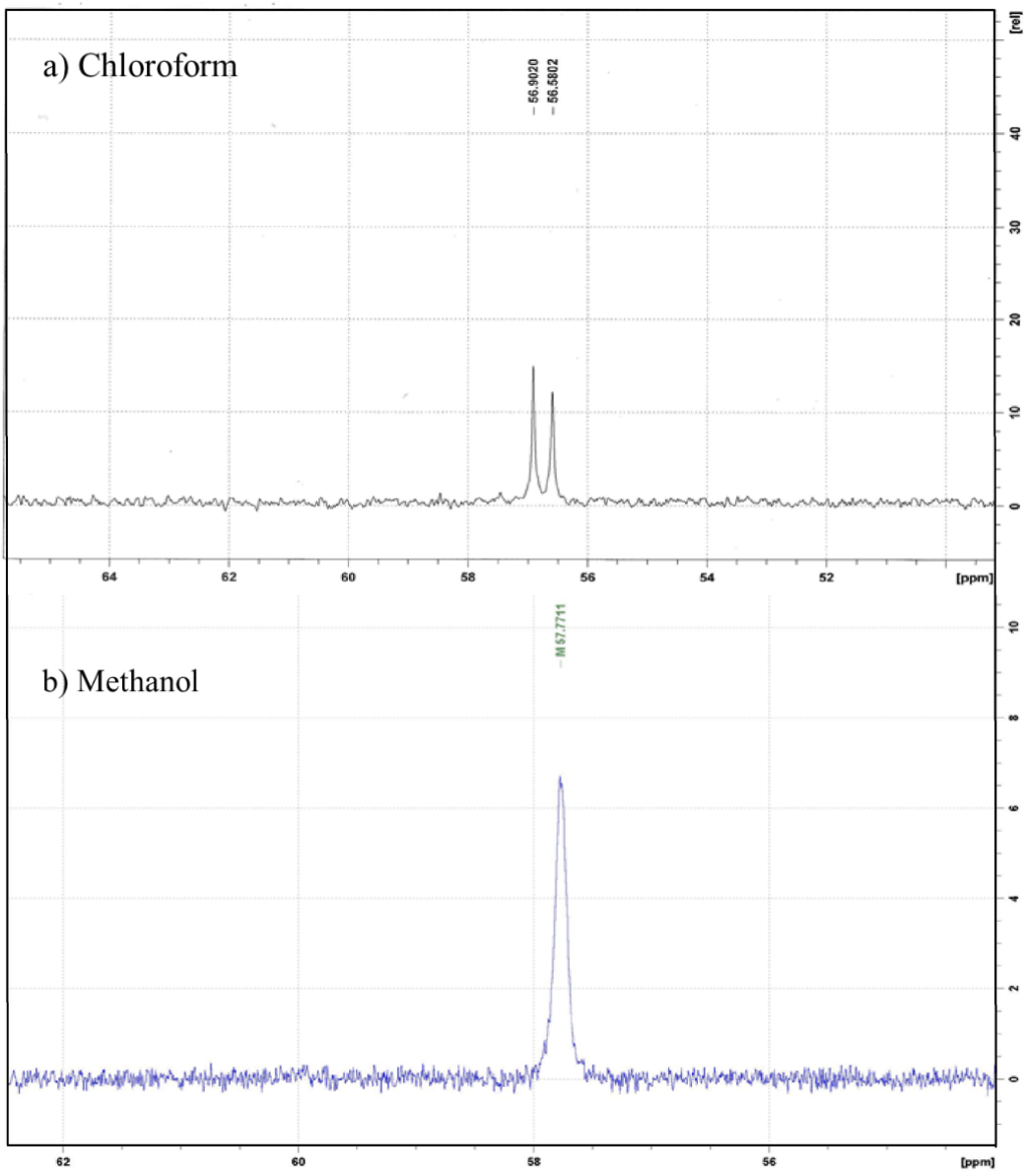
a) Chloroform
56.9020
56.5802
[rel]
64
62
60
58
56
54
52
[ppm]
b) Methanol
57.7711
62
60
58
56
[ppm]

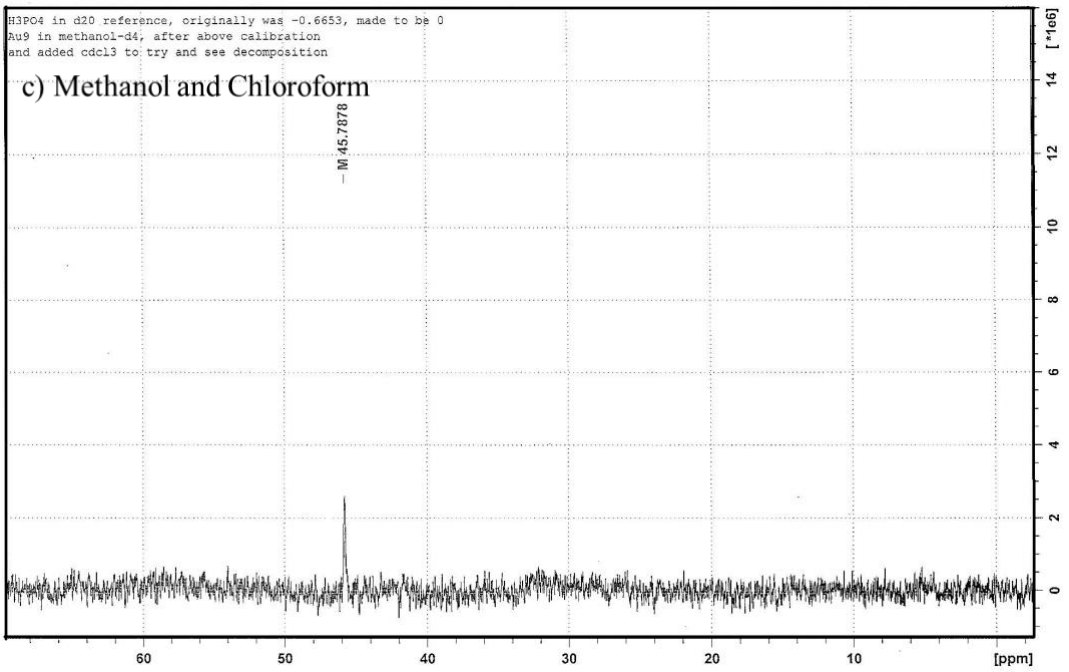

Figure 4.1. ^{31}P NMR of $Au_9(PPh_3)_8(NO_3)_3$ a) in $CDCl_3$ b) in CD_3OD c) combination of $CDCl_3$ in CD_3OD

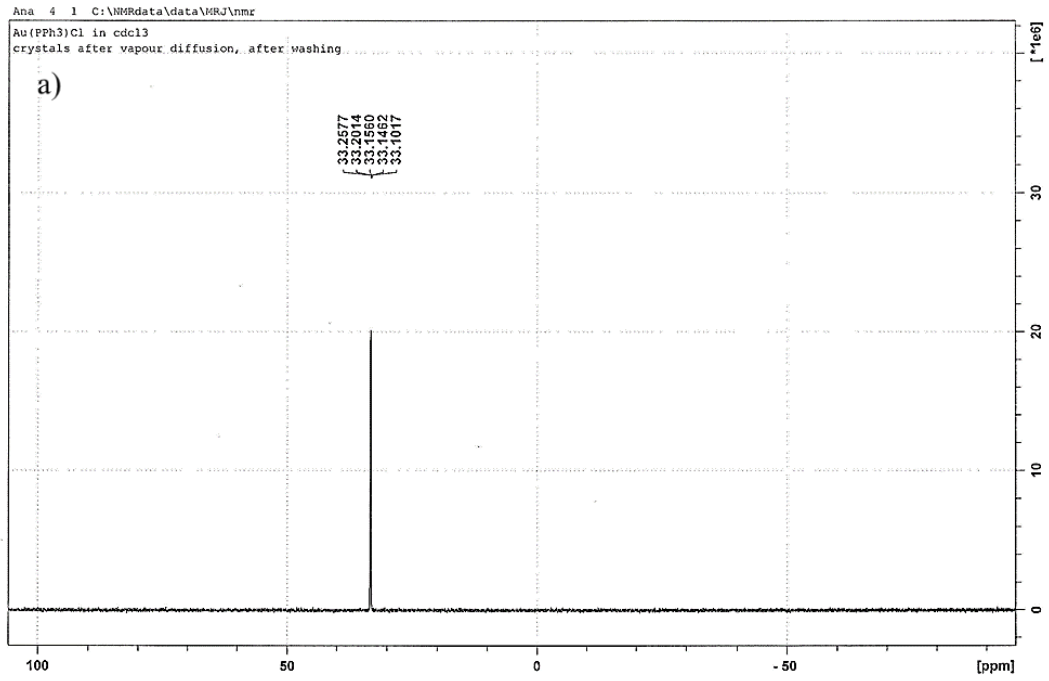

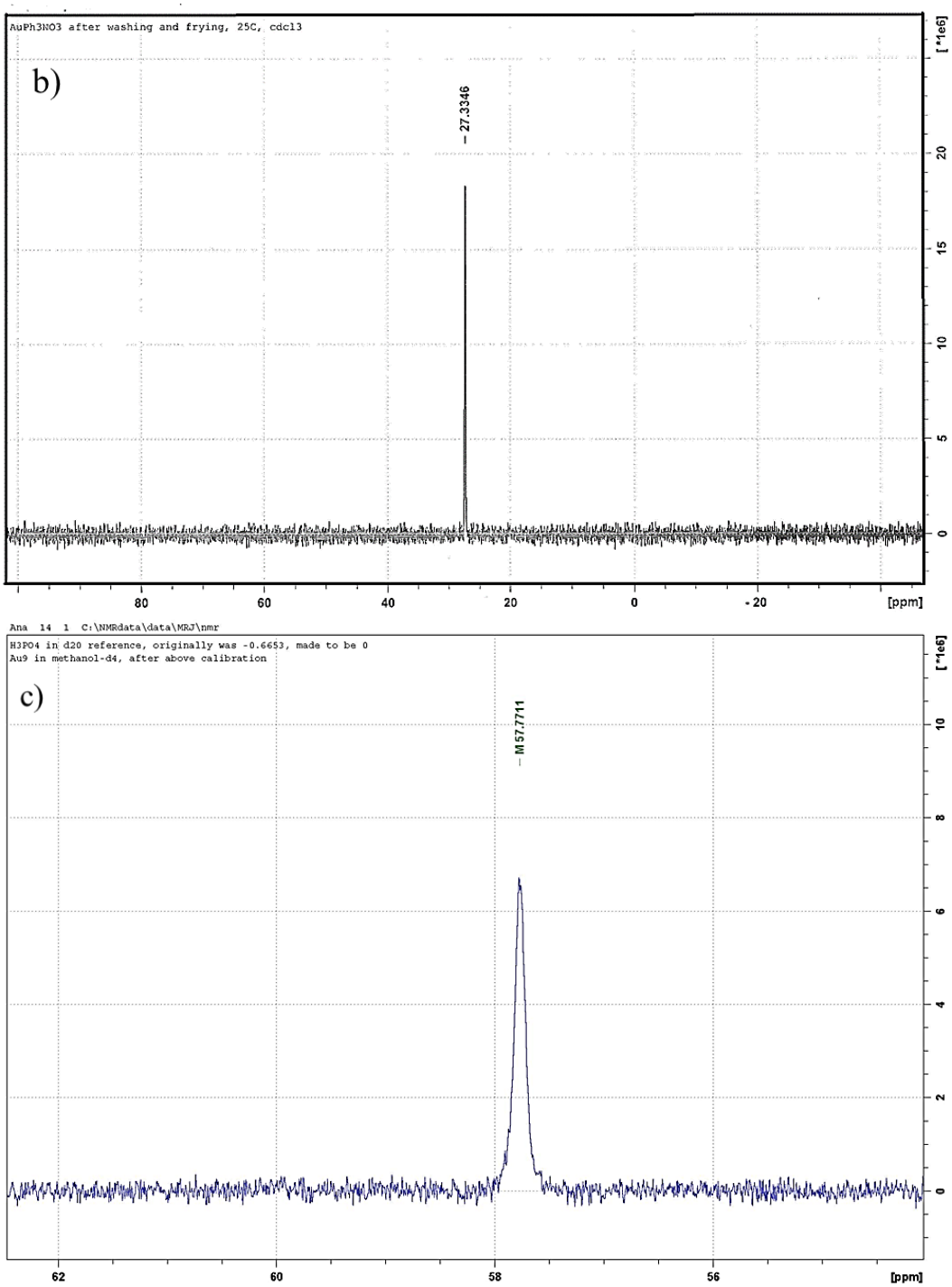

Figure 4.2. ^{31}P NMR of a) $AuPPh_3(Cl)$ b) $AuPPh_3(NO_3)$ c) $Au_9(PPh_3)_8(NO_3)_3$

Au_9 NCs are studied optically using UV-Visible spectroscopy. It is possible to distinguish nanoparticles and clusters using UV-Visible spectroscopy. The absorption spectra were collected from 230 to 800 nm. The molecular-like optical properties of Au_9 NCs display distinct peaks in the absence of the characteristic peak of the surface plasmon resonance (LSPR) which is a feature of larger Au NPs with metallic state.[23]

UV-Vis was used to determine the $Au_9(PPh_3)_8(NO_3)_3$ structure. Figure 4.3 shows a UV-Vis spectrum in methanol solution including three faint shoulders, centered in 354, 384 and 450 nm and

one sharp peak centered in 319 nm, that are in agreement with the reference sample peaks confirming successful synthesis of Au_9 NCs.[12]

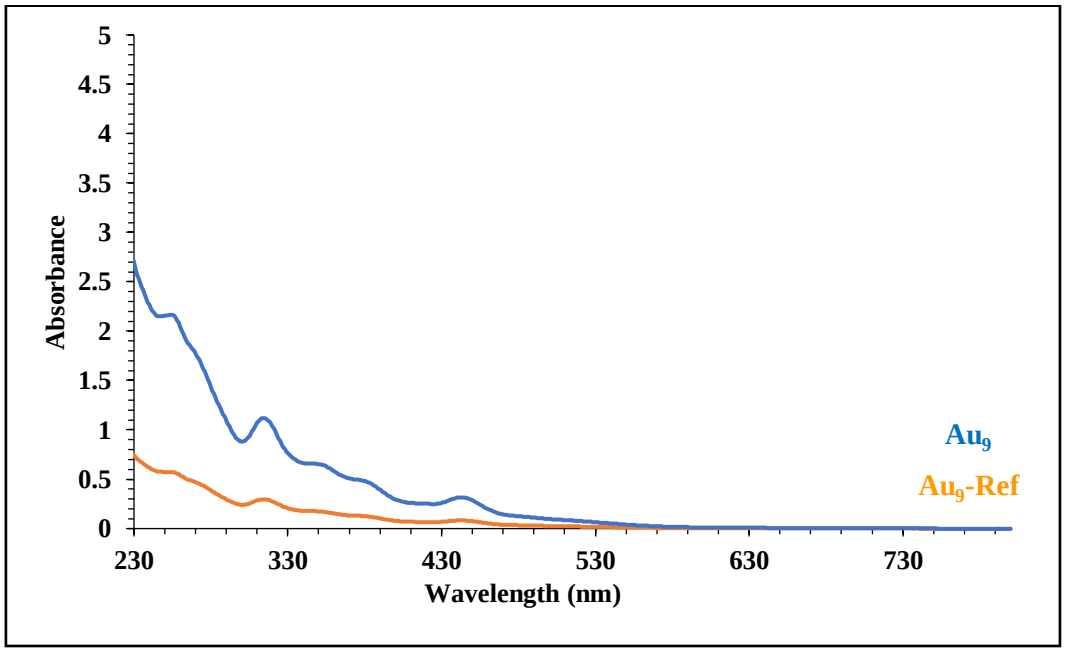

Figure 4.3. UV-Vis spectra of prepared Au_9 cluster and reference sample

Characterisation of the product distributions were performed using a positive ESI mode on Waters Synapt HDMS. Following preparation, mass spectrometry played a significant role in detection of accurate formula and structure of developed Au_9 NCs. TOF-MS is considered a high-resolution method, providing precise information on the formula and mass of the substances undergoing separation.[24] The extended ion path within the flight tubes facilitates the differentiation of compounds with subtle variations in their mass and charge. This technique is proper for compounds containing low and high mass, as the flight tube length can be enhanced by adding a reflector. This enhanced length can enable separation of very high mass substances. As a result, the resolution of the instrument can be increased by focusing the ions of the same mass with different speed to charge ratio.[24,25]

The most challenging part of this study was establishing an appropriate solvent and conditions for MS analysis that produced reasonable data, since this type of MS spectrometer has not yet been reported for Au NCs characterisation.

In this successful procedure, mass range was 500-4000 m/z. The heater on the source inlet was maintained at 80 ^oC but desolvation temperature was set on 150 ^oC. Ions were sprayed at 2.25 kV using Ar carrier gas. Solutions of the raw synthetic mixture of Au_9 NCs were prepared using UHPLC grade methanol. External mass calibration was conducted by introducing sodium iodide (2 µg/µL) through injection. Values of m/z, and high-resolution MS intensity for Au_9 NCs were summarised in Table 4.2. The data in Table 4.2 and a pattern for molecular ion peak for the $[Au_9(PPh_3)_8]_3^+$ in Figure

4.4 show the Au_9 NCs has been successfully synthesised as they are consistent with what has already been reported.[12]

Table 4-2. Values of m/z, and intensity Au_9 NCs fragments using high-resolution positive ESI-TOF mass spectrometry.

Mass/ Charge	Intensity
1289.8	63
1290.13	100
1290.47	73
1290.81	35
1291.16	16
1291.5	6
1291.81	4
1292.13	4
1292.48	5
1292.81	5.5
1293.15	6.2

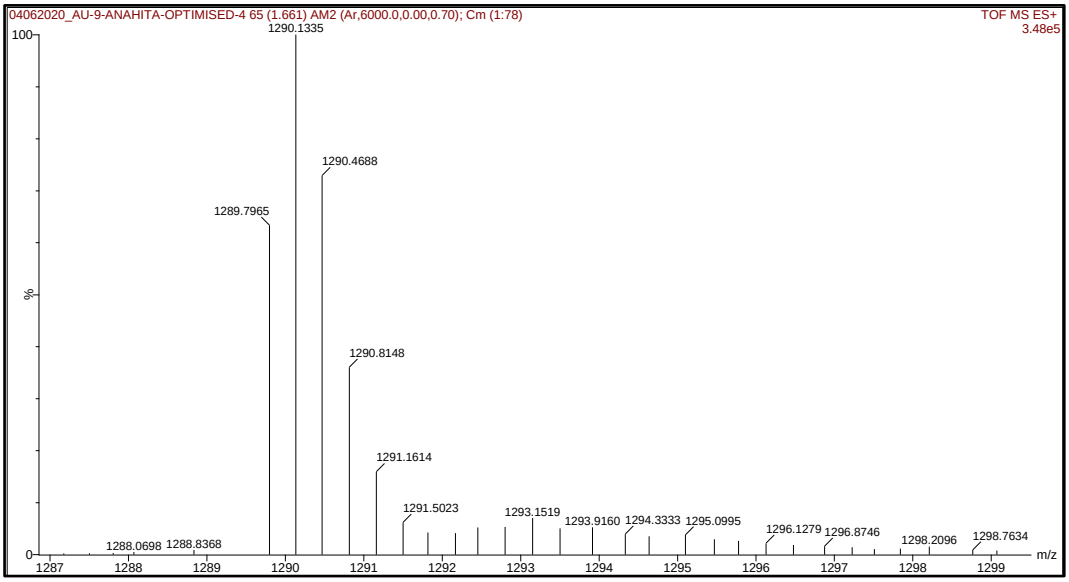

Figure 4.4. Molecular ion peak for the $[Au_9(PPh_3)_8]^{3+}$

4.5. Conclusion

In this study, UV/Vis spectrum,^{31}PNMR, and MS analyses were used to show that Au_9 NCs were successfully synthesised. Mass spectrometry also used as one of the most powerful analytical tools available to determine the accurate formula of the developed nanoclusters. It provided information that is essential for understanding the properties of new materials containing nanoclusters in future projects. This development has dramatically influenced our comprehension of tiny atomic

nanostructures, laying the foundation for the increasing curiosity surrounding their exceptional catalytic characteristics.

4.6. Reference

1 Li, H. *et al.* Recent developments in metal nanocluster-based catalysts for improving photocatalytic CO2 reduction performance. (2023).

2 Zhu, S., Wang, X., Cong, Y. & Li, L. Regulating the optical properties of gold nanoclusters for biological applications. *ACS omega* **5**, 22702-22707 (2020).

3 Qu, X. *et al.* Fluorescent gold nanoclusters: synthesis and recent biological application. *Journal of Nanomaterials* **2015**, 4-4 (2015).

4 Cheng, D., Liu, R. & Hu, K. Gold nanoclusters: Photophysical properties and photocatalytic applications. *Frontiers in Chemistry* **10**, 958626 (2022).

5 Ding, J. *et al.* Aptamer-modified atomically precise gold nanoclusters as targeted nanozymes to scavenge reactive oxygen species in white adipocytes. *Nanotechnology* (2023).

6 Anderson, D. P. An investigation into the surface chemistry of supported gold phosphine clusters. (2013).

7 Anderson, D. P. *et al.* Chemically synthesised atomically precise gold clusters deposited and activated on titania. Part II. *Physical chemistry chemical physics* **15**, 14806-14813 (2013).

8 Harkness, K. M., Cliffel, D. E. & McLean, J. A. Characterization of thiolate-protected gold nanoparticles by mass spectrometry. *Analyst* **135**, 868-874 (2010).

9 Gutrath, B. S. *et al.* [Au 14 (PPh 3) 8 (NO 3) 4]: An Example of a New Class of Au (NO 3)-Ligated Superatom Complexes. *Angewandte Chemie International Edition* **12**, 3529-3532 (2013).

10 Adnan, R. H., Madridejos, J. M. L., Alotabi, A. S., Metha, G. F. & Andersson, G. G. A review of state of the art in phosphine ligated gold clusters and application in catalysis. *Advanced Science* **9**, 2105692 (2022).

11 Gutrath, B. S. *et al.* Molecular and Electronic Structure of the Cluster [Au8 (PPh3) 8](NO3) 2. *European Journal of Inorganic Chemistry* **2016**, 975-981 (2016).

12 Wen, F., Englert, U., Gutrath, B. & Simon, U. (Wiley Online Library, 2008).

13 Pettibone, J. M. & Hudgens, J. W. Gold cluster formation with phosphine ligands: etching as a size-selective synthetic pathway for small clusters? *ACS nano* **5**, 2989-3002 (2011).

14 Zhang, S.-S. *et al.* Diphosphine-protected ultrasmall gold nanoclusters: opened icosahedral Au 13 and heart-shaped Au 8 clusters. *Chemical Science* **9**, 1251-1258 (2018).

15 Adnan, R. H., Andersson, G. G., Polson, M. I., Metha, G. F. & Golovko, V. B. Factors influencing the catalytic oxidation of benzyl alcohol using supported phosphine-capped gold nanoparticles. *Catalysis Science & Technology* **5**, 1323-1333 (2015).

16 Takano, S., Hirai, H., Muramatsu, S. & Tsukuda, T. Hydride-doped gold superatom (Au9H) 2+: synthesis, structure, and transformation. *Journal of the American Chemical Society* **140**, 8380-8383 (2018).

17 Liu, J. *et al.* Facile synthesis of carbon-doped mesoporous anatase TiO2 for the enhanced visible-light driven photocatalysis. *Chemical Communications* **50**, 13971-13974 (2014).

18 Li, Y.-Z. & Leong, W. K. A comparative study on atomically precise Au nanoclusters as catalysts for the aldehyde–alkyne–amine (A 3) coupling reaction: ligand effects on the nature of the catalysis and efficiency. *RSC advances* **9**, 5475-5479 (2019).

19 Malatesta, L., Naldini, L., Simonetta, G. & Cariati, F. Triphenylphosphine-gold (0)/gold (I) compounds. *Coordination Chemistry Reviews* **1**, 255-262 (1966).

20 Anderson, D. P. *et al.* Chemically-synthesised, atomically-precise gold clusters deposited and activated on titania. *Physical chemistry chemical physics* **15**, 3917-3929 (2013).

21 Mueting, A. *et al.* Mixed-Metal-Gold Phosphine Cluster Compounds. *Inorganic Syntheses*, 279-298 (1992).

22 Sharma, R. *et al.* NMR characterization of ligand binding and exchange dynamics in triphenylphosphine-capped gold nanoparticles. *The Journal of Physical Chemistry C* **113**, 16387-16393 (2009).

23 Adnan, R. H. & Golovko, V. B. Benzyl alcohol oxidation using gold catalysts derived from Au 8 clusters on TiO 2. *Catalysis Letters* **149**, 449-455 (2019).

24 El-Aneed, A., Cohen, A. & Banoub, J. Mass spectrometry, review of the basics: electrospray, MALDI, and commonly used mass analyzers. *Applied spectroscopy reviews* **44**, 210-230 (2009).

25 Moule, E. *An Evaluation of Direct Sample Analysis Time of Flight Mass Spectrometry for Forensic Analysis*, Flinders University, College of Science and Engineering., (2020).

CHAPTER 5: TAILORING Au_9 NANOCLUSTER SIZE VIA TiO_2 SURFACE MODIFICATION: INSIGHTS FROM XPS ANALYSIS

5.1. Abstract

Triphenylphosphine ligated Au_9 nanoclusters, $Au_9(PPh_3)_8(NO_3)_3$, were deposited onto (3-mercaptopropyl) trimethoxysilane (MPTMS) modified and unmodified mesoporous screen printed TiO_2. The presence of thiol groups was determined using FTIR, TGA, EDS, and XPS analysis. Through XPS it was found that S modified $MTiO_2$ ($SMTiO_2$) surfaces increase the ratio of Au_9 nanoclusters (Au_9 NCs) by a factor of 10 and prevent the Au_9 cluster agglomeration after deposition and annealing.

5.2. Introduction

Metal clusters of various sizes, from a few to about a hundred atoms, are smaller than metal nanoparticles. In nanoclusters (NCs) sized smaller than 1.5 nm, the surface area-to-volume ratio is greater than nanoparticles providing more active sites. The unique features of metal clusters allow them to be used in diverse applications due to their size, stability, electronic, and catalytic characteristics. When particles grow larger, transitioning into the nanoparticle size range, typically exceeding around 100 atoms in size, they shift from cluster-like properties to displaying more metallic behaviour. Like molecules, clusters feature discrete electron energies, as opposed to bulk metals[1-3]. NCs are of interest for modifying semiconductor surfaces because they can act as co-catalysts, increasing the lifetime of the electrons and holes generated through light absorption of the respective semiconductor. This can improve the function of the semiconductor as a photocatalyst by enhancing its reactivity and optical properties.[4]

In the present work, phenyl phosphine-protected Au_9 nanoclusters (PPh_3-Au_9 NCs) are used as ligand-protected Au nanoclusters. Au nanoclusters (Au NCs) have sparked significant interest owing to their distinct electronic and catalytic features, which can be adjusted by altering the ligands and the quantity of gold atoms within the cluster. Researchers have identified several common types of ligand-protected Au NCs based on their structural features and ligands, including thiolate-protected Au NCs, protein-protected Au NCs, polymer-protected Au NCs, DNA-protected Au NCs, and phosphine-protected Au NCs. These ligands play a crucial role in controlling the size, structure, and properties of the Au nanoclusters.[5-8] PPh_3-Au NCs with bulky or electron-donating ligands have weaker binding energies for the attachment of the ligands to the Au core surfaces than other ligand-protected Au NCs. Therefore, they tend to be easily removed.[9,10]

To create an efficient photocatalytic system, ligands must often be removed via heat treatment such that the Au cluster cores are in direct contact with the semiconductor surface and that the reactants can be in contact with the Au cluster core [9,10]. However, this process can cause an undesired increase in Au cluster size, as they can be agglomerated by heat treatment and lose their unique properties.[11]

To maximize the efficiency of photocatalytic systems, controlling the size of Au NCs attached to the semiconductor surfaces is crucial. Additionally, photocatalytic efficiency can be improved by optimising the amount of Au NCs loaded onto semiconductor surfaces.[12-14]

To address these two issues, a range of procedures on semiconductor surfaces have been applied to reduce the agglomeration of the clusters for enhancing the activity of the photocatalysts. Reducing agglomeration can be achieved through two types of modification: i) morphological modification and ii) chemical modification.

Morphological modification can be achieved by using porous networks, reducing Au nanocluster mobility during deposition and the heating process. Mesoporous TiO_2 ($MTiO_2$) has superior photocatalytic activities over other forms of TiO_2, as it has a large surface area, an appropriate pore size, and a high degree of crystallinity. The mesoporous structure of TiO_2 provides a network of interconnected pores which may prevent Au nanocluster mobility and thereby prevent their agglomeration.[15-17]

Chemical modification of the substrate surface can be obtained by incorporating additional components onto the semiconductor surfaces for binding the clusters and reducing their mobility. Au nanocluster cores and semiconductor surfaces can form a stronger complex when these functional groups are present.[18] S functionalisation is a chemical modification technique that can be used to improve the Au nanocluster attachment to $MTiO_2$ surfaces. In this approach, a thiol (-SH) functional group is introduced onto the $MTiO_2$ surface through a chemical reaction, creating a surface able to bind the Au NCs because the S atom in the thiol group binds strongly to Au.[19-21] The S(sp3) hybrid orbitals form covalent bonds with Au(6s) electrons through a sp3-type hybridisation.[22] A variety of studies have shown that thiols (RSHs) mediate these interactions via their sulfhydryl (SH) functional groups.[19-21]

The present study uses screen printing to produce mesoporous TiO_2 films, followed by 3-mercaptopropyl trimethoxysilane (MPTMS) modification of the surface and $[Au_9(PPh_3)_8](NO_3)_3$ (Au_9 NCs) deposition as cocatalysts (Figure 5.1). The loading of the surface with Au NCs and the degree of their agglomeration are investigated with XPS.

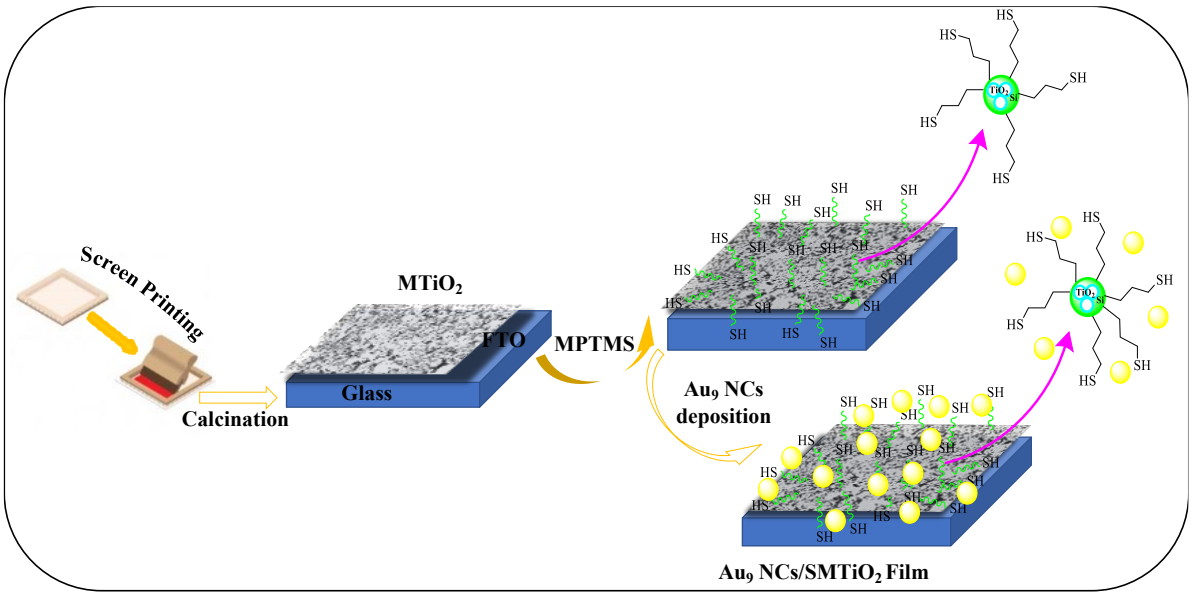

Figure 5.1. Au_9NCs/$SMTiO_2$ nanocomposites preparation procedure using screen printing and modification of the $MTiO_2$ surface by (3-mercaptopropyl) trimethoxysilane (MPTMS) and Au_9 nanocluster (Au_9 NCs).

5.3. Experimental section

5.3.1. Materials

All solvents, AgCl, tetrachloroauric acid, triphenylphosphine, and $AgNO_3$, which are necessary to produce Au_9 clusters and (3-mercaptopropyl) trimethoxysilane (MPTMS), and toluene anhydrous for the synthesis of $SMTiO_2$ film were purchased from Sigma-Aldrich. A transparent conductive oxide (TCO) substrate doped with fluorine, denoted as FTO (with resistivity values of 15 Ω/cm^2 and 7 Ω/cm^2, dimensions of 100 mm × 100 mm × 2.2 mm), was procured from Dyesol. The titania paste used, named 18NR-AO, was a mixture containing active anatase particles with an average size of approximately 20 nm, along with anatase scatter particles with sizes less than or equal to 450 nm, and it was obtained from GreatCell.

5.3.2. Sample Preparation

5.3.2.1. Preparation of $Au_9(PPh_3)_8(NO_3)_3$ nanoclusters (NCs):

Detailed information on the synthesis, purification, and the characterisation of the Au_9 NCs can be found in Chapter 4.

5.3.2.2. Preparation of the mesoporous TiO_2 Film:

The FTO (TEC 15) substrate underwent a cleaning process involving ultrasonication, initially with detergent and deionized water, followed by another ultrasonication step in ethanol. Subsequently, TiO_2 films were created by applying TiO_2 paste onto the FTO substrate through a screen-printing method, after which they were dried at 120°C for 5 minutes. The FTO substrate, now

coated with titania, was then placed in a covered petri dish, and subjected to a furnace. The heating process involved sequential steps at 120°C for 5 minutes, 325°C for 10 minutes, 375°C for 10 minutes, and finally 500°C for 30 minutes.[23]

5.3.2.3. Preparation of the S-functionalised mesoporous TiO_2 film (S-$MTiO_2$):

$MTiO_2$ films were submerged in 5 ml of toluene, to which 0.5 ml of (3-mercaptopropyl) trimethoxysilane was introduced. The mixture was then subjected to reflux heating at 110°C for a duration of 8 hours, resulting in the formation of an $SMTiO_2$ film with the desired functionalsation. Following this process, the functionalised film was washed with ethanol and left to air dry at room temperature overnight.

5.3.2.4. Deposition of $Au_9(PPh_3)_8(NO_3)_3$ clusters onto S-$MTiO_2$:

In the preparation of the Au_9 cluster solutions, the $Au_9(PPh_3)_8(NO_3)_3$ (1 mg, 4.63×10^{-6} mol) crystals were dispersed in approximately 2 ml of methanol and then stirred until completely dissolved. Subsequently, 2 ml of a methanol solution containing Au_9 clusters was introduced to the fully dried $SMTiO_2$ film, and the film was immersed in the solution for a period of 1 hour. During this process, the films transitioned in color from white to a yellowish hue. In the subsequent step, the crude sample was subjected to vacuum conditions at room temperature for a duration of 5 hours, to eliminate any remaining methanol. To mitigate the risk of aggregation or degradation, the samples were placed in sealed vials and stored in darkness at a temperature of 4°C.

5.3.2.5. Heat treatment for removing the phosphine ligands:

The Au_9 clusters, attached to the $MTiO_2$ film, were subjected to heating at 200°C in an ultra-high vacuum environment for a duration of 10 minutes. Following this step, the sample was taken out of the chamber and allowed to gradually cool down to room temperature under reduced pressure conditions. The resulting material was then stored in a refrigerator at a temperature of 4°C, while being shielded from light.

5.3.3. Characterisation

Detailed information on the surface characterisation methods can be found in Chapter 2.

5.4. Results and discussion

5.4.1. FTIR

Figure 5.2 shows the FTIR spectra over a wavenumber range of 400 to 4000 cm^{-1} of (a) MPTMS, (b) $SMTiO_2$, and (c) $MTiO_2$. In Figure 5.2, graph (a) was used as a reference to monitor if MPTMS charactristic peaks can be detected in $SMTiO_2$ compounds (graph b). In graphs b and c, a

characteristic broad band centred at 3374 cm^{-1}, a peak at 1648 cm^{-1}, and a broad peak centred at 400–700 cm^{-1} are assigned to adsorbed water, characteristic bending vibration of hydroxyl groups, and Ti-O-Ti bending vibration and Ti-O stretching modes, [24-26] respectively. These observations confirm the existence of TiO_2 nanoparticles (NPs) in our compounds prepared as a substrate.

The peaks at 2958 cm^{-1}, 2913 cm^{-1} and 1440 cm^{-1} in graph b (Figure 5.2) are attributed to the stretching and - CH_2 bending vibration of the propyl groups, introduced with MPTMS as they can also be identified in the reference graph (a) with some shift [27]. However, no peak was observed in this region in graph c in Figure 5.2, indicating all organic compounds used as templates were removed during calcination and crystallisation process of the $MTiO_2$ NPs.[28,29]

The vibrational peaks at 1042 cm^{-1} and 940 cm^{-1} (graph b in Figure 5.2) which are new compared to the pristine $MTiO_2$ film (graph c), are attributed to the vibration band of Si–O–Si and Ti–O–Si groups, respectively.[30,31] In addition, a peak at 1240 cm^{-1}, observed in both graphs a and b in Figure 5.2, can be attributed to the Si-C vibrational peak.[30,31] The presence of the -SH peak at 2560 cm^{-1} (shown in graph a), which corresponds to the attachment of MPTMS molecules, was not discernible in the spectra of the modified $MTiO_2$ (illustrated in graph b). This is primarily due to the relatively low weight percentage of MPTMS that was grafted onto the surface of $MTiO_2$. [28,29,32] The stretching vibration peak of C-O at 1186 cm^{-1} in graph a is related to the Si-OCH_3 groups of MPTMS. As no peak was observed in this region in graph b, it shows that Si-OCH_3 groups were hydrolysed for attaching the Si to the TiO_2 NPs surfaces during functionalisation process.

The strong peak at 2360 cm^{-1} in all absorption spectra corresponds to the CO_2 molecules in the atmosphere.

Overall, the FTIR findings indicate that MPTMS molecules were successfully grafted to the $MTiO_2$ surface to produce $SMTiO_2$, an SH-functionalised mesoporous titanium oxide film.

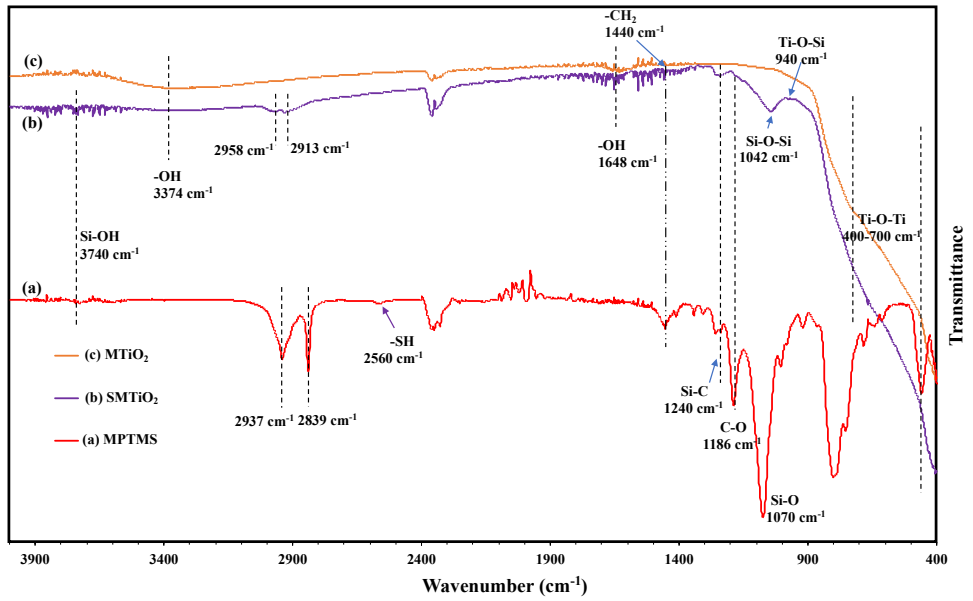

Figure 5.2. IR spectra of (a) MPTMS (b) $SMTiO_2$ and (c) $MTiO_2$.

5.4.2. SEM and EDS

In Figure 5.3 (a) and b the SEM images of $MTiO_2$ and $SMTiO_2$ Films can be seen. **Error! Reference source not found.** (c) shows the EDS result of the $SMTiO_2$ films.

The red numbers in the SEM micrograph (Figure 5.3 a) show that pore sizes are in the 2-50 nm range, confirming the formation of a mesoporous framework. Indeed, Figure 5.3 (a and b) demonstrate that $MTiO_2$ and $SMTiO_2$ films have a rough morphology formed by many pores distributed uniformly across the surface of the substrate. However, in Figure 5.3 (b), the appearance of the large particles shown by the red circles, can be explained by the accumulation of TiO_2 NPs during the modification process. Therefore, a degree of polydispersity in TiO_2 NP shapes and sizes can be formed after MPTMS functionalisation.

EDS in Figure 5.3 (c) shows the presence of Ti, O, Si, S, and C in $SMTiO_2$ films. It can confirm that MPTMS has been successfully grafted onto the surface.

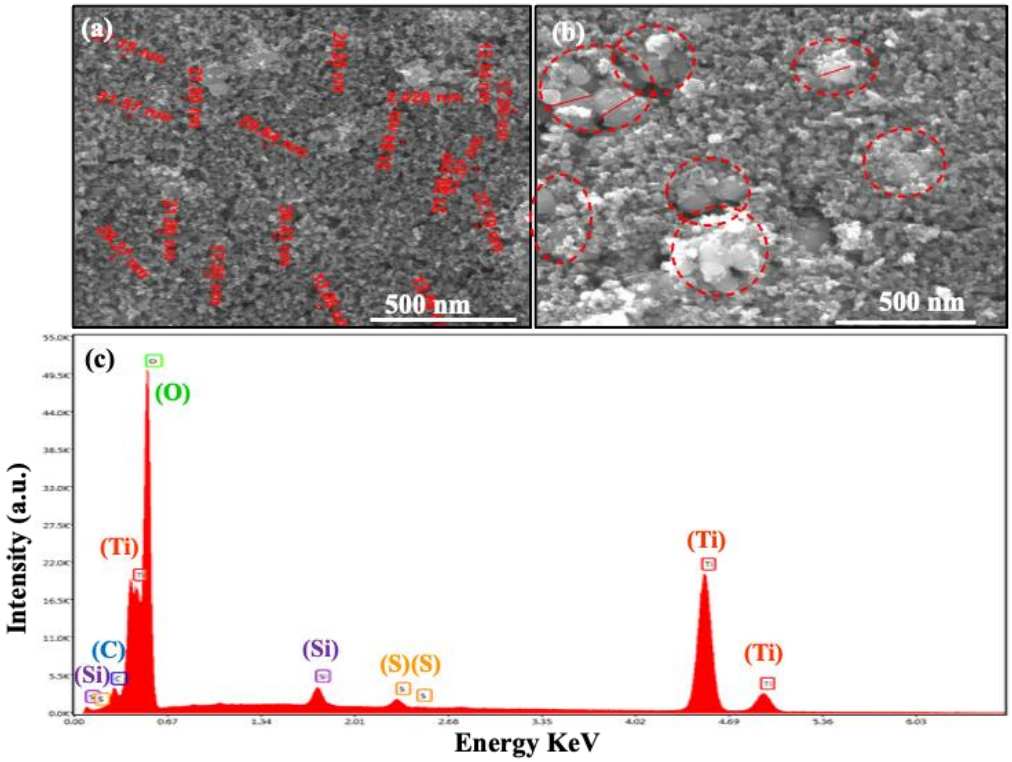

Figure 5.3. SEM images of (a) $MTiO_2$ film (b) $SMTiO_2$ film, and EDS analysis of (c) $SMTiO_2$ film

5.4.3. TG analysis

The changes in the mass of TiO_2 and $SMTiO_2$ over temperature were followed by TG analyses shown in Figure 5.4 (a and b).

Figure 5.4 (a) shows the degradation and total weight loss of 1.5 % in mesoporous titania ($MTiO_2$) in three stages. It is observed that the first shoulder occurs between 35 °C and 150 °C, where physisorbed water and intercalated water molecules evaporated with a weight loss of 0.5 %. Weight loss of 0.7% is observed within the temperature range of 150–450 °C, which could be attributed to the removal of chemisorbed water molecules[33,34]. A faint shoulder appeared at the range between 450°C and 800°C is related to 0.3% weight loss. This may be due to the phase transition from anatase to rutile phase.[17,35,36]

In Figure 5.4 (b), the thermal behaviour and weight loss of S-functionalised mesoporous titania ($SMTiO_2$) in two stages can be detected. The temperature range of 30 °C to 190 °C led to the first stage of weight loss (1%) attributed to the adsorbed water evaporation. The pyrolysis process at 190–800 °C resulted in a sharp decrease in the weight of modified $MTiO_2$. This loss of approximately 4% is assigned to the removal of chemisorbed water and large-scale decomposition of MPTMS chains[32,37]. As the same $MTiO_2$ as in Figure 5.4 (a) was used to react chemically with MPTMS, we assume that the difference in weight losses between two compounds before and after functionalisation may be due to the weight loss of MPTMS grafted to the surface which was almost 3.5 % (Figure 5.4 a and b).[37,38]

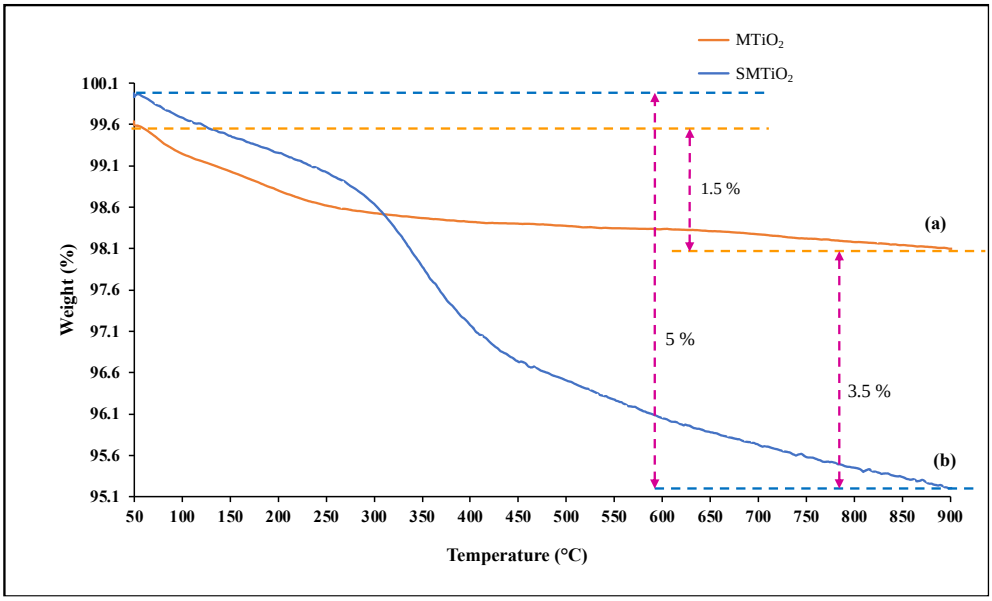

Figure 5.4. TG analysis of a) $MTiO_2$, b) $SMTiO_2$

5.4.4. XRD

Figure 5.5. a and b show the XRD pattern of $MTiO_2$ and $SMTiO_2$ samples, respectively. The diffraction peaks at 2θ = 25.3, 37.9, 48.2, 55.0, and 55.3° and the major peak of 2 thetas, crystal plane (101), correspond to the anatase phases.[39] The comparable and similar patterns observed in both spectra suggest that the MPTMS coating on the surface had no impact on the crystal phase of $MTiO_2$.

The average crystal sizes of the $MTiO_2$ and $SMTiO_2$ films in Table 5.1 are 29.9 nm and 37.5 nm, respectively. It shows that the MPTMS modification of the surfaces significantly affected the mean crystal size of $MTiO_2$ while their mean crystallinity index stayed almost the same (≅ 70) (Table 5.1).

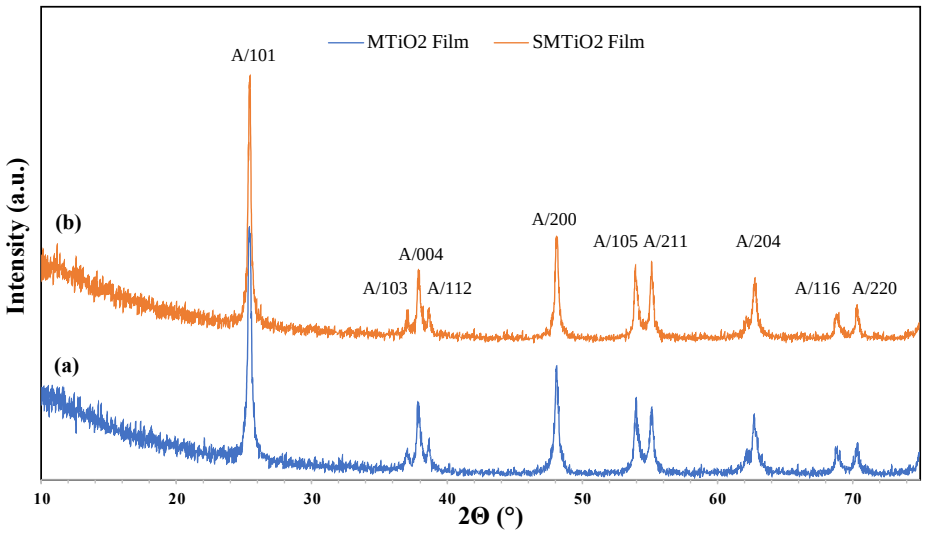

Figure 5.5. XRD patterns of (a) MTiO2 Film and (b) $SMTiO_2$ Film

Table 5-1. Mean crystallinity size (nm) and mean crystallinity index (%)

Sample	Mean crystal size (nm)	Mean crystallinity index (%)
$MTiO_2$	29.9 ± 1.0	72.2 ±1.0
$SMTiO_2$	37.5 ± 1.0	70.0 ±1.0

5.4.5. XPS analysis

The XP survey spectra of photocatalysts prepared using $MTiO_2$ semiconductors modified by MPTMS and Au_9 NCs are shown in Figure 5.6. Ti2p, O1s, C1s, S2p, Si2p, and Au4f are indexed as characteristic peaks. S and Si are related to the MPTMS chemically grafted onto $MTiO_2$. The Au in the spectrum is due to the presence of Au_9 NCs bound to the surface of $SMTiO_2$. XPS therefore shows the modification with MPTMS and the attachment of the Au_9 NCs.

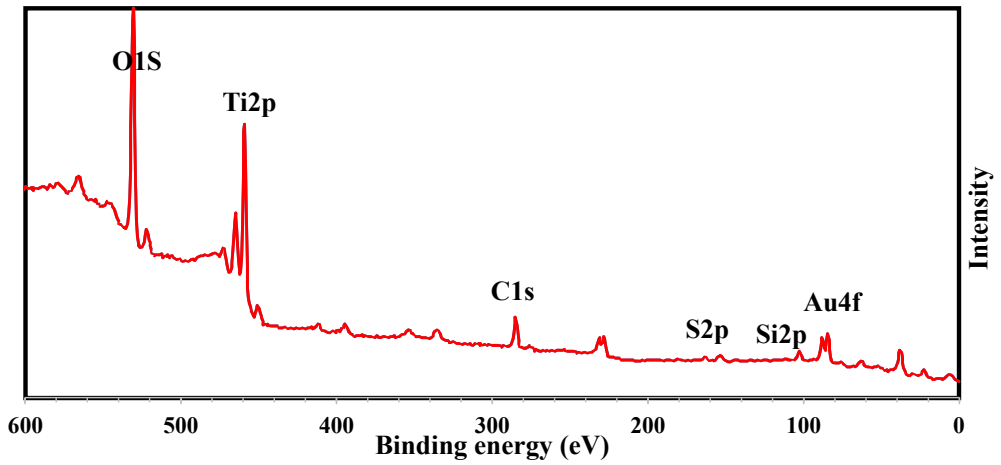

Figure 5.6. XPS survey of Au_9 NCs/$SMTiO_2$ nanocomposites

The final state effect is utilised to identify the size of Au_9 NCs from the peak position of Au 4f7/2 and its full-width-half maximum (FWHM).[40-43] The 84.6–85.2 eV range with an FWHM of 1.7 ± 0.2 eV is related to non-agglomerated Au_9 NCs and is named high binding peak (HBP).The range of binding energies of 83.7–84.4 eV with an FWHM of 1.0 ± 0.2 eV is attributed to agglomerated and large Au_9 NCs named low binding peak (LBP).[44-47]

The aggregation and relative intensity of Au_9 NCs ligated by triphenyl phosphine were investigated using XPS after deposition on $MTiO_2$ substrates and annealing treatment to remove the ligands. The effect of the surface modification with MPTMS on relative intensities and the size of the Au_9 NCs after both deposition and annealing processes was also investigated by XPS, as can be seen in Figure 5.6 a and b. In Table 5.2 the peak positions of Au4f and the Au_9 NCs relative intensity ratios deposited on $MTiO_2$ and $SMTiO_2$ surfaces are summarised.

In Figure 5.6 a and entry 1 in Table 5.2, it can be seen that after Au_9 NCs were deposited onto the $MTiO_2$ substrate, the Au 4f7/2 peak position appeared at 84.4 eV. This peak position is for partially agglomerated clusters called low binding peak (LBP) position. When the $MTiO_2$ substrate was modified by MPTMS, the peak position was found at 84.8 eV, and thus in the HBP range of non-agglomerated clusters (entry 2 of Table 5.2 and Figures 5.7 a and b).

In Figure 5.7 b and entries 1 and 2 of Table 5.2, the relative intensity of Au_9 NCs adsorbed on $MTiO_2$ and $SMTiO_2$ surfaces are shown. Changing the substrate from $MTiO_2$ to $SMTiO_2$, an increase of the ratio of Au_9 NCs by a factor of 10 can be seen (the Au_9 XPS intensity increased from 0.1 to 1.1 %). Therefore, $SMTiO_2$ is more efficient than $MTiO_2$ in both preventing the agglomeration and increasing the adsorption of Au_9 NCs due to the strong complexes between the thiol groups grafted onto the surface and the Au_9 cores.

The binding energies and relative intensities for Au for the samples after heating are shown in entries 3 and 4 of Table 5.2. When $MTiO_2$ films were used as the substrate (see entry 3 of Table 5.2), two Au species were found. One appeared at 85.1 eV in the HBP range of non-agglomerated clusters with 0.009% intensity, and another appeared at 83.6 eV with 0.08% relative intensity, as LBP or agglomerated Au_9 NCs (see Figure 5.7 c. showing Au4f doublet peaks as mentioned above). In contrast, as can be seen in Figure 5.6 a and b and Table 5.2 entry 4, when the substrate changed from $MTiO_2$ to $SMTiO_2$, the Au peak position appeared at 84.6 eV, a high binding energy peak (HBP), with an intensity ratio of 1.0 %, which is still interpreted as non-aggregated Au_9 NCs (Figure 5.7 d). The results show that S-functionalised $MTiO_2$ films can improve the results related to the size of Au_9 NCs after annealing compared to $MTiO_2$.

Thus, the S functionalisation process allows more clusters to be adsorbed onto the surface during the Au_9 deposition process compared to $MTiO_2$. Additionally, Au_9 agglomeration was lower on $SMTiO_2$ films than on $MTiO_2$ films.

Table 5-2. Assessment of binding energies and loading ratio of Au_9 NCs deposited on $MTiO_2$ Film and $SMTiO_2$ Film after deposition and annealing. (HBP and LBP means non-agglomerated and agglomerated cluster, respectively)

Condition	Entry	Sample	HBP		LBP	
			Binding energy (eV)	Relative intensity (%)	Binding energy (eV)	Relative intensity (%)
After Deposition	1	Au_9NCs@$MTiO_2$ Film	-	-	84.4	0.1
	2	Au_9NCs@$SMTiO_2$ Film	84.8	1.1	-	-

After Annealing	3	Au_9NCs@$MTiO_2$ Film	85.1	0.009	83.6	0.08
	4	Au_9NCs@$SMTiO_2$ Film	84.6	1.0	-	-

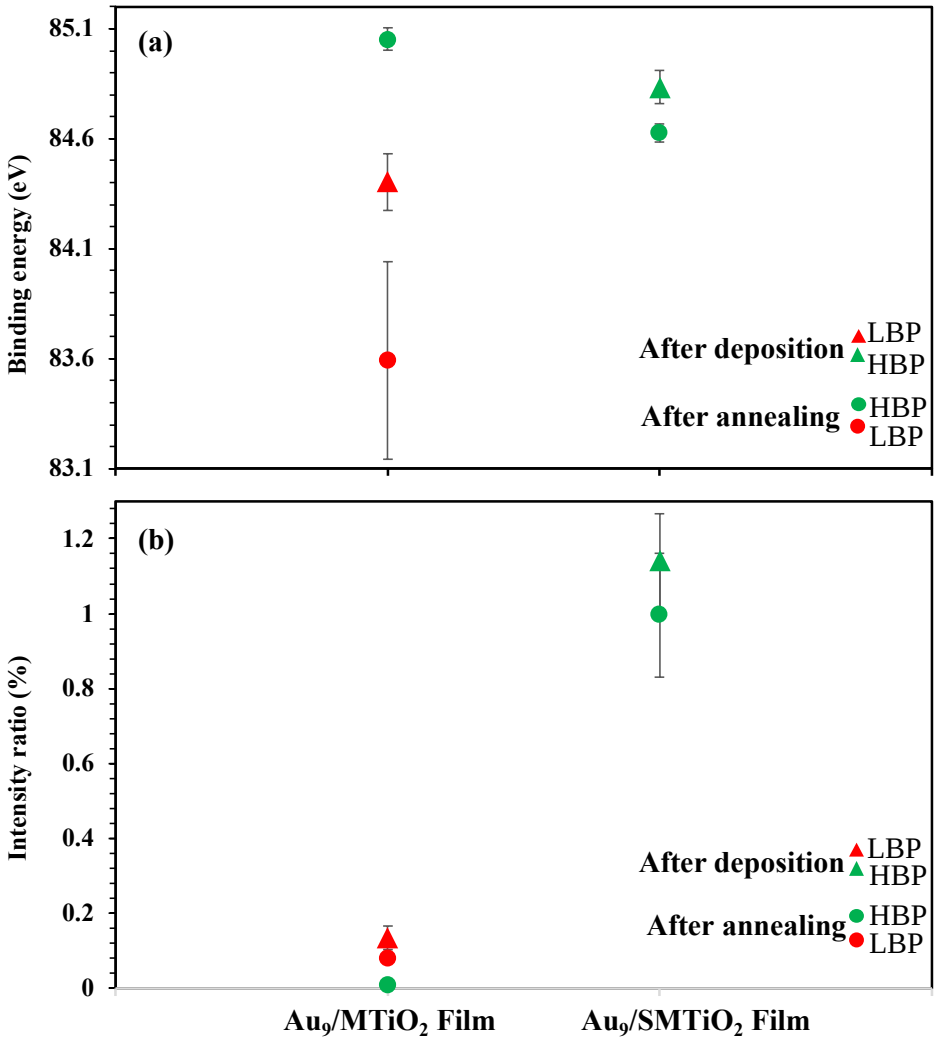

Figure 5.7. Investigation of Au_9 nanoclusters a) binding energies and b) ratios

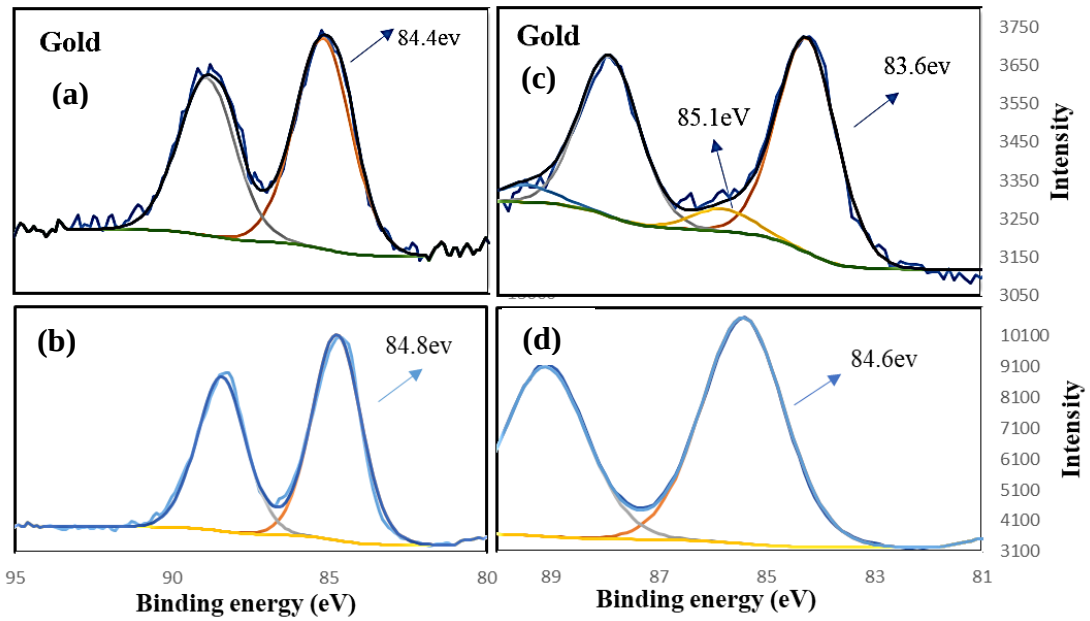

Figure 5.8. XPS High resolution of Au4f after deposition process of Au_9 NCs on (a) $MTiO_2$ film (b) $SMTiO_2$ film and after annealing process of (c) $Au_9/MTiO_2$ (d) $Au_9/SMTiO_2$ films.

5.5. Discussion

In this study, mesoporous TiO_2 films were first prepared by screen printing. Au_9 NCs were then deposited onto S functionalised $MTiO_2$ films following the MPTMS grafting process to produce an efficient photocatalytic system. FTIR, EDS, and XPS results showed that the surface of $MTiO_2$ was successfully coated by MPTMS molecules. XPS results showed that the S functionalisation process caused to adsorb more Au_9 NCs and to prevent their agglomeration after deposition and annealing processes. The XRD analysis revealed that both the prepared unfunctionalised and S-functionalised $MTiO_2$ films exhibited a dominant crystalline phase identified as anatase. This crystalline phase is of particular importance as it has the potential to enhance the efficiency of the photocatalyst, warranting further investigations in the future.

5.6. Conclusion:

In conclusion, the S-functionalised surface of TiO_2 influences the loading and size of Au_9 clusters. From XPS analysis, it is evident that the introduction of S groups onto the TiO_2 surface engenders two effects: reduced agglomeration and increased Au_9 cluster loading compared to unfunctionalised $MTiO_2$. These phenomena can be attributed to the interaction between the core of the Au clusters and the S moieties residing on the modified TiO_2 surface. Therefore, S functionalised $MTiO_2$ films can be considered as a promising substrate to adsorb a high level of ultra-small Au_9 NCs even after annealing treatment.

5.7. References:

1 Sharma, S., Kurashige, W., Niihori, Y. & Negishi, Y. in *Supra-materials Nanoarchitectonics* 3-32 (Elsevier, 2017).

2 Wang, X. *et al.* Atomic-precision Pt6 nanoclusters for enhanced hydrogen electro-oxidation. *Nature Communications* **13**, 1596 (2022).

3 Bera, R. K., Park, H., Ko, S. H. & Ryoo, R. Highly dispersed Pt nanoclusters supported on zeolite-templated carbon for the oxygen reduction reaction. *RSC advances* **10**, 32290-32295 (2020).

4 Li, H. *et al.* Recent developments in metal nanocluster-based catalysts for improving photocatalytic CO2 reduction performance. (2023).

5 Jin, R., Zhu, Y. & Qian, H. Quantum-sized gold nanoclusters: bridging the gap between organometallics and nanocrystals. *Chemistry–A European Journal* **17**, 6584-6593 (2011).

6 van de Looij, S. M. *et al.* Gold nanoclusters: imaging, therapy, and theranostic roles in biomedical applications. *Bioconjugate Chemistry* **33**, 4-23 (2021).

7 Weng, B., Lu, K.-Q., Tang, Z., Chen, H. M. & Xu, Y.-J. Stabilizing ultrasmall Au clusters for enhanced photoredox catalysis. *Nature communications* **9**, 1543 (2018).

8 Zhang, B., Chen, J., Cao, Y., Chai, O. J. H. & Xie, J. Ligand design in ligand-protected gold nanoclusters. *Small* **17**, 2004381 (2021).

9 Adnan, R. H., Madridejos, J. M. L., Alotabi, A. S., Metha, G. F. & Andersson, G. G. A review of state of the art in phosphine ligated gold clusters and application in catalysis. *Advanced Science* **9**, 2105692 (2022).

10 Cui, H., Shao, Z.-S., Song, Z., Wang, Y.-B. & Wang, H.-S. Development of gold nanoclusters: from preparation to applications in the field of biomedicine. *Journal of Materials Chemistry C* **8**, 14312-14333 (2020).

11 Menard, L. D., Xu, F., Nuzzo, R. G. & Yang, J. C. Preparation of TiO2-supported Au nanoparticle catalysts from a Au13 cluster precursor: Ligand removal using ozone exposure versus a rapid thermal treatment. *Journal of Catalysis* **243**, 64-73 (2006).

12 Cargnello, M. *et al.* Efficient removal of organic ligands from supported nanocrystals by fast thermal annealing enables catalytic studies on well-defined active phases. *Journal of the American Chemical Society* **137**, 6906-6911 (2015).

13 Chen, S. *et al.* Ligand removal of Au25 nanoclusters by thermal and electrochemical treatments for selective CO2 electroreduction to CO. *The Journal of chemical physics* **155**, 051101 (2021).

14 Krishnan, G. *et al.* Investigation of Phosphine Ligand Protected Au13 Clusters on Defect Rich Titania. *The Journal of Physical Chemistry C* **123**, 6642-6649 (2019).

15 Niu, B., Wang, X., Wu, K., He, X. & Zhang, R. Mesoporous titanium dioxide: Synthesis and applications in photocatalysis, energy and biology. *Materials* **11**, 1910 (2018).

16 Scarpelli, F., Mastropietro, T. F., Poerio, T. & Godbert, N. Mesoporous TiO2 thin films: State of the art. *Titanium Dioxide-Material for a Sustainable Environment* **508**, 135-142 (2018).

17 Muniz, E. *et al.* Synthesis and characterization of mesoporous TiO2 nanostructured films prepared by a modified sol–gel method for application in dye solar cells. *Ceramics International* **37**, 1017-1024 (2011).

18 Chan, C.-C., Chang, C.-C., Hsu, W.-C., Wang, S.-K. & Lin, J. Photocatalytic activities of Pd-loaded mesoporous TiO2 thin films. *Chemical Engineering Journal* **152**, 492-497 (2009).

19 Maksymovych, P., Voznyy, O., Dougherty, D. B., Sorescu, D. C. & Yates Jr, J. T. Gold adatom as a key structural component in self-assembled monolayers of organosulfur molecules on Au (1 1 1). *Progress in Surface Science* **85**, 206-240 (2010).

20 Daniel, M.-C. & Astruc, D. Gold nanoparticles: assembly, supramolecular chemistry, quantum-size-related properties, and applications toward biology, catalysis, and nanotechnology. *Chemical reviews* **104**, 293-346 (2004).
21 Jin, R. Quantum sized, thiolate-protected gold nanoclusters. *Nanoscale* **2**, 343-362 (2010).
22 Häkkinen, H. The gold–sulfur interface at the nanoscale. *Nature chemistry* **4**, 443-455 (2012).
23 Adhikari, S. G., Shamsaldeen, A. & Andersson, G. G. The effect of TiCl4 treatment on the performance of dye-sensitized solar cells. *The Journal of Chemical Physics* **151**, 164704 (2019).
24 Yu, J., Su, Y., Cheng, B. & Zhou, M. Effects of pH on the microstructures and photocatalytic activity of mesoporous nanocrystalline titania powders prepared via hydrothermal method. *Journal of Molecular Catalysis A: Chemical* **258**, 104-112 (2006).
25 Wang, G., Xu, L., Zhang, J., Yin, T. & Han, D. Enhanced photocatalytic activity of powders (P25) via calcination treatment. *International Journal of Photoenergy* **2012** (2012).
26 Al-Taweel, S. S. & Saud, H. R. New route for synthesis of pure anatase TiO2 nanoparticles via utrasound-assisted sol-gel method. *J. Chem. Pharm. Res* **8**, 620-626 (2016).
27 Mansur, H. *et al.* FTIR and UV-vis study of chemically engineered biomaterial surfaces for protein immobilization. *Spectroscopy* **16**, 351-360 (2002).
28 Nuengmatcha, P., Mahachai, R. & Chanthai, S. Adsorption of functionalized thiol-graphene oxide for removal of mercury from aqueous solution. *Asian Journal of Chemistry* **27**, 4167 (2015).
29 Senkevich, J. J., Mitchell, C. J., Yang, G.-R. & Lu, T.-M. Surface chemistry of mercaptan and growth of pyridine short-chain alkoxy silane molecular layers. *Langmuir* **18**, 1587-1594 (2002).
30 Rasalingam, S. *et al.* Influence of Ti–O–Si hetero-linkages in the photocatalytic degradation of Rhodamine B. *Catalysis communications* **31**, 66-70 (2013).
31 Chellappa, M., Thejaswini, B. & Vijayalakshmi, U. Biocompatibility assessment of SiO2–TiO2 composite powder on MG63 osteoblast cell lines for orthopaedic applications. *IET nanobiotechnology* **11**, 77-82 (2017).
32 Wu, J., Ling, L., Xie, J., Ma, G. & Wang, B. Surface modification of nanosilica with 3-mercaptopropyl trimethoxysilane: Experimental and theoretical study on the surface interaction. *Chemical Physics Letters* **591**, 227-232 (2014).
33 Ozin, G. Glycometallate surfactants Part 2: non-aqueous synthesis of mesoporous titanium, zirconium and niobium oxides. *Journal of Materials Chemistry* **9**, 1491-1500 (1999).
34 Kite, S., Sathe, D., Kadam, A., Chavan, S. & Garadkar, K. Highly efficient photodegradation of 4-nitrophenol over the nano-TiO 2 obtained from chemical bath deposition technique. *Research on Chemical Intermediates* **46**, 1255-1282 (2020).
35 Lal, M., Chhabra, V., Ayyub, P. & Maitra, A. Preparation and characterization of ultrafine TiO2 particles in reverse micelles by hydrolysis of titanium di-ethylhexyl sulfosuccinate. *Journal of materials research* **13**, 1249-1254 (1998).
36 Zhu, X. *et al.* The effect of heat treatment on the anatase–rutile phase transformation and photocatalytic activity of Sn-doped TiO 2 nanomaterials. *RSC advances* **8**, 14249-14257 (2018).
37 Bach, L. G., Islam, R., Jeong, Y. T., Park, C. & Lim, K. T. Synthesis of PS-g-TiO2 Nanocomposites through a Simple Method of Surface Initiated Radical Polymerization. *Molecular Crystals and Liquid Crystals* **568**, 162-169 (2012).
38 Lee, G., Lee, J. & Kang, C. Strong and sustainable chemical bonding of TiO 2 on nylon surface using 3-mercaptopropyltrimethoxysilane (3-MPTMS): analysis of antimicrobial and decomposition characteristics of contaminants. *Journal of Coatings Technology and Research* **16**, 1399-1409 (2019).
39 Zhang, G. *et al.* Enhanced photocatalytic activity of TiO2/carbon@ TiO2 core–shell nanocomposite prepared by two-step hydrothermal method. *Applied surface science* **311**, 384-390 (2014).
40 Krishnan, G. *et al.* Investigation of ligand-stabilized gold clusters on defect-rich titania. *The Journal of Physical Chemistry C* **121**, 28007-28016 (2017).

41 Anderson, D. P. *et al.* Chemically-synthesised, atomically-precise gold clusters deposited and activated on titania. *Physical chemistry chemical physics* **15**, 3917-3929 (2013).
42 Anderson, D. P. *et al.* Chemically synthesised atomically precise gold clusters deposited and activated on titania. Part II. *Physical chemistry chemical physics* **15**, 14806-14813 (2013).
43 Al Qahtani, H. S. *et al.* Aggregation behavior of ligand-protected Au9 clusters on sputtered atomic layer deposition TiO2. *The Journal of Physical Chemistry C* **121**, 10781-10789 (2017).
44 Al Qahtani, H. S. *et al.* Atomically resolved structure of ligand-protected Au9 clusters on TiO2 nanosheets using aberration-corrected STEM. *The Journal of Chemical Physics* **144**, 114703 (2016).
45 Ruzicka, J.-Y. *et al.* Toward control of gold cluster aggregation on TiO2 via surface treatments. *The Journal of Physical Chemistry C* **119**, 24465-24474 (2015).
46 Alotabi, A. S., Gibson, C. T., Metha, G. F. & Andersson, G. G. Investigation of the Diffusion of Cr2O3 into different phases of TiO2 upon Annealing. *ACS Applied Energy Materials* **4**, 322-330 (2021).
47 Alotabi, A. S. *et al.* Suppression of phosphine-protected Au 9 cluster agglomeration on SrTiO 3 particles using a chromium hydroxide layer. *Materials Advances* **3**, 3620-3630 (2022).

CHAPTER 6: Au_9 CLUSTERS DEPOSITED AS CO-CATALYSTS ON S-MODIFIED MESOPOROUS TiO_2 FOR PHOTOCATALYTIC DEGRADATION OF METHYL ORANGE.

6.1. Abstract

Au_9 nanoclusters (Au_9 NCs) were deposited onto S-functionalised mesoporous TiO_2 ($SMTiO_2$) to produce efficient photocatalysts for Methyl Orange (MO) dye degradation. The morphology, surface composition and size of the deposited Au_9 NCs of the catalyst was analysed. $SMTiO_2$ could adsorb more clusters with less Au_9 cluster agglomeration than unmodified $MTiO_2$. This finding is attributed to the thiol group's ability to form strong bonds with the Au_9 clusters. To study Au_9 NCs effect on dye degradation activity, the MO degradation reaction constants for $SMTiO_2$ nanoparticles (NPs) and Au_9 NCs decorated $SMTiO_2$ photocatalysts were studied and were 0.07 min^{-1} and 0.149 min^{-1}, respectively. Hence, it takes almost half the time to completely degrade MO using Au_9 NCs decorated $SMTiO_2$ photocatalysts compared to $SMTiO_2$ substrate. Results were analysed using the response surface methodology (RSM) to study the interaction between the reaction parameters.

6.2. Introduction

Water pollution is a growing concern due to its impact on human health and other living species. There are a variety of hazardous water contaminants, including dyes, heavy metals, and organic compounds. These contaminants are found in water for various reasons and need to be removed.[1, 2] For example, the dye manufacturing, textile, rubber, plastic, and cosmetics industries discharge toxic, carcinogenic, and nonbiodegradable dyes into nearby water bodies. These dyes threaten human health and aquatic life.[3] Traditional wastewater treatment methods do not effectively remove these contaminants from wastewater. The reason for this is that some chemicals, especially those with aromatic rings, are resistant to biological, photochemical, and chemical degradation. In addition, they generate dangerous by-products by oxidising, hydrolysing, or undergoing other chemical reactions of synthetic dyes containing wastewater, which are detectable wherever they are disposed of.[2, 4] Considering this, research has focused on developing efficient methods for removing or degrading such hazardous materials as dyes from wastewater. Dye degradation can be achieved through various processes, which photocatalysis systems are one of the most promising due to their high potential to ensure the full degradation of dyes. For this purpose, it is necessary to design robust and efficient photocatalytic systems focussing primarily on semiconductors and nanomaterials based on metal oxides, sulphides, and nitrides.[3, 5, 6]

TiO_2 is a valuable substance for the photocatalytic degradation of dyes. In addition to its remarkable optical and electronic characteristics, it exhibits exceptional photocatalytic efficacy when exposed to UV light and maintains strong chemical stability. It is also low in cost, biocompatible, and environmentally friendly compared to other nanometals and is highly used in different food, medical and cosmetic applications.[7] Absorption of photons with energy exceeding the band gap results in the generation of excited electrons in the conduction band and the formation of holes in the valence band. These photo-induced electron-hole pairs can then engage in oxidation and reduction reactions with various substances adsorbed on the surfaces of semiconductor particles. This is why they can completely break down organic pollutants and even mineralize them. However, the high recombination rate between photo-generated electrons and holes reduces the activity of photocatalytic systems.[5, 8]

The lifetime of excited electrons and holes can be improved by deposition of noble metals as co-catalysts onto TiO_2 leading to increased photocatalytic efficiency. Several studies have investigated how different noble metal loadings (Au, Ag, and Pt) affect the photodegradation of organic molecules on the surface of commercial TiO_2.[3, 9] The deposition procedures greatly affect the photocatalytic activity. It has been reported that when small particles of Pt are deposited on semiconductors, electrons are captured by Pt^0 and compete with the undesired recombination reactions of generated electrons and holes so that the noble metal deposited on the semiconductor surfaces can act as a sink to capture of photoinduced electrons.[10]

In a recent study, we used ligand-protected metal nanoclusters (NCs). The core of the clusters comprises from several to tens of metal atoms, and the outer shell consists of organic ligands protecting the core from agglomeration. NCs can be synthesised with high purity and a precise number of atoms forming the core. Besides the usual metal nanoclusters of Ag, Au, and Cu, the study of Au nanoclusters (Au NCs) has received considerable attention in recent decades. A correlation exists between the number of Au atoms in atomically precise Au nanoclusters and their photophysical properties[11]. The excellent suitability of Au nanoclusters as co-catalysts arises from their combination of a high specific surface area and a substantial quantity of unsaturated reaction sites, resulting in high catalytic efficiency and unique selectivity.[12]

A Au nanocluster (Au NCs) is typically less than 1.5 nm and thus of a size between small molecules and metal nanoparticles (NPs). Au NCs can have discrete energy levels and a variety of molecular-like characteristics, including high catalytic activity[13, 14] due to their small size comparable with the Fermi wavelength of electrons.[12, 15]

During the chemical preparation of Au NCs, stabilising ligands should be added to control the growth of Au NCs, prevent their agglomeration through metal-metal interactions, and ensure they are dissolved properly in the reaction media. Phosphine-ligated Au clusters are prepared using

triphenylphosphine (PPh_3) ligands as they allow the production of ultrasmall-size clusters with narrow size distributions.[16] Cluster reactivity and electronic structure can also be improved using phosphine ligands due to their unique steric and electronic features.[16, 17] Hence, catalytically active Au nanoclusters represented as $Au_n(PPh_3)_m$, including examples like $Au_{101}(PPh_3)_{21}Cl_5$ and $Au_9(PPh_3)_8(NO_3)_3$, have demonstrated their effectiveness in various chemical reactions, including hydrogenation of terminal alkynes into alkenes,[13] as well as oxidation of CO,[18] styrene,[19] and benzyl alcohol.[20]

Ligand removal via heat treatment is often necessary to allow for direct contact between the cluster core and substrate surfaces. This might be needed to access adsorption sites at the surface of clusters.[21] However, two effects may occur when support-immobilised clusters are heated at 200°C under vacuum. First, larger Au particles can form when the ultrasmall clusters aggregate together while still attached to the phosphine ligands due to their mobility. Second, a fraction of Au clusters displays Au–O bonds, probably to the oxygen of the TiO_2 surface. These bonds occur simultaneously with phosphine ligand loss and enhanced phosphorus oxidation.[22] Averting the first scenario is imperative since nanocluster features differ according to their size and, therefore, will change upon agglomeration. However, it has been reported that thermal treatment causes some amount of cluster agglomeration owing to the relatively weak interaction between Au and the metal oxide substrate allowing for the mobility of the deposited clusters.[23] Hence, controlling the attachment to the substrate surface and determining the cluster size is crucial for the efficiency of the photocatalytic systems for oxidation and reduction reactions.[16] It should be noted that enhanced loading levels of atomically precise Au nanoclusters onto the TiO_2 surface can also improve the photocatalytic efficiency.

To address these two issues crucial for increasing the photocatalytic efficiency, two different surface modifications have been applied to generate porous structures and to graft additional components onto the surface. Morphological modification to attract Au NCs to specific sites on the substrate surface results in reduced cluster mobility and subsequent agglomeration. Chemical modifications bind the clusters to the semiconductor surfaces more strongly.

Mesoporous TiO_2 has a large surface area with a high density of surface defects and a 3D connected pore network which both aid in avoiding Au clusters agglomeration.[24] This strategy follows similar recent attempts to enhance the adsorption of clusters by pre-treatment processes such as UV irradiation, sputtering, and heating to generate surface defects [25, 26]. Here, we use a different approach by generating active adsorption sites containing functional groups to which the Au clusters can strongly bind onto the $MTiO_2$ surfaces.

S-functionalisation is an appropriate chemical surface modification for attaching Au species to surfaces. The covalent bond between Au and S provides a robust but modifiable bond. Covalent bonds are formed between the S(sp3) hybrid orbitals and Au(6s) electrons, suggesting S undergoes sp3-type

hybridisation.[27] Au(d) electrons also play a significant role in the Au-S bond. In several studies the sulfhydryl (SH) functional groups in thiols (RSHs) are used to mediate these interactions.[15, 28]

In the present study, a facile method was utilised for synthesis of $MTiO_2$, along with modification of the surface with 3-Mercaptopropyltrimethoxysilane MPTMS and then Au_9 NCs deposition as the cocatalysts (Figure 6.1). We have also investigated how the surfaces and their (SH)-functionalisation can be effective to prevent the Au_9 NCs agglomeration and achieve a high loading level based on the relative ratio and size assessment of Au_9 NCs after deposition and annealing process by using the XPS analysis.

This study focuses on developing an efficient photocatalytic system and determining the parameters for the photodegradation of methyl orange (MO) using response surface methodologies (RSM) along with central composite designs (CCD) and python for analysing the photocatalytic reactions which have been widely applied in various engineering fields, such as water treatment processes.[29] Using this methodology not only minimises the number of experiments but also cuts down on the cost and time required to study the process parameters and their interactions.

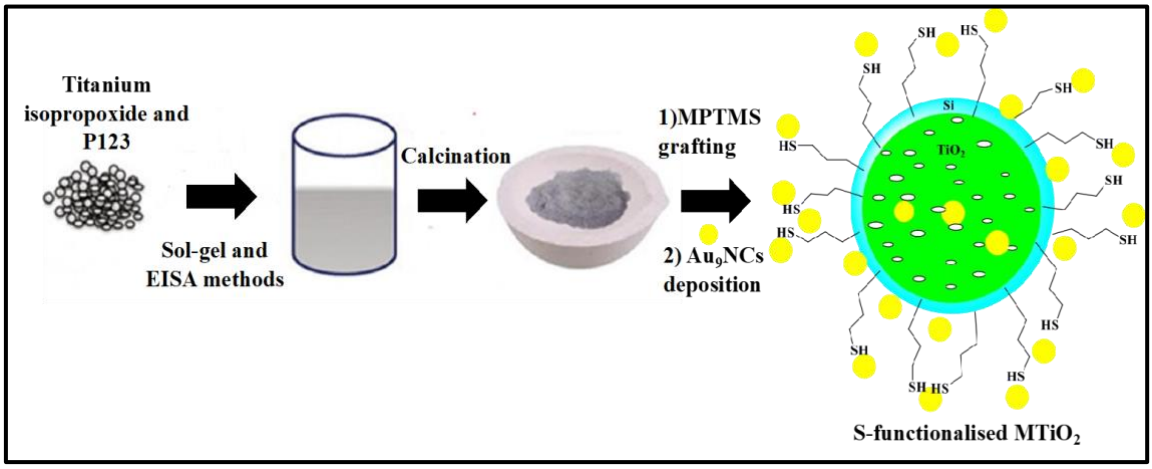

Figure 6.1. Au_9NCs/S$MTiO_2$ nanocomposites preparation procedure

6.3. Experimental Section

6.3.1. Materials

P123, absolute ethanol, titanium tetraisopropoxide (TTIP), (3-mercaptopropyl) trimethoxysilane (MPTMS), toluene anhydrous, HCl (37% w/w), AgCl, tetrachloroauric acid, triphenylphosphine, and $AgNO_3$ AR grade were purchased from Sigma Aldrich Co. All chemicals and solvents are used without further purification.

6.3.2. Sample Preparation

6.3.2.1. Preparation of $Au_9(PPh_3)_8(NO_3)_3$ nanoclusters:

Chapter 4 contains detailed information on the synthesis and characterisation of Au_9 NCs.

6.3.2.2. Preparation of the mesoporous TiO_2:

The process begins by dissolving the required amount of the triblock copolymer surfactant P123 in 12 g of absolute ethanol through 30 minutes of stirring. Following this, a solution containing 9.84 g (equivalent to 0.035 mol) of titanium tetraisopropoxide and 1.44 ml (equivalent to 0.046 mol) of HCl is introduced while vigorously stirring for 10 minutes. Next, the resulting solution is cast into a Petri dish, where it gels at 40°C in an open-air environment for 30 minutes. Afterward, it is left to dry under regular ambient conditions for 24 hours, which facilitates the crosslinking and oligomerization of the TiO_2 sol/gel precursor. Finally, the prepared samples undergo calcination at 400°C for 4 hours in the presence of air. This calcination process serves to entirely eliminate the polymeric surfactant, encourage the crystallization of TiO_2 into the anatase phase, and introduce interparticle mesopores.

6.3.2.3. Preparation of the S-functionalised mesoporous TiO_2 ($SMTiO_2$):

$MTiO_2$ nanoparticles (0.1 g) was dispersed in 5 ml toluene which had been before deoxidised by N_2 purging for 15 minutues, then 0.5 ml MPTMS was added. The mixture was heated under reflux at 110 °C for 8 h to make $SMTiO_2$. Nitrogen gas flow continued throughout the reaction. After completion of the reaction, products were centrifuged, and they were then rinsed with ethanol twice and dried at room temperature overnight.

6.3.2.4. Deposition of $Au_9(PPh_3)_8(NO_3)_3$ cluster onto the prepared surfaces:

In the preparation of Au_9 NCs solutions, the $Au_9(PPh_3)_8(NO_3)_3$ (1 mg, 4.63×10^{-6} mol) crystals were dispersed in approximately 2 ml of methanol and then stirred until completely dissolved. To remove water from nanoparticles and films, $SMTiO_2$ (10 mg) was placed under vacuum for one day. Then, 2 ml of methanol containing Au_9 cluster solution was added to the dried $SMTiO_2$, stirring with a magnetic stirrer for both 1 and 24 hours separately resulting in the yellow suspensions. In the following step, the off-white suspension was centrifuged, and the crude samples were placed under vacuum at room temperature for 5 hours to remove any residual methanol. To minimize the possibility of aggregation or degradation, the samples were placed in a vial, capped, and stored in the dark at 4 °C.

6.3.2.5. Heat treatment for removing the phosphine ligands:

The Au_9 NCs supported on $MTiO_2$ were applied to a silicon wafer using a drop-casting method. Subsequently, the sample was subjected to heating at 200°C under vacuum conditions for 10 minutes. Following this step, the sample was taken out of the chamber and allowed to cool down to room temperature under reduced pressure. The resulting material was stored in a light-free refrigerator at a temperature of 4°C.

6.3.2.6. Photocatalytic activity test:

To study the dye degradation experiments at laboratory scale, Au_9 NCs/SMTiO_2 nanocomposites were applied to degrade MO dye through photocatalysis by a set of experiments using the rotation function of a Vortex Fluidic Device (VFD) at low rotation speed for mixing purpose and equipped with two 10 W Hg lamps as sources for UV light (254 nm). This study is designed to determine the degradation efficiency as a function of three independent factors: A) the MO dye concentration (ppm), B) catalyst amount (mg), C) reaction time (min), as described in Table 6.1. A, B, and C are coded values of the MO concentration, catalyst amount, and time, respectively. Table 6.1 also presents three different coded and actual levels for each factor. To evaluate the relation between the factors, the coded levels from minimum (-1) to maximum (+1) amount are used to make them unitless and suitable to plot together.

Table 6-1. Experimental and coded levels of the selected factors.

Factor	**Unit**	**Code for each factor**	**Levels**			
			Coded levels	-1	0	+1
MO concentration	ppm	A	**Actual levels**	10	15	20
Catalyst amount	mg	B		1	1.5	2
Time	min	C		10	15	20

For this purpose, we used the central composite design (CCD) by using self-written Python codes (Ver. 3.10.7) using different libraries (numpy, pandas, pyDOE2, statsmodels, and matplotlib). Various amounts of the photocatalyst were added to 3 ml of dye solution and exposed to UV light for the selected time. The rotation speed was set to 900 rpm under constant UV light irradiation. To measure the MO concentration, a spectrophotometer (UV-Visible, PerkinElmer) was used at a maximum wavelength of 466 nm after separation of the suspended photocatalyst particles using centrifuge (12000 rpm for 10 mins). The MO degradation was calculated using the following formula (Equation 6.1).[30]

$$D(\%) = \frac{(C_0 - C_t) \times 100}{C_0} \qquad \text{Equation 6.1}$$

where, C_0, and C_t, are the initial concentration of MO (ppm), and the concentration at the time when the dye concentration was measured in the course of the photocatalysis experiment, respectively.

6.3.3. Modelling

6.3.3.1. Response surface methodology (RSM):

To ensure the statistical validity of the outcomes, the experiments were structured using a Central Composite Design (CCD), and the results were subjected to statistical analysis using Response Surface Methodology (RSM). In this design, as outlined in Table 6.2, three independent factors were chosen: reaction time, catalyst quantity, and MO dye concentration. The response variable selected to establish a mathematical relationship and describe interactions among these factors was the MO degradation efficiency. According to the CCD, a total of 15 experiments were conducted. (Table 6.2). A quadratic polynomial equation was used to evaluate the dependence of the response on several factors.

$$D = \beta_0 + \sum_{i=1}^{k} \beta_i X_i + \sum_{i=1}^{k} \beta_{ii} X_{ii}^2 + \sum_{i=1}^{k-1} \sum_{j=2}^{k} \beta_{ij} X_i X_j + \varepsilon \qquad i \neq j \qquad \text{Equation 6.2}$$

In the above equation (Equation 6.2), D is the predicted RSM response as shown in **Error! Reference source not found.** ε and k are the random errors and number of independent factors (k = 3), respectively. Xj and Xi are the input factors. β0, βi, βii, and βij are the constant, linear, quadratic, and interaction terms, respectively.

The adequacy of the proposed model was assessed through the analysis of variance (ANOVA) by testing P values (confidence level), coefficients of determination (R^2), and adjusted coefficients of determination (adj. R^2). After accurate curve fitting, equation 6.2 will be used to predict all the experimental points as presented in Table 6.2. As evidence showing our experiments and data evaluation have been conducted with a high precision, RSM predicted results are close to those achieved through the actual experiments presented in Table 6.2.

Table 6-2. Centre composite design with experimental and predicted responses

Factor 1	Factor 2	Factor 3	Response 1	RSM
A:Dye conc.	B:Cat. amount	C:Time	Experimental degradation	Predicted degradation
ppm	mg	min	%	%
10	1	10	62.90	63.93
20	1	10	50.11	50.26
15	1.5	10	77.97	76.00
10	2	10	80.04	80.69
20	2	10	73.15	73.28
15	1	15	70.29	69.23
10	1.5	15	87.23	85.17
15	1.5	15	81.22	83.88
20	1.5	15	72.88	73.61
15	2	15	89.86	89.59

10	1	20	80.06	80.26
20	1	20	64.88	64.56
15	1.5	20	91.16	91.79
10	2	20	97.79	97.97
20	2	20	89.23	88.53

6.3.4. Characterisation:

Detailed information for charactrisation methods has been reported in Chapter 2.

6.4. Results and discussion:

6.4.1. FTIR:

FTIR was used to investigate the surface of the (3-mercaptopropyl) trimethoxysilane (MPTMS) with the primary purpose of confirming whether MPTMS was successfully grafted onto the mesoporous TiO_2 ($MTiO_2$) to form S functionalised mesoporous TiO_2 ($SMTiO_2$) (Figure 6.2). For reference, FTIR was also applied to MPTMS and $MTiO_2$.

It should be noted that the strong peak appeared at 2360 cm^{-1} is related to CO_2 and is a common in spectra in the presence of normal atmosphere.

The broad peak centred at 3200-3500 cm^{-1} and a peak at 1650 cm^{-1} in the $MTiO_2$, and $SMTiO_2$ spectra (graph b and c in Figure 6.2) are attributed to water adsorbed to the surface and characteristic bending vibration of hydroxyl groups, respectively. Also, the broad peak centred at 400–700 cm^{-1} correspond to Ti-O-Ti bending vibration and Ti-O stretching modes [31] referring to the presence of TiO_2 nanoparticles (NPs) in our compounds.

The peaks at 2972 cm^{-1} and 2901 cm^{-1} in $SMTiO_2$ (graph c in Figure 6.2) are attributed to the C-H stretch mode of CH_3 and CH_2 groups which were also observed in MPTMS (graph a in Figure 6.2). This peak in graph c and a is an additional peak compared to graph b in Figure 6.2, confirming all organic compounds used as templates were removed during the formation of the $MTiO_2$ NPs.[32, 33] It is primarily due to the propyl group introduced with MPTMS during the functionalisation of the $MTiO_2$ surface.[34] The peaks at 1047 cm^{-1} and 885 cm^{-1} (graph c in Figure 6.2) are additional peaks compared to the spectrum of pristine $MTiO_2$ (graph b in Figure 6.2) and are attributed to the vibration band of Si–O–Si and Ti–O–Si groups, respectively, based on previous studies.[35] These peaks provide evidence for the attachment of MPTMS. Also, in graph a and c in Figure 6.2, a weak adsorption peak observed at 1408 cm^{-1} is attributed to the S–C stretching vibration of MPTMS[36]. In addition, a peak at 1240 cm^{-1}, which is observed in both graphs a and c in Figure 6.2, can be identified as the Si-C vibrational peak.[35] The peak appeared around 2560–2650 cm^{-1} can be assigned to the thiol groups.[32]

However, the small peak at 2560 cm^{-1} in MPTMS was shifted to 2650 cm^{-1} in $SMTiO_2$ which might be due to low weight percentage of MPTMS grafted to the $MTiO_2$ surface.[32, 33]

The stretching vibrational peak of C-O at 1189 cm^{-1} in graph a in Figure 6.2 which is also related to the Si-OCH_3 groups of MPTMS. In addition, the presence of this peak indicates that Si-OCH_3 groups were also hydrolysed to attach the MPTMS to the TiO_2 NPs surfaces during functionalisation process.

In summary, FTIR shows that MPTMS molecules were successfully grafted to the $MTiO_2$ surface to produce S functionalised mesoporous titanium oxide ($SMTiO_2$).

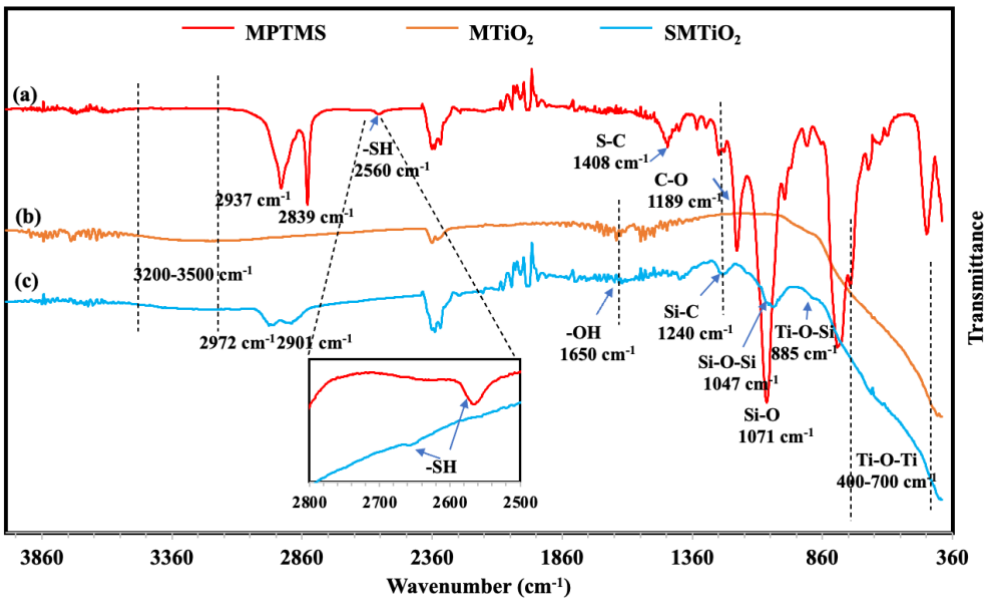

Figure 6.2. IR spectra of the (a) MPTMS, (b)$MTiO_2$, and (c) $SMTiO_2$.

6.4.2. BET surface area and pore distribution:

The result of the N_2 adsorption isotherms (BET and BJH Adsorption) recorded at 77 K for P25, $MTiO_2$ and $SMTiO_2$ are summarised in Table 6.3. The specific surface area was analysed using the conventional multipoint BET method. Additionally, a Barrett–Joyner–Halenda (BJH) model was employed to assess the size and volume distribution of the pores based on the adsorption isotherm.

The N_2 adsorption-desorption isotherms indicate that the calcined TiO_2 nanoparticles possess mesoporous characteristics, with an average pore size measuring 4 nm.

TiO_2 nanoparticles have a BET surface area of 117 m^2/g and a pore volume of 0.19 cm^3/g after preparation. In contrast, the surface area and pore volume of the latter particle, $SMTiO_2$, have been considerably reduced after functionalisation to 61 m^2/g and 0.1 cm^3/g, respectively. The pore size of all samples, however, did not change noticeably. It is likely that small TiO_2 crystals fuse together during the functionalisation resulting in a reduction in particle surface area. The result corresponds to what we can observe in the SEM images in Figure 6.4 as discussed later.

Table 6-3. BET and BJH Adsorption analysis from P25, $MTiO_2$, and $SMTiO_2$

Sample	P25	$MTiO_2$	$SMTiO_2$
Surface area(m^2/g)	79	117	61
Pore volume(cm^3/g)	0.15	0.19	0.1
Pore size(nm)	4.1	4.4	4.4

6.4.3. XRD:

Figure 6.3 (a and b) show the XRD pattern of $SMTiO_2$ and $MTiO_2$ samples, respectively, with the diffraction peaks indicated by red lines corresponding to the anatase phases. As the two spectra exhibit identical patterns, it indicates that the surface coating with MPTMS did not notably alter the crystal phase of the $MTiO_2$.

The grain size of 19.1± 0.1 nm was determined from the FWHM of the diffraction peak of the anatase (101) plane using the Scherrer equation and are shown in the supporting information (ESI†). The Scherrer formula gives the average or "apparent" size of the crystallites and not necessarily their actual size because polydispersity is not considered in the Scherrer formula. Partially crystalline powders and aggregated powders made up of smaller primary particles contribute to this phenomenon. In addition, the powder is typically not monodispersed but has a size distribution. The average grain size of both prepared $MTiO_2$ samples is summarised in Table 6.4 showing similar values for both types of samples, meaning that the modification of $MTiO_2$ surfaces has not affected the mean crystallite size.

Table 6-4. Mean crystallite size (nm)

Sample	Anatase (101)	Rutile
$MTiO_2$	19.1± 0.1	-
$SMTiO_2$	19.1± 0.1	-

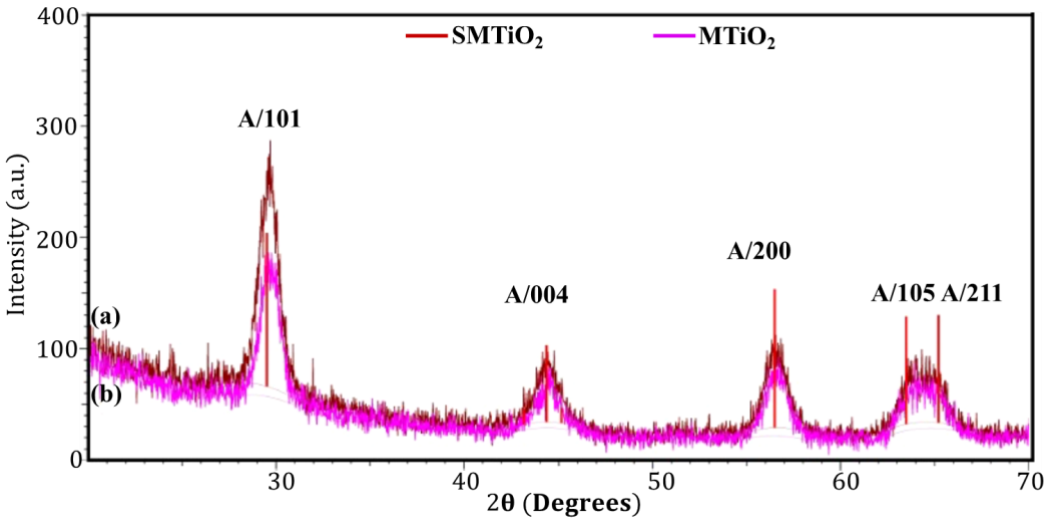

Figure 6.3. XRD patterns (Co Kα radiation) of (a) $SMTiO_2$ and (b) $MTiO_2$

6.4.4. SEM:

SEM images of the $MTiO_2$ and $SMTiO_2$ nanoparticles, shown in Figure 6.4 (a and b), provide information about particle sizes and morphology. As seen in Figure 6.4 (a), $MTiO_2$ with a rough surface forms aggregates with a size of hundreds of nanometres, showing a degree of polydispersity of shapes and sizes, especially after the functionalisation process making larger TiO_2 nanoparticles with a size of thousands of nanometres (Figure 6.4 b). The $SMTiO_2$ sample (Figure 6.4 b) has a significant difference in particle size and morphology compared to the non-functionalised sample (Figure 6.4 a), suggesting that MPTMS grafting onto TiO_2 surfaces results in large and agglomerated particles with a wide range of shapes, which may result in a reduced surface area which is consistent with BET result (Table 6.3).

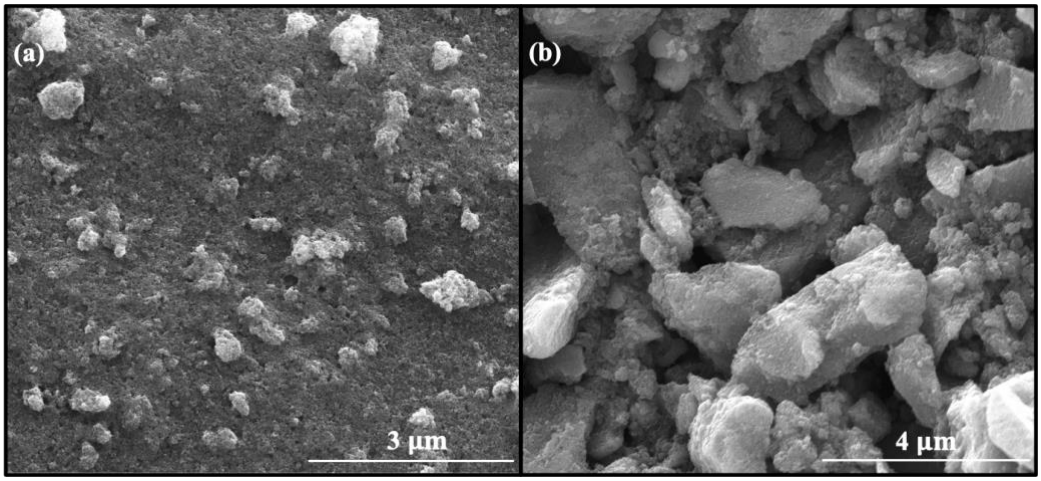

Figure 6.4. SEM images of (a) $MTiO_2$ and (b) $SMTiO_2$

6.4.5. NEXAFS:

In Figure 6.5 a, the Ti L-edge NEXAFS spectrum of the $MTiO_2$ and $SMTiO_2$ nanoparticles is compared with those of the reference samples including amorphous, anatase, and rutile TiO_2 samples. In addition, the S K-edge and L-edge x-ray absorption spectra (XANES) of $SMTiO_2$ NPs are presented in Figure 6.5 (b) and Figure 6.14 (S1), ESI†, respectively. Cysteine was also used as a reference.

As illustrated in Figure 6.5 (a), the Ti L-edge spectra of all samples exhibit two doublet peaks within the energy range of 455 eV to 470 eV. These peaks correspond to excitations of the Ti 2p levels into the vacant Ti 3d orbitals. These 3d orbitals are further divided into t2g and eg orbitals due to the presence of octahedral symmetry.[37] The overall pattern of all samples is the same, except for the region between 458.7 eV and 461.7 eV. Therefore, the Ti 2p L-edge spectra of the references and two prepared samples can be compared using the peaks at 460 eV and 461 eV. Both spectra related to the prepared samples show a larger peak at 460 eV than at 461 eV. Accordingly, the pattern of the graph in this region are similar to those in the anatase reference sample, indicating that the anatase phase is dominant in both samples, as confirmed by the XRD results (Figure 6.3).

The S K-edge and L-edge absorption spectra of $SMTiO_2$ nanocomposites and cysteine as the reference are presented in Figure 6.5 (b) and Figure 6.14 (S1), ESI†, respectively. The main peaks of the S K-edge and L-edge spectra appeared at 2472.6 eV and 165.9 eV indicated by the black arrow corresponds to the $S1s \rightarrow \sigma^*$ (S-C) transition[38]. $SMTiO_2$ nanocomposites and cysteine, measured at the same conditions, show a fairly similar pattern in both absorption spectra with the similar positions of the main peaks. Therefore, the features of the S group bonded to the C of MPTMS grafted onto the $MTiO_2$ surfaces are similar to those of the cysteine with the thiol group available for the attachment of the Au_9 clusters.

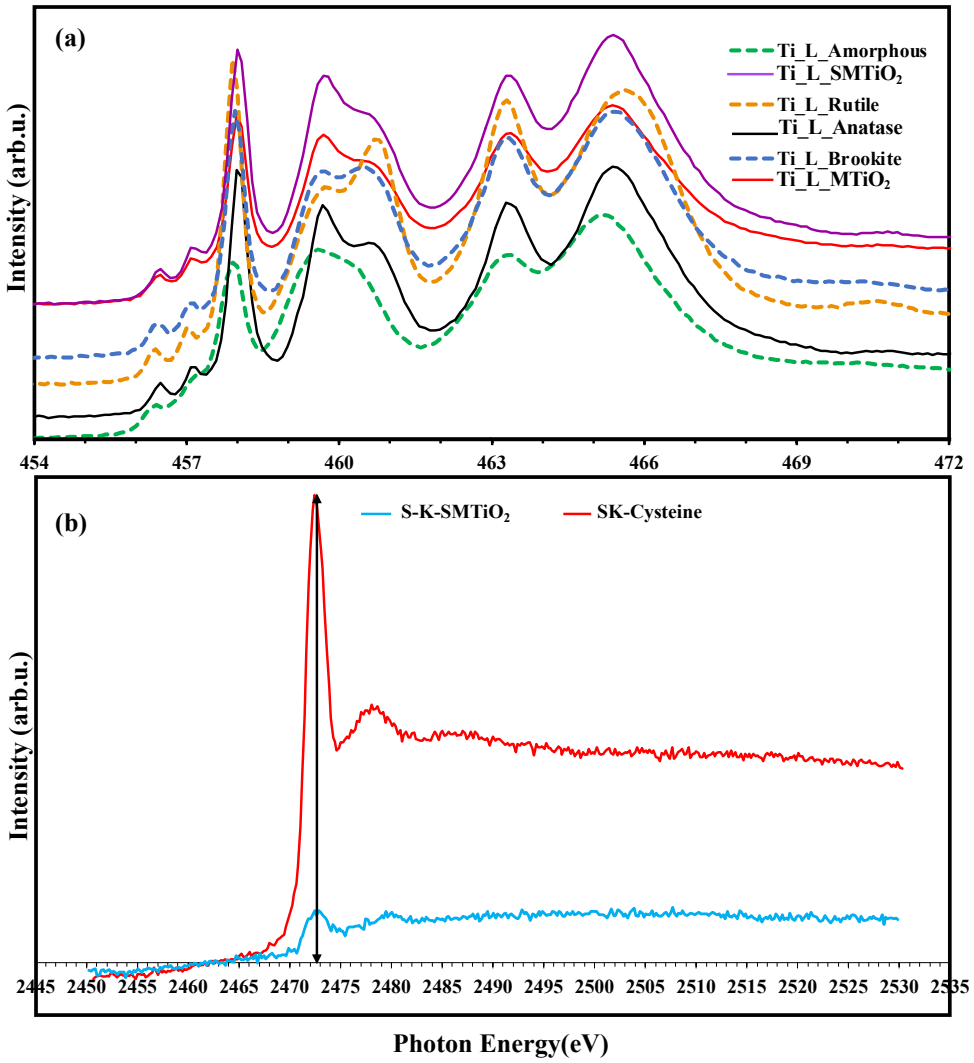

Figure 6.5. NEXAFS spectra at the Ti L-edge recorded on Amorphous TiO_2, Anatase TiO_2, Rutile TiO_2, $MTiO_2$, and $SMTiO_2$ (a) NEXAFS spectra at the S K-edge recorded on cysteine as a reference, and $SMTiO_2$ sample (b).

6.4.6. XPS measurements:

To further investigate how MPTMS is binding to titania, $SMTiO_2$ NPs was heated under UHV conditions at 10^{-8} mbar for 10 mins at 200 °C to remove hydrocarbon contaminations and adsorbed water from the surface. The sample was subsequently sputtered by 3 keV Ar^+ under UHV with a sputter dose of $1.2 \times 10^{+15}$ ions/cm^2 to remove approximately a few atom layers.[39] Subsequent to sputtering and heating, XPS was applied.

Through the XPS data in Figure 6.6, the changes in the elemental fractions of Ti, S, C, and O can be monitored after heating and sputtering. As shown in Figure 6.6, the amount of S and carbon after sputtering has declined, while that of Ti and O has been enhanced. Since only a few surface layers can be removed through sputtering, it may be concluded that the TiO_2 surface has been covered with an organic compound containing the S functional groups, indicating the existence of MPTMS

grafted onto the TiO_2 surface. When the amount of MPTMS is reduced after sputtering, it makes sense that the ratio of other elements, such as Ti and O, should be increased.

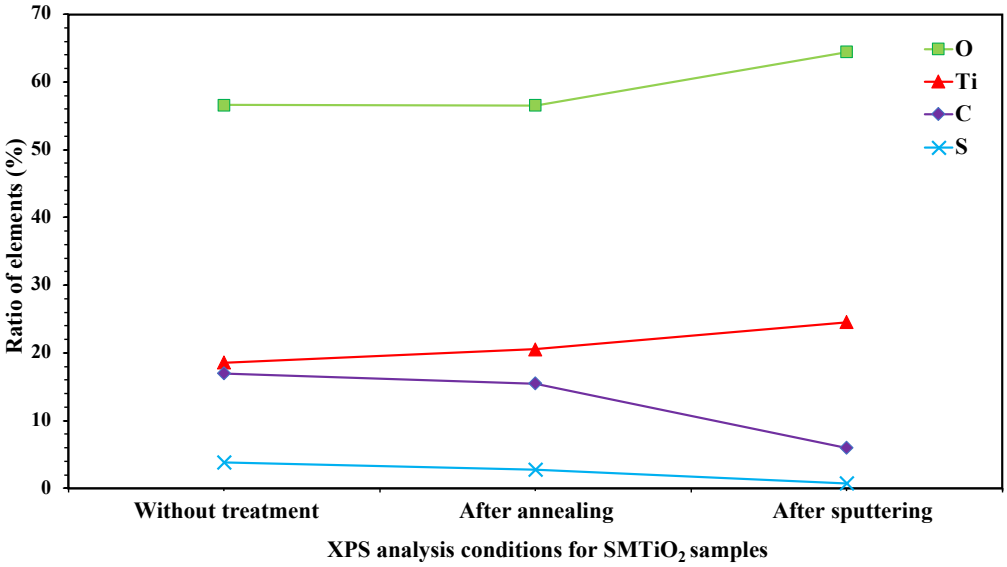

Figure 6.6. Investigation of changes in amount of the elements after heating and sputtering

Figure 6.7 depicts that the XP survey spectra of the prepared photocatalyst with a $MTiO_2$ semiconductor functionalised by MPTMS molecules and modified by Au_9 NCs. Six peaks are indexed to be the characteristic peaks: Ti2p, O1s, C1s, S2p, Si2p, and Au4f. Si and S are from MPTMS that are chemically bonded on the $MTiO_2$ surface. Au is from the Au_9 NCs bonded on the $SMTiO_2$ surface.

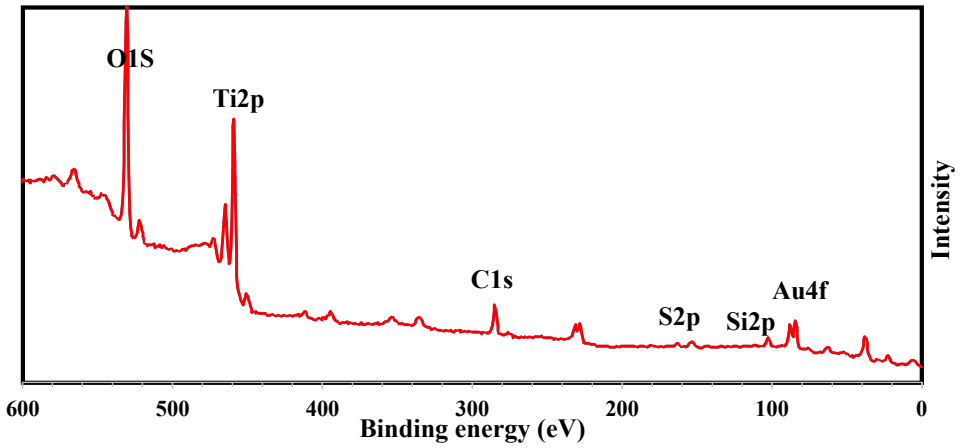

Figure 6.7. XPS survey of Au_9 NCs/$SMTiO_2$ nanocomposites

The size of the phosphine-ligated Au_9 nanoclusters (Au_9 NCs) is identified through the final state effect by analysing the Au 4f7/2 peak position and its full-width-half maximum (FWHM).[22, 26, 40] The peak position of non-agglomerated phosphine-ligated Au_9 NCs is usually in the range of 84.6–85.2 eV, with a FWHM of 1.7 ± 0.2 eV (HBP), while agglomerated Au_9 NCs are found at binding energies of 83.7–84.4 eV with a FWHM of 1.0 ± 0.2 eV (LBP).[21, 41]

In addition to investigating the agglomeration and relative intensity of phosphine ligated Au_9 NCs after their deposition onto the prepared $MTiO_2$ substrates, the effect of the surface modification with MPTMS, annealing treatment to remove the ligands, and variation of the deposition time on the size of Au_9 NCs was investigated through XPS (see Figure 6.8 a and b). A summary of the Au 4f peak positions and Au_9 NCs ratios deposited on $MTiO_2$ and $SMTiO_2$ surfaces is presented in Table 6.5.

In Figure 6.8 (a) and in Table 6.5 (entries 1 and 2), it can be found that after the deposition process of Au_9 NCs onto $MTiO_2$ and $SMTiO_2$, they have still preserved their size and have a similar Au $4f_{7/2}$ peak positions, 84.8 eV and 84.9 eV, respectively, showing the Au_9 NCs binding energies are found in the range of non-agglomerated clusters as described above referred to the high binding energy peaks (HBP). Peaks between 83.7 and 84.4 eV are referred to as low binding energy peaks (LBP) representing agglomerated clusters. In Figure 6.8 (b), the intensity ratio of Au_9 clusters on both substrates under the same conditions is compared. When the substrate changed from $MTiO_2$ to $SMTiO_2$, we observed that the ratio of Au_9 NCs increased more than three times (the Au_9 XPS intensity increased from 0.4 to 1.5 %). Thus, $SMTiO_2$ is more efficient than $MTiO_2$ in the adsorption of Au_9 NCs due to the presence of thiol functional groups grafted onto the surface.

In the next step, we investigated the effect of heat treatment on the size of Au_9 clusters and the ratio of agglomerated versus non-agglomerated clusters. After Au_9 NCs were deposited onto $MTiO_2$ NPs, an annealing treatment under vacuum was performed. According to Figure 6.8 (a and b) and the comparison between entries 1 and 4 of Table 6.5, the annealing process of the ligated Au_9 NCs/$MTiO_2$ nanocomposites resulted in a shift of the Au 4f peak from 84.8 eV to a lower binding energy of 84.1 eV (LBP) with the same relative intensities, 0.4 %. The interpretation of this finding is that the bond between $MTiO_2$ surface and Au_9 NCs is not strong enough to limit their mobility and consequently their agglomeration at elevated temperatures (see Figure 6.14 a (S2). ESI†). Thus, Au_9 NCs size was significantly increased after annealing. In contrast, when $SMTiO_2$ NPs was used as substrate with otherwise same conditions as the above (see entry 5 of Table 6.5), two Au species were found with two main $4f_{7/2}$ peaks at 84.6 and 84.2 eV and two different coverage at 1.1% and 0.3% relative XPS intensity for Au. This finding is interpreted as non-agglomerated and fully agglomerated Au_9 NCs, respectively (see Figure 6.14 (S2 b). ESI†). The result shows that $SMTiO_2$ NPs compared to $MTiO_2$, could not only increase the intensity ratio of deposited Au_9 NCs but could also improve the results related to the size of Au_9 NCs after annealing. Thus, $SMTiO_2$ substrates were generally more efficient at preserving the size and increasing the ratio of Au_9 NCs than $MTiO_2$. Accordingly, $SMTiO_2$ substrates were used to study deposition time effects on the size and relative intensity ratio of clusters.

By comparison between entries 2 and 3 of Table 6.5, it can be found that the binding energy (84.9 eV) of clusters deposited on $SMTiO_2$ nanoparticles stayed the same when deposition time for clusters was reduced from 24 h to 1 h. The relative intensity decreased from 1.5% to 0.6% due to the

reduction in exposure time of $SMTiO_2$ surfaces to Au_9 NCs. However, the results after annealing were most important (entry 6 in Table 6.5). There was no significant difference between the binding energy positions and intensity ratios of Au_9 NCs after annealing (85.1 eV with 0.6%, entry 6 in Table 6.5) and after deposition (84.9 eV with 0.6%, entry 3 in Table 6.5).

As a result, no agglomeration of Au_9 occurred with a decrease in Au_9 deposition time and its content attached to the surface. The most likely explanation is that with increasing loading of the sample surface the distance between clusters decreases and the probability of agglomeration during heating increases due to the increased mobility of the Au clusters at elevated temperatures.

In this regard, the Au_9 NCs/$SMTiO_2$ nanocomposites with an hour of deposition time were chosen for further analysis, including HRTEM and dye degradation studies.

Table 6-5. Study of binding energies and relative intensity of Au_9 NCs deposited on $MTiO_2$ and $SMTiO_2$ after deposition and annealing. (HBP and LBP means non-agglomerated and agglomerated clusters, respectively

Condition	Entry	Sample/Deposition time	HBP		LBP	
			Binding energy(eV)	Relative intensity(%)	Binding energy(eV)	Relative intensity(%)
After deposition	1	Au_9NCs@$MTiO_2$/24 h	84.8	0.4	-	-
	2	Au_9NCs@$SMTiO_2$ /24 h	84.9	1.5	-	-
	3	Au_9NCs@$SMTiO_2$/1 h	84.9	0.6	-	-
After annealing	4	Au_9NCs@$MTiO_2$/24 h	-	-	84.1	0.4
	5	Au_9NCs@$SMTiO_2$/24 h	84.6	1.1	84.2	0.4
	6	Au_9NCs@$SMTiO_2$/1 h	85.1	0.6	-	-

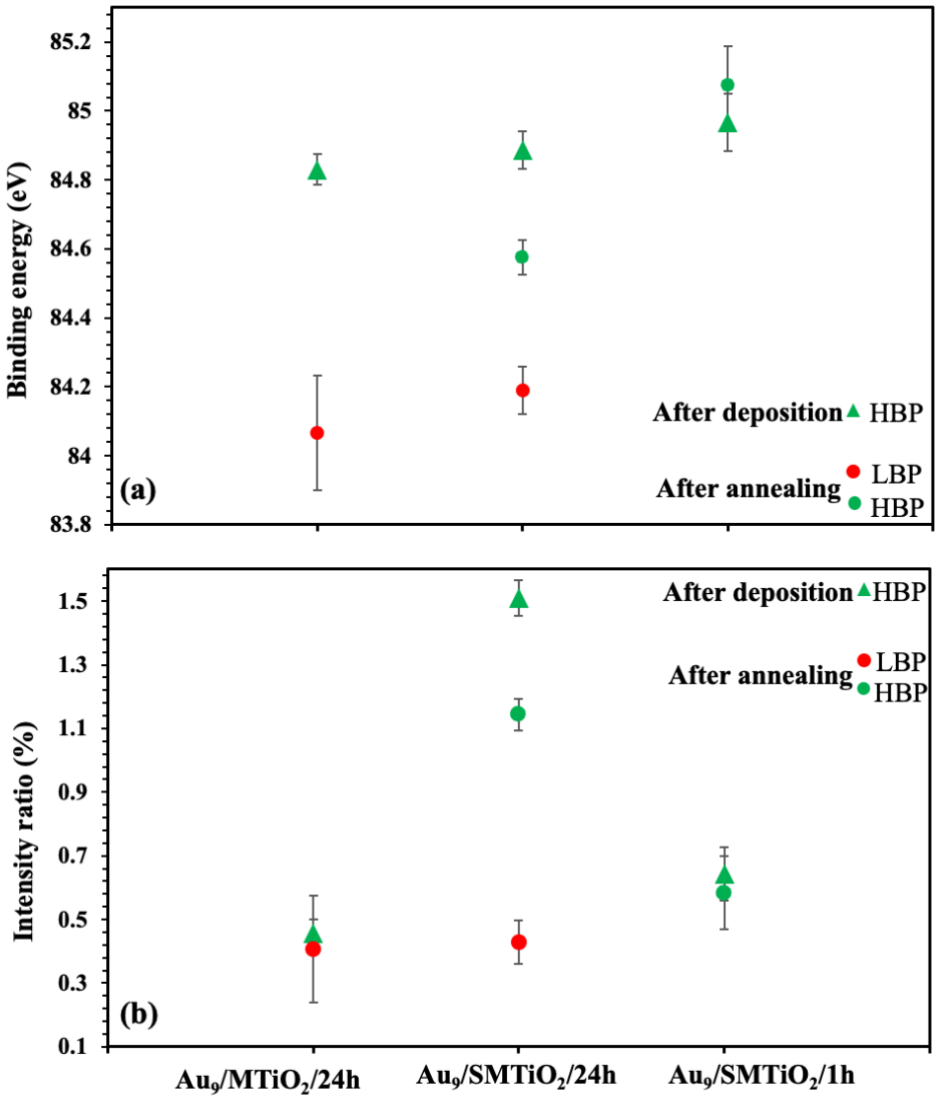

Figure 6.8. Investigation of Au_9 nanoclusters a) binding energies and b) ratios

6.4.7. HAADF-STEM images of Au_9 NCs deposited on $SMTiO_2$ and $MTiO_2$:

HAADF-STEM was used to investigate the size and morphology of $MTiO_2$ and $SMTiO_2$ photocatalysts, the size of Au_9 NCs onto the surface, and the distribution of Au_9 NCs across the surface. Figure 6.9 shows the STEM images of $MTiO_2$ and $SMTiO_2$ surfaces after phosphine ligated Au_9 NCs deposition (Figure 6.9 a, c) and annealing process to remove the ligands (Figure 6.9 b, d). Energy dispersive x-ray spectroscopy was used to determine their elemental compositions (see Figures S4, S6, S10, S13, ESI†) and the small bright spots were identified as Au_9 NCs.

The size distribution of $MTiO_2$ and $SMTiO_2$ NPs in Figure 6.9 is in the range of 5-10 nm, which is smaller than the crystallites size obtained by XRD (see Table 6.3). Furthermore, most of them have cubic-like shapes with a very narrow size distribution. The 3-6 nm dark patches distributed throughout the light grey background in Figure 6.9 are due to the presence of pores in the TiO_2 framework and are consistent with the results from BJH analysis in Table 6.3.

The size distribution of Au_9 NCs decorated on the $MTiO_2$ before heating shown in Figure 6.9 (a) varies from 0.7 to 1.2 nm with the average found at 0.8 ± 0.2 nm (see Figures S5, S15 a, ESI†), while the size of Au_9 NCs on $MTiO_2$ after heating shown in Figure 6.9 (b) are 2.0 nm to 5.0 nm with the average found at 3.5 ± 2.0 nm (see Figures S8, S15 b, ESI†). The enhancement in size is attributed to agglomeration of the Au_9 clusters upon heating to remove the ligands. This is also consistent with the XPS data in Figure 6.8 (a) and entries 1 and 4 of Table 6.5.

The size of the Au_9 NCs decorated on $SMTiO_2$ before heating in Figure 6.9 (c) varies from 0.9 to 1.5 nm with the average found at 1.2 ± 0.3 nm (see Figures S11, S15 c, ESI†), and the size of the Au_9 NCs on $SMTiO_2$ after heating in Figure 6.9 (d) varies from 0.9 nm to 1.4 nm with the average found at 1.1 ± 0.2 nm (see Figures S14, S15 d, ESI†). The lack of significant change in size indicates no agglomeration occurred upon heating to remove the ligands due to the presence of thiol groups. According to the EDX data, they have been uniformly grafted onto the $SMTiO_2$ surfaces allowing the highly loaded Au_9 NCs to be dispersed more uniformly across the surface compared to $MTiO_2$ (see Figures S10, S13. ESI†).

Evidence from Table XPS data (6.5) in entries 1 and 3 also suggests that the substrates host similar-sized Au NCs with similar binding energies. A comparison of Au_9 binding energies in Table 6.5 entries 1 and 4 indicates that the Au_9 binding energy was significantly decreased by heat treatment, meaning agglomeration of Au_9 NCs has occurred. Table 6.5 entries 3 and 6 show that by changing the substrate from $MTiO_2$ to $SMTiO_2$, no significant changes and subsequently no aggregation of the clusters was observed after annealing.

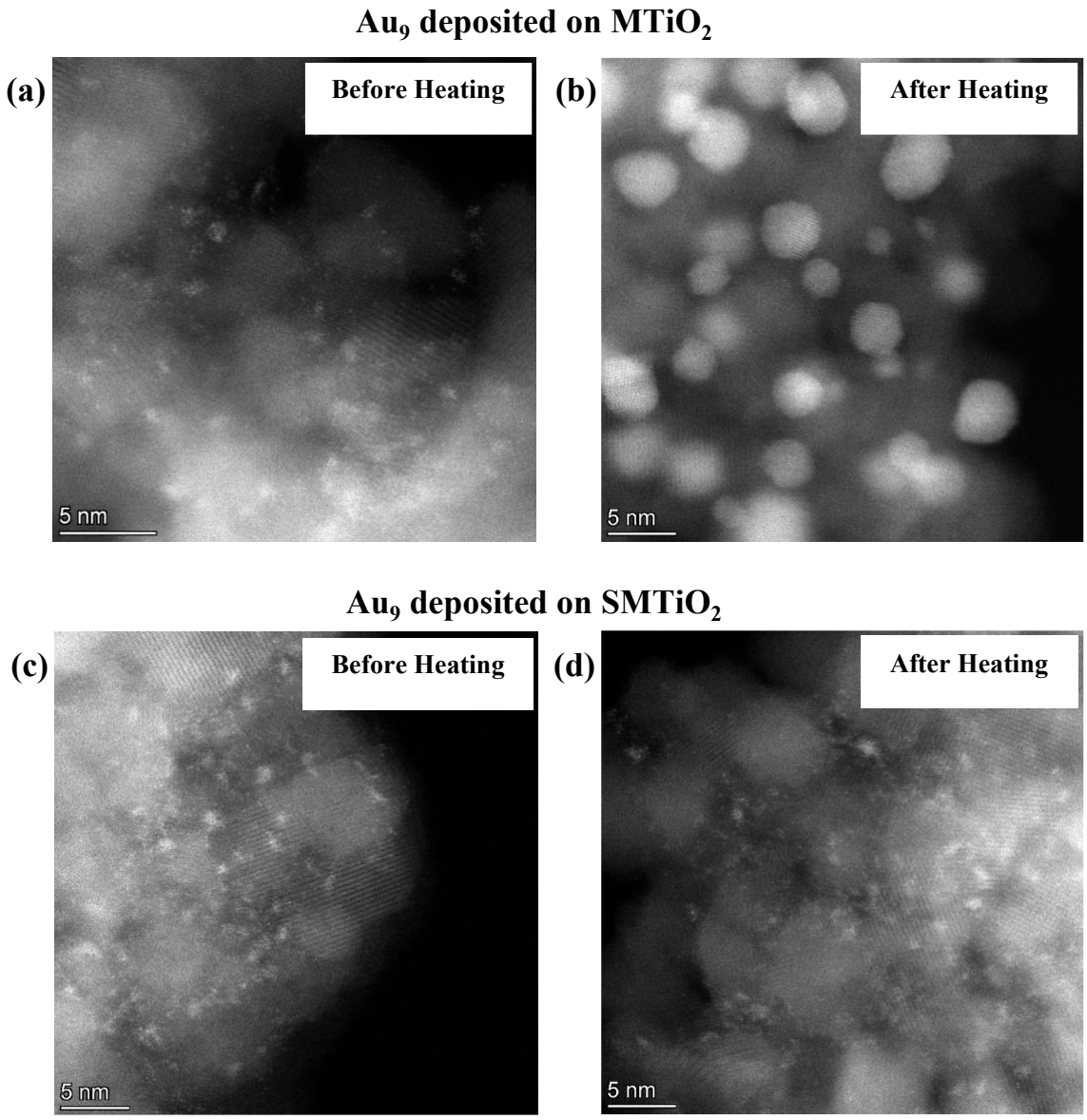

Figure 6.9. HRTEM images of Au_9 deposited on photocatalyst substrates before and after heating to remove ligands from Au_9. Image a) Au_9 on $MTiO_2$ before heating, b) Au_9 on $MTiO_2$ after heating, c) Au_9 on $SMTiO_2$ before heating, and d) Au_9 on $SMTiO_2$ after heating. The

6.5. Photocatalytic activity evaluation of Au_9 NCs/$SMTiO_2$ nanocomposites:

In Figure 6.10 (a), the MO degradation is presented for $SMTiO_2$-supported Au_9 NCs photocatalysts and $SMTiO_2$ nanoparticles. Also, the result for the dye degradation without catalyst under UV irradiation was plotted as a control. The experimental data for degradation were shown with markers and their trends over time are presented using solid lines.

Through this experiment, the degradation of 3 ml of 15 ppm MO dye solution was monitored over time using 1.5 mg of each catalyst under the constant UV irradiation at room temperature. In (Figure 6.10 a), it was observed that the colour of the suspension completely disappears within less than 25 mins in the presence of Au_9 NCs/$SMTiO_2$ photocatalysts while the same was found after

around 70 minutes for the $SMTiO_2$ NPs. However, the colour of the solution never disappeared, even after 3 hours, when the UV light was used for MO dye degradation without any photocatalysts. As a result, the degradation process was significantly higher for $SMTiO_2$-supported Au_9 NCs photocatalysts compared to $SMTiO_2$ NPs and UV exposure only.

As can be seen in Figure 6.10 (b), the experimental results can be fitted with a first-order reaction with the reaction constants of 0.149, 0.0702, and 0.004 min^{-1} for Au_9 NCs/$SMTiO_2$, $SMTiO_2$, and control (only under UV), respectively. The high amount of the reaction constant (0.149) obtained for the dye degradation catalysed by Au_9 NCs/$SMTiO_2$ nanocomposites shows how active the prepared photocatalysts can be, in comparison with other photocatalysts. Finally, the $R^2 \sim 0.99$ for all plots reveals accurate reactions.

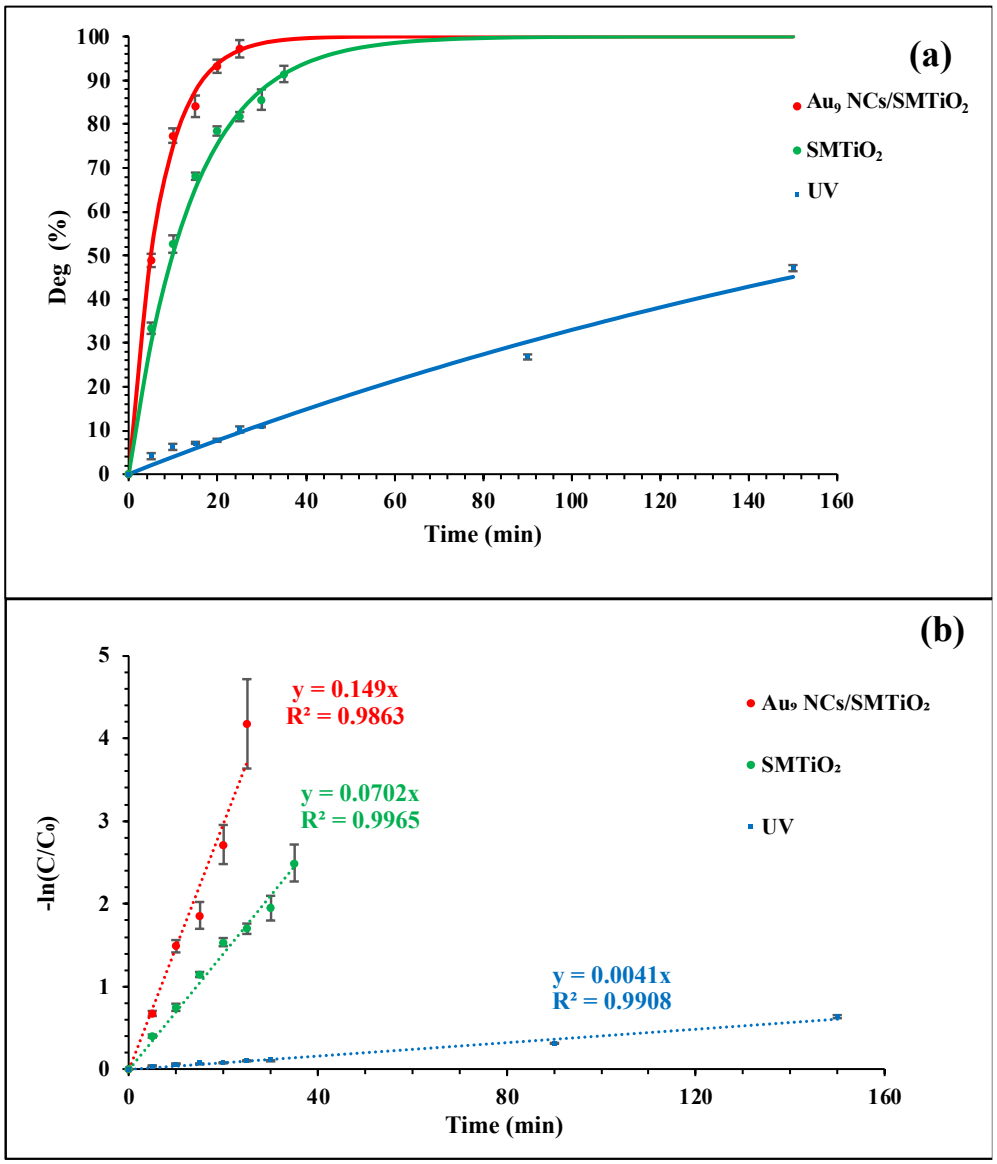

Figure 6.10. (a) MO dye degradation efficiency and (b) kinetic assessment of the reaction based on -ln (C/C_0) over time using Au_9 NCs/$SMTiO_2$ nanocomposites, $SMTiO_2$ and UV.

6.5.1. Response surface methodology analysis (RSM):

A statistically significant analysis of RSM was carried out using ANOVA (Analysis of Variance). Table 6.2 shows the extensive range of MO dye degradation (from 50.11 to 97.79 %). According to Equation 6.2, curve fitting, and ANOVA were done using the statsmodels library of the Python. The coded form of the quadratic polynomial model implies communication between factors and response (Equation 6.3).

$$\text{Degradation (\%)} = 83.881-5.777\times A+10.183\times B+7.895\times C+1.565\times A\times B-0.508\times A\times C+0.238\times B\times C-4.492\times A^2-4.472\times B^2+0.018\times C^2 \quad \text{Equation 6.3}$$

Here A, B, and C are the selected codes for the MO concentration, catalyst amount, and time respectively. The coded values for minimum, middle, and maximum actual values are -1, 0, and +1, respectively. To access the relation between the factors, the coded levels from minimum (-1) to maximum (+1) amounts are used to do curve fitting and statistical analysis without considering effects of order magnitude and units of the factors.

Table 6.6 presents the statistical results showing that the model is significant due to the low p-value ($0.000<0.05$). P value can be considered stand alone as the best decision parameter to check if the model is significant or not. Finally, the $R^2=0.991$ and adjusted $R^2=0.975$ reveals that the model is very accurate. Refer to Table 6.2, the predicted data closely match the experimental data, demonstrating that the suggested model (Equation 6.3) effectively describes and navigates the design space.[42]

Table 6-6. Analyse of variance results for the quadratic model and the significance of RSM model.

Dep. Variable:	Degradation	R-squared:	0.991
Model:	OLS	Adj. R-squared: 0.975	
Method: Squares	Least	Prob (F-statistic):	0.000

	coef	std err	t	P value
const	83.881	1.062	78.961	0.000
A	-5.777	0.625	-9.243	0.000
B	10.183	0.625	16.293	0.000
C	7.895	0.625	12.632	0.000
AB	1.565	0.699	2.240	0.075
AC	-0.508	0.699	-0.726	0.500
BC	0.238	0.699	0.340	0.748

A^2	-4.492	1.233	-3.644	0.015
B^2	-4.472	1.233	-3.628	0.015
C^2	0.018	1.233	0.015	0.989

Figure 6.11 shows perturbation plots to analyse the certain effect of three factors (reaction time, catalyst amount, and MO dye concentration) on dye degradation. To plot each of these factors, one factor is varied from -1 to +1 coded values or from its minimum to maximum relevant actual levels, while the other factors were set to their centre point or their middle-coded values (zero).

represents all coded and actual values for each factor. At the centre point, the dye concentration is 15 ppm, the catalyst amount is 1.5 mg, and the time is 15 minutes. Based on this plot, each factor is perturbed from its centre point to observe the effect of each factor on the response.

According to Figure 6.11, the sharp curvature in the plot for factors A (MO dye concentration) and B (catalyst amount) in comparison with factor C (reaction time) shows that dye degradation is very responsive to these two factors. In Figure 6.11, the relevant plot for factor C shows that the degradation ratio increases linearly over time from 10 to 20 mins or its -1 to +1 coded values as the trend is linear and ascending but since its slope is constant, the change in the degradation trend is not sensitive to time. Also, it is in agreement with Table 6.6 data that the p-value for C^2 (0.989) is much higher than the 0.05 confidence level and is not significant.

In Figure 6.11, the plot for factor B shows that the catalyst amount trend ascends, and its slope declines after the centre point. Although the degradation ratio increases with the catalyst amount from 1 to 2 mg, further catalyst addition can negatively impact the degradation rate after its centre point as a critical point in the catalyst amount is reached. It might be due to the accumulation of photocatalyst nanoparticles and the loss of their active sites. The changes in B plot behaviour can also be observed in Table 6.6 as the P-value for parameter B^2 is 0.015 and significant. Therefore, factor B changes can significantly affect the degradation trend.

To study factor A, it should be noted that the plot slope decreases slightly with increasing dye concentration from 10 to 15 ppm or its -1 to 0 coded values. Then, it declines sharply from the centre point onwards. It means that although increase of dye concentration can reduce dye degradation, its effect can be increased after the centre point. It might be due to the absorption of a maximum amount of ultraviolet light by dye molecules instead of the catalyst particles. Essentially, it serves as a barrier that prevents light from reaching the catalyst surface. According to **Error! Reference source not found.**, the P-value for parameter A^2 is 0.015, which is also significant.

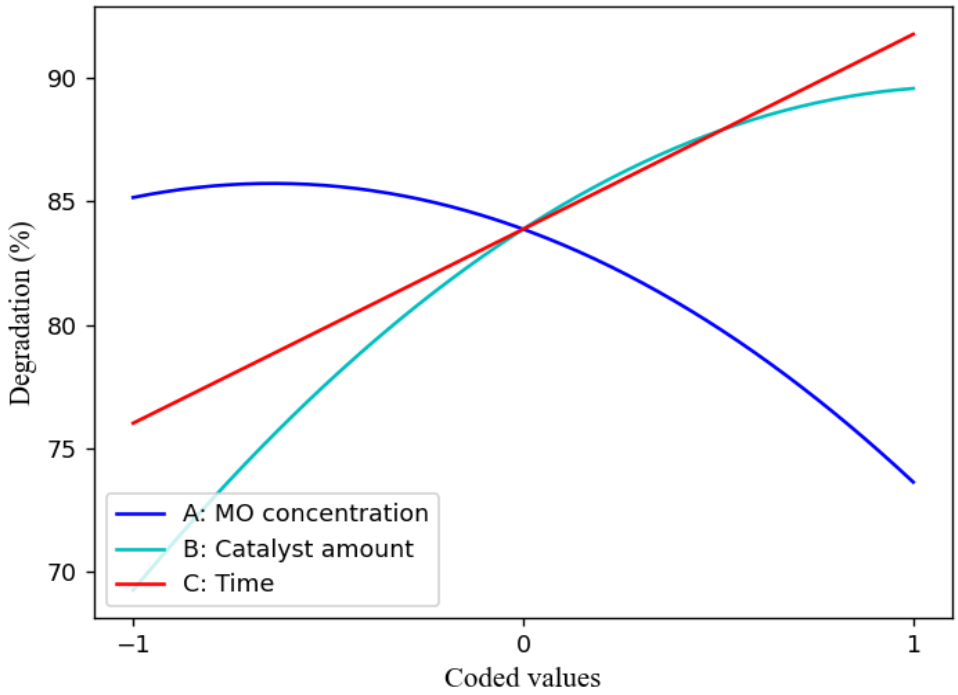

Figure 6.11. Perturbation plot of each process factor (A: MO concentration, B: catalyst amount, and C: time).

Figure 6.12 (a-c) portrays the impact of different factors on the response (degradation ratio) through 3D plots. In each of these plots, two factors are altered across their full range from minimum to maximum actual values, while the third factor remains fixed at its intermediate level. Changing the colour from dark blue to yellow is used as a mark to show the response changes. Dark blue and yellow have been placed in the lowest and highest levels of degradation ratio, respectively, considering the effect of relative factors.

Figure 6.12 (a) indicates the interaction of two factors, A and B, MO concentration and the catalyst amount, respectively, on the degradation ratio at a constant time (15 min), as factor C. It also shows that by increasing the catalyst amount from 1 to 2 mg, the degradation ratio is increased. These plots demonstrate that increasing the amount of catalyst can neutralise the effect of high concentration of MO dye due to the increased probability of UV light collision with the photocatalyst particles. However, the effect of increasing the amount of catalyst at low dye concentration (10 ppm) is more than at a high concentration (20 ppm) as the slope of the relevant point (yellow area) is in the highest possible place. Increasing the catalyst amount enhances the number of active sites required for the reaction, but after increasing the MO dye molecules in the solution, they may compete to absorb the UV light. Because the amount of MO dye molecules in high concentrations is much more than the threshold point, most of the UV light can be absorbed by dye molecules instead of the photocatalyst surfaces, reducing the formation of electron and hole charges.

Figure 6.12 (b) has been plotted by considering the interaction between factors A and C, MO concentration and time on the degradation ratio at a constant amount of photocatalyst (1.5 mg), as

factor B. It shows that the dye degradation ratio linearly increases over time while it decreases over dye concentration at a constant catalyst amount. It means that to neutralise the negative effect of the high MO concentration, the reaction time can be modified. In contrast, to save energy and time, it is better to use a low concentration of dye. However, in the case of keeping the amount of catalyst constant, the best result is achieved once the maximum time and the minimum dye concentration are selected as the conditions for the large-scale reactions.

Figure 6.12 (c) shows the interaction of two factors B and C, catalyst amount and time, respectively, on the degradation ratio at a constant MO concentration (15 ppm). It shows that when a minimum amount of catalyst (1 mg) is used for the reaction, even by increasing the time, the result is placed in the blue area and is not worth mentioning yet. However, when applying moderated or maximum catalyst amounts, the result is significant even using the minimum time. It means that the effect of catalyst amount on the degradation ratio is much higher than that of time, and it can play an important role in controlling the efficiency. According to Figure 6.12 (c), the simultaneous increase of reaction time and catalyst amount shows the best result for the degradation ratio near 100 % degradation by creating a suitable and enough interaction between UV light and active sites on photocatalyst surfaces to generate enough charge carriers to interact with dye molecules. Also, fewer electron and hole charges are produced to react with MO molecules at a lower catalyst amount, and the dye degradation is thus reduced. However, in the middle range of catalyst amounts, time can play a significant role in achieving high efficiency. As a result, to monitor the reaction at a larger scale, engineers can decide which changes are more reasonable to implement according to the price of energy and materials used for the fabrication of the photocatalysts.

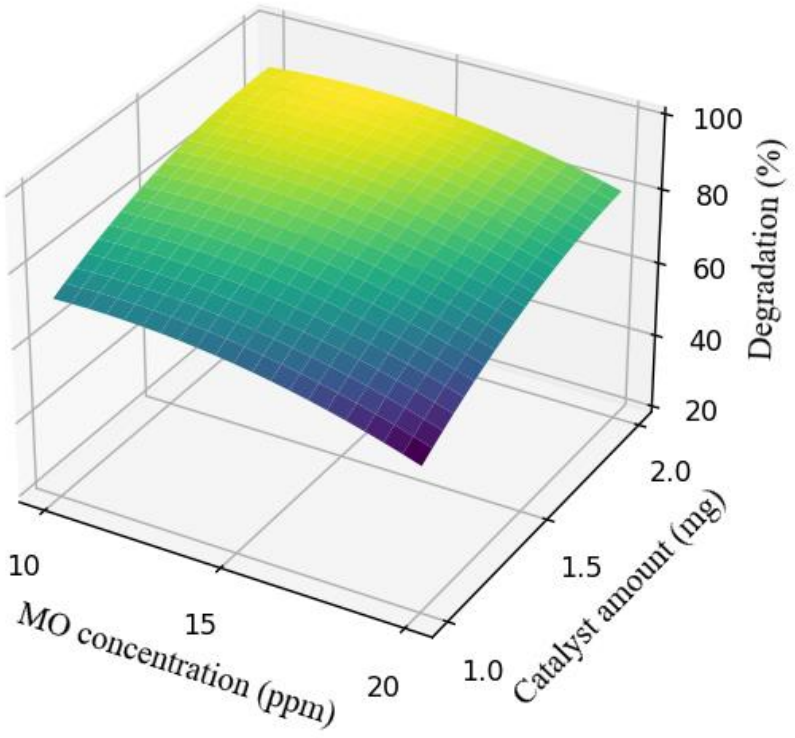
100
80
60
40
20
Degradation (%)
10
15
20
MO concentration (ppm)
1.0
1.5
2.0
Catalyst amount (mg)

(a)

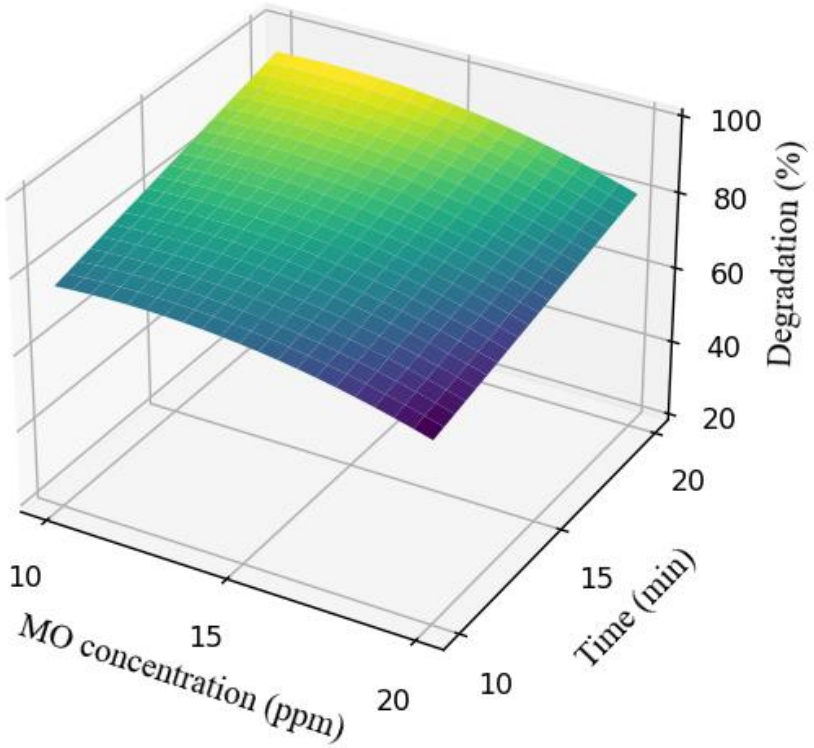
100
80
60
40
20
Degradation (%)
10
15
20
MO concentration (ppm)
10
15
20
Time (min)

(b)

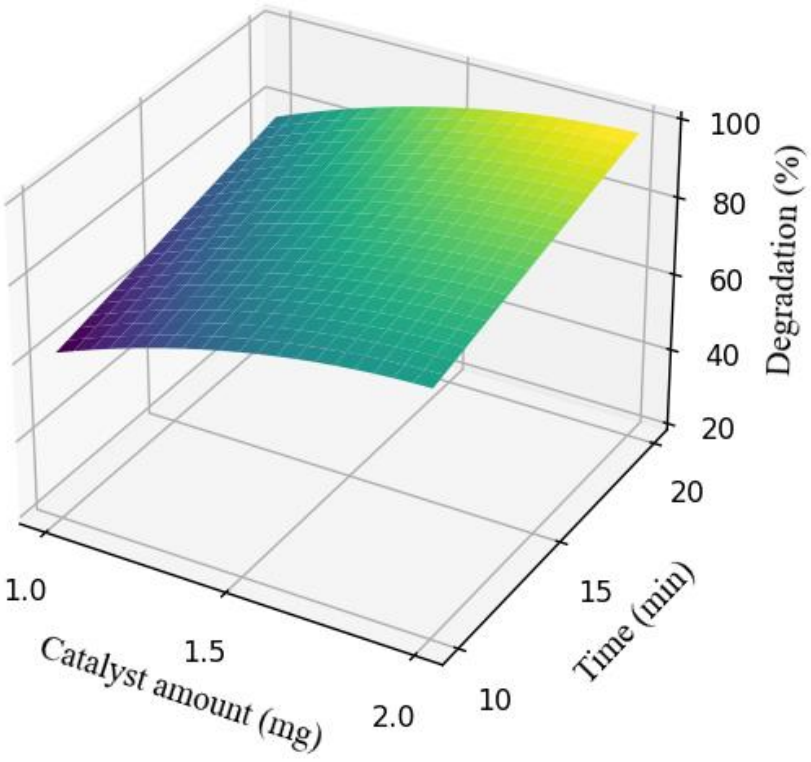

(c)

Figure 6.12. 3D response surface plots of dye degradation rate in terms of (a) MO dye concentration (ppm) and catalyst amount (mg) (b) reaction time (min) and MO dye concentration (ppm), and (c) catalyst amount (mg) and reaction time (min).

6.5.2. Characterisation of Au_9NCs/SMTiO_2 photocatalyst after dye degradation by XPS

The MO dye solution, including the dispersed photocatalysts, was centrifuged after finalising the reaction and decanted the mother solution. The precipitated solids were then washed two times with deionised water and ethanol and after being dried, were characterised by XPS. According to Figure 6.13, the Au_9 NCs high-resolution XPS result showed that the Au_9 biding energy after the reaction (84.5 eV) still stayed at the range of nanoclusters features. Therefore, no significant agglomeration has occurred during the photocatalytic dye degradation, and it can be reused in the second cycle.

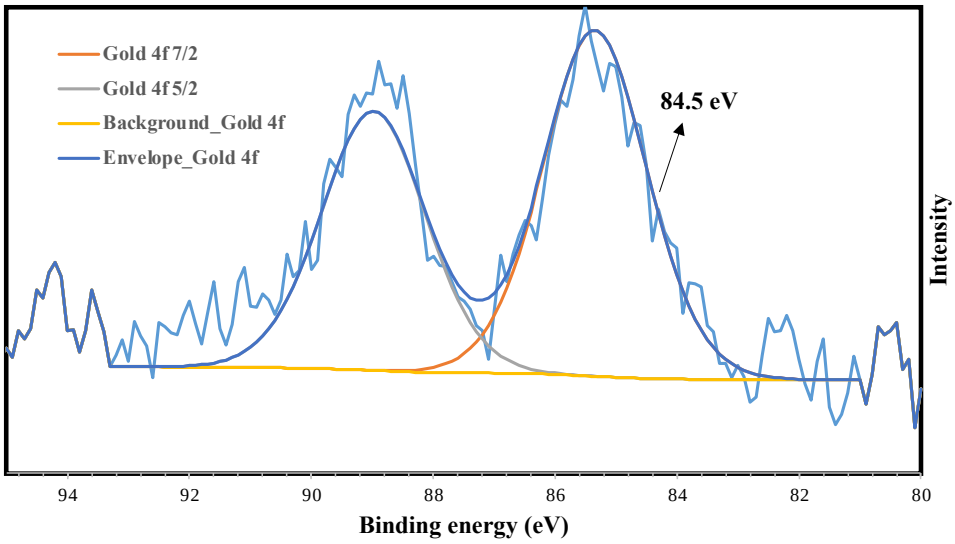

Figure 6.13. High resolution XPS analysis of Au_9 NCs after dye degradation reaction.

6.6. Conclusion:

The results of XPS and HRTEM analyses revealed that morphologically and chemically modified TiO_2 nanoparticles represent a promising substrate to adsorb a high level of non-agglomerated Au_9 NCs even after heat treatment. To produce an efficient photocatalysis system, the MPTMS molecules were first grafted onto the $MTiO_2$ surfaces, and Au_9 NCs were then deposited onto SH functionalised $MTiO_2$ nanoparticles and heated to remove the ligands bonded to the Au_9 core. According to our best knowledge, the photoactivity of the prepared catalysts depends on the size and loading level of Au_9 NCs. Therefore, making a porous structure was our first strategy to avoid cluster mobility and agglomeration. However, when heat treatment was utilised, it was found that the binding between clusters and $MTiO_2$ surfaces was not strong enough at the enhanced temperature, resulting in agglomeration. Therefore, the second strategy, S functionalisation, was applied to improve the $MTiO_2$ surface to gain our aim that was to preserve the Au cluster sizes even after annealing. S groups formed stronger complexes between Au_9 NCs and $MTiO_2$ substrates, reducing the extent of agglomeration during annealing. Also, BET and XRD were used to analyse the porosity status and crystallinity size and phase of the prepared substrates. The anatase phase of TiO_2 exhibits superior photoactivity compared to other phases. NEXAFS, FTIR, and sputtering methods proved that S functionalisation was successfully performed. The photoactivity of the prepared photocatalysts, $Au_9NCs/SMTiO_2$, was tested in methyl orange (MO) dye degradation. The MO degradation was monitored at different dye concentrations, times, and catalyst amounts based on the central composite design and the results, along with the effects of parameters and their interaction on MO degradation, were discussed using response surface methodology (RSM).

6.7. Supplementary Section:

The relevant information for each section has been reported in the main context.

6.7.1. Scherrer's equation:

Particle Size = (0.9 x λ)/ (d cos θ)

λ = 1.79 Å (in the case of Co Ka1)

Θ = 2θ/2

d = the full width at half maximum intensity of the peak (in Rad)

To convert from angle to rad

Rad = (22 x angle) / (7 x 180) = angle x 0.01746

$MTiO_2$ $\tau = \frac{0.9x1.79Å}{(\frac{22*0.5angle}{7*180}=0.00873\text{rad})\cos 29.6/2} = 190.87\ Å =$ 19.09 ± 0.1 nm

$SMTiO_2$ $\tau = \frac{0.9x1.79Å}{(\frac{22*0.5angle}{7*180}=0.00873\text{rad})\cos 29.7/2} = 190.91\ Å =$ 19.09 ± 0.1 nm

6.7.2. NEXAFS analysis:

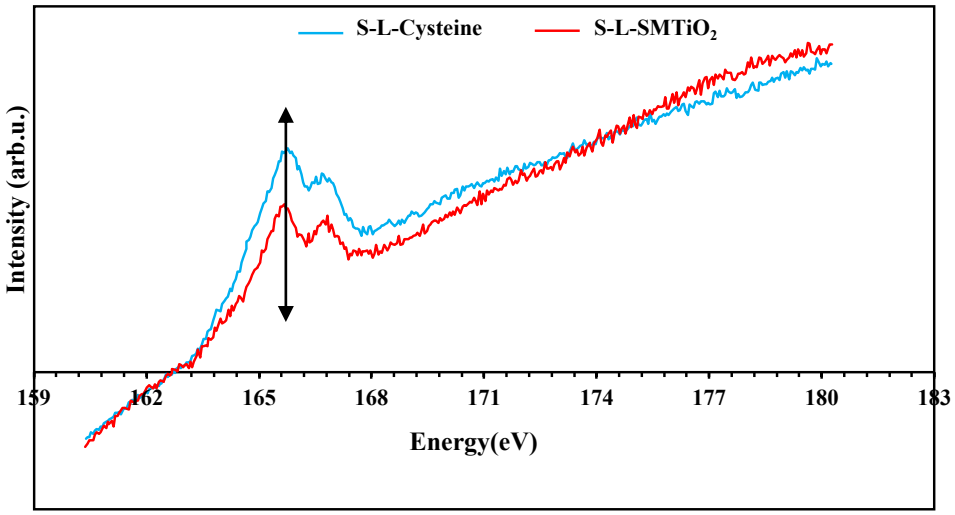

Figure 6.14.(S1) NEXAFS spectra at the S L-edge Cysteine as a reference, and $SMTiO_2$ sample.

6.7.3. XPS analysis:

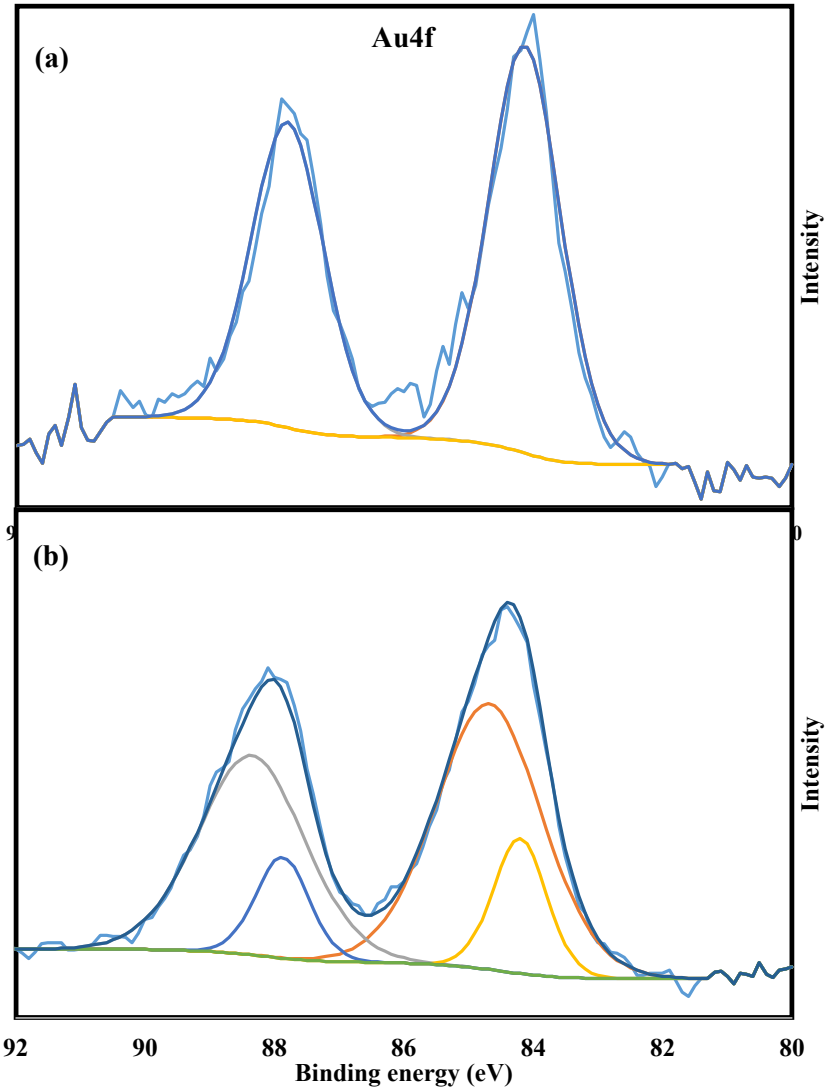

Figure 6.15. (S2) High resolution XPS of Au4f in (a) Au_9 NCs/$MTiO_2$ and (b) Au_9 NCs/$SMTiO_2$ nanocomposites after annealing treatment to remove the ligands.

6.7.4. STEM section notes

6.7.4.1. Ligated Au_9 clusters, mesoporous TiO_2

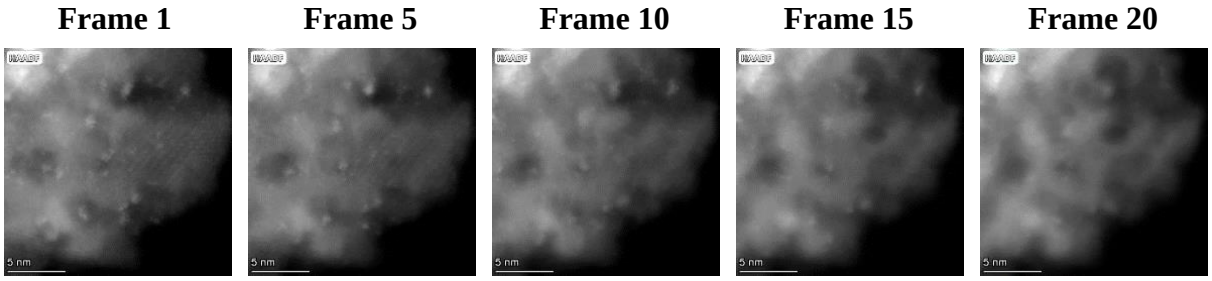

Figure 6.16. (S3) HAADF frames from EDS mapping of $MTiO_2$ after deposition of Au_9 clusters showing migration of Au during the scanning of the scanning of the electron beam across the surface. The sample was not heated to remove the ligands on the Au_9 clusters.

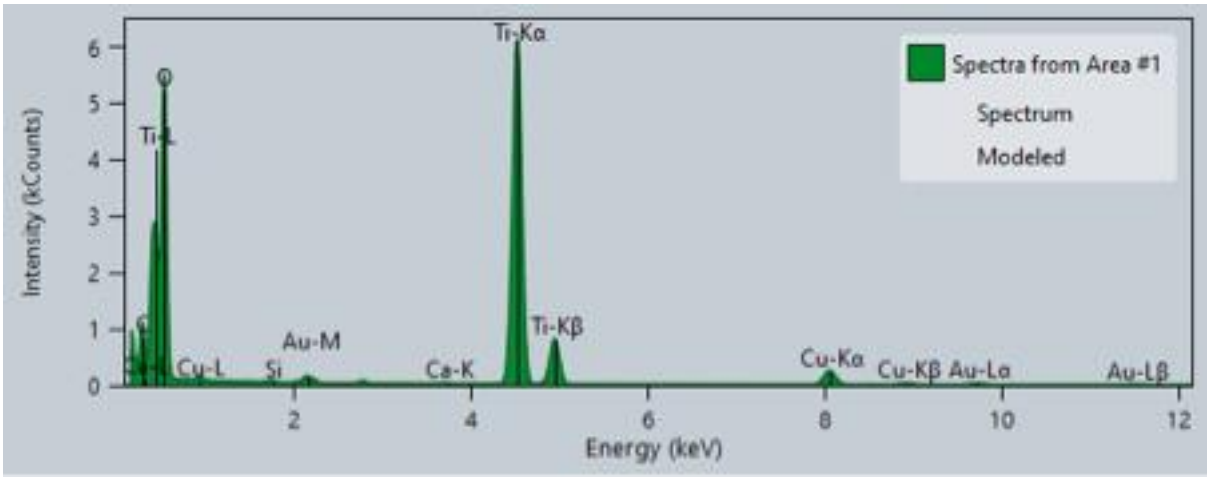

Figure 6.17. (S4) Integrated spectrum from EDS mapping of $MTiO_2$ after deposition of Au_9 clusters showing the presence of Au, Ti, and O. The sample was not heated to remove the ligands on the Au_9 clusters.

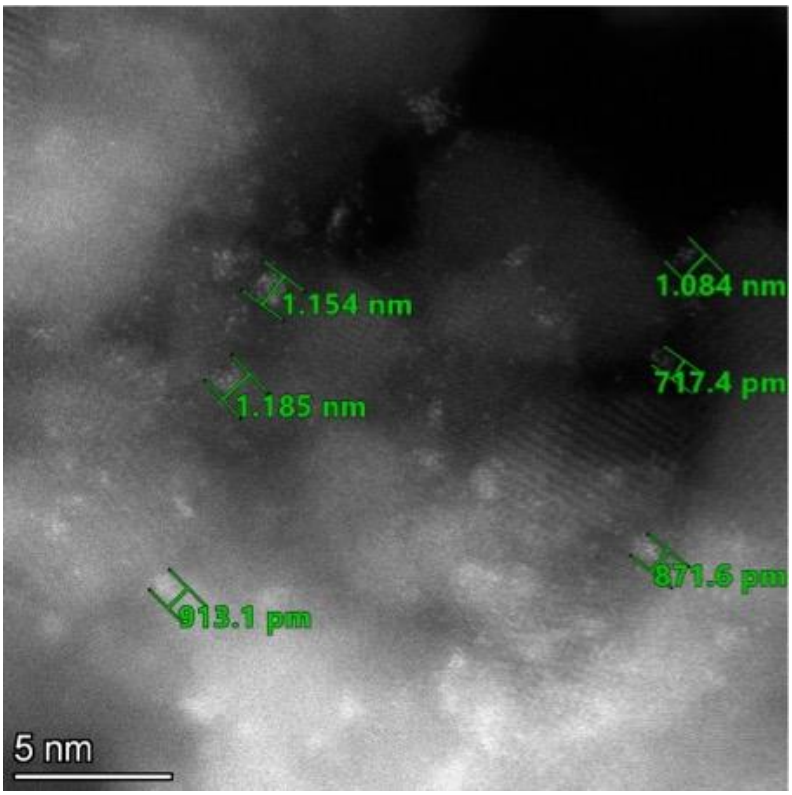

Figure 6.18. (S5) HAADF image of $MTiO_2$ after deposition of Au_9 clusters showing measurements of some of the Au nanoclusters. The sample was not heated to remove the ligands on the Au_9 clusters.

6.7.4.2. Au_9 core, mesoporous TiO_2

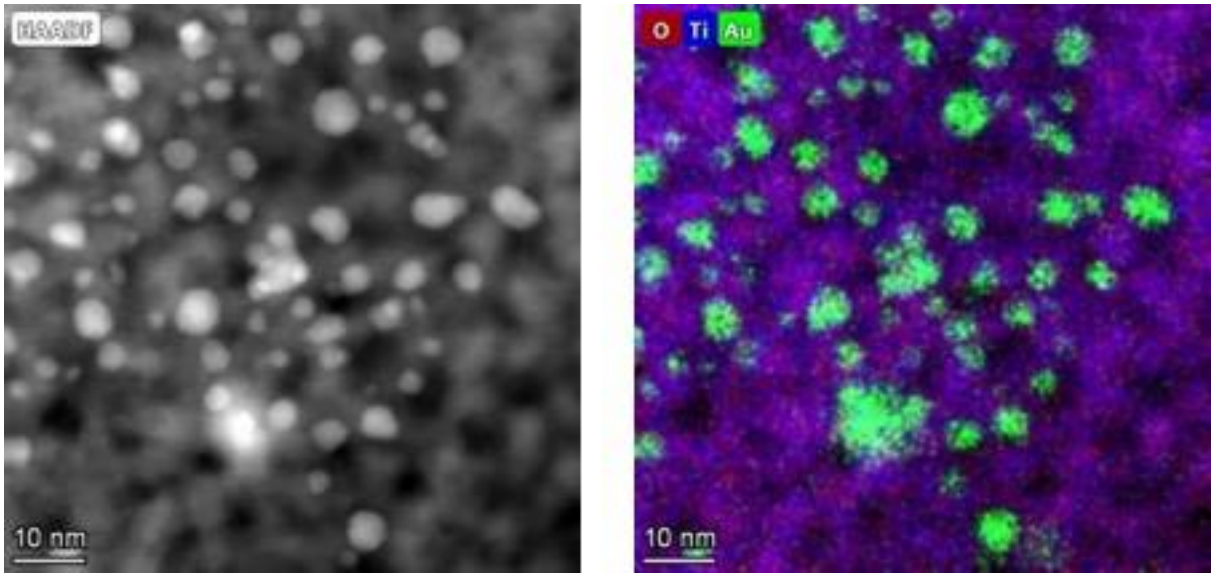

Figure 6.19. (S6) EDS maps of $MTiO_2$ after deposition of Au_9 clusters after heating to remove ligands showing presence of O, Ti, and Au.

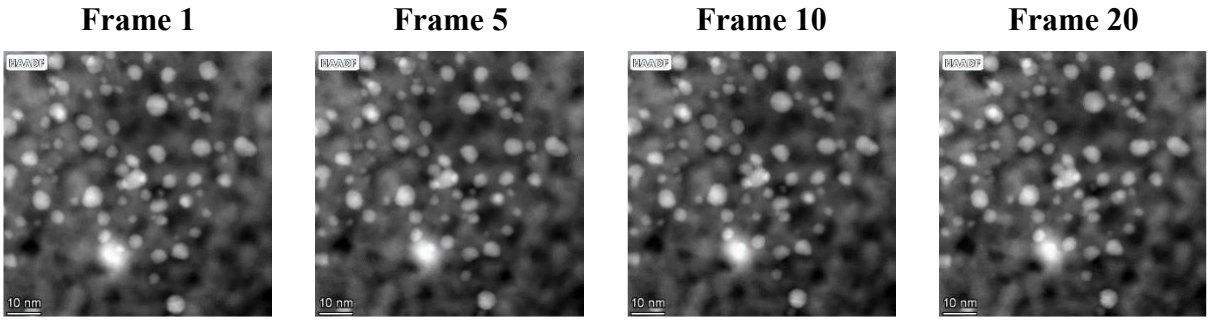

Figure 6.20. (S7) HAADF frames from EDS mapping of $MTiO_2$ after deposition of Au_9 clusters and heating to remove ligands showing very little migration of Au during the scanning of the scanning of the electron beam across the surface.

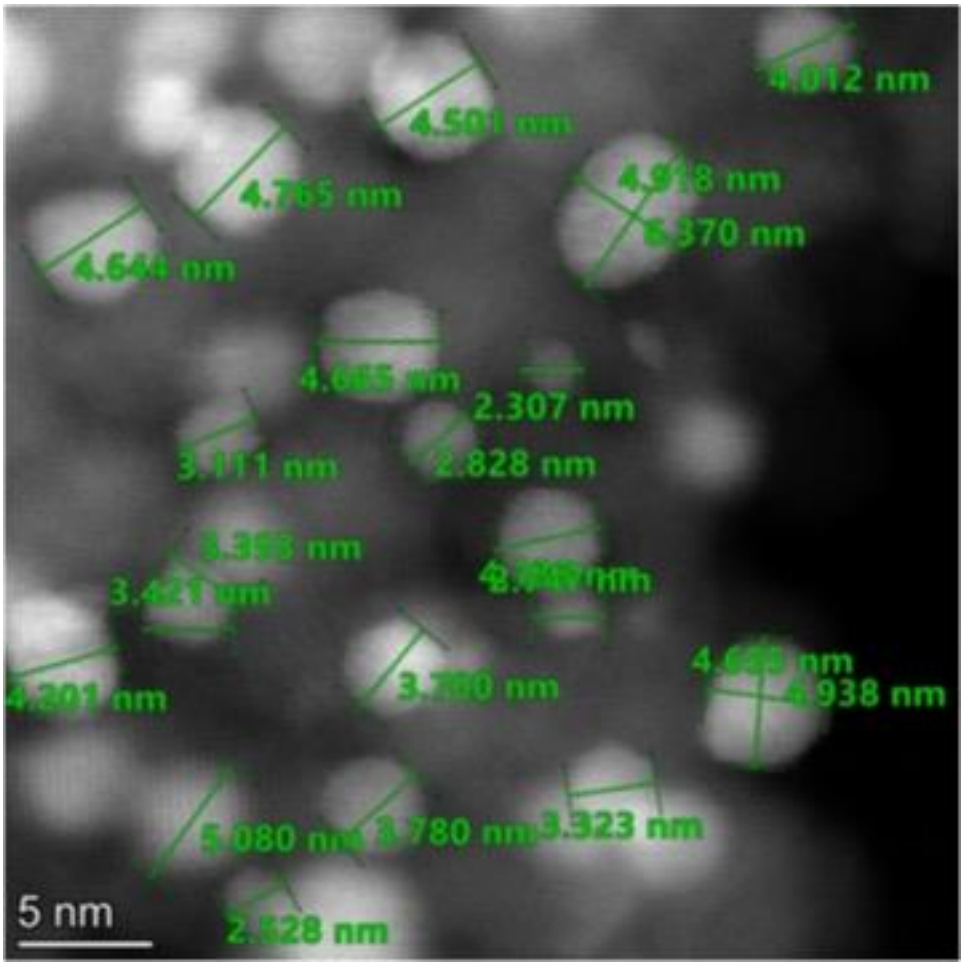

Figure 6.21. (S8) HAADF image of $MTiO_2$ after deposition of Au_9 clusters and heating to remove ligands showing measurements of some of the Au nanoclusters.

6.7.4.3. Ligated Au_9 clusters/$SMTiO_2$ nanocomposite

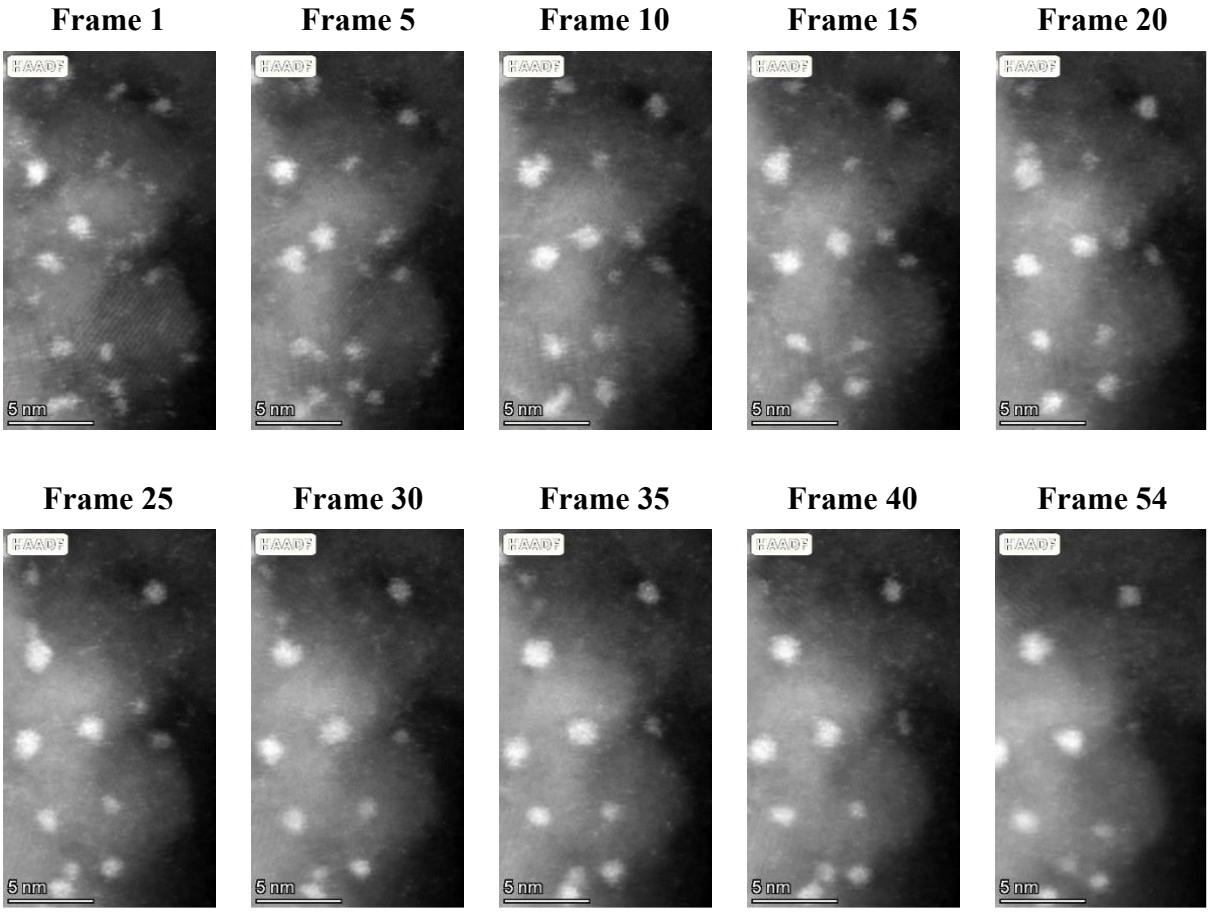

Figure 6.22. (S9) HAADF frames from EDS mapping of $SMTiO_2$ after deposition of Au_9 clusters showing migration of Au during the scanning of the scanning of the electron beam across the surface. The sample was not heated to remove the ligands on the Au_9 clusters.

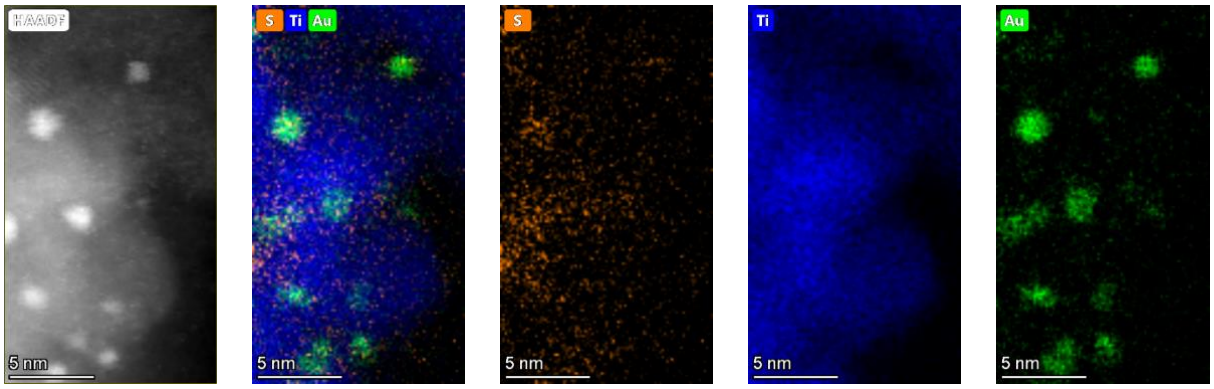

Figure 6.23. (S10) EDS maps of $SMTiO_2$ after deposition of Au_9 clusters showing presence of S, Ti, and Au. The sample was not heated to remove the ligands on the Au_9 clusters. Note that significant agglomeration of Au atoms has occurred due to interaction with the electron beam.

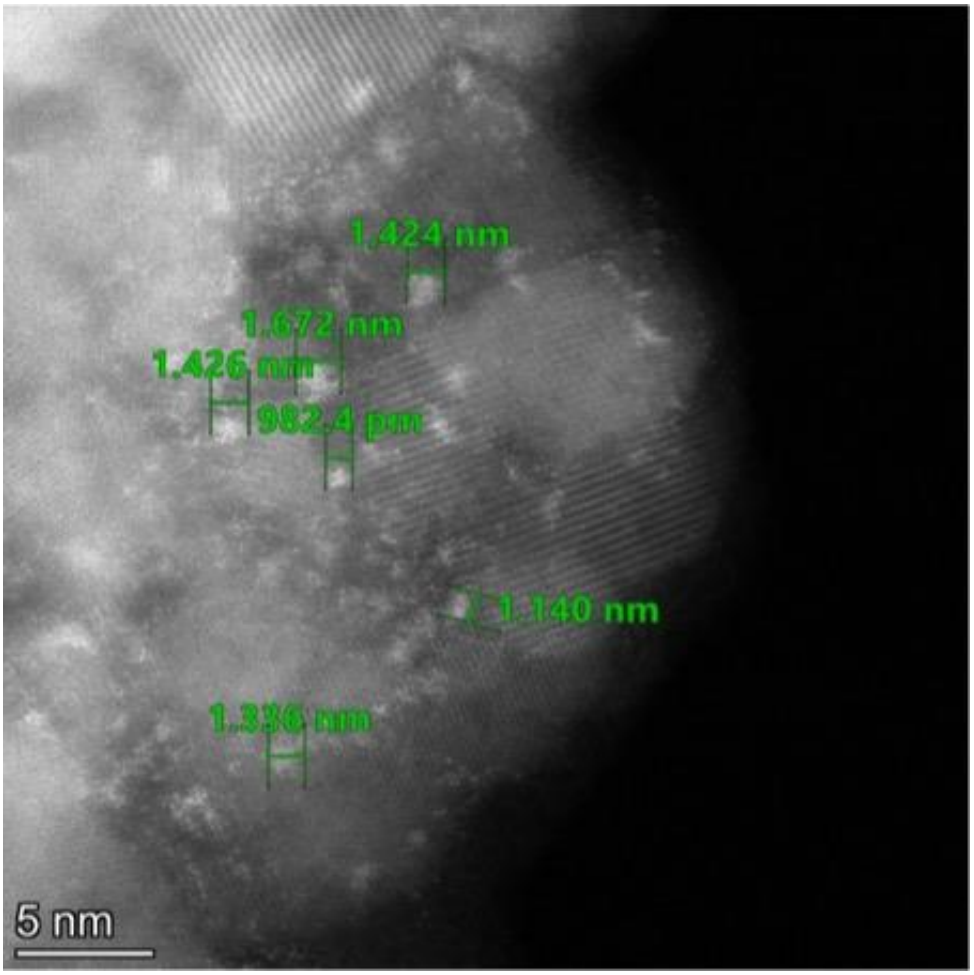

Figure 6.24. (S11) HAADF image of $SMTiO_2$ after deposition of Au_9 clusters showing measurements of some of the Au nanoclusters. The sample was not heated to remove the ligands on the Au_9 clusters.

6.7.4.4. Au_9 core /$SMTiO_2$ nanocomposite after heating to remove ligands.

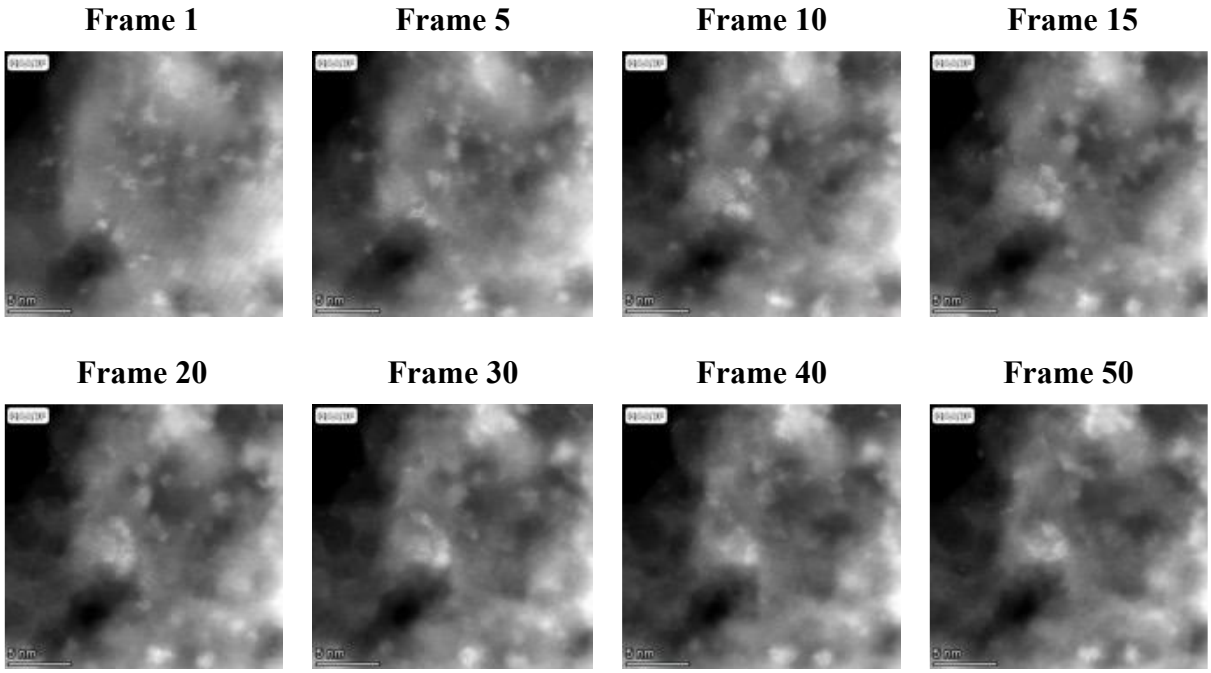

Figure 6.25. (S12) HAADF frames from EDS mapping of $SMTiO_2$ after deposition of Au_9 clusters and heating to remove ligands showing migration of Au during the scanning of the scanning of the electron beam across the surface.

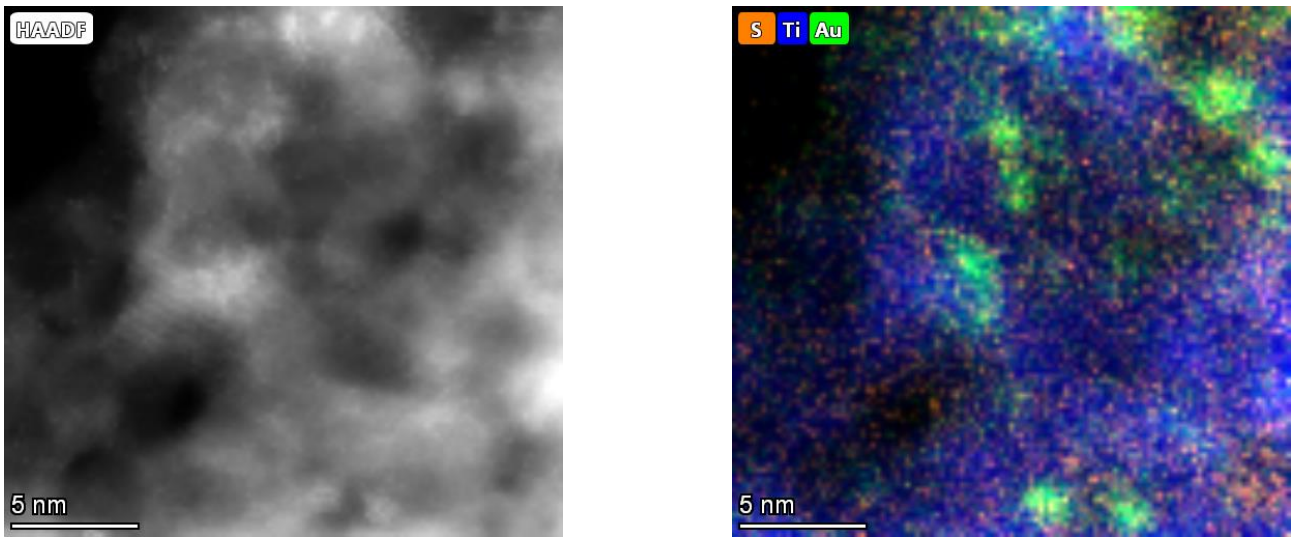

Figure 6.26. (S13) EDS maps of $SMTiO_2$ after deposition of Au_9 clusters after heating to remove ligands showing the presence of S, Ti, and Au. Note that significant agglomeration of Au atoms has occurred due to interaction with the electron beam.

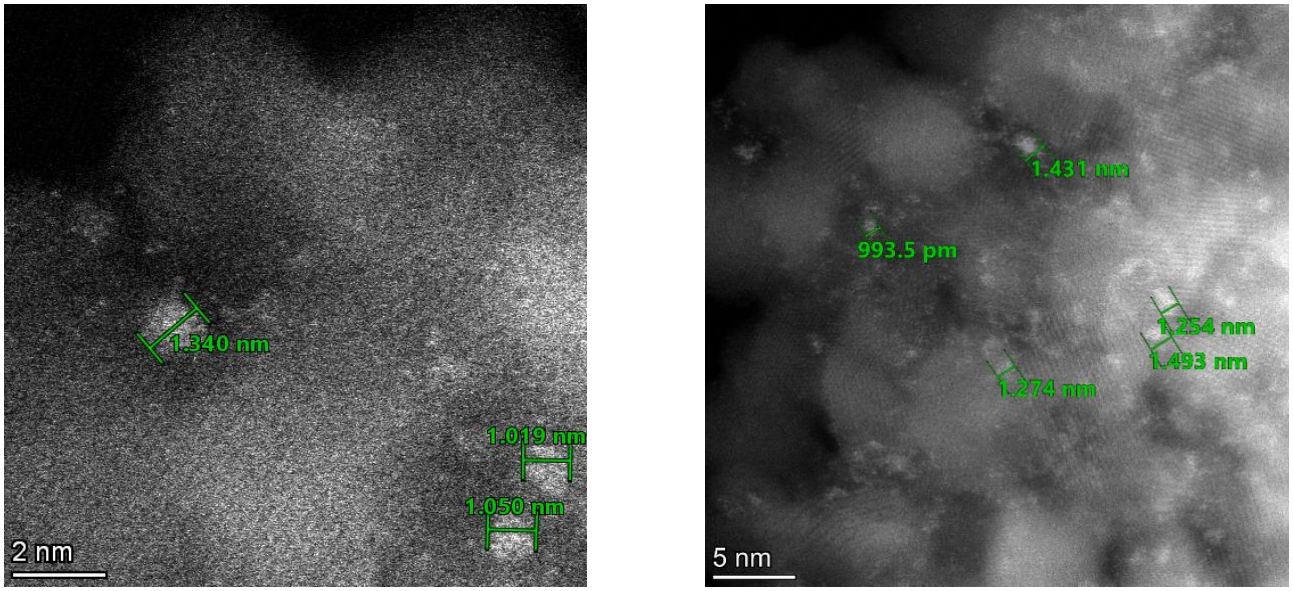

Figure 6.27. (S14) HAADF image of $SMTiO_2$ after deposition of Au_9 clusters and heating to remove ligands showing measurements of some of the Au nanoclusters.

Au_9 deposited on $MTiO_2$

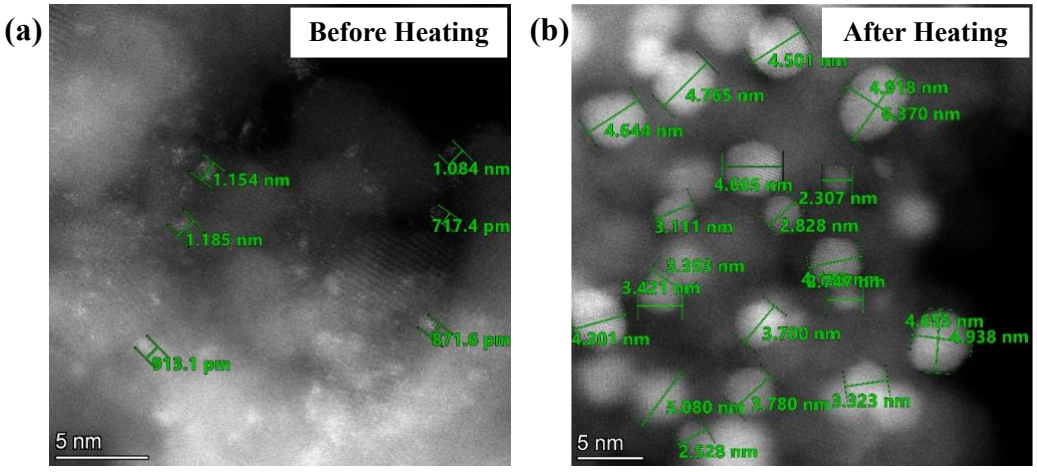

Au_9 deposited on $SMTiO_2$

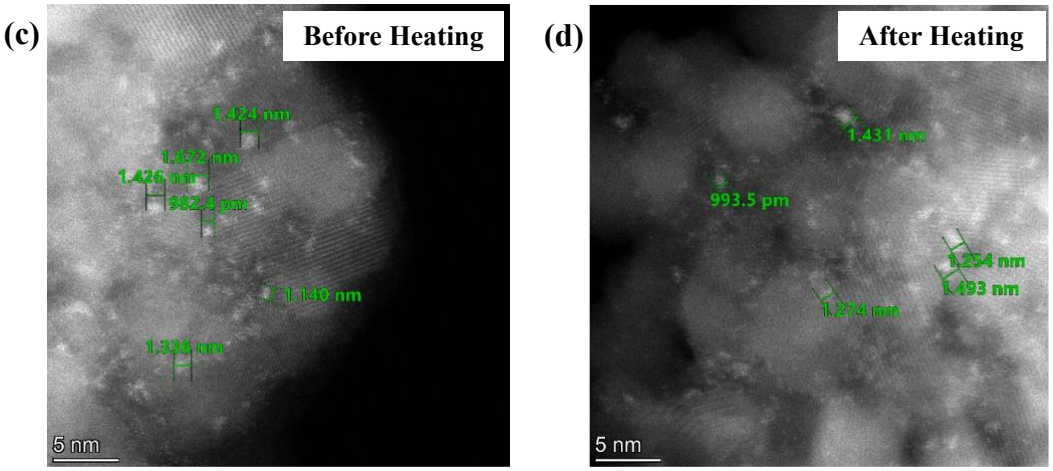

Figure 6.28. (S15) HAADF images of Au_9 deposited on photocatalyst substrates before and after heating to remove ligands from Au_9. Image a) Au_9 on $MTiO_2$ before heating, b) Au_9 on $MTiO_2$ after heating, c) Au_9 on $SMTiO_2$ before heating, and d) Au_9 on $SMTiO_2$ after heating

6.8. References:

(1) Bo, Z. J.; Maochu, G.; Li, W. J.; Min, L. Z.; Ming, Z.; Chen, Y. Effect of metal doping into Ce0. 5Zr0. 5O2 on photocatalytic activity of TiO2/Ce0. 45Zr0. 45M0. 1OX (M= Y, La, Mn). *Journal of hazardous materials* **2007**, *143* (1-2), 516-521.
(2) Mahlambi, M. M.; Ngila, C. J.; Mamba, B. B. Recent developments in environmental photocatalytic degradation of organic pollutants: the case of titanium dioxide nanoparticles—a review. *Journal of Nanomaterials* **2015**, *2015*, 5-5.
(3) Oros-Ruiz, S.; Gómez, R.; López, R.; Hernandez-Gordillo, A.; Pedraza-Avella, J.; Moctezuma, E.; Pérez, E. Photocatalytic reduction of methyl orange on Au/TiO2 semiconductors. *Catalysis Communications* **2012**, *21*, 72-76.
(4) Choi, H.; Stathatos, E.; Dionysiou, D. D. Photocatalytic TiO2 films and membranes for the development of efficient wastewater treatment and reuse systems. *Desalination* **2007**, *202* (1-3), 199-206.
(5) Mrowetz, M.; Villa, A.; Prati, L.; Selli, E. Effects of Au nanoparticles on TiO 2 in the photocatalytic degradation of an azo dye. *Gold Bulletin* **2007**, *40*, 154-160.
(6) Prabha, A. S.; Vijaya, N.; Dorothy, R.; Sasilatha, T.; Umasankareswari, T.; Keerthana, R.; Devi, N. R.; Rajendran, S.; Singh, G. Use of Nanocomposites as Photocatalysts. In *Nanocomposites*, Jenny Stanford Publishing, 2023; pp 283-327. An, L.; Wang, G.; Cheng, Y.; Zhao, L.; Gao, F.; Cheng, Y. Synthesis of CdS/ZnO nanocomposite and its enhanced photocatalytic activity in degradation of methyl orange. *Russian Journal of Physical Chemistry A* **2015**, *89*, 1878-1883. Liu, D.; Song, J.; Chung, J. S.; Hur, S. H.; Choi, W. M. ZnO/Boron Nitride Quantum Dots Nanocomposites for the Enhanced Photocatalytic Degradation of Methylene Blue and Methyl Orange. *Molecules* **2022**, *27* (20), 6833.
(7) Dedman, C. J.; King, A. M.; Christie-Oleza, J. A.; Davies, G.-L. Environmentally relevant concentrations of titanium dioxide nanoparticles pose negligible risk to marine microbes. *Environmental Science: Nano* **2021**, *8* (5), 1236-1255. Rashid, M. M.; Forte Tavčer, P.; Tomšič, B. Influence of titanium dioxide nanoparticles on human health and the environment. *Nanomaterials* **2021**, *11* (9), 2354.
(8) Amy, L. L.; Guangquan, L.; John, T. Y. Photocatalysis on TiO2 surfaces: principles, mechanisms, and selected results. *Chemical Reviews* **1995**, *95* (3), 735-758. Guo, Q.; Zhou, C.; Ma, Z.; Yang, X. Fundamentals of TiO2 photocatalysis: concepts, mechanisms, and challenges. *Advanced Materials* **2019**, *31* (50), 1901997. Nakata, K.; Fujishima, A. TiO2 photocatalysis: Design and applications. *Journal of photochemistry and photobiology C: Photochemistry Reviews* **2012**, *13* (3), 169-189.
(9) Sakthivel, S.; Shankar, M.; Palanichamy, M.; Arabindoo, B.; Bahnemann, D.; Murugesan, V. Enhancement of photocatalytic activity by metal deposition: characterisation and photonic efficiency of Pt, Au and Pd deposited on TiO2 catalyst. *Water research* **2004**, *38* (13), 3001-3008.
(10) Li, F.; Li, X. The enhancement of photodegradation efficiency using Pt–TiO2 catalyst. *Chemosphere* **2002**, *48* (10), 1103-1111. Kasarevic-Popovic, Z.; Behar, D.; Rabani, J. Role of excess electrons in TiO2 nanoparticles coated with Pt in reduction reactions studied in radiolysis of aqueous solutions. *The Journal of Physical Chemistry B* **2004**, *108* (52), 20291-20295.
(11) Cheng, D.; Liu, R.; Hu, K. Gold nanoclusters: Photophysical properties and photocatalytic applications. *Frontiers in Chemistry* **2022**, *10*.
(12) Cui, H.; Shao, Z.-S.; Song, Z.; Wang, Y.-B.; Wang, H.-S. Development of gold nanoclusters: from preparation to applications in the field of biomedicine. *Journal of Materials Chemistry C* **2020**, *8* (41), 14312-14333.
(13) Li, G.; Jin, R. Gold nanocluster-catalyzed semihydrogenation: A unique activation pathway for terminal alkynes. *Journal of the American Chemical Society* **2014**, *136* (32), 11347-11354.
(14) Halder, A.; Curtiss, L. A.; Fortunelli, A.; Vajda, S. Perspective: Size selected clusters for catalysis and electrochemistry. *The Journal of Chemical Physics* **2018**, *148* (11), 110901.

(15) Jin, R. Quantum sized, thiolate-protected gold nanoclusters. *Nanoscale* **2010**, *2* (3), 343-362.
(16) Mousavi, H.; Yin, Y.; Howard-Fabretto, L.; Sharma, S. K.; Golovko, V.; Andersson, G. G.; Shearer, C. J.; Metha, G. F. Au 101–rGO nanocomposite: Immobilization of phosphine-protected gold nanoclusters on reduced graphene oxide without aggregation. *Nanoscale Advances* **2021**, *3* (5), 1422-1430.
(17) Burgos, J. C.; Mejía, S. M.; Metha, G. F. Effect of Charge and Phosphine Ligands on the Electronic Structure of the Au8 Cluster. *ACS omega* **2019**, *4* (5), 9169-9180. Golosnaya, M.; Pichugina, D.; Kuz'menko, N. Structure and reactivity of gold cluster protected by triphosphine ligands: DFT study. *Structural Chemistry* **2019**, *30*, 501-507.
(18) Lopez-Acevedo, O.; Kacprzak, K. A.; Akola, J.; Häkkinen, H. Quantum size effects in ambient CO oxidation catalysed by ligand-protected gold clusters. *Nature chemistry* **2010**, *2* (4), 329-334.
(19) Pei, Y.; Shao, N.; Gao, Y.; Zeng, X. C. Investigating active site of gold nanoparticle Au55 (PPh3) 12Cl6 in selective oxidation. *ACS nano* **2010**, *4* (4), 2009-2020.
(20) Adnan, R. H.; Andersson, G. G.; Polson, M. I.; Metha, G. F.; Golovko, V. B. Factors influencing the catalytic oxidation of benzyl alcohol using supported phosphine-capped gold nanoparticles. *Catalysis Science & Technology* **2015**, *5* (2), 1323-1333.
(21) Ruzicka, J.-Y.; Abu Bakar, F.; Hoeck, C.; Adnan, R.; McNicoll, C.; Kemmitt, T.; Cowie, B. C.; Metha, G. F.; Andersson, G. G.; Golovko, V. B. Toward control of gold cluster aggregation on TiO2 via surface treatments. *The Journal of Physical Chemistry C* **2015**, *119* (43), 24465-24474.
(22) Anderson, D. P.; Adnan, R. H.; Alvino, J. F.; Shipper, O.; Donoeva, B.; Ruzicka, J.-Y.; Al Qahtani, H.; Harris, H. H.; Cowie, B.; Aitken, J. B. Chemically synthesised atomically precise gold clusters deposited and activated on titania. Part II. *Physical chemistry chemical physics* **2013**, *15* (35), 14806-14813.
(23) Menard, L. D.; Xu, F.; Nuzzo, R. G.; Yang, J. C. Preparation of TiO2-supported Au nanoparticle catalysts from a Au13 cluster precursor: Ligand removal using ozone exposure versus a rapid thermal treatment. *Journal of Catalysis* **2006**, *243* (1), 64-73.
(24) Li, H.; Zhao, G.; Song, B.; Han, G. Preparation of macroporous and mesoporous TiO2 film with various solvents. *Materials Letters* **2008**, *62* (19), 3395-3397. Li, C.; Colella, N. S.; Watkins, J. J. Low-temperature fabrication of mesoporous titanium dioxide thin films with tunable refractive indices for one-dimensional photonic crystals and sensors on rigid and flexible substrates. *ACS applied materials & interfaces* **2015**, *7* (24), 13180-13188.
(25) Krishnan, G.; Eom, N.; Kirk, R. M.; Golovko, V. B.; Metha, G. F.; Andersson, G. G. Investigation of Phosphine Ligand Protected Au13 Clusters on Defect Rich Titania. *The Journal of Physical Chemistry C* **2019**, *123* (11), 6642-6649. Al Qahtani, H. S.; Higuchi, R.; Sasaki, T.; Alvino, J. F.; Metha, G. F.; Golovko, V. B.; Adnan, R.; Andersson, G. G.; Nakayama, T. Grouping and aggregation of ligand protected Au 9 clusters on TiO 2 nanosheets. *RSC advances* **2016**, *6* (112), 110765-110774.
(26) Krishnan, G.; Al Qahtani, H. S.; Li, J.; Yin, Y.; Eom, N.; Golovko, V. B.; Metha, G. F.; Andersson, G. G. Investigation of ligand-stabilized gold clusters on defect-rich titania. *The Journal of Physical Chemistry C* **2017**, *121* (50), 28007-28016.
(27) Häkkinen, H. The gold–sulfur interface at the nanoscale. *Nature chemistry* **2012**, *4* (6), 443-455.
(28) Maksymovych, P.; Voznyy, O.; Dougherty, D. B.; Sorescu, D. C.; Yates Jr, J. T. Gold adatom as a key structural component in self-assembled monolayers of organosulfur molecules on Au (1 1 1). *Progress in Surface Science* **2010**, *85* (5-8), 206-240. Daniel, M.-C.; Astruc, D. Gold nanoparticles: assembly, supramolecular chemistry, quantum-size-related properties, and applications toward biology, catalysis, and nanotechnology. *Chemical reviews* **2004**, *104* (1), 293-346.
(29) Soleimani, S.; Heydari, A.; Fattahi, M.; Motamedisade, A. Calcium alginate hydrogels reinforced with cellulose nanocrystals for methylene blue adsorption: Synthesis, characterization, and modelling. *Industrial Crops and Products* **2023**, *192*, 115999.

(30) Yan, B.; Chen, Z.; Cai, L.; Chen, Z.; Fu, J.; Xu, Q. J. A. S. S. Fabrication of polyaniline hydrogel: synthesis, characterization and adsorption of methylene blue. **2015**, *356*, 39-47.
(31) Yu, J.; Su, Y.; Cheng, B.; Zhou, M. Effects of pH on the microstructures and photocatalytic activity of mesoporous nanocrystalline titania powders prepared via hydrothermal method. *Journal of Molecular Catalysis A: Chemical* **2006**, *258* (1-2), 104-112. Wang, G.; Xu, L.; Zhang, J.; Yin, T.; Han, D. Enhanced photocatalytic activity of powders (P25) via calcination treatment. *International Journal of Photoenergy* **2012**, *2012*. Al-Taweel, S. S.; Saud, H. R. New route for synthesis of pure anatase TiO2 nanoparticles via utrasound-assisted sol-gel method. *J. Chem. Pharm. Res* **2016**, *8* (2), 620-626.
(32) Nuengmatcha, P.; Mahachai, R.; Chanthai, S. Adsorption of functionalized thiol-graphene oxide for removal of mercury from aqueous solution. *Asian Journal of Chemistry* **2015**, *27* (11), 4167.
(33) Senkevich, J. J.; Mitchell, C. J.; Yang, G.-R.; Lu, T.-M. Surface chemistry of mercaptan and growth of pyridine short-chain alkoxy silane molecular layers. *Langmuir* **2002**, *18* (5), 1587-1594.
(34) Mansur, H.; Oréfice, R.; Pereira, M.; Lobato, Z.; Vasconcelos, W.; Machado, L. FTIR and UV-vis study of chemically engineered biomaterial surfaces for protein immobilization. *Spectroscopy* **2002**, *16* (3-4), 351-360.
(35) Rasalingam, S.; Kibombo, H. S.; Wu, C.-M.; Budhi, S.; Peng, R.; Baltrusaitis, J.; Koodali, R. T. Influence of Ti–O–Si hetero-linkages in the photocatalytic degradation of Rhodamine B. *Catalysis communications* **2013**, *31*, 66-70. Chellappa, M.; Thejaswini, B.; Vijayalakshmi, U. Biocompatibility assessment of SiO2–TiO2 composite powder on MG63 osteoblast cell lines for orthopaedic applications. *IET nanobiotechnology* **2017**, *11* (1), 77-82.
(36) Guo, J.; Wang, J.; Gao, Y.; Wang, J.; Chang, W.; Liao, S.; Qian, Z.; Liu, Y. pH-Responsive Sponges Fabricated by Ag–S Ligands Possess Smart Double-Transformed Superhydrophilic–Superhydrophobic–Superhydrophilic Wettability for Oil–Water Separation. *ACS Sustainable Chemistry & Engineering* **2017**, *5* (11), 10772-10782.
(37) Bittencourt, C.; Krüger, P.; Lagos, M. J.; Ke, X.; Van Tendeloo, G.; Ewels, C.; Umek, P.; Guttmann, P. Towards atomic resolution in sodium titanate nanotubes using near-edge X-ray-absorption fine-structure spectromicroscopy combined with multichannel multiple-scattering calculations. *Beilstein journal of nanotechnology* **2012**, *3* (1), 789-797. Mardegan, J.; Christensen, D.; Chen, Y.; Parchenko, S.; Avula, S.; Ortiz-Hernandez, N.; Decker, M.; Piamonteze, C.; Pryds, N.; Staub, U. Magnetic and electronic properties at the γ− Al 2 O 3/SrTiO 3 interface. *Physical Review B* **2019**, *99* (13), 134423.
(38) Simões, G.; Rodrigues, F.; Bernini, R.; Castro, C.; de Souza, G. A NEXAFS and mass spectrometry study of cysteine, cystine and insulin irradiated with intermediate energy (0.8 keV) electrons. *Journal of Electron Spectroscopy and Related Phenomena* **2014**, *193*, 21-26.
(39) Veisfeld, N.; Geller, J. D. Ion sputtering yield measurements for submicrometer thin films. *Journal of Vacuum Science & Technology A: Vacuum, Surfaces, and Films* **1988**, *6* (3), 2077-2081.
(40) Anderson, D. P.; Alvino, J. F.; Gentleman, A.; Al Qahtani, H.; Thomsen, L.; Polson, M. I.; Metha, G. F.; Golovko, V. B.; Andersson, G. G. Chemically-synthesised, atomically-precise gold clusters deposited and activated on titania. *Physical chemistry chemical physics* **2013**, *15* (11), 3917-3929. Al Qahtani, H. S.; Metha, G. F.; Walsh, R. B.; Golovko, V. B.; Andersson, G. G.; Nakayama, T. Aggregation behavior of ligand-protected Au9 clusters on sputtered atomic layer deposition TiO2. *The Journal of Physical Chemistry C* **2017**, *121* (20), 10781-10789.
(41) Al Qahtani, H. S.; Kimoto, K.; Bennett, T.; Alvino, J. F.; Andersson, G. G.; Metha, G. F.; Golovko, V. B.; Sasaki, T.; Nakayama, T. Atomically resolved structure of ligand-protected Au9 clusters on TiO2 nanosheets using aberration-corrected STEM. *The Journal of Chemical Physics* **2016**, *144* (11), 114703. Alotabi, A. S.; Gibson, C. T.; Metha, G. F.; Andersson, G. G. Investigation of the Diffusion of Cr2O3 into different phases of TiO2 upon Annealing. *ACS Applied Energy Materials* **2021**, *4* (1), 322-330. Alotabi, A. S.; Osborn, D.; Ozaki, S.; Kataoka, Y.; Negishi, Y.; Tesana, S.; Metha, G. F.; Andersson, G. G. Suppression of phosphine-protected Au 9 cluster agglomeration on SrTiO 3 particles using a chromium hydroxide layer. *Materials Advances* **2022**, *3* (8), 3620-3630.

(42) Soleimani, S.; Heydari, A.; Fattahi, M. Swelling prediction of calcium alginate/cellulose nanocrystal hydrogels using response surface methodology and artificial neural network. *Industrial Crops and Products* **2023**, *192*, 116094.

CHAPTER 7: ENHANCED PHOTOCATALYTIC DEGRADATION OF METHYL ORANGE USING NITROGEN-FUNCTIONALISED MESOPOROUS TIO_2 DECORATED WITH AU_9 NANOCLUSTERS

7.1. Abstract

Nanocomposites of N functionalised mesoporous TiO_2 ($NMTiO_2$) embedded with Au_9 nanoclusters (Au_9 NCs) were created using a chitosan-assisted soft templating method and chemical deposition of Au_9 NCs. Chitosan, acting as a biocompatible template, facilitated chemical and morphological modification of the surface. The calcination atmosphere influenced the substrate colour and surface properties associated with the Au_9 NC adsorption. Through XPS, it was found that substrate surface modifications prevented the agglomeration of Au_9 NCs adsorbed to the material surface and enhanced the overall loading with Au_9 NCs. The photocatalytic effectiveness of these materials was probed in methyl orange (MO) dye degradation and studied by kinetic plots. The results showed that Au_9 NCs loaded on black $NMTiO_2$ were highly effective, completely degrading MO dyes within 20 minutes due to its large reaction constant (0.176 min^{-1}). Parameter interactions were explored using response surface methodology (RSM) and the dependency of MO degradation on the affecting parameters was evaluated based on the statistical analysis and 3D plots.

7.2. Introduction

Water pollution resulting from chemical and food industry runoff is of growing ecological concern.[1] A wide range of chemical industries, including dye manufacture, textile and cosmetics production, release toxic, and nonbiodegradable dyes into the environment. Nearly half of the dyes utilised in the textile and dye industry are azo dyes. Methyl orange (MO) is widely used as a water-soluble azo dye. The elimination of harmful and persistent organic compounds from water involves a range of physical, chemical, and biological processes. Multipurpose chemical processes have demonstrated high efficiency and yield in pollutant degradation.[2,3]

Heterogeneous semiconductor-mediated photocatalysis systems provide a significant advantage over other advanced chemical processes. It facilitates the mineralization of all organic pollutants, like azo dyes, into water and carbon dioxide molecules with a high degradation efficiency.[4,5]

Among the semiconducting metal oxides studied, Titanium dioxide (TiO_2) is a commonly employed photocatalytic material in environmental applications due to its exceptional performance, chemical durability, resistance to photo corrosion, minimal toxicity, cost-effectiveness, and environmentally friendly nature.[6,7] Due to rapid electron-hole recombination, photocatalysis is

limited. To solve this problem, semiconducting photocatalysis can be decorated with different noble metals like Au as electron sinks.[8,9]

Most previous studies focused on metallic nanoparticles with sizes between 5 and 100 nm, concluding that the activity increased with decreasing size.[10-12] It is also common to observe a volcano-type trend with an optimum particle size for the catalytic reaction.[13] Rarely, the catalytic activity of nanoparticles may decline with smaller size or be unaffected by size.[12,14,15] The achievement in synthesizing atomically precise nanoclusters (NCs) has opened up new opportunities to study the catalytic reactions.[16] They have shown to be active electrochemical,[17,18] photo,[19,20] and thermo[13,21,22] catalytically in a variety of reactions. Au NCs smaller than 1.5 nm exhibit a molecule-like quantized electronic structure owing to the quantum confinement effect.[12,17,19]

Due to their well-defined atomic structures and unique features, triphenylphosphine ligand-protected Au nanoclusters (Au NCs) have recently attracted interest as co-catalysts in photocatalysis. To develop an effective photocatalytic setup, eliminating ligands through thermal treatment is often necessary. The objective is to promote direct interaction between the Au cluster cores and the semiconductor surface, facilitating contact between reactants and the Au cluster cores. Ligand removal can impact the size of the Au clusters, potentially causing them to aggregate due to heat treatment, thereby compromising their distinct characteristics.[23-27]

To enhance the productivity of photocatalytic processes, precise monitoring of the size and optimisation of the quantity of Au NCs loaded onto semiconductor surfaces is paramount. Morphological and chemical modifications are applied to TiO_2 surfaces by making porous frameworks and adding functional groups to the surfaces to address the above-mentioned issues. In this study, both modifications were combined into a simple synthesis procedure.

Several studies have been conducted on mesoporous TiO_2 ($MTiO_2$) synthesis because of their unique properties, including a high surface area, a high density of surface defects and an extremely well-defined porous structure [28]. In most instances, mesoporous TiO_2 ($MTiO_2$) is synthesised using soft templating methods using surfactants, polymers and biopolymers as templates.[29,30] There are three steps in creating samples using this method: template preparation, target production by a sol-gel or hydrothermal method and removing the template with a physical (pulverization and spray) method, or chemical reaction (calcination method).[31]

Biopolymers like chitosan can be used as soft templates, which are also used as natural N and C resources for making $NMTiO_2$. The biodegradability and biocompatibility of chitosan[32], a polycationic polysaccharide, make it an ideal choice as a template[33]. Since chitosan consists of glucosamine and acetylglucosamine units containing carboxyl and amine functional groups, it requires no chemical modifications to form the chelate with TiO_2 unites, to fabricate the mesoscopic phases, and to facilitate N functionalisation after the calcination step.[34] N attached to the surface can

be used as active sites to make strong complexes between co-catalysts and $MTiO_2$ surfaces to increase the loading level and decrease the agglomeration of cocatalysts.[35-37]

This study focuses on developing an efficient heterogeneous photocatalysis system using high-loaded Au_9 NCs decorated $NMTiO_2$ nanoparticles. XPS was employed to investigate how surface modifications influenced both the agglomeration of Au_9 NCs and intensity ratios. The photoactivity of the nanocomposites was then studied in the degradation of methyl orange azo dyes. A central composite design along with RSM made it possible to identify critical factors and their interactions, reducing the required experiments.

7.3. Experimental section

7.3.1. Materials and Methods:

7.3.1.1. Materials and synthesis procedure of Au_9 clusters:

Detailed information of synthesis and characterisation of Au_9 NCs has been reported in Chapter 4.

7.3.1.2. Materials and synthesis procedure of the white and black $NMTiO_2$ substrates:

Chitosan with a medium molecular weight, acetic acid, ammonia solution (25% w/w), absolute ethanol, methanol, titanium tetraisopropoxide (TTIP), methyl orange, and HCl (37% w/w) were purchased from Sigma Aldrich and utilised without further purification.

Three grams of chitosan powder were mixed with 100 ml of aqueous acetic acid (5% v/v) for one hour to obtain a solution (3% w/w). Titanium chloride solution was prepared by adding 1.5 g (0.0053 mol) of titanium (IV) isopropoxide to 10 ml of HCl (37%) mixed with 50 ml of deionized water. The prepared solution was then added to the chitosan solution (1:1 (w/w) of Ti precursor to chitosan solution) and stirred at room temperature for two hours. After preparing the solution, it was added dropwise into 50% aqueous ammonia while being stirred. A gel was formed after stabilising for 1 hour in the ammonia solution. Finally, the particles were centrifuged and subsequently washed 2 times with deionized water and 3 times with methanol, dried at 40 °C and, calcined at 400 °C, 500 °C, and 600 °C in air to remove the chitosan. The photocatalyst is termed as $NMTiO_2$ (1:1). The template was removed from the sample during calcination, and black colouration occurred when the atmosphere was changed from air to Ar.

7.3.1.3. Synthesis of $NMTiO_2/Au_9$ NCs photocatalysts:

In summary, as can be seen in Figure 7.1, to prepare the $NMTiO_2$ substrates, the sol-gel method was combined with homogeneous precipitation and xerogel carbonization in both air and hypoxic atmospheres. Chitosan was used as a template to generate a mesoporous structure and a suitable resource for N modifying. The colour of the substrate turned black when the carbonization atmosphere changed from air to Ar. To synthesise the desired nanocomposites, Au_9 NCs were chemically deposited onto the surface of the prepared substrates. Finally, phosphine ligands were removed by annealing to prepare photocatalysts based on Au cluster modified $MNTiO_2$ surfaces.

To deposit Au_9 NCs onto $NMTiO_2$ surfaces, the solution of Au_9 NCs was firstly prepared by dissolving (1 mg, 4.63×10^{-6} mol) of the dark green $[Au_9(PPh_3)_8](NO_3)_3$ crystals in 2 ml of methanol. 10 mg of each black and white $MTiO_2$ was then mixed with 2 ml of Au_9 NC solution while stirring with a magnetic stirrer for 1 hour at room temperature to give a white or black suspension. The suspension was centrifuged, and the crude sample was then placed under vacuum at room temperature for ~5 hours to remove the residual methanol. The sample was then placed in a vial, capped, and stored in the dark at ~4 °C to minimize any potential aggregation and/or degradation.

To remove the triphenyl phosphine ligands by thermal treatment, $NMTiO_2$ compounds decorated by Au_9 NCs were drop casted on the Si wafers. They were then annealed at 200 °C under vacuum for 10 mins. Samples were then cooled at room temperature under reduced pressure. The materials were preserved by storing them in a refrigerator maintained at 4°C.

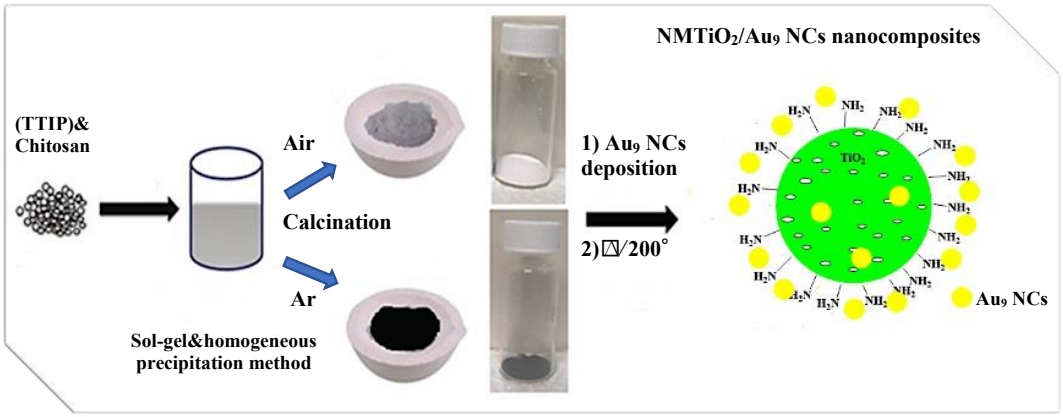

Figure 7.1. Synthesis procedure of $NMTiO_2$ decorated by Au_9 NCs

7.3.1.4. Photocatalytic test using black $NMTiO_2/Au_9$ NCs nanocomposites:

White and black $NMTiO_2/Au_9$ NCs nanocomposites and their relevant substrates were suspended in 3 ml of MO dye solution to study MO dye degradation. The tube and its contents were then exposed to UV light. For mixing, a Vortex Fluidic Device[38-40] (VFD) equipped with two 10 W Hg lamps with UV light (254 nm) was used. This study is designed to evaluate the photoactivity of the prepared nanocomposites based on their kinetic plots (-ln C/C_0 over time). After the selection of the best photocatalyst based on the obtained reaction constants, which was the black $NMTiO_2/Au_9$

NCs, its degradation efficiency was studied as a function of three independent factors presented by the codes A for the MO dye concentration (ppm), B for the catalyst amount (mg), and C for the reaction time (min) as described in Table 7.1.

Table 7-1. Experimental and coded levels of the selected factors.

Factor	**Unit**	**Code for each factor**	**Levels**			
			Coded levels	-1	0	+1
MO concentration	ppm	A	**Actual levels**	10	15	20
Catalyst amount	mg	B		1	1.5	2
Time	min	C		5	10	20

Table 7.1 shows there are three coded and actual levels for each parameter. Coded levels from minimum (-1) to maximum (+1) are used to make all the parameters unitless to observe the relation between them as will be discussed below. The central composite design using a self-written Python codes (Ver. 3.10.7) and different libraries (NumPy, Pandas, etc.) was used to design a minimum set of experiments for the most photoactive nanocomposite, black NMTiO$_2$/Au$_9$ NCs, to study the relation between factors by RSM. Accordingly, the total number of required experiments is fifteen, as can be seen in Table 7.2. Evidence our experiments have been carried out with a high precision is that the results predicted by RSM are close to those achieved through the experimental results as presented in Table 7.2.

Table 7-2. Centre composite design with experimental and predicted responses

Factor 1	**Factor 2**	**Factor 3**	**Response 1**	**RSM**
A:MO Conc.	B:Cat. amount	C:Time	Deg.	Deg
ppm	mg	min	%	%
10	1	10	64.45	65.52
20	1	10	52.25	51.70
15	1.5	10	82.33	81.40
10	2	10	84.95	84.62
20	2	10	77.55	78.29
15	1	15	73.85	73.78
10	1.5	15	90.19	89.66
15	1.5	15	89.83	89.70
20	1.5	15	78.14	78.73

15	2	15	93.74	93.88
10	1	20	85.55	84.80
20	1	20	68.95	69.26
15	1.5	20	96.09	97.08
10	2	20	97.87	98.41
20	2	20	91.45	90.36

A selected amount of the photocatalyst was dispersed in 3 ml of dye solution and exposed to UV light for the chosen time. Experiments were carried out with 900 rpm rotation speed and under constant UV light intensity. The suspended catalyst particles were centrifuged under 12000 rpm for 10 mins. The MO concentration was assessed by employing a UV-Visible spectrophotometer (PerkinElmer) set to measure at its maximum wavelength of 466 nm. The degradation was calculated using the formula reported in our previous work as can be found in references.[41,42]

7.3.2. Modelling

7.3.2.1. Response surface methodology (RSM):

Experiments were designed based on the central composite design (CCD) and the results were analysed by RSM to achieve statistically significant results as described in Chapters 3 and 6.

7.3.3. Characterisation

Chapter 2 provides a detailed description of all the methods used for characterisation.

7.4. Results and discussion

7.4.1. FTIR

FTIR spectroscopy was used to identify the functional groups on the surface of black NMTiO$_2$, white NMTiO$_2$, hybrid of TiO$_2$ and chitosan before calcination and pure chitosan (Figure 7.2). All spectra have a same broad peak in the region 3200–3600 cm^{-1} corresponding to N-H and O-H stretching vibration.[43]

In Figure 7.2 (a-c), the broad peak centred at 3400 cm^{-1} and a peak at 1649 cm^{-1} in the white NMTiO$_2$, black NMTiO$_2$, and P25 spectra are attributed to the stretching vibration of moisture adsorbed to the surface and characteristic bending modes of Ti-OH, respectively.[44] Also, Ti-O stretching modes and Ti-O-Ti bending vibration can be detected as broad peak in the range of 600–800 cm^{-1} confirming TiO$_2$ nanoparticles (NPs) exist in our compounds.[45-47]

In Figure 7.2 (a, d, and e), peaks at around 2901, and 2974 are assigned to asymmetric, and symmetric stretching vibration of –CH and peak at 1065 cm^{-1} corresponds to the stretching vibration of C-O–C.[48] These peaks in Figure 7.2 a show the detectable existence of the organic compounds in the black $NMTiO_2$ while this was not the case in the white $NMTiO_2$ due to the minimal residual organic compounds remaining after the calcination process in air (Figure 7.2 b). As depicted in Figure 7.1 a, the C–N stretching peaks appear at 1394 cm^{-1} and 1252 cm^{-1}, confirming the presence of characteristic chitosan peaks.[49,50]

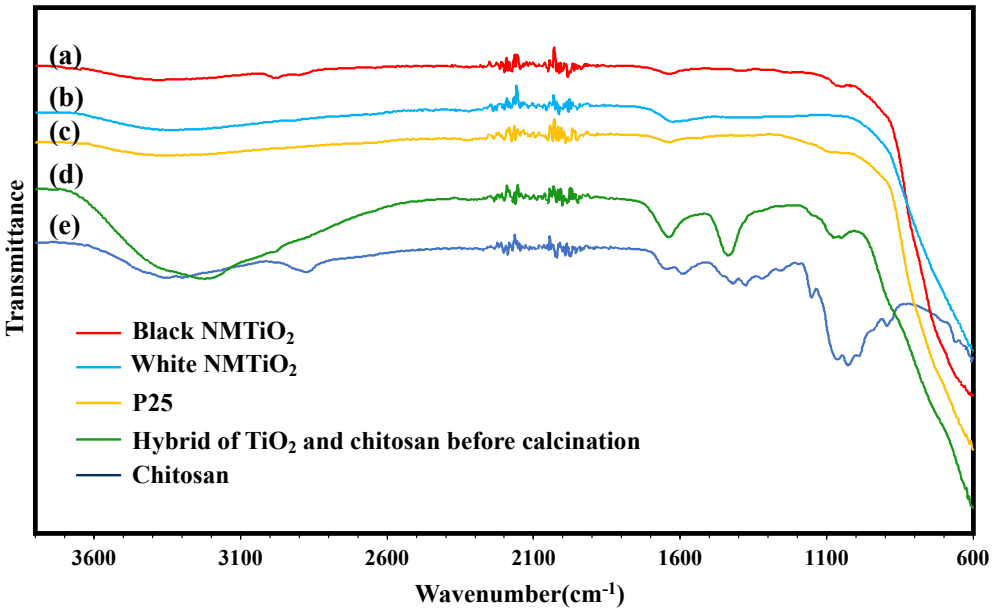

Figure 7.2. FTIR spectrum of (a) black $NMTiO_2$ (b) white $NMTiO_2$ (c) P25 (d) Hybrid of TiO_2 and chitosan before calcination (e) chitosan

This is in agreement with the TGA results showing black $NMTiO_2$ has higher C content (8.6%) than white $NMTiO_2$ (2%), as presented in Figure 7.3. This figure shows TGA analysis of the white $NMTiO_2$ and the black $NMTiO_2$. The effect of the gas phase atmosphere during calcination was investigated at constant temperature, 600 °C. Change in the atmosphere from air to Ar caused a change in colour from white to black. The thermal behaviour and weight loss curves of the prepared white and black $NMTiO_2$ were studied.

In Figure 7.3 (a), the weight losses of a white $NMTiO_2$ are shown in four stages and are in total 2%. First and second stage losses are in the range of 35 °C to 230 °C with a weight loss of 1.2%, in which probably the total physically and chemically absorbed water molecules evaporated.[33,51-53] Therefore, two small sholders in the temperature range between 230 °C and 800 °C with a weight loss of 0.8% can be attributed to the chitosan molecular chains breaking free and its decomposition.[51]

In Figure 7.3 (b), the decomposition of black $NMTiO_2$ can be divided into two separate stages. Its total weight loss is 8.2%. In the initial phase, occurring between 30°C and 250°C, there is a 3.2% reduction in weight primarily due to moisture evaporation.[33,51-53] Subsequently, between 250°C and

700°C, there is a significant weight decrease of about 5% in the prepared black $NMTiO_2$. This second stage is associated with the combustion of organic compounds and the dihydroxylation of $NMTiO_2$.

The weight difference between the two substrates in the temperature range of 250 °C to 800 °C, which can be related to the combustion of organic compounds and phase transitions, is approximately 4.2%. It shows the black $NMTiO_2$ exhibits a higher degree of organic moieties compared to the white $NMTiO_2$. In addition, the weight loss difference of the two substrates in the temperature range of 25 °C to 250 °C corresponds to adsorbed water and is 2%. Therefore, more water molecules adsorbed on the black $NMTiO_2$ surface. This is most likely due to a larger surface area and higher porosity. BET results support this explanation and are discussed later.

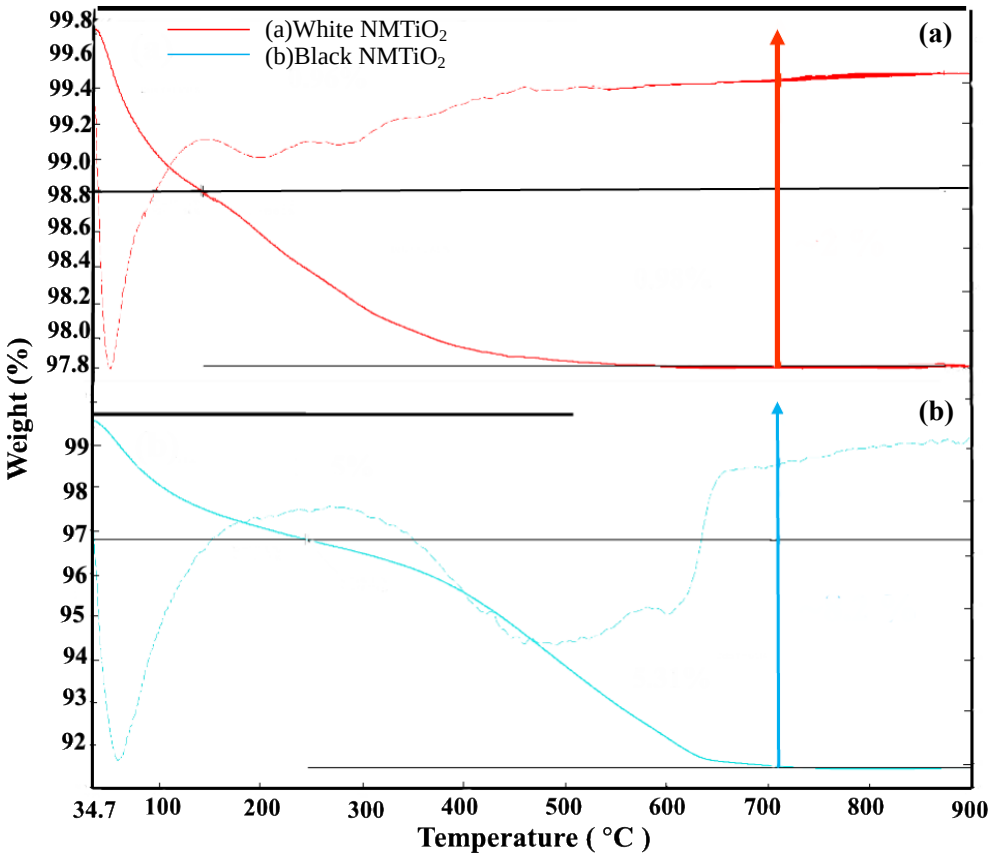

Figure 7.3. Thermogravimetric analysis (TGA/DTG) of (a) white $NMTiO_2$ calcined in air with 2% weight loss and (b) black $NMTiO_2$ calcined in Ar with 8.2% weight loss.

7.4.2. NEXAFS and XRD analysis:

As depicted in Figure 7.4, the Ti L-edge spectra of all examined samples, including references in Figure 7.4 (a) and two prepared substrates in Figure 7.4 (b), exhibit two doublet peaks within the range of 455 eV to 470 eV. These peaks correspond to excitations of the Ti 2p levels into the unoccupied Ti 3d orbitals. Notably, these orbitals are divided into t2g and eg orbitals due to octahedral symmetry characteristics.[54,55] The overall spectral pattern remains consistent across all samples, with an exception observed within the 458.7 eV to 461.7 eV range. Consequently, a comparison of the Ti 2p L-edge spectra for four examined references and two prepared samples was facilitated using the

peaks at 459.8 eV and 460.8 eV. In both spectra associated with the prepared samples, a more intense peak is discernible at 459.8 eV than at 460.8 eV. This specific pattern in the spectral region bears resemblance to that observed in the anatase reference sample.

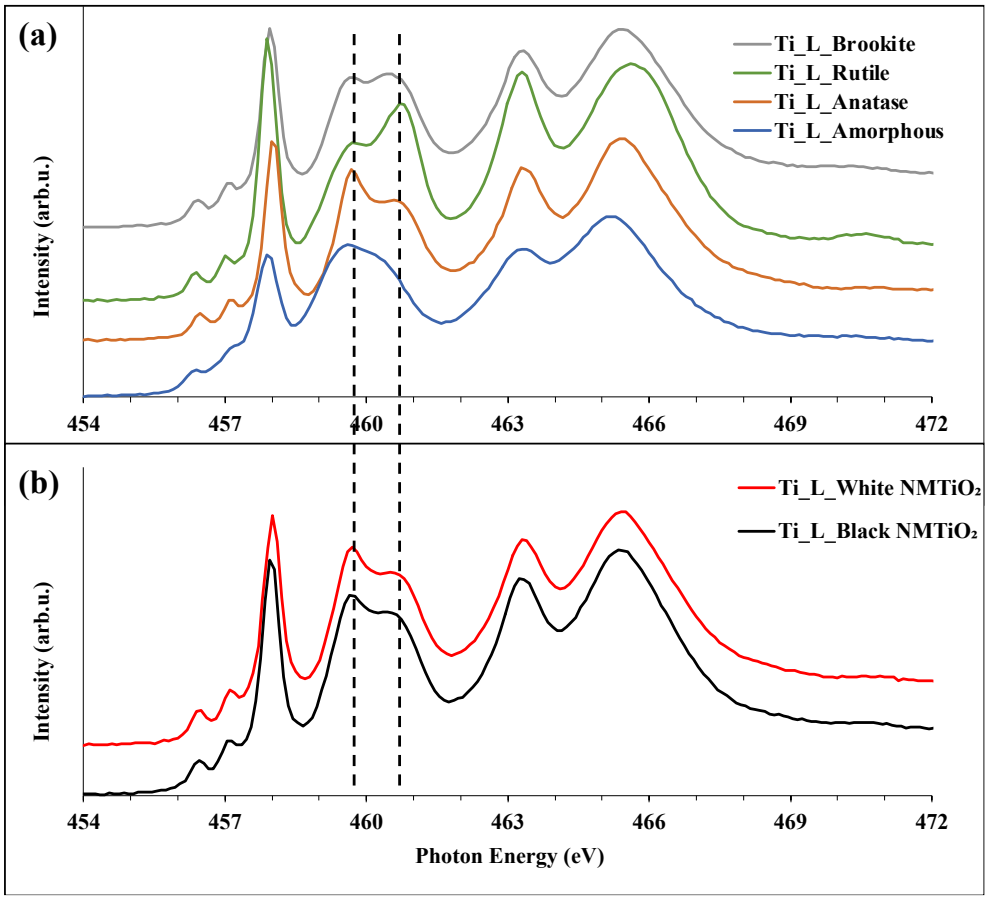

Figure 7.4. Ti 2p L-edge NEXAFS spectra of (a) TiO_2 references and (b) prepared samples.

These findings collectively indicate that the anatase phase dominates within both prepared samples, a conclusion corroborated by the results obtained from X-ray Diffraction (XRD) analyses. As depicted in Figure 7.5, the structural features of white $NMTiO_2$ and black $NMTiO_2$ were determined by using XRD. The main XRD patterns of the white and black $NMTiO_2$ nanostructures show diffraction peaks at $2\theta = 25.3°$, 37.9°, 48.2°, 55.0°, 55.3°, and 62.8°, which are consistent with the anatase phase (A) of TiO_2.[56] In addition, small peaks are observed in white $NMTiO_2$, consistent with the pattern for rutile phase[57] (R) which are negligible compared to Anatase phase. The XRD pattern shows two small broad peaks at about 23.5° and 43.9° in the white $NMTiO_2$ nanocomposites and a broad peak at 31° in the black $NMTiO_2$ nanocomposites corresponding to the chitosan used as the template which may be partially graphitized during calcination.[58-60]

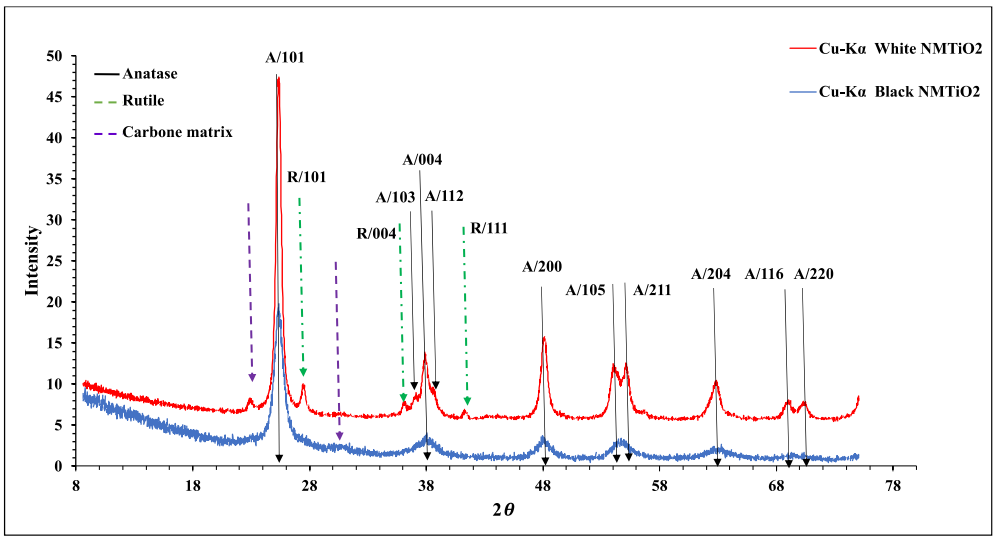

Figure 7.5. XRD patterns of the white and black $NMTiO_2$ nanostructures.

NEXAFS spectroscopy was also used to determine the geometry and bonding of N species. In NK-edge NEXAFS spectra of the black $NMTiO_2$ (Figure 7.6), there are three well-defined N 1s → π* transition features around 398.6 eV, 401.6 eV, and 406.7 eV. Peaks around 401.6 eV and 406.7 eV are common in both white and black $NMTiO_2$ spectra. The features at 401.6 eV can be associated with different N forms including amidic N groups (N species with oxygen-rich groups such as carboxyl as neighbours)[61] and potentially graphitic N referring to the N atoms directly substituting the carbon atoms.[62] The features at 406.7 eV corresponds to overlapped N1s → π* transition of different N species of e.g. pyridinic, amides and amines[61]. In the black $NMTiO_2$ spectrum, the first resonance at 398.6 eV can be associated with aromatic N-containing compounds like pyridines and pyrazines.[61] Considering the absence of these N species in chitosan, it is plausible that the structure of chitosan undergoes transformation during the calcination process in an Ar atmosphere. These changes are hypothesized to involve the incorporation of N atoms at the edges of the graphene structure, a configuration commonly referred to as pyridinic N[62]. This proposed transformation highlights the dynamic nature of the chitosan structure under specific calcination conditions, potentially leading to the formation of distinct N-containing groups at the graphene edges, contributing to the observed N 1s → π * transition features.[63] However, the nature of N attached to the surface is not certain. It should be noted that the above assignment of the features in the N NEXAF spectrum is not exhaustive and potentially could also be assigned to other species.

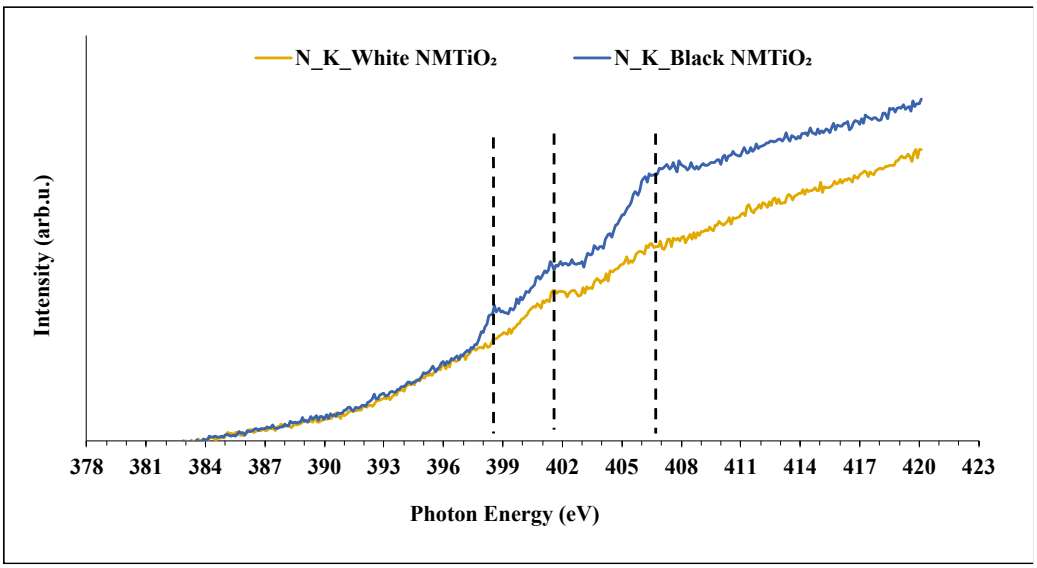

Figure 7.6. N K-edge NEXAFS spectra of white and black $NMTiO_2$ substrates

7.4.3. XPS analysis:

To further investigate the surface chemistry and elemental composition of the prepared photocatalysts, black and white $NMTiO_2$ NPs were separately sputtered under UHV with 3 keV Ar^+ and a sputter dose of $1.2 \times 10^{+15}$ ions/cm^2. After the heating process, sputtering was applied in a UHV environment at a pressure of 10^{-8} mbar and a temperature of 200 °C for a duration of 10 minutes. This procedure aimed to eliminate any moisture and hydrocarbon impurities that had been adsorbed onto the surface. Sputtering resulted in the removal of a thin layer of surface atoms, enabling an investigation into the inner layers and overall bulk structures of both black and white $NMTiO_2$ nanoparticles. After heating and sputtering, XPS was applied.

Figure 7.7 depicts the high-resolution XPS N1s spectra of both black and white $NMTiO_2$ nanoparticles. The spectra are presented in three states: without any treatment (a, a'), following a heating treatment designed for surface cleaning (b, b'), and after sputtering (c, c').

In all spectra presented in Figure 7.7, a consistent peak is evident at approximately 401 eV. This peak is likely attributed to substitutional/graphitic N[64-66] or N atoms that are bonded to different surface oxygen sites within the lattice, such as the Ti–O–N linkage.[67,68]

Another notable peak observed solely in the black $NMTiO_2$ spectrum (Figure 7.7 a-c) at 398.4 eV can be plausibly attributed to pyridinic N[64,65,69] or in the form of an O–Ti–N linkage [68,70]. Following sputtering (Figure 7.7 c and c'), new peaks emerged at around 396.5 eV for both samples. This emergence is likely linked to chemisorbed N in the graphite-like N[66] or the formation of Ti-N linkages.[68,71] Consequently, the detection of distinct N peak positions across all samples, even post-sputtering, implies the successful functionalisation of diverse N configurations within both prepared $NMTiO_2$ structures. It should be noted that N XPS in this case does not reveal the nature of the N species unambiguously. However, it can be noted that the 398.4 and 396.5 eV N species are more on

the nitride side of the possibilities and the 401 eV species on the ammonium or organic matrix side of the possibilities according to the reference.[72]

The relative XPS intensities (Table 7.3) show that black $NMTiO_2$ has three times greater N content and four times higher C content in atomic percentage compared to those of white $NMTiO_2$. The results demonstrated that the percentage of C and N was contingent upon the atmosphere environment for calcination.

Table 7-3. XPS C 1s and N 1s relatively intensity ratio in black $NMTiO_2$, and white $NMTiO_2$

Samples	N intensity (%)	C intensity (%)
Black $NMTiO_2$	0.9	13.7
White $NMTiO_2$	0.3	3.0

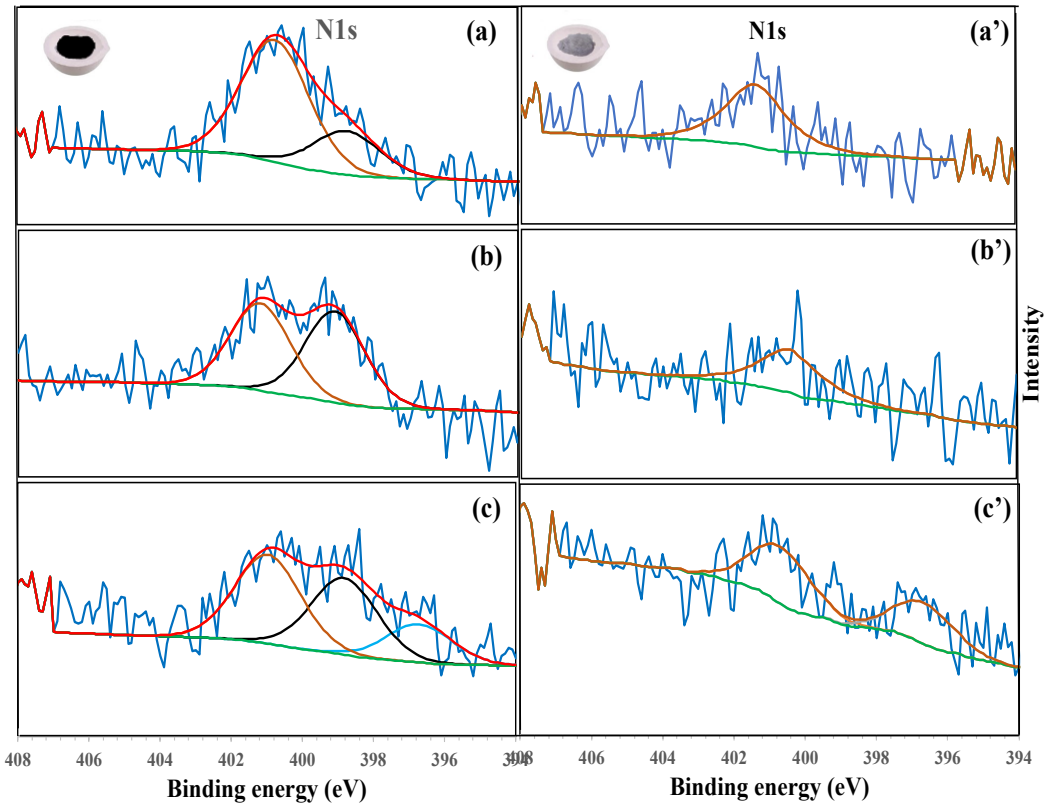

Figure 7.7. N 1s XPS spectra of (a-c) black $NMTiO_2$ and (a'-c') white $NMTiO_2$ in different conditions (a and a') Before treatment, (b and b') After heating treatment, and (c and c') After sputtering.

7.4.4. BET and BJH analysis:

In Table 7.4, Textural properties such as BET surface area, pore size, and pore volume were assessed and compared between black $NMTiO_2$, white $NMTiO_2$, and the commercially available Degussa P25 photocatalyst. To determine the specific surface area and pore volume, the BET method and BJH model were applied, which also allowed for the examination of pore size distribution.

Table 7.4 shows that the average pore size of Degussa P25 photocatalyst, black NMTiO$_2$, and white NMTiO$_2$ are 4.1 nm, 5.6 nm, and 6.00 nm, respectively. It shows that all TiO$_2$ nanoparticles represented in Table 7.4 have mesoporous structures[73].

Table 7.4 also illustrates that the BET surface area of black NMTiO$_2$ is 108.2 m^2/g, which is significantly greater than that of white NMTiO$_2$ (63.23 m^2/g) and Degussa P25 (79.15 m^2/g) which plays key role in photocatalytic processes.

As can be seen in Table 7.4, the pore volume value for black NMTiO$_2$ estimated by using BJH method is 0.19 cm^3/g, and higher than that of white NMTiO$_2$ (0.13 cm^3/g) and commercially Degussa P25 (0.15 cm^3/g) samples.

The results indicate that calcination of TiO$_2$ under Ar to remove the chitosan resulted in a black NMTiO$_2$ substrate with the advantages of the higher BET surface area and pore volume in comparison with other substrates (P25 and white NMTiO$_2$), which can be important to have more loading level and minimum aggregation of co-catalysts.

Table 7-4. BET/BJH Adsorption analysis from P25, black NMTiO$_2$, and white NMTiO$_2$

Sample	Surface Area m^2/g	Pore Volume cm^3/g	Pore Size nm
P25	79.15	0.15	4.10
Black NMTiO$_2$	108.02	0.19	5.60
White NMTiO$_2$	63.23	0.13	6.00

7.4.5. Morphology

In Figure 7.8, the morphology of white and black NMTiO$_2$ are shown. The surface roughness in Figure 7.8 (b) for the black NMTiO$_2$ is greater than Figure 7.8 (a) for the white NMTiO$_2$ which might contribute to a greater surface area, aligning with the findings from the BET results presented in Table 7.4.

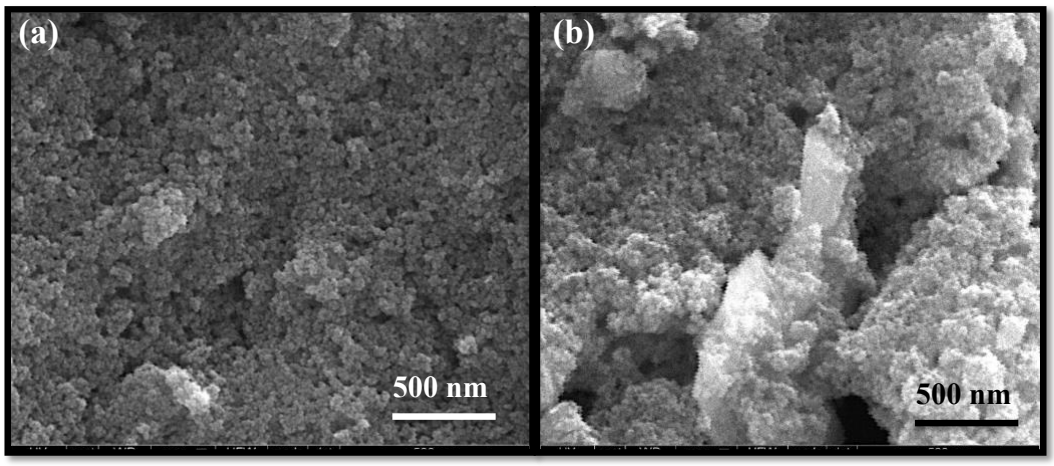

Figure 7.8. SEM images of (a) white $NMTiO_2$, and (b) black $NMTiO_2$

7.4.6. Attachment of Au_9 clusters onto the $NMTiO_2$ surfaces:

As can be seen in Figure 7.9 (a and b), XPS was used to study the binding energies and relatively intensities of Au_9 clusters after the deposition and annealing process, assessing the effect of each process on size and ratio of Au_9 NCs attached to the white and black $NMTiO_2$ semiconductors. All peak positions and intensity ratios of Au_9 NCs are also summarised in Table 7.5.

The final state effects in XPS [74] provide an opportunity to identify the Au_9 NCs size based on the Au 4f7/2 peak position and the full-width-half maximum (FWHM) [23,75-77]. Non-agglomerated (namely high binding peak, HBP) and agglomerated (namely low binding peak, LBP) Au_9 NCs exhibit binding energies between 84.6-85.2 eV and 83.7-84.4 eV, respectively.[24,78-80] Thus, cluster peaks are generally shifted to higher binding energies in comparison with larger nanoparticles.

In entries 1 and 2 in Table 7.5. (as shown in Figure 7.9 (a and b)), it can be observed that after deposition of Au_9 NCs onto white $NMTiO_2$ Au 4f7/2 binding energies appeared at 84.9 eV with 0.13 % intensity. In black $NMTiO_2$, they were observed at 85.13 eV with 0.21 %, intensity. As described above, both can be considered as non-agglomerated Au NCs (HBP). However, when switching from white $NMTiO_2$ to black $NMTiO_2$, the intensity ratio of Au_9 NCs increases from 0.13% to 0.21%. This trend implies that black $NMTiO_2$ exhibits greater efficacy in adsorbing Au_9 NCs compared to white $NMTiO_2$. This enhanced activity can potentially be attributed to the greater surface area and porosity observed in black $NMTiO_2$ (as indicated in Table 7.4), alongside higher N content (also presented in Table 7.3) compared to white $NMTiO_2$. These characteristics enable stronger interactions with the Au_9 core, forming robust complexes.

XPS peak positions and intensity ratios of Au_9 NCs were then studied after annealing. The peak position of Au_9 NCs loaded on white $NMTiO_2$ NPs was at 84.5 eV with 0.13 % intensity. The Au peak position shift to lower binding energy (LBP) means that the clusters are partially agglomerated Au_9 NCs (entry 3 in Table 7.5). In contrast, as can be seen in entry 4 in Table 7.5, when using black $NMTiO_2$ substrate, Au 4f binding energy appeared at 85.2 eV, a high binding energy peak (HBP),

with an intensity ratio of 0.18 %, which is still interpreted as non-aggregated Au_9 NCs (Figure 7.9 a and b).

The outcomes of the study revealed that black $NMTiO_2$ surfaces are superior in adsorbing Au_9 NCs to the surface and avoiding agglomeration after annealing in comparison with white $NMTiO_2$. Consequently, it can be concluded that the utilisation of black $NMTiO_2$ substrates yields enhanced binding intensities and mitigates the tendency of loaded Au_9 NCs to agglomerate, both following deposition and subsequent annealing procedures.

Table 7-5. Assessment of binding energies and intensity ratio of Au_9 NCs deposited on white $NMTiO_2$ and black $NMTiO_2$ nanoparticles after deposition and heating treatment to remove the ligands (HBP and LBP means non-agglomerated and agglomerated cluster, respectively).

Condition	Entry	Sample	HBP		LBP	
			Binding energy (eV)	Relative intensity (%)	Binding energy (eV)	Relative intensity (%)
After deposition	1	White $NMTiO_2$@Au_9NCs	84.9	0.13	-	-
	2	Black $NMTiO_2$@Au_9NCs	85.1	0.21	-	-
After annealing	3	White $NMTiO_2$@Au_9NCs	-	-	84.50	0.13
	4	Black $NMTiO_2$@Au_9NCs	85.2	0.18	-	-

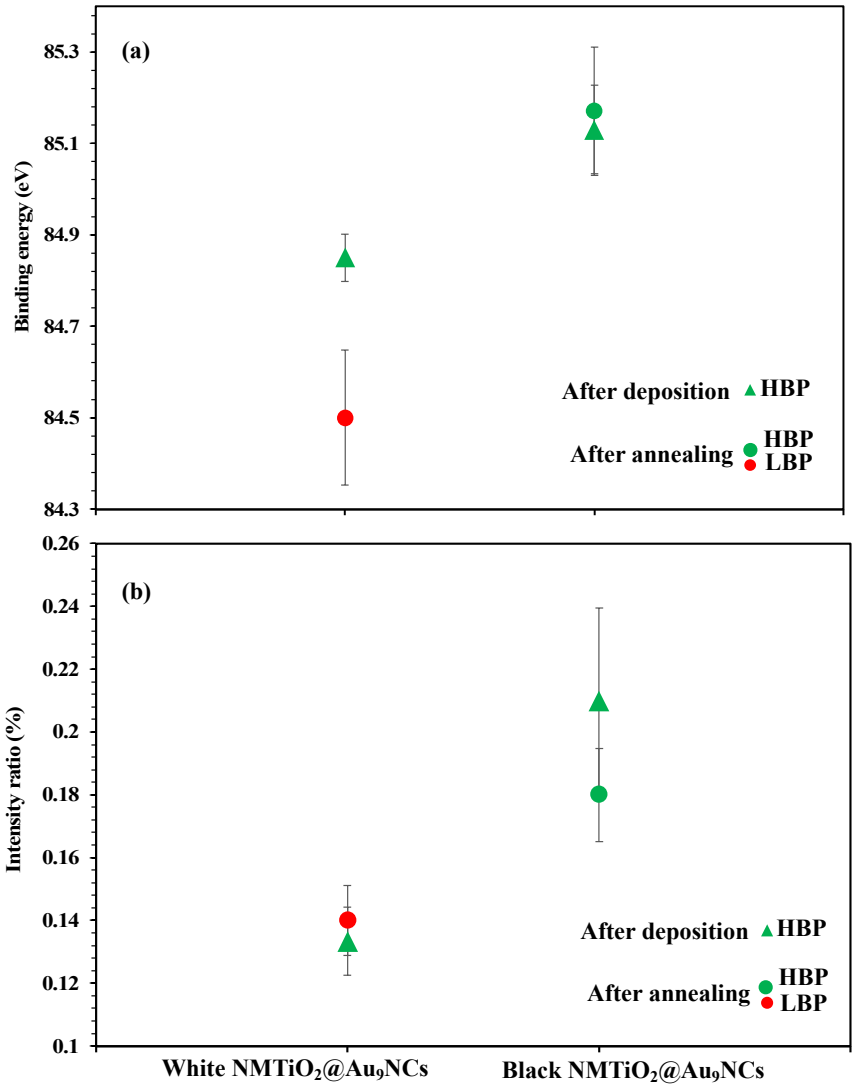

Figure 7.9. Investigation of Au_9 NCs a) binding energies and b) intensity ratios

7.5. Photocatalytic activity

7.5.1. Assessment of photocatalytic reaction kinetics for the fabricated photocatalysts and corresponding substrates:

Figure 7.10 (a) shows the MO degradation efficiency plots for prepared samples, including black and white $NMTiO_2$-supported Au_9 NCs photocatalysts and black and white $NMTiO_2$ nanoparticles. Additionally, dye degradation results were plotted in the absence of the catalysts under UV irradiation as a control. In this experiment, degradation data were shown with symbols, and their trends over time were presented as solid lines.

Degradation of MO dye solutions (3 ml of 15 ppm) over time is monitored at room temperature using 1.5 mg of the respective photocatalysts under constant UV light intensity. MO degradation efficiency plots in Figure 7.10 (a and b) show that the suspension became colourless around 20 minutes in the presence of black $NMTiO_2$@Au_9 NCs photocatalyst. In contrast, employing the white

$NMTiO_2$@Au_9 NCs photocatalyst extended the timeframe to approximately 90 minutes before the suspension became colourless. This shows that the degradation process exhibited a notably accelerated rate for photocatalysts containing black $NMTiO_2$-supported Au_9 NCs, surpassing the degradation rates of the other samples as well as UV exposure alone. Moreover, when studying the substrate variations, black $NMTiO_2$ nanoparticles displayed higher activity in comparison to the white $NMTiO_2$ nanoparticles.The significance of the photocatalyst presence was substantiated by a very slow decrease in the MO concentration over time in the UV-only control plot (blue line in Figure 7.10 (a and b)).

According to Figure 7.10 (b), MO dye degradaton results for all photocatalysts were well fitted with the first order reaction and their reaction constants were summarised in Table 7.6. Also, a **R^2 ~ 0.99** for all plots indicates high accuracy in the performed experiments. The order of the photoactivity of the prepared samples is presented in Table 7.6 based on their reaction constants which is black $NMTiO_2$ NPs@Au_9 NCs (0.176 min^{-1}) > white $NMTiO_2$ NPs@Au_9 NCs (0.056 min^{-1}) > black $NMTiO_2$ NPs (0.033 min^{-1}) > white $NMTiO_2$ NPs (0.031 min^{-1}) > UV exposure alone (0.004 min^{-1}).

Table 7-6. The MO degradation reaction constants for the prepared samples

Sample	Reaction constant (min^{-1})
Black $NMTiO_2$ NPs@Au_9 NCs	0.176
Black $NMTiO_2$ NPs	0.033
White $NMTiO_2$ NPs@Au_9 NCs	0.056
White $NMTiO_2$ NPs	0.031
UV only (without catalyst)	0.004

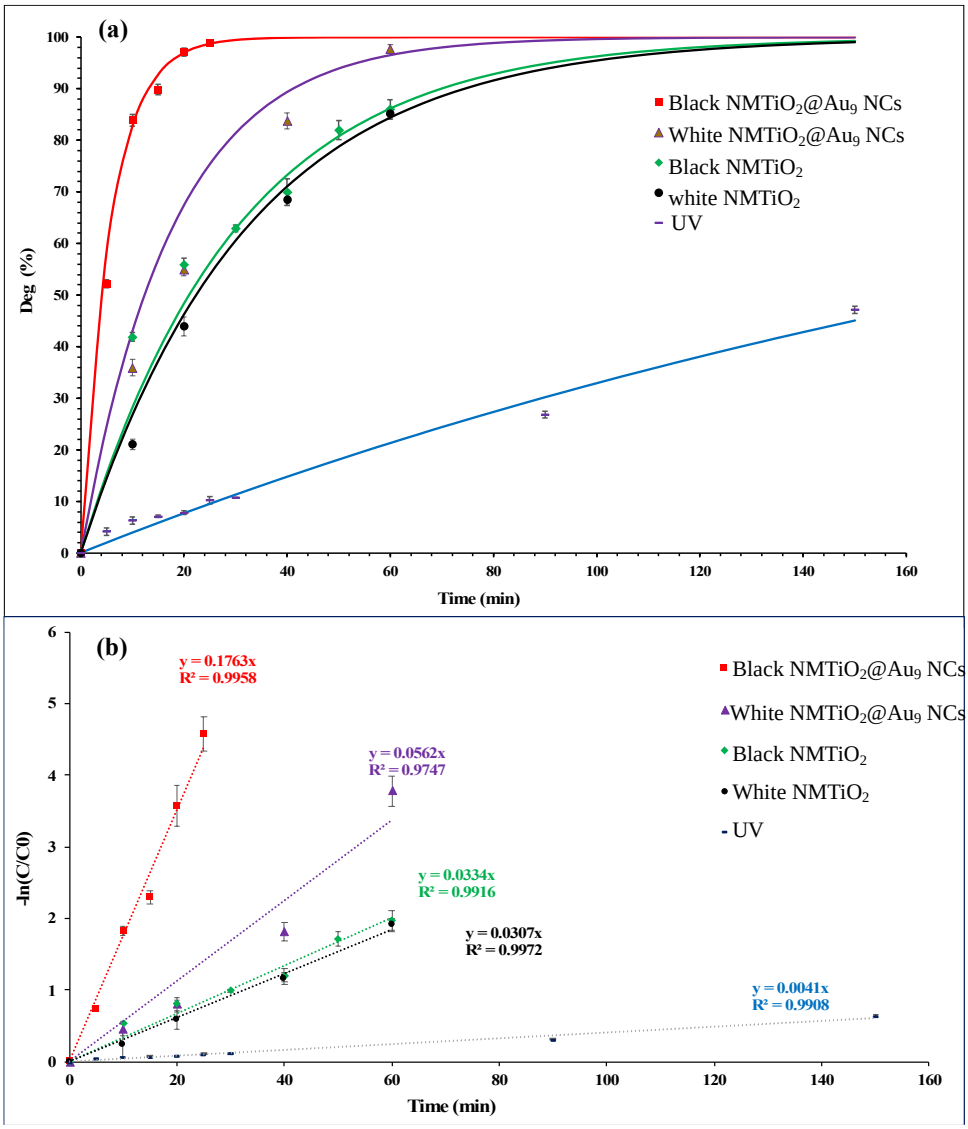

Figure 7.10. (a) MO dye degradation efficiency and (b) MO dye degradation kinetic using black NMTiO₂@ Au₉ NCs and white NMTiO₂@ Au₉ NCs photocatalysts, their relevant substrates and UV only .

7.5.2. Response surface methodology analysis:

The experimental data was fit using a second order polynomial. Curve fitting and ANOVA were performed with a self-written Python code. Different Python packages were applied for statistical analysis and plotting the graphs. The statistical analysis of RSM using ANOVA is presented in Table 7.6. Curve fitting and ANOVA were done using the Python statsmodels library. The quadratic polynomial model, presented in coded form as Equation 7.1, signifies the relationship between factors and responses.

$$\text{Degradation}(\%)=74.868-6.296\times A+10.068\times B+8.547\times C+1.809\times A\times B-0.714\times A\times C-0.116\times B\times C-5.522\times A^2-4.832\times B^2+0.553\times C^2. \quad \text{Equation 7.1}$$

Here A, B, and C are the coded factors for the MO concentration, catalyst amount, and reaction time, respectively. The values of the coded levels for minimum, middle, and maximum actual values are -1, 0, and +1, respectively as described in Table 7.1.

According to the statistical results demonestrated in Table 7.7, the model adequacy is very good and the R^2=0.997 and adjusted R^2=0.992 reveals that the model is appropriate. Also, the model is significant as the p-value (0.000) is lower than 0.05. Finally, as reported in Table 7.2, it was observed that the predicted data were close to the experimental data.[81]

Table 7-7. Analyse of variance results for the quadratic model and the significance of RSM model.

Dep. Variable:	Degradation		R-squared:	0.997
Model:	OLS		Adj. R-squared:	0.992
Method:	Least Squares		Prob (F-statistic):	0.000
	coef	std err	t	P value
const	89.699	0.624	143.709	0.000
A	-5.467	0.367	-14.887	0.000
B	10.051	0.367	27.370	0.000
C	7.838	0.367	21.343	0.000
AB	1.873	0.411	4.561	0.006
AC	-0.428	0.411	-1.041	0.345
BC	-1.373	0.411	-3.343	0.020
A^2	-5.502	0.724	-7.597	0.001
B^2	-5.872	0.724	-8.108	0.000
C^2	-0.457	0.724	-0.631	0.556

Figure 7.11 illustrates the perturbation plots providing a concise knowledge to observe the effect of each factor on dye degradation. In this plot, one factor is varied from -1 to +1, while the other ones were set to their middle-coded values (zero). For factors A (MO dye concentration) and B (catalyst amount), the sharp curvature is observed in comparison with factor C (time) representing that dye degradation is very responsive to these two factors more than time. Increasing the reaction time can increase degradation rate as the trend is linear and ascending. B (catalyst amount) trend ascends, and its slope declines after the central point. It can be concluded that adding more catalysts can negatively impact the degradation rate in excess of the centre point catalyst level. This may be due to the aggregation of the photocatalyst NPs which would reduce the availability of active sites.

To study parameter A in Figure 7.11, it should be noted that the slope of the relevant plot reduces slightly with enhancing dye concentration and it declines sharply from the centre point. It means that increasing the initial dye concentration can reduce the dye degradation rate and after the central point, its effect can be significantly increased. It was likely due to the absorption of a maximum amount of ultraviolet light by dye molecules instead of catalyst particles, inhibiting light exposure to the catalyst surface.

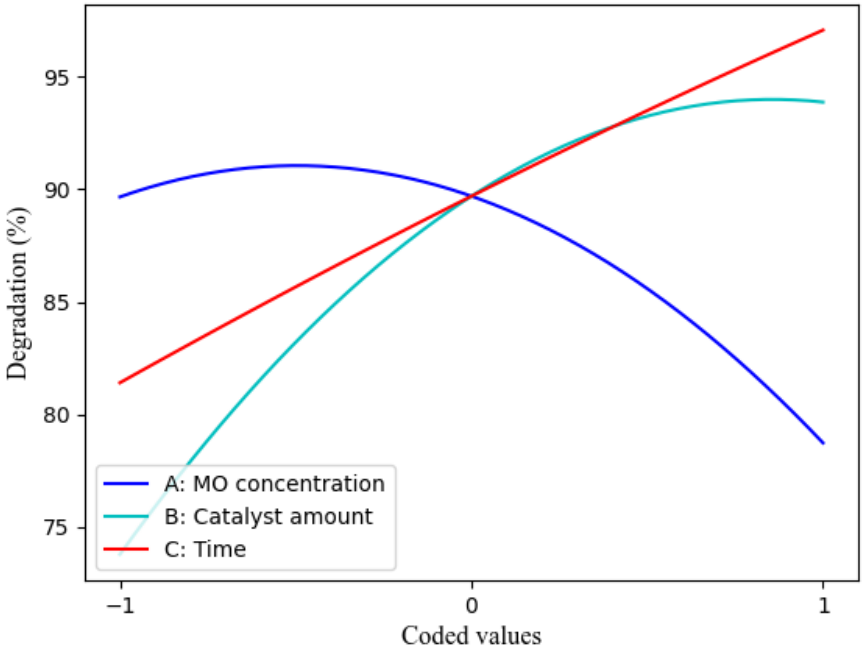

Figure 7.11. Perturbation plot of each process factor a) MO concentration, b) catalyst amount, and c) time

In each of the 3D plots in Figure 7.12, two factors are varied from their minimum to their maximum, while the third factor was kept constant at middle level. To indicate the change in response, the colour is changed from a dark blue zone to a yellow zone. Dark blue and yellow zones are considered as the lowest and highest degradation levels, respectively.

Figure 7.12 a depicts the effect of the interaction of two factors (catalyst amount and MO concentration) at constant reaction time (15 min) on the MO degradation ratio. The positive relationship is evident through the pronounced upward trend in the entire graph, extending from one mg to two mg of the catalyst. It can be noted that when working with a higher dye concentration, it becomes necessary to either increase the catalyst amount. Raising the amount of catalyst boosts the number of active sites essential for the reaction.

Figure 7.12 b shows the interaction between time and dye concentration on the MO degradation rate while the catalyst amount is costant at its middle range (1.5 mg). At this condition, the most favorable outcome for achieving optimal degradation is the MO concentration range from 10 to 15

ppm at a reaction duration of 20 minutes as indicated with the yellow zone in Figure 7.12 b. For higher MO concentrations the reaction will have to be extended.

Figure 7.12 c shows the relation between reaction time and catalyst amount for the MO degradation rate at constant MO concentration (15 ppm). When the catalyst quantity is in the range of 1.4 to 2 mg during a reaction time of 15 to 20 minutes, the degradation ratio attains its optimal state, as indicated with the yellow zone in Figure 7.12 c. This discovery underscores that both augmenting the catalyst quantity and extending the reaction time lead to enhanced degradation rates within the specified parameter range.

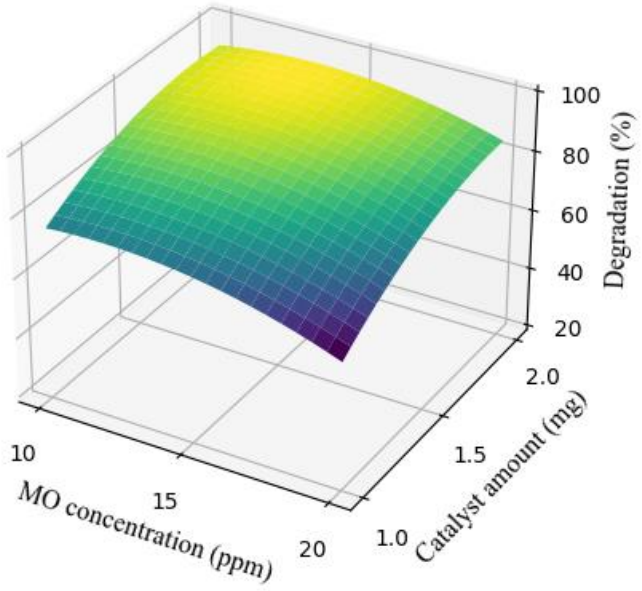

(a)

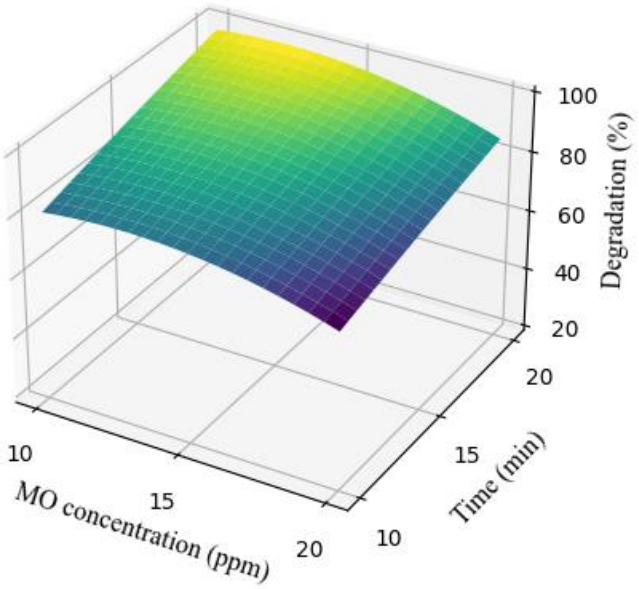

(b)

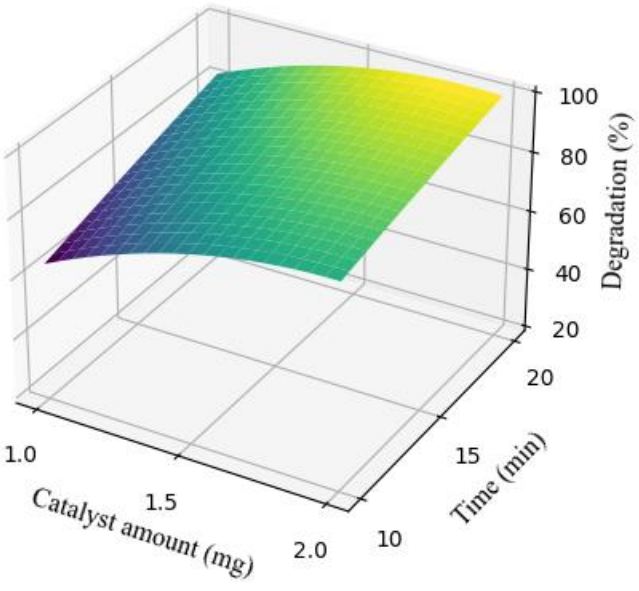

(c)

Figure 7.12.3D response surface plots of dye degradation rate in terms of (a) MO dye concentration (ppm) and catalyst amount (mg) (b) reaction time (min) and MO dye concentration (ppm), and (c) catalyst amount (mg) and reaction time (min).

7.6. Discussion and Conclusion

In this study, NMTiO$_2$ NPs were synthesised using a soft templating method. Chitosan, a sustainable choice of template, was removed by calcination under two different atmospheres

conditions, namely air and Ar, resulting in the creation of various types of substrates with several chemical and physical features including porosity, surface area, colour, adsorption capacity and photoactivity. The surface and structural features of the substrates were studied with TGA, XRD, XPS, NEXAFS, and BET. Anatase was the dominant phase for both substrates as found with XRD and NEXAFS. XPS and NEXAFS results showed that various types of N species have been successfully attached to the white and black coloured $NMTiO_2$ surfaces. However, a higher amount of N was found for black coloured $NMTiO_2$ NPs. Also, a greater specific surface area and pore volume in black $NMTiO_2$ NPs were found with BET and BJH. To create the efficient photocatalysts for MO dye degradation, Au_9 NCs were deposited onto the prepared $NMTiO_2$ surfaces. XPS showed black $NMTiO_2$ NPs could adsorb more clusters without any agglomeration even after annealing. This can be due to combination of the greater surface area and the amount of N in black $NMTiO_2$ NPs compared to white one, which can cause to adsorb more Au_9 NCs. The photocatalytic activity results revealed that the black coloured $NMTiO_2$ NPs@Au_9 NCs nanocomposites are more efficient than the white material for MO dye degradation. To investigate the photoactivity of the chosen nanocomposites, concentrations, reaction times, and catalyst quantities were varied for MO degradation, all following the central composite design framework. Subsequently, the obtained data were analysed using RSM. It was found that predictive model is accurate and significant. Due to the 3D plots, the relationship between parameters and their interactions were discussed. Within our engineered photocatalytic setups, when the MO concentration falls within the bracket of 10 to 17 ppm and the catalyst quantity ranges from 1.5 to 2 mg at constant time (15 min), the degradation rate achieves its maximum.

7.7. References:

1 Mahlambi, M. M., Ngila, C. J. & Mamba, B. B. Recent developments in environmental photocatalytic degradation of organic pollutants: the case of titanium dioxide nanoparticles—a review. *Journal of Nanomaterials* **2015**, 5-5 (2015).

2 Jiang, X., He, P., Wu, L. & Tang, L. Increased oxygen vacancies and Sc doping in ZnO promote bacterial disinfection and methyl orange degradation. *Applied Surface Science*, 158026 (2023).

3 Kumar, N., Jung, U., Jung, B., Park, J. & Naushad, M. Zinc hydroxystannate/zinc-tin oxide heterojunctions for the UVC-assisted photocatalytic degradation of methyl orange and tetracycline. *Environmental Pollution* **316**, 120353 (2023).

4 Pirkanniemi, K. & Sillanpää, M. Heterogeneous water phase catalysis as an environmental application: a review. *Chemosphere* **48**, 1047-1060 (2002).

5 Bahnemann, D. Photocatalytic water treatment: solar energy applications. *Solar energy* **77**, 445-459 (2004).

6 Mahlambi, M. M. *et al.* Comparison of rhodamine B degradation under UV irradiation by two phases of titania nano-photocatalyst. *Journal of thermal analysis and calorimetry* **110**, 847-855 (2012).

7 Suhan, M. B. K., Shuchi, S. B., Al-Mamun, M. R., Roy, H. & Islam, M. S. Enhanced UV light-driven photocatalytic degradation of methyl orange using MoO3/WO3-fluorinated TiO2 nanocomposites. *Environmental Nanotechnology, Monitoring & Management* **19**, 100768 (2023).

8 Rahmawati, T. *et al.* Green synthesis of Ag-TiO2 nanoparticles using turmeric extract and its enhanced photocatalytic activity under visible light. *Colloids and Surfaces A: Physicochemical and Engineering Aspects* **665**, 131206 (2023).

9 Regraguy, B. *et al.* Photocatalytic degradation of methyl orange in the presence of nanoparticles NiSO4/TiO2. *Nanotechnology for Environmental Engineering* **7**, 157-171 (2022).

10 Jin, R., Li, G., Sharma, S., Li, Y. & Du, X. Toward active-site tailoring in heterogeneous catalysis by atomically precise metal nanoclusters with crystallographic structures. *Chemical Reviews* **121**, 567-648 (2020).

11 Du, Y., Sheng, H., Astruc, D. & Zhu, M. Atomically precise noble metal nanoclusters as efficient catalysts: a bridge between structure and properties. *Chemical reviews* **120**, 526-622 (2019).

12 Li, S. *et al.* Size Effects of Atomically Precise Gold Nanoclusters in Catalysis. *Precision Chemistry* **1**, 14-28 (2023).

13 Yamazoe, S., Koyasu, K. & Tsukuda, T. Nonscalable Oxidation Catalysis of Gold Clusters. *Acc. Chem. Res.* **47**, 816-824 (2014). https://doi.org:10.1021/ar400209a

14 Seong, H. *et al.* Atomically precise gold nanoclusters as model catalysts for identifying active sites for electroreduction of CO2. *Angewandte Chemie* **133**, 14684-14691 (2021).

15 Li, S. *et al.* Dissecting critical factors for electrochemical CO2 reduction on atomically precise Au nanoclusters. *Angewandte Chemie* **134**, e202211771 (2022).

16 Zhu, Y., Qian, H. & Jin, R. An atomic-level Strategy for unraveling gold nanocatalysis from the perspective of Aun (SR) m nanoclusters. *Chemistry–A European Journal* **16**, 11455-11462 (2010).

17 Mousavi, H. *et al.* Au 101–rGO nanocomposite: Immobilization of phosphine-protected gold nanoclusters on reduced graphene oxide without aggregation. *Nanoscale Advances* **3**, 1422-1430 (2021).

18 Naveen, M. H., Khan, R. & Bang, J. H. Gold nanoclusters as electrocatalysts: Atomic level understanding from fundamentals to applications. *Chemistry of Materials* **33**, 7595-7612 (2021).
19 Adnan, R. H., Madridejos, J. M. L., Alotabi, A. S., Metha, G. F. & Andersson, G. G. A review of state of the art in phosphine ligated gold clusters and application in catalysis. *Advanced Science* **9**, 2105692 (2022).
20 Mousavi, H. *et al.* Graphene Bridge for Photocatalytic Hydrogen Evolution with Gold Nanocluster Co-Catalysts. *Nanomaterials* **12**, 3638 (2022).
21 Xu, Y. *et al.* Layered double hydroxides supported atomically precise Aun nanoclusters for air oxidation of benzyl alcohol: Effects of size and active site structure. *Journal of catalysis* **389**, 409-420 (2020).
22 Yang, D. *et al.* Selective CO 2 conversion tuned by periodicities in Au 8 n+ 4 (TBBT) 4 n+ 8 nanoclusters. *Nano Research* **14**, 807-813 (2021).
23 Anderson, D. P. *et al.* Chemically synthesised atomically precise gold clusters deposited and activated on titania. Part II. *Physical chemistry chemical physics* **15**, 14806-14813 (2013).
24 Ruzicka, J.-Y. *et al.* Toward control of gold cluster aggregation on TiO2 via surface treatments. *The Journal of Physical Chemistry C* **119**, 24465-24474 (2015).
25 Menard, L. D., Xu, F., Nuzzo, R. G. & Yang, J. C. Preparation of TiO2-supported Au nanoparticle catalysts from a Au13 cluster precursor: Ligand removal using ozone exposure versus a rapid thermal treatment. *Journal of Catalysis* **243**, 64-73 (2006).
26 Anderson, D. P. An investigation into the surface chemistry of supported gold phosphine clusters. (2013).
27 Adnan, R. H. & Golovko, V. B. Benzyl alcohol oxidation using gold catalysts derived from Au 8 clusters on TiO 2. *Catalysis Letters* **149**, 449-455 (2019).
28 Li, H., Zhao, G., Song, B. & Han, G. Preparation of macroporous and mesoporous TiO2 film with various solvents. *Materials Letters* **62**, 3395-3397 (2008).
29 Gajjela, S. R., Ananthanarayanan, K., Yap, C., Grätzel, M. & Balaya, P. Synthesis of mesoporous titanium dioxide by soft template based approach: characterization and application in dye-sensitized solar cells. *Energy & Environmental Science* **3**, 838-845 (2010).
30 Zhou, W. & Fu, H. Mesoporous TiO2: preparation, doping, and as a composite for photocatalysis. *ChemCatChem* **5**, 885-894 (2013).
31 Niu, B., Wang, X., Wu, K., He, X. & Zhang, R. Mesoporous titanium dioxide: Synthesis and applications in photocatalysis, energy and biology. *Materials* **11**, 1910 (2018).
32 Liu, S. *et al.* Biocompatible gradient chitosan fibers with controllable swelling and antibacterial properties. *Fibers and Polymers*, 1-9 (2022).
33 Al-Taweel, S. S., Saud, H. R., Kadhum, A. A. H. & Takriff, M. S. The influence of titanium dioxide nanofiller ratio on morphology and surface properties of TiO2/chitosan nanocomposite. *Results in Physics* **13**, 102296 (2019).
34 Joshi, M. M. *et al.* Visible light induced photoreduction of methyl orange by N-doped mesoporous titania. *Applied Catalysis A: General* **357**, 26-33 (2009).
35 Kitazawa, N., Sato, H. & Watanabe, Y. Effects of post-deposition chemical treatment on the formation of mesoporous titania films. *Journal of materials science* **42**, 5074-5079 (2007).
36 Martínez-Ferrero, E. *et al.* Nanostructured Titanium Oxynitride Porous Thin Films as Efficient Visible-Active Photocatalysts. *Advanced Functional Materials* **17**, 3348-3354 (2007).
37 Viswanathan, B. & Krishanmurthy, K. Nitrogen incorporation in TiO2: does it make a visible light photo-active material? *International Journal of Photoenergy* **2012** (2012).
38 Yasmin, L., Chen, X., Stubbs, K. A. & Raston, C. L. Optimising a vortex fluidic device for controlling chemical reactivity and selectivity. *Scientific reports* **3**, 2282 (2013).

39 Alharbi, T. M., Li, Q. & Raston, C. L. Thin film mechano-energy induced slicing of carbon nanotubes under flow. *ACS Sustainable Chemistry & Engineering* **9**, 16044-16051 (2021).
40 Alharbi, T. M., Alotaibi, A. E. & Raston, C. L. Architected C70/Graphene Oxide Composites Prepared under Continuous Flow in a Vortex Fluidic Device: Implications for Supercapacitors. *ACS Applied Nano Materials* (2023).
41 Yan, B. *et al.* Fabrication of polyaniline hydrogel: synthesis, characterization and adsorption of methylene blue. **356**, 39-47 (2015).
42 Anahita Motamedisade, A. H., D. J. Osborn, Gunther G. Andersson. Au9 clusters deposited as Co-Catalysts on S-Modified Mesoporous TiO2 for Photocatalytic Degradation of Methyl Orange. *ACS Catalysis* **submitted** (2023).
43 Fonseca, D. F. *et al.* Swellable gelatin methacryloyl microneedles for extraction of interstitial skin fluid toward minimally invasive monitoring of urea. *Macromolecular Bioscience* **20**, 2000195 (2020).
44 Wang, G., Xu, L., Zhang, J., Yin, T. & Han, D. Enhanced photocatalytic activity of TiO2 powders (P25) via calcination treatment. Inter. *J. Phot Article ID* **265760** (2012).
45 Yu, J., Su, Y., Cheng, B. & Zhou, M. Effects of pH on the microstructures and photocatalytic activity of mesoporous nanocrystalline titania powders prepared via hydrothermal method. *Journal of Molecular Catalysis A: Chemical* **258**, 104-112 (2006).
46 Wang, G., Xu, L., Zhang, J., Yin, T. & Han, D. Enhanced photocatalytic activity of powders (P25) via calcination treatment. *International Journal of Photoenergy* **2012** (2012).
47 Al-Taweel, S. S. & Saud, H. R. New route for synthesis of pure anatase TiO2 nanoparticles via utrasound-assisted sol-gel method. *J. Chem. Pharm. Res* **8**, 620-626 (2016).
48 Ma, Z.-W., Zhang, K.-N., Zou, Z.-J. & Lü, Q.-F. High specific area activated carbon derived from chitosan hydrogel coated tea saponin: One-step preparation and efficient removal of methylene blue. *Journal of Environmental Chemical Engineering* **9**, 105251 (2021).
49 Pourjavadi, A., Doroudian, M., Ahadpour, A. & Azari, S. Injectable chitosan/κ-carrageenan hydrogel designed with au nanoparticles: A conductive scaffold for tissue engineering demands. *International journal of biological macromolecules* **126**, 310-317 (2019).
50 Pourjavadi, A., Tavakoli, E., Motamedi, A. & Salimi, H. Facile synthesis of extremely biocompatible double-network hydrogels based on chitosan and poly (vinyl alcohol) with enhanced mechanical properties. *Journal of Applied Polymer Science* **135**, 45752 (2018).
51 Spoială, A. *et al.* Preparation and characterization of chitosan/TiO2 composite membranes as adsorbent materials for water purification. *Membranes* **12**, 804 (2022).
52 Ozin, G. Glycometallate surfactants Part 2: non-aqueous synthesis of mesoporous titanium, zirconium and niobium oxides. *Journal of Materials Chemistry* **9**, 1491-1500 (1999).
53 Kite, S., Sathe, D., Kadam, A., Chavan, S. & Garadkar, K. Highly efficient photodegradation of 4-nitrophenol over the nano-TiO 2 obtained from chemical bath deposition technique. *Research on Chemical Intermediates* **46**, 1255-1282 (2020).
54 Bittencourt, C. *et al.* Towards atomic resolution in sodium titanate nanotubes using near-edge X-ray-absorption fine-structure spectromicroscopy combined with multichannel multiple-scattering calculations. *Beilstein journal of nanotechnology* **3**, 789-797 (2012).
55 Mardegan, J. *et al.* Magnetic and electronic properties at the γ− Al 2 O 3/SrTiO 3 interface. *Physical Review B* **99**, 134423 (2019).
56 Zhang, G. *et al.* Enhanced photocatalytic activity of TiO2/carbon@ TiO2 core–shell nanocomposite prepared by two-step hydrothermal method. *Applied surface science* **311**, 384-390 (2014).
57 Du, J. & Sun, H. Polymer/TiO2 hybrid vesicles for excellent UV screening and effective encapsulation of antioxidant agents. *ACS applied materials & interfaces* **6**, 13535-13541 (2014).

58 Zhu, Z., Li, A., Zhong, S., Liu, F. & Zhang, Q. Preparation and characterization of polymer-based spherical activated carbons with tailored pore structure. *Journal of applied polymer science* **109**, 1692-1698 (2008).
59 Wu, H. *et al.* Calcined chitosan-supported layered double hydroxides: An efficient and recyclable adsorbent for the removal of fluoride from an aqueous solution. *Materials* **10**, 1320 (2017).
60 Barakat, N. A., Ahmed, E., Amen, M. T., Abdelkareem, M. A. & Farghali, A. N-doped Ni/C/TiO2 nanocomposite as effective photocatalyst for water splitting. *Materials Letters* **210**, 317-320 (2018).
61 Kiersch, K., Kruse, J., Regier, T. Z. & Leinweber, P. Temperature resolved alteration of soil organic matter composition during laboratory heating as revealed by C and N XANES spectroscopy and Py-FIMS. *Thermochimica acta* **537**, 36-43 (2012).
62 Shlyakhova, E. *et al.* Synthesis of nitrogen-containing porous carbon using calcium oxide nanoparticles. *physica status solidi (b)* **251**, 2607-2612 (2014).
63 Khan, A., Goepel, M., Colmenares, J. C. & Gläser, R. Chitosan-based N-doped carbon materials for electrocatalytic and photocatalytic applications. *ACS Sustainable Chemistry & Engineering* **8**, 4708-4727 (2020).
64 Matsoso, B. J. *et al.* Time-dependent evolution of the nitrogen configurations in N-doped graphene films. *RSC advances* **6**, 106914-106920 (2016).
65 Li, O. L., Chiba, S., Wada, Y., Lee, H. & Ishizaki, T. Selective nitrogen bonding states in nitrogen-doped carbon via a solution plasma process for advanced oxygen reduction reaction. *RSC advances* **6**, 109354-109360 (2016).
66 Lazar, P., Mach, R. & Otyepka, M. Spectroscopic fingerprints of graphitic, pyrrolic, pyridinic, and chemisorbed nitrogen in N-doped graphene. *The Journal of Physical Chemistry C* **123**, 10695-10702 (2019).
67 Liu, H. *et al.* Nitrogen-doped black TiO 2 spheres with enhanced visible light photocatalytic performance. *SN Applied Sciences* **1**, 1-9 (2019).
68 Hsu, J.-C., Lin, Y.-H. & Wang, P. W. X-ray photoelectron spectroscopy analysis of nitrogen-doped TiO2 films prepared by reactive-ion-beam sputtering with various NH3/O2 gas mixture ratios. *Coatings* **10**, 47 (2020).
69 Pillar-Little, T. & Kim, D. Y. Differentiating the impact of nitrogen chemical states on optical properties of nitrogen-doped graphene quantum dots. *RSC advances* **7**, 48263-48267 (2017).
70 Le, P. H. *et al.* Enhanced photocatalytic performance of nitrogen-doped TiO2 nanotube arrays using a simple annealing process. *Micromachines* **9**, 618 (2018).
71 Braun, A. *et al.* Nitrogen doping of TiO2 photocatalyst forms a second eg state in the oxygen 1s NEXAFS pre-edge. *The Journal of Physical Chemistry C* **114**, 516-519 (2010).
72 Chastain, J. & King Jr, R. C. Handbook of X-ray photoelectron spectroscopy. *Perkin-Elmer Corporation* **40**, 221 (1992).
73 Bonelli, B., Esposito, S. & Freyria, F. S. Mesoporous Titania: Synthesis, properties and comparison with non-porous titania. *Titanium dioxide*, 119-141 (2017).
74 Peters, S., Peredkov, S., Neeb, M., Eberhardt, W. & Al-Hada, M. Size-dependent XPS spectra of small supported Au-clusters. *Surface science* **608**, 129-134 (2013).
75 Krishnan, G. *et al.* Investigation of ligand-stabilized gold clusters on defect-rich titania. *The Journal of Physical Chemistry C* **121**, 28007-28016 (2017).
76 Anderson, D. P. *et al.* Chemically-synthesised, atomically-precise gold clusters deposited and activated on titania. *Physical chemistry chemical physics* **15**, 3917-3929 (2013).
77 Al Qahtani, H. S. *et al.* Aggregation behavior of ligand-protected Au9 clusters on sputtered atomic layer deposition TiO2. *The Journal of Physical Chemistry C* **121**, 10781-10789 (2017).

78 Al Qahtani, H. S. *et al.* Atomically resolved structure of ligand-protected Au9 clusters on TiO2 nanosheets using aberration-corrected STEM. *The Journal of Chemical Physics* **144**, 114703 (2016).
79 Alotabi, A. S., Gibson, C. T., Metha, G. F. & Andersson, G. G. Investigation of the Diffusion of Cr2O3 into different phases of TiO2 upon Annealing. *ACS Applied Energy Materials* **4**, 322-330 (2021).
80 Alotabi, A. S. *et al.* Suppression of phosphine-protected Au 9 cluster agglomeration on SrTiO 3 particles using a chromium hydroxide layer. *Materials Advances* **3**, 3620-3630 (2022).
81 Soleimani, S., Heydari, A. & Fattahi, M. Swelling prediction of calcium alginate/cellulose nanocrystal hydrogels using response surface methodology and artificial neural network. *Industrial Crops and Products* **192**, 116094 (2023).

CHAPTER 8: DISCUSSION AND CONCLUSION

Transitioning to more sustainable industrial processes has become increasingly important as energy demand, fossil fuel depletion, and environmental pollution have become substantial global challenges. This study focuses on addressing the pressing issue of clean drinking water scarcity, a potential ecological disaster threatening human well-being. One of the primary contributors to water pollution today is hazardous run-offs from chemical industries like textile, cosmetic, and dye manufacturing.[1,2]

Methyl orange (MO) is a commonly used dye in chemistry and laboratory experiments. It is an azo dye, which means it contains the azo group (-N=N-) as part of its chemical structure[3]. Methyl orange dye poses environmental hazards when mishandled or improperly disposed of, encompassing concerns such as potential toxicity due to its components, persistent presence in the environment, bioaccumulation in organisms, water pollution from discharge into water bodies, and alteration of water quality.[4,5]

To combat these environmental hazards effectively, this research explores the application of semiconductor-mediated photocatalysis. This approach offers several advantages, including cost-effectiveness, reduced environmental impact, recyclability, accessibility, and exceptional degradation effectiveness. Various procedures are used to increase the photocatalytic efficiency of semiconductors, falling into two categories: morphological modifications and chemical modifications.[6-11]

Morphological modifications involve creating porous networks to increase the specific surface area and active sites for photocatalysis. Chemical modifications, on the other hand, entail incorporating additional components onto the semiconductor's surface to inhibit the recombination of photogenerated electron-hole pairs, form the strong binding between co-catalysts and semiconductor surfaces, and further enhance photocatalytic activity.[12,13]

In this study, Au_9 nanoclusters (NCs), which are smaller than Au nanoparticles (NPs), are employed to alter surface characteristics. The catalytic traits of these Au NCs are significantly influenced by the number of atoms composing them, underscoring the importance of preventing their aggregation.[14,15] Aggregation could result in an enlargement of these nanoclusters, leading to the loss of properties that depend on their size.[15]

8.1. Surface design to prevent Au_9 NC agglomeration.

To control agglomeration, our first effort was to use a morphological modification approach and enhanced surface area and porosity. In Chapter 5, as this study's first project, we prepared mesoporous TiO_2 ($MTiO_2$) films. XPS results showed that Au_9 NCs undergo agglomeration after

deposition and annealing to remove the ligands (See Table 8.2 entries 1 and 7). We concluded that the surface porosity is insufficient to prevent Au_9 NC mobility and agglomeration.

In Chapter 6, to study the effect of the semiconductor forms on Au_9 NC adsorption and agglomeration, we synthesised mesoporous TiO_2 nanopowders with Au_9 NCs decorated. XPS results in Table 8.2 entries 3 and 9 showed that although the size of Au_9 NCs did not change much after deposition, Au_9 NCs were agglomerated after removing the ligands by annealing and, subsequently, their size was increased.

Consequently, these observations prompted us to try another type of surface modification to reduce the probability of Au_9 Nc agglomeration by adding influential functional groups on the semiconductor surface and creating a strong bond between the Au_9 Nc and the added functional groups. We also aimed to increase the amount of Au_9 NC loaded onto the surface to increase photoactivity. As a result, our hypothesis to create a strong bond between the Au_9 NCs and the surface of the substrate could also help us to achieve this goal. With the knowledge that Au elements have a strong affinity for bonding with S functional groups, we first attempted to modify the prepared $MTiO_2$ surfaces by MPTMS grafting in Chapters 5 and 6.

The findings from Chapters 5 and 6, where XPS and BET analyses were conducted, provided compelling evidence that surface functionalisation with thiol (SH) functional groups had a significant impact. Despite the observed reduction in surface area and pore volume, as indicated in Table 8.1 (with values of 61 compared to 117 m^2/g for BET surface area and 0.1 compared to 0.19 cm^3/g for pore volume), this functionalisation played a crucial role in preventing agglomeration and increasing the loading of Au_9 NCs on the surface. This positive outcome was confirmed by the XPS results presented in Table 8.2, specifically entries 2, 4, 8, and 10. This represents a noteworthy achievement in our study.

Continuing our research, we aimed to synthesise a substrate that could effectively bond with Au through functional groups while maintaining a high surface area. In Chapter 7, we adopted a different synthetic approach compared to Chapter 6. We utilised chitosan as a natural template and a source of hydrocarbon and N. This method offered significant advantages, including time and energy savings, reduced material usage, and cost-effectiveness, as both types of modifications occurred simultaneously on the surface through a single-step calcination process. By employing two distinct atmospheres, air, and Ar, during the calcination process, we successfully synthesised two different N-modified TiO_2 ($NMTiO_2$) variants with distinct physical appearances and chemical properties: white and black $NMTiO_2$. Our BET and XPS results revealed that the black $NMTiO_2$, calcined under Ar, exhibited superior characteristics compared to the white $NMTiO_2$. Specifically, it possessed a higher surface area (108 m^2/g > 63.2 m^2/g), greater pore volume (0.19 cm^3/g > 0.13 cm^3/g), and higher N content (0.9% > 0.3%), as indicated in Table 8.1 and Table 7.3. Furthermore, XPS analysis of

binding energies and intensity ratios for Au confirmed that this substrate was more effective in adsorbing a higher level of Au_9 NCs and preventing their agglomeration after annealing. This is evident when comparing Table 8.2 entries 6 and 12 for black $NMTiO_2/Au_9$ NCs with entries 5 and 11 for white $NMTiO_2/Au_9$ NCs.

Table 8-1. BET and BJH adsorption analysis for $MTiO_2$, $SMTiO_2$, black $NMTiO_2$, and white $NMTiO_2$.

Sample	Surface Area m^2/g	Pore Volume cm^3/g	Pore Size nm
$MTiO_2$	117.0	0.19	4.4
$SMTiO_2$	61.0	0.10	4.4
Black $NMTiO_2$	108.0	0.19	5.6
White $NMTiO_2$	63.2	0.13	6.0

Table 8-2. Study of binding energies and relative intensity of Au_9 NCs deposited on $MTiO_2$, $SMTiO_2$, white $NMTiO_2$@Au_9NCs, and Black $NMTiO_2$@Au_9NCs after deposition and annealing. (HBP and LBP mean non-agglomerated and agglomerated clusters, respectively)

Condition	Entry	Sample	HBP		LBP	
			Binding energy (eV)	Relative intensity (%)	Binding energy (eV)	Relative intensity (%)
After deposition	1	$MTiO_2$ Film/Au_9NCs	-	-	84.4	0.1
	2	$SMTiO_2$ Film/Au_9NCs	84.8	1.1	-	-
	3	$MTiO_2$ NPs/Au_9NCs	84.9	0.11	-	-
	4	$SMTiO_2$ NPs/Au_9NCs	84.9	0.6	-	-
	5	White $NMTiO_2/Au_9$NCs	84.9	0.13	-	-
	6	Black $NMTiO_2/Au_9$NCs	85.1	0.21	-	-
After annealing	7	$MTiO_2$ Film/Au_9NCs	85.1	0.009	83.6	0.08
	8	$SMTiO_2$ Film/Au_9NCs	84.6	1.0	-	-

9	$MTiO_2$ NPs/Au_9NCs	-	-	84.3	0.10
10	$SMTiO_2$ NPs/Au_9NCs	85.1	0.6	-	-
11	White $NMTiO_2$/Au_9NCs	-	-	84.5	0.13
12	Black $NMTiO_2$/Au_9NCs	85.2	0.18	-	-

8.2. Comparison between activity of the prepared photocatalysts.

In the next step, we assessed the photocatalytic activity of the prepared photocatalysis systems in chapters 6 and 7 in the degradation of MO dye. All photocatalysts' results were well-fitted with first-order reaction kinetics, and their reaction constants are summarised in Table 8.3. The high R^2 value (~0.99) for all plots indicates the experiments' high accuracy. The photoactivity order of the prepared samples, based on their reaction constants, is presented in Table 8.3 as follows: black $NMTiO_2$ NPs/Au_9 NCs (0.176 min^{-1}) > $SMTiO_2$ NPs/Au_9 NCs (0.149 min^{-1}) > $SMTiO_2$ NPs (0.070 min^{-1}) > white $NMTiO_2$ NPs/Au_9 NCs (0.056 min^{-1}) > black $NMTiO_2$ NPs (0.033 min^{-1}) > white $NMTiO_2$ NPs (0.031 min^{-1}).

Figure 8.1 illustrates the reduction of methyl orange concentration over time due to photocatalytic degradation in various experimental setups, including different catalysis systems such as $SMTiO_2$ NPs/Au_9 NCs, black $NMTiO_2$ NPs/Au_9 NCs and white $NMTiO_2$ NPs/Au_9 NCs as well as their respective substrates lacking Au_9 NCs.

In Figure 8.1, the efficiency of the synthesised catalysts was compared, and their trends were plotted. Specifically, the suspension lost its colour within different time intervals: around 23 minutes for black $NMTiO_2$ NPs/Au_9 NCs, and 25 minutes when using $SMTiO_2$ NPs/Au_9 NCs. In contrast, employing white $NMTiO_2$ NPs/Au_9 NCs photocatalyst and $SMTiO_2$ NPs, along with white and black $NMTiO_2$ NPs, extended the time required for dye degradation to over 60 minutes.

The reaction constants and efficiency results indicate that both nanocomposites containing un-agglomerated Au_9 NCs which are black $NMTiO_2$ NPs/Au_9 NCs and $SMTiO_2$ NPs/Au_9 NCs can further enhance the dye degradation rate compared to white one with agglomerated Au_9 NCs and all substrates without cocatalyst.

Additionally, in the analysis of substrate variations, it is worth noting that $SMTiO_2$ NPs demonstrated greater activity, as indicated by its reaction constant in Table 8.3 (0.070 min^{-1}), in comparison to black $NMTiO_2$ (0.033 min^{-1}) and white $NMTiO_2$ (0.031 min^{-1}) NPs. This discrepancy in activity can likely be attributed to the presence of N atoms within the $NMTiO_2$ structure, which may serve as recombination centres in the catalytic process.[28,29]

Significantly, the deposition of Au_9 NCs onto the surfaces of black $NMTiO_2$ NPs has a profound impact on the photoactivity of the nanocomposite. The reaction constant for black $NMTiO_2$ NPs/Au_9 NCs is notably high at 0.176 min^{-1}, which is nearly six times greater than that of its substrate (0.033 min^{-1}). Similarly, for $SMTiO_2$ NPs/Au_9 NCs, the reaction constant is 0.149 min^{-1}, almost double the value of its substrate (0.070 min^{-1}). This substantial increase in reaction constant underscores the significant enhancement in photoactivity achieved through the deposition of Au_9 NCs on the respective substrates.

Table 8-3. Reaction constants of methyl orange dye degradation using different photocatalytic systems

Sample	Reaction constant (min^{-1})
Black $NMTiO_2$ NPs/Au_9 NCs	0.176
$SMTiO_2$ NPs/ Au_9 NCs	0.149
$SMTiO_2$ NPs	0.070
White $NMTiO_2$ NPs/Au_9 NCs	0.056
Black $NMTiO_2$ NPs	0.033
White $NMTiO_2$ NPs	0.031

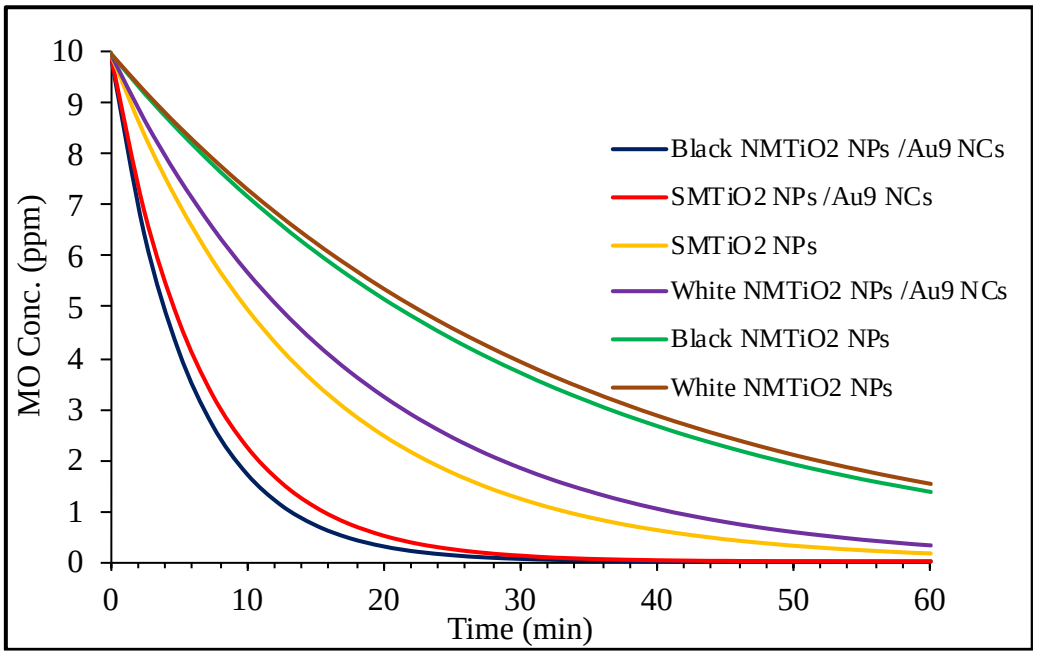

Figure 8.1. Reduction in methyl orange concentration over time due to different photocatalytic systems

Our results unequivocally designated $SMTiO_2$/Au_9 NCs and black $NMTiO_2$/Au_9 NCs nanocomposites as promising and efficient photocatalysts for MO dye wastewater treatment, surpassing their unfunctionalised counterparts and respective substrates.

To comprehensively investigate the photoactivity of these selected nanocomposites, in Chapters 6 and 7 a series of experiments varying dye concentrations, reaction times, and catalyst quantities were executed based on the central composite design method (CCD) at three levels. This approach has been widely applied in various engineering fields, particularly in processes related to water and wastewater treatments.[16-19] The findings were rigorously analysed using response surface methodology (RSM), identifying the significant impacts of parameters and their interactions on MO degradation. The advantage of using this methodology is that it reduces the number of experiments and lowers the associated costs and time required to investigate process parameters and their interactions. We also employed Python programming language for the analysis of photocatalytic reactions.

In summation, our multi-chapter exploration has unveiled the potential of S and N-functionalised $MTiO_2$ surfaces in enhancing the photoactivity of Au_9 NCs-decorated photocatalysts. However, Advantages and disadvantages of $SMTiO_2$ and black $NMTiO_2$ as the substrates used for preparation of our most photoactive systems are briefly summarised in Table 8.4. Accordingly, both substrates are efficient in adsorbing the Au_9 NCs and preventing their agglomeration to create the efficient photocatalysts. However, $NMTiO_2$ because of having more surface area and pore volume is superior to $SMTiO_2$ to make the photocatalysts as the comparison between their photocatalytic activities in Figure 8.1 confirms our assertion.

These findings significantly contribute to the formation of advanced materials for environmental remediation, emphasizing the pivotal role of nanotechnology in addressing contemporary environmental challenges.

Table 8-4. Advantages and disadvantages of two different substrates

$SMTiO_2$		Black $NMTiO_2$	
Advantage	Disadvantage	Advantage	Disadvantage
Prevention of agglomeration of Au_9 NCs	Reduced surface area	High surface area:	Surface adsorption probability of dyes which needs to be tested
Increased loading of Au_9 NCs	Reduced pure volume	Greater pore volume	Potential process complexity which needs more characterisation to study N type

			attached to the surface or lattice
Strong bond formation with Au.	The probability of decreased loading efficiency for other elements than Au as indicated by the reduction in surface area and pore volume.	Cost-effective and energy-efficient synthetic method as functionalisation process does not need an extra step and material	Low photoactivity without cocatalyst
Easy detection of surface characteristics and S type attached to the surface.	Extra stage to functionalise the surface of $MTiO_2$	High N content	
Excellent dispersity of Au onto the surface	Possible constraints on other applications where a larger surface area and pore volume are required.	Prevention of agglomeration of Au_9 NCs	
Anatase crystallinity phase is prominent		Effective adsorption of Au_9 NCs	
High photoactivity		Diversity in template selection and functional groups	
		Anatase crystallinity phase is prominent	

8.3. Reference

1 Madhav, S. *et al.* Water pollutants: sources and impact on the environment and human health. *Sensors in water pollutants monitoring: Role of material*, 43-62 (2020).

2 Ghangrekar, M. & Chatterjee, P. Water pollutants classification and its effects on environment. *Carbon nanotubes for clean water*, 11-26 (2018).

3 Al-Qaradawi, S. & Salman, S. R. Photocatalytic degradation of methyl orange as a model compound. *Journal of Photochemistry and photobiology A: Chemistry* **148**, 161-168 (2002).

4 Aljuaid, A. *et al.* g-C3N4 Based Photocatalyst for the Efficient Photodegradation of Toxic Methyl Orange Dye: Recent Modifications and Future Perspectives. *Molecules* **28**, 3199 (2023).

5 Rajput, R. B., Jamble, S. N. & Kale, R. B. Solvothermal synthesis of anatase TiO2 for the detoxification of methyl orange dye with improved photodegradation efficiency. *Engineered Science* **17**, 176-184 (2021).

6 Li, Y., Li, X., Li, J. & Yin, J. Photocatalytic degradation of methyl orange by TiO2-coated activated carbon and kinetic study. *Water research* **40**, 1119-1126 (2006).

7 Tripathy, N. *et al.* Photocatalytic degradation of methyl orange dye by ZnO nanoneedle under UV irradiation. *Materials Letters* **136**, 171-174 (2014).

8 Waghchaure, R. H., Adole, V. A. & Jagdale, B. S. Photocatalytic degradation of methylene blue, rhodamine B, methyl orange and Eriochrome black T dyes by modified ZnO nanocatalysts: A concise review. *Inorganic Chemistry Communications*, 109764 (2022).

9 Tran, V. A., Kadam, A. N. & Lee, S.-W. Adsorption-assisted photocatalytic degradation of methyl orange dye by zeolite-imidazole-framework-derived nanoparticles. *Journal of Alloys and Compounds* **835**, 155414 (2020).

10 Weldegebrieal, G. K. & Sibhatu, A. K. Photocatalytic activity of biosynthesized α-Fe2O3 nanoparticles for the degradation of methylene blue and methyl orange dyes. *Optik* **241**, 167226 (2021).

11 Halmann, M. M. *Photodegradation of water pollutants*. (CRC press, 1995).

12 Yang, X. *et al.* Functionalization of mesoporous semiconductor metal oxides for gas sensing: Recent advances and emerging challenges. *Advanced Science* **10**, 2204810 (2023).

13 Machado, A. E. *et al.* Applications of mesoporous ordered semiconductor materials—case study of TiO2. *Solar Radiation Applications*, 87-118 (2015).

14 Mousavi, H. *et al.* Factors influencing catalytic activity of size-specific triphenylphosphine-ligated gold nanoclusters in the electrocatalytic hydrogen evolution reaction. *The Journal of Physical Chemistry C* **126**, 246-260 (2021).

15 Adnan, R. H., Madridejos, J. M. L., Alotabi, A. S., Metha, G. F. & Andersson, G. G. A review of state of the art in phosphine ligated gold clusters and application in catalysis. *Advanced Science* **9**, 2105692 (2022).

16 Mousavi, M., Soleimani, M., Hamzehloo, M., Badiei, A. & Ghasemi, J. B. Photocatalytic degradation of different pollutants by the novel gCN-NS/Black-TiO2 heterojunction photocatalyst under visible light: Introducing a photodegradation model and optimization by response surface methodology (RSM). *Materials Chemistry and Physics* **258**, 123912 (2021).

17 Hosseini, O., Zare-Shahabadi, V., Ghaedi, M. & Azqhandi, M. A. Experimental design, RSM and ANN modeling of tetracycline photocatalytic degradation using LDH@ CN. *Journal of Environmental Chemical Engineering* **10**, 108345 (2022).

18 Mortazavian, S., Saber, A. & James, D. E. Optimization of photocatalytic degradation of acid blue 113 and acid red 88 textile dyes in a UV-C/TiO2 suspension system: application of response surface methodology (RSM). *Catalysts* **9**, 360 (2019).

19 AttariKhasraghi, N., Zare, K., Mehrizad, A., Modirshahla, N. & Behnajady, M. A. Achieving the enhanced photocatalytic degradation of ceftriaxone sodium using CdS-gC 3 N 4 nanocomposite under visible light irradiation: RSM modeling and optimization. *Journal of Inorganic and Organometallic Polymers and Materials* **31**, 3164-3174 (2021).
20 Krishnan, G. *et al.* Investigation of ligand-stabilized gold clusters on defect-rich titania. *The Journal of Physical Chemistry C* **121**, 28007-28016 (2017).
21 Anderson, D. P. *et al.* Chemically-synthesised, atomically-precise gold clusters deposited and activated on titania. *Physical chemistry chemical physics* **15**, 3917-3929 (2013).
22 Anderson, D. P. *et al.* Chemically synthesised atomically precise gold clusters deposited and activated on titania. Part II. *Physical chemistry chemical physics* **15**, 14806-14813 (2013).
23 Al Qahtani, H. S. *et al.* Aggregation behavior of ligand-protected Au9 clusters on sputtered atomic layer deposition TiO2. *The Journal of Physical Chemistry C* **121**, 10781-10789 (2017).
24 Al Qahtani, H. S. *et al.* Atomically resolved structure of ligand-protected Au9 clusters on TiO2 nanosheets using aberration-corrected STEM. *The Journal of Chemical Physics* **144**, 114703 (2016).
25 Ruzicka, J.-Y. *et al.* Toward control of gold cluster aggregation on TiO2 via surface treatments. *The Journal of Physical Chemistry C* **119**, 24465-24474 (2015).
26 Alotabi, A. S., Gibson, C. T., Metha, G. F. & Andersson, G. G. Investigation of the Diffusion of Cr2O3 into different phases of TiO2 upon Annealing. *ACS Applied Energy Materials* **4**, 322-330 (2021).
27 Alotabi, A. S. *et al.* Suppression of phosphine-protected Au 9 cluster agglomeration on SrTiO 3 particles using a chromium hydroxide layer. *Materials Advances* **3**, 3620-3630 (2022).
28 Khan, S. *et al.* Revealing the true impact of interstitial and substitutional nitrogen doping in TiO 2 on photoelectrochemical applications. *Journal of Materials Chemistry A* **9**, 12214-12224 (2021).
29 Hou, R. *et al.* The promoted photocatalytic mechanism of N-doped graphene/TiO2 composites: From experiment to theory. *Diamond and Related Materials* **126**, 109107 (2022).

CHAPTER 9: FUTURE WORKS

Based on our research findings to date, several avenues for continued investigation present themselves:

1- Enhanced investigation of black $NMTiO_2$ surface and type of N attached to the surface: Further characterisation of black $NMTiO_2$ surfaces including UPS and UV-Vis with a focus on studying whether adding N has changed the band gap. Study the N species type attached to the surface or lattice will shed light on the interplay between the modified surface, the N elements, and the Au clusters, potentially uncovering novel properties for advanced applications.

2- Exploration of Au cluster attachment: Another intriguing possibility is a comprehensive study and comparison of Au clusters adhered to the $MTiO_2$ surface in terms of their photocatalytic activity. This may uncover synergistic effects arising from different combinations of metal clusters and photocatalysts, potentially leading to breakthroughs in photocatalytic reaction studies.

3- Comparative study of photocatalytic activity for dye degradation: A comprehensive comparison of the photocatalytic activities of various prepared photocatalysts in the degradation of diverse types of dyes is a critical step. This comparative analysis could unveil catalyst-specific affinities and provide insights into optimal choices for different dye degradation applications.

4- Assessment of photocatalytic activity for different fields of science and applications: Our investigation could be broadened by examining the photocatalytic activity of the prepared photocatalysts in diverse applications. For instance, exploring their efficacy in water splitting could uncover their potential use for sustainable energy generation.

5- Investigation of dye adsorption on photocatalytic surfaces: Dye adsorption onto catalyst surfaces is an integral component of the photocatalytic dye degradation process and is worthy of a more thorough evaluation. Further research to this effect will contribute to our understanding of the intricate mechanisms underlying photocatalysis and shed light on the dynamic interplay between the catalyst and dye molecules. Through this investigation, we anticipate findings surrounding the kinetics, thermodynamics, and factors influencing the adsorption process. This knowledge will not only enrich our understanding of dye-catalyst interactions but also empower us to fine-tune and optimize photocatalytic systems for enhanced efficiency in environmental remediation and other pertinent applications.

6- Application of response surface methodology (RSM): The study focused on examining the impact of various independent parameters on dye degradation using RSM. The efficiency of this approach so far indicates RSM would also be suitable for comprehensively studying the parameters employed in substrate fabrication. A key response variable to model response will be

the size of pores, and appropriate parameters would include pH, amount of Ti precursors, and templates. This data-driven approach could uncover optimal conditions and lead to a better understanding of the interplay between the influencing parameters and the resulting response and performance of chemical reactions for substrate design.

7- Application of artificial neural network (ANN) for photocatalytic activity study: Artificial intelligence (AI) has found widespread use in various scientific and technological fields. One popular AI technique for scientific applications is the artificial neural network. In many recent published papers[1-7] in the RSM field, ANN is utilised alongside RSM to compare their performance. It is advisable to use ANN for the experimental data obtained. Additionally, incorporating bio-inspired optimisation methods can enhance the performance of ANN. There are various software packages available to model experimental data using ANN. Matlab is one such commonly used software, and luckily, Flinders University has a valid license for the latest version (R2023a). Matlab offers a professional package called "Neural Network Fitting," which is user-friendly and has several online tutorials for assistance. As an alternative, we can use Python programming language for this application. Indeed, applying ANN presents an exciting opportunity to further our understanding of photocatalytic activity. By leveraging machine learning techniques, we can unravel intricate relationships between catalyst properties and activity outcomes.

These proposed directions signify our commitment to advancing our understanding of photocatalysis, broadening its applications, and applying innovative methodologies to address complex challenges. Each avenue promises to contribute to the evolving landscape of materials science and sustainable technologies.

9.1. Reference:.

1 Berkani, M., Bouchareb, M. K., Bouhelassa, M. & Kadmi, Y. Photocatalytic degradation of industrial dye in semi-pilot scale prototype solar photoreactor: optimization and modeling using ANN and RSM based on Box–Wilson approach. *Topics in Catalysis* **63**, 964-975 (2020).

2 Hosseini, O., Zare-Shahabadi, V., Ghaedi, M. & Azqhandi, M. A. Experimental design, RSM and ANN modeling of tetracycline photocatalytic degradation using LDH@ CN. *Journal of Environmental Chemical Engineering* **10**, 108345 (2022).

3 Yang, Y. *et al.* Fabrication, characterization, and photocatalytic degradation potential of chitosan-conjugated manganese magnetic nano-biocomposite for emerging dye pollutants. *Chemosphere* **306**, 135647 (2022).

4 Malika, M. & Sonawane, S. S. The sono-photocatalytic performance of a novel water based Ti+ 4 coated Al (OH) 3-MWCNT's hybrid nanofluid for dye fragmentation. *International Journal of Chemical Reactor Engineering* **19**, 901-912 (2021).

5 Ayodele, B. V., Alsaffar, M. A., Mustapa, S. I. & Vo, D. V. N. Backpropagation neural networks modelling of photocatalytic degradation of organic pollutants using TiO2-based photocatalysts. *Journal of Chemical Technology & Biotechnology* **95**, 2739-2749 (2020).

6 Asoubar, S., Mehrizad, A., Behnajady, M. A., Ramazani, M. E. & Gharbani, P. Hexavalent chromium reduction and Rhodamine B degradation by visible-light-driven photocatalyst of stannum indium sulfide-samarium vanadate. *npj Clean Water* **6**, 27 (2023).

7 Chandrika, K., Prabhu, T. N., Kiran, R. S. & Krishna, R. H. Applications of artificial neural network and Box-Behnken Design for modelling malachite green dye degradation from textile effluents using TiO 2 photocatalyst. *Environmental Engineering Research* **27** (2022).